NUMERICAL INVESTIGATION OF FLOATING WIND TURBINE WAKE INTERACTIONS USING LES-AL TECHNIQUE

YUANTSO LI

AUGUST, 2023

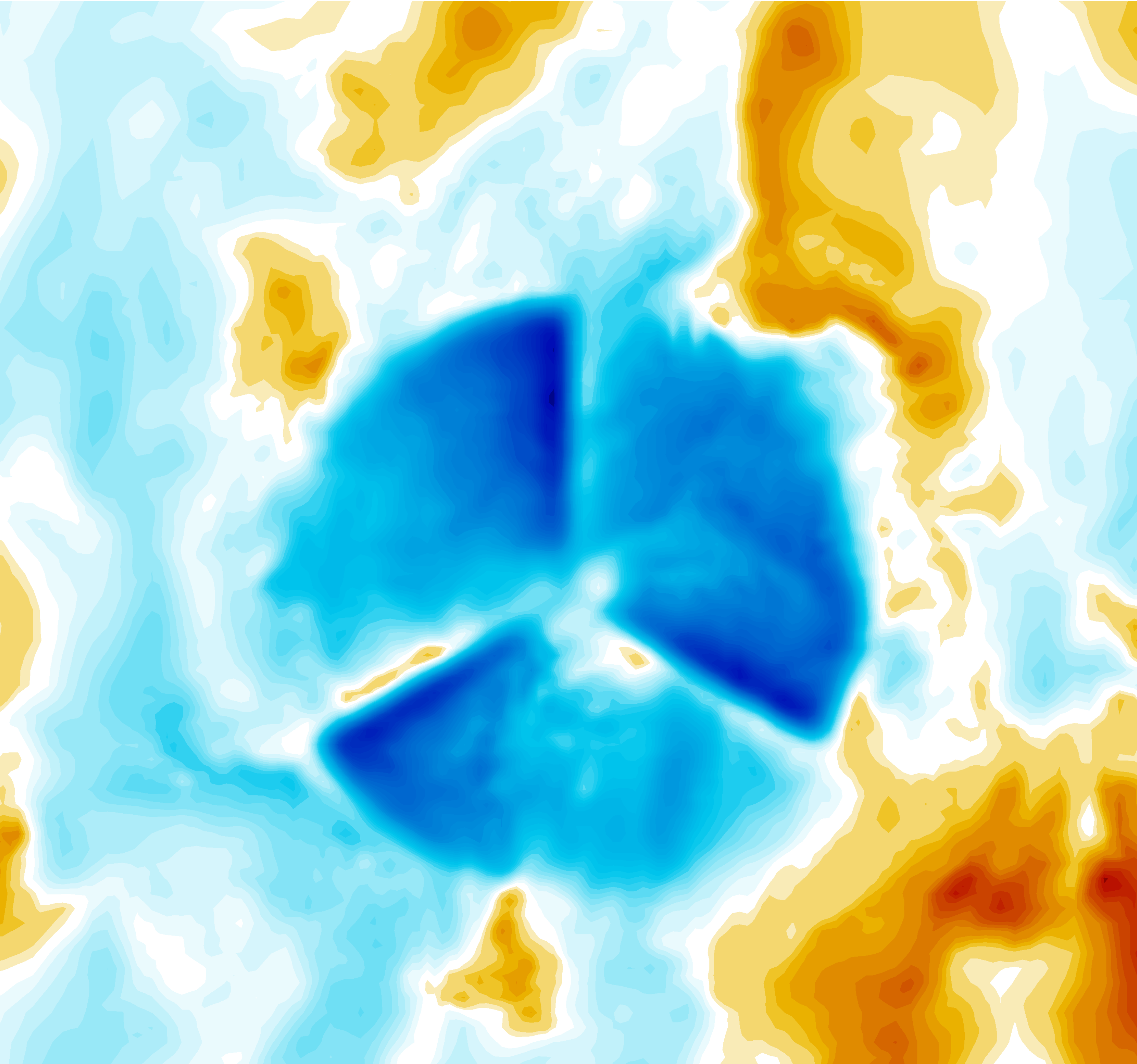

Numerical Investigation of Floating Wind Turbine Wake Interactions Using LES-AL Technique

by

YuanTso Li

s213775	DTU
5556619	TU Delft

EUROPEAN WIND ENERGY MASTER - ROTOR DESIGN

Double Degree Joint Education Master Programme

to obtain the degree of Master of Science
at the Technical University of Denmark and the Delft University of Technology,
to be defended publicly on August 22, 2023

THESIS COMMITTEE

Dr. Hamid Sarlak	Technical University of Denmark
Prof. Carlos Simão Ferreira	Delft University of Technology
Dr. Wei Yu	Delft University of Technology
Dr. Alexander van Zuijlen	Delft University of Technology

Preface

I have always dreamed to become an engineer, especially the one dealing with *big* things. As I was an undergraduate, this dream have eventually brought me to the realm of wind energy, where there have giant rotors spinning and huge impacts on people's everyday lives. To continue my journey with wind energy, I enrolled European Wind Energy Master (EWEM) program to pursue my master's degree, and this thesis is the final project of the program. EWEM program not only provided me vast amount of wind energy related knowledge, it also showed me the world is much bigger than I had thought; travelling, moving, and meeting people all over the world really were the main theme of the program. After exploring multiple aspects of wind energy with EWEM program, I have decided to focus on modelling rotor aerodynamics with CFD for my thesis, where there are super computers and large amount of data.

The topics of the thesis projects were first formulated through heuristic conversations with my supervisors, Hamid Sarlak and Carlos Simão Ferreira, and Wei Yu, who joined as another supervisor afterwards, also provided some valuable thoughts. I would like to thank you all for sharing your insights, allowing me to appreciate the topics more deeply.

Now, as I am finishing this thesis, the journey of EWEM has came to an end, and I would like to thank all people who have participated the journey with me, including my cohorts, professors, flatmates, new friends made during the program, and friends & family back in Taiwan. Without you guys, this two years would not be as wonderful as it is. Even though leaving is another daily events occurring during the EWEM days, I believe our memories of these days will last forever, and probably we are still going enjoy exiting future together.

YuanTso Li
August 2023, Copenhagen

Summary

Large scale wind farms consisting with floating offshore wind turbines (FOWTs) will be a solution for offshore wind energy industry to access more wind resources. However, wake structures and wake interactions of FOWTs subject to motions are still not yet been fully understand, especially when they are under turbulent inflow conditions with realistic turbulent intensities. These will be critical for designing floating offshore wind farms. Note that the majority of previous research are conducted with single rotor using models having relatively low fidelities and/or focusing on laminar inflow conditions. To advance the knowledge about wake and wake interactions of FOWTs, numerical studies about rotors of FOWT with prescribed harmonic surging motions are conducted in this thesis project with high fidelity CFD models, namely large eddy simulation (LES) coupled with actuator line model (ALM). Cases with single rotor without controller, dual rotors in tandem without controller, and dual rotors in tandem with controller are simulated with various of settings, including different surging settings and different inflow turbulence intensities.

For the cases with single rotor without controller, it is found that the differences of wake structures between fixed and surging rotors are pronounced when under laminar inflow conditions, where the periodic structures related to the harmonic surging motions can be detected straightforwardly; while the differences are much less significant when under inflow conditions with realistic turbulence intensities, and the periodic structures are clearly revealed only after phase-locked averaging. Moreover, surging cases with laminar inflow conditions have wake recovery rates which are significantly higher than the fixed case with laminar inflow; however, with turbulent inflow, wake recovery rates for surging cases are only slightly higher than the fixed case.

For the cases with dual rotors without controller, it is found that the wake interaction modes between the two rotors are significantly affected by the surging settings for the laminar cases, while the turbulent cases are insensitive. However, the power performances of the downstream rotors will be increased slightly with surging upstream rotors for the turbulent cases.

For the cases with dual rotors with controller, it is found that the implemented simple controller cannot improve the performances of the rotors as designed due to the large rotational inertia, and thus the modes of wake interactions are not altered a lot. However, the downstream rotors' operational parameters were successfully changed to more desirable values by the controller, demonstrating the controller's potential for numerical analysis of wake interactions between wind turbine rotors.

The findings of this effort demonstrates that the wake structures due to the surging motions of FOWT rotors will be smeared out by the ambient turbulence; and to achieve better power performances, more advanced controlling strategies may have to be implemented for FOWTs subject to surging motions.

Key words: Floating offshore wind turbines, Surging, Wake and wake interactions, Controller of FOWT, LES, Actuator line model

Contents

List of Tables

List of Figures

Nomenclature

Abbreviations

ADM	Actuator disk model
AEP	Annual energy production
ALM	Actuator line model
BEM	Blade element momentum
CFD	Computational fluid dynamics
CFL	Courant-Friedrichs-Lewy
DCC	DTU Computing Center
DFSEM	Divergence-free synthetic eddy method
DIC	Dynamical axial induction control
DNS	Direct numerical simulation
DoF	Degree of freedom
DWM	Dynamic wake meandering
FAST	Fatigue, Aerodynamics, Stress, and Turbulence
FF	Fixed upstream rotor with fixed downstream rotor
FOWT	Floating offshore wind turbine
FS	Fixed upstream rotor with surging downstream rotor
HAWT	Horizontal axis wind turbine
HIT	Homogeneous isotropic turbulence
IDDES	Improved delay detached eddy simulation
LCoE	Levelised Cost of Energy
LES	Large eddy simulation
LLT	Lifting-line theory
MPPT	Maximum power point tracking
NREL	National Renewable Energy Laboratory
PLSB	Periodic low speed bubbles
POD	Proper orthogonal decomposition
RANS	Reynolds-averaged Navier-Stokes equations
SF	Surging upstream rotor with fixed downstream rotor
SGS	Sub-grid scale
SOWFA	Simulator for Wind Farm Application
SS	Fixed upstream rotor with surging downstream rotor
TI	Turbulence intensity [%]
TKE	(Specific) turbulent kinetic energy [m^2/s^2]
TLP	Tension-leg platforms

UNAFLOW	Unsteady Aerodynamics for Floating Wind	
URANS	Unsteady RANS	
VM	Vorticity model	

Greek symbol

α	Angle of attack	[deg]
α_{stall}	Stalling angle	[deg]
Δp	Pressure difference with ambient pressure	[Pa]
Δt	Time step size	[s]
Δ	Grid size	[m]
Δ_D	Inter-distance between the two rotors	[m]
Δ_r	Inter-distance of actuator line points	[m]
$\Delta_{\phi_{S_0}}$	Phase differences of the two surging motions	[rad]
δ_{ij}^r	Kronecker delta	
η_ε	Gaussian regularization kernel	[m^{-3}]
γ	Twist (plus pitch) angle	[deg]
λ	Tip speed ratio	[-]
λ_{opt}	Optimal λ	[-]
ν	Kinematic molecular viscosity	[m^2/s]
ν_T	(Kinematic) Eddy viscosity	[m^2/s]
Ω	Rotational speed of rotor	[rad/s]
ω	Vorticity	[s^{-1}]
ω_S	Surging frequency	[rad/s]
ω_x	x-component ω	[s^{-1}]
Ω_{Tar}	Targeted Ω	[rad/s]
$\overline{\Omega}^{\text{quasi}}$	Quasi-steady states solution of $\overline{\Omega}$	[rad/s]
$\overline{\Omega}^{\text{quasi}}_{\text{Tar}}$	Targeted values of $\overline{\Omega}^{\text{quasi}}$	[rad/s]
ϕ	Inflow angle	[deg]
ϕ_S	Phase angle of surging	[rad]
ϕ_{Ω_0}	Phase angle shifting of ϕ_Ω	[rad]
ϕ_Ω	Phase angle of rotation	[rad]
ϕ_{S_0}	Phase angle shifting of ϕ_S	[rad]
ρ	Flow density	[kg/m^3]
ρ_{u_x}	Autocorrelation function of u in x-direction	[-]
σ_u	Standard deviation of u	[m/s]
τ_{Aero}	Aerodynamic torque	[Nm]
τ_{Gen}	Generator torque	[Nm]
τ_{ij}	Subgrid-scale stress tensor	[m^2/s^2]
τ_{ij}^r	Deviatoric part of τ_{ij}	[m^2/s^2]
θ_p	Blade pitch angle	[deg]
ε	Smoothing factor	[m]
ξ_{C_P}	Instantaneous power conversion rate	[kg/m]
ξ_{C_T}	Instantaneous thrust conversion rate	[kg/m]
Ω_{rated}	The value of Ω under rated condition	[rad/s]

Latin symbol

$<\text{TKE}>_{0\pi}$	Phase-locked TKE based on $\phi_S = 0\pi$ or $\phi_\Omega = 0\pi$	[m^2/s^2]

$< \sigma_u >_{0\pi}$	Standard deviation of $u_{0\pi}$	[m/s]
$< C_T >$	Cycle-averaged C_T	[-]
$< C_T >^+$	Maximum of $< C_T >$	[-]
$< C_T >^-$	Minimum of $< C_T >$	[-]
$< u >_{0\pi}$	Phase-locked averaged u based on $\phi_S = 0\pi$ or $\phi_\Omega = 0\pi$	[m/s]
$\mathbb{V}$	Ratio of maximum V_{WT} and V_0	[-]
$\mathbb{W}$	Reduced frequency (based on D)	[-]
$\overline{C}_P^{\text{down}}$	$\overline{C}_P$ for the downstream rotor	[-]
$\overline{C}_P^{\text{up}}$	$\overline{C}_P$ for the upstream rotor	[-]
$\overline{u}$	Time-averaged u	[m/s]
$\overline{u}_{\text{Disk}}$	Time-averaged u_{Disk}	[m/s]
$\overline{u}_{\text{Disk}}^{3D}$	$\overline{u}_{\text{Disk}}$ at $x = 3D$	[m/s]
$\overline{u}_{\text{Disk}}^{8D}$	$\overline{u}_{\text{Disk}}$ at $x = 8D$	[m/s]
$\boldsymbol{D}$	Drag force per unit span	[N/m]
$\boldsymbol{e}$	Unit vector	[m]
$\boldsymbol{f}_{2\text{D}}$	Local blade element force per unit span	[N/m]
$\boldsymbol{f}_{\text{body}}$	(Specific) Body force	[N/m^3]
$\boldsymbol{L}$	Lift force per unit span	[N/m]
$\boldsymbol{x}$	Position vector	[m]
$_{(\text{sur})}\overline{G}_{C_P}$	Gains of $\overline{C}_P$ due to the surging motions	[%]
A	Rotor swept area	[m^2]
A_S	Surging amplitude	[m]
B	Number of blade	[-]
c	Chord length	[m]
C_k	Model constant of Smagoransky model	[-]
C_P	Power coefficient	[-]
C_T	Thrust coefficient	[-]
C_ε	Model constant of Smagoransky model	[-]
$C_{P,\text{Aero}}$	C_P based on P_{Aero}	[-]
$C_{P,\text{Gen}}$	C_P based on P_{Gen}	[-]
$C_{P,\text{opt}}$	Optimal C_P	[-]
$C_{P,\text{Tar}}$	Targeted C_P	[-]
D	Rotor diameter	[m]
f	Frequency	[Hz]
F_n	Normal force per span	[N/m]
f_n	Normal force component (per unit span)	[N/m]
F_t	Tangential force per span	[N/m]
f_{tip}	Glauert tip correction factor	[-]
f_θ	Tangential force component (per unit span)	[N/m]
I	Rotational inertia of the system	[kg m^2]
I_{Gen}	Rotational inertia of generator	[kg m^2]
I_{hub}	Rotational inertia of hub	[kg m^2]
I_B	Rotational inertia of single blade	[kg m^2]
I_R	Rotational inertia of rotor	[kg m^2]
k_{sgs}	Sub-grid scale turbulence kinetic energy	[m^2/s^2]
K_τ	Coefficient of the controller	[m^{2}kg]

L_u	Integral length scale of u (in x-direction)	[m]
P	Power	[W]
p	Pressure	[Pa]
p_R	Position of the rotor center	[m]
p_R^{down}	p_R for the downstream rotor	[m]
p_R^{up}	p_R for the upstream rotor	[m]
P_{Aero}	Aerodynamic power	[W]
P_{Gen}	Generator power	[W]
p_{R_0}	Neutral position of the rotor center	[m]
q	Dynamic pressure	[Pa]
R	Rotor radius	[m]
r	Radial position	[m]
r_{hub}	Radius of hub	[m]
Re	Reynolds number	[-]
Re_c	Chord based Reynolds number	[-]
$S_u(f)$	Power spectrum of u	[m^2/s]
$S_{C_P^{\text{down}}}(f)$	Frequency spectrum of C_P^{down}	[s]
S_{ij}	Strain rate tensor	[s^{-1}]
T	Thrust	[N]
t	Simulation time	[s]
T_S	Period of a surging cycle	[s]
T_Ω	Period of a rotation	[s]
u	Instantaneous x-component velocity	[m/s]

u^*	Unresolved part of u after LES filtering	[m/s]
u'	Fluctuation part of u	[m/s]
$u_{0\pi}$	Phase-locked u based on $\phi_S = 0\pi$ or $\phi_\Omega = 0\pi$	[m/s]
u_{Disk}	Disk-averaged u	[m/s]
V	Velocity	[m/s]
v	Instantaneous y-component velocity	[m/s]
V_0	Inflow velocity	[m/s]
V_n	Normal (component) velocity	[m/s]
$V_{0,\text{app}}$	Apparent V_0	[m/s]
$V_{0,\text{rated}}$	The value of V_0 for rated condition	[m/s]
V_{ref}	Reference velocity	[m/s]
V_{rel}	Magnitude of relative velocity	[m/s]
V_{WT}	Surging velocity of rotor	[m/s]
V_θ	Tangential (component) velocity	[m/s]
$V_{n,\text{app}}$	Apparent V_n	[m/s]
w	Instantaneous z-component velocity	[m/s]
TKE_{sgs}	Sub-grid scale TKE	[m^2/s^2]
$\text{TKE}_{\text{total}}$	Total TKE	[m^2/s^2]

Operator

$< \cdot >$	Cycle-averaging
$\overline{\cdot}$	Time-averaging
$\tilde{\cdot}$	LES filtering

Chapter 1

Introduction

1.1 Background of Floating Offshore Wind Turbines and its Aerodynamics

Offshore wind energy has been widely developed since the 1990s as a solution to meet the rapidly increasing demand for sustainable energy [1, 2]. Numerous multibillion-dollar offshore wind farm projects are underway around the world and the installation rates are expected to rise steadily. Moreover, by 2050, a quarter to one-third of the total global electricity is expected to be supplied by wind power [3, 4]. The rapid development of offshore wind has pushed the industry to seek sites further away from coasts for more space and better wind resources, implying some of the future offshore wind farm sites will likely be deep enough (> 60 m) to give the floating concept an economic advantage over the traditional bottom-mounted one [1, 4, 5]. Thus, concepts of wind farms made up of floating offshore wind turbines (FOWT) arose as a result. However, as of 2023, only a few small scale pilot projects of floating offshore wind farms, such as HYWIND$^{\text{TM}}$ and WindFLoat$^{\text{TM}}$, have already been installed. Despite this, several countries have stated their intention to install large-scale FOWT projects within the next 15 years, including capacities of 15 GW in the United States [6], 14.5 GW in Scotland [7], and 1.2 GW in South Korea [8].

Though FOWT appears to be viable and promising at the moment, several aspects such as the effects of unsteady aerodynamics caused by platform motions have yet to be thoroughly explored [1, 4, 9]. Wind, wave, and current introduced by different wind conditions and sea states will affect the aerodynamic response of the FOWT rotor through the platform motions, and the aerodynamics of the FOWT rotors are considered highly unsteady based on reduced frequency analysis [10]. Several experimental and numerical studies have indicated that additional degree of freedom (DoF) introduced with platform motions will affect power performance and fatigue life time of FOWTs [10, 11, 12]. Furthermore, FOWTs' wake characteristics, such as the vortex system of its wake, have been reported to differ from bottom-mounted ones [9, 13]. These all pointed to that wake interactions of floating offshore wind farms may differ significantly to the traditional bottom-mounted counterparts, and it is a topic which is not yet been fully studied [9].

Understanding wind turbine wake properties and wake interactions is critical because they affect optimal wind farm layout, overall wind farm annual energy production (AEP), and fatigue life times for turbine components, which all heavily affect the levelised cost of energy (LCoE) [9, 14, 15]. Although wake interactions between traditional bottom-mounted wind turbines have already been studied for more than four decades [15, 16, 17, 18, 19], research about wake interactions between FOWTs is still very scarce in the literature [9].

It is proposed that wake recovery rate may be faster for FOWTs due to the extra unsteadiness (instabilities) introduced, and this may lead to shorter optimal inter-distances between turbines for floating wind farms when compared to the bottom-mounted ones [20, 21]. However, it is still unclear how much the motion effects impact the FOWTs wake recovery rates, especially when the inflow conditions are turbulent [22]. Thus, studies with experiments and high-fidelity simulations about the wakes and wake interactions of FOWTs are needed to better understand them. With this, LCoE of the future floating wind farms may be further optimized. Therefore, this research project will focus on high-fidelity simulations about wake and wake interactions of FOWTs.

Among the six types of platform motion (Figure 1.1), surging and pitching are the two that have the greatest impact on the rotor performances and wake aerodynamics of FOWTs. This is due to the fact that the apparent axial wind velocity perceived by the turbine rotors will be directly influenced. It is observed that surge motions are the most prevalent for FOWTs with tension-leg platforms (TLP) and semi-submersible types, whereas pitch motions are the most prevalent for spar types; as for the barge type, both motions are significant (Figure 1.2). In addition, small amplitudes of pitch motions can be linearized to surge motions, which simplifies the system dynamic [9, 23]. Thus, this thesis project will concentrate on studying FOWTs in surge motions.

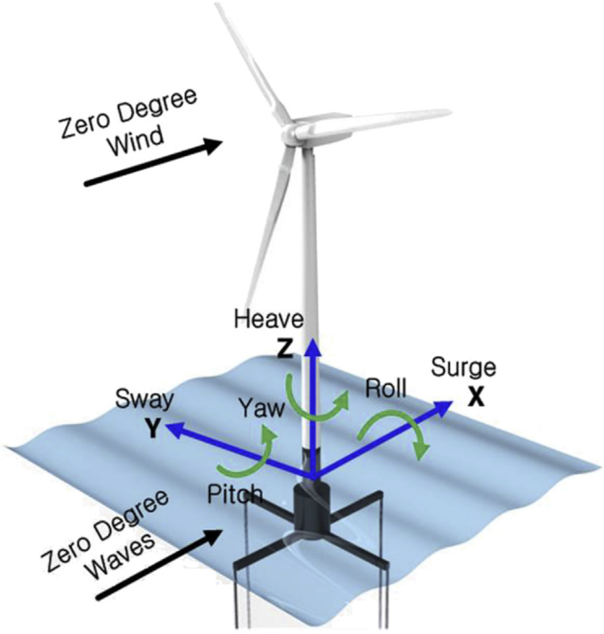

Figure 1.1: Diagram describing the six degree of freedoms for FOWT's platform motions. Taken from Tran et al. [10].

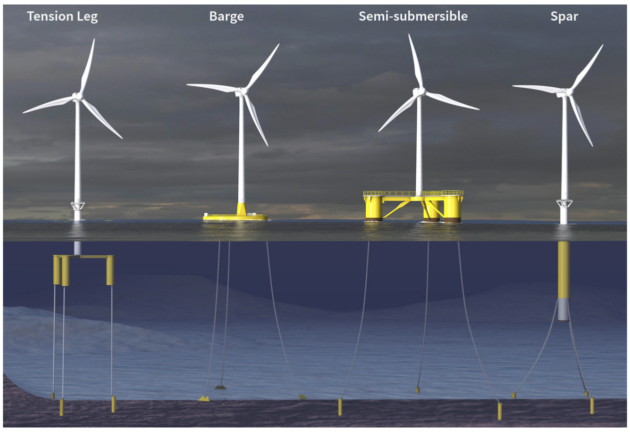

Figure 1.2: Typical floating platform concepts for FOWTs including TLP, barge, semi-submersible, and spar. Taken from Acteon [24].

1.2 Literature Review

Currently, there are three major approaches for studying wind turbine wakes, which are field tests, wind tunnel experiments, and numerical modelings [14]. These approaches also apply to floating offshore wind turbines (FOWTs) that are subjected to motions [9, 25]. However, employing full-scale FOWTs for both field tests and wind tunnel studies is exceedingly expensive and time-consuming, and scaling down FOWTs while meeting all the scaling laws, such as Reynolds number and Froude numbers, is nearly impossible [9, 25, 26]. Given that resources are limited, it is reasonable to investigate full scale FOWTs under motions using numeric methods.

Methods of numerical analysis of wind turbines can be further classified into three broad categories based on the model they are mostly employed. They are the blade element momentum (BEM) method group, the vorticity model (VM) group, and the computational fluid dynamics (CFD) group. All three groups are capable of performing numerical analysis of FOWT in motions with different degrees of fidelity, and have been validated and benchmarked using experimental data [9, 12, 23, 27]. Although BEM is the most popular method for developing and designing wind turbines in the industry due to its efficiency, it has the lowest fidelity among the three mainly due to engineering models are required and only rotor plane solutions are provided [28, 29]. In contrast, VM and CFD-based models provide flow field solutions for wakes. Despite that Sebastian et al. [30], Lee et al. [31], and Mancini et al. [23] have successfully used VM-based methods to capture the wake dynamics of FOWTs and revealed some distinct phenomena when compared to bottom-mounted ones, VM has its limitations since it assumes the flow is inviscid and irrotational [12]. These assumptions are not particularly valid when the flow scales are small and when the flow has large shear, which unfortunately is common for wind turbine wakes. Moreover, VM cannot handle turbulent inflow conditions well, which is its another major drawback. As for CFD-based approaches, they utilize the discritized three-dimensional Navier Stokes equations, which account for viscous effects and permit sheared flow. Though CFD-based methods are able to provide high-fidelity solutions of FOWT wakes, running it without modelling, namely direct numerical simulation (DNS), is still out of reach for wind turbine simulations at this stage due to the required computational resources being too intense. Hence, adequate modelling and parameterization are essential. Turbulence closure is the most relevant modeling in the realm of CFD, and for wind energy, Reynolds-averaged Navier-Stokes equations (RANS) are most commonly utilized, while large eddy simulation (LES) has gained favor in recent years [1, 18, 19, 32].

Since the time-averaged nature of RANS limits its utility for observing temporal variations, CFD with LES is frequently used nowadays if detailed information about wind turbine wake structures is interested. LES resolved the majority of turbulent fluctuations, only those with scales less than the filtering length are modeled through the sub-grid scale (SGS) model. Nonetheless, due to the high Reynolds number Re for typical running wind turbines and the required computational resources for LES scale with Re^2. Up until present, only very few studies had ran LES with completely represented wind turbine geometry [33], and it is too computationally intensive for parameter studies [32, 34, 35]. In lieu of inserting the geometry of the wind turbines in the flow field, the Navier-Stokes equations are solved by imposing body force fields representing wind turbines, which is widely known as actuator models. The concept of actuator models began to gain their popularity in the wind energy realm during the early 2000s [36, 37], currently these approaches are frequently utilized both with URANS (unsteady RANS) and LES [19, 32, 34]. Actuator models enable CFD simulations to be done without resolving the boundary layers of the blades, hence drastically reducing the grid number and increasing the time step size. It has been shown that URANS with full geometry representation of wind turbines requires about $\mathcal{O}(10^2)$ more CPU hours compared to LES with actuator line model, and adopting LES instead of URANS for blade-resolved representation would require another ten times more [10, 21, 33, 38].

Actuator disk model (ADM) and actuator line model (ALM) are the two most used actuator models for simulations of horizontal axis wind turbines (HAWT) with RANS and LES currently [18, 19, 39]. ADM reduces the complex geometry of the wind turbine rotor to a disk and then utilises the disk to apply body force to the flow. ALM, which was first developed by Sørensen et al. [36], degenerates the wind turbine rotor into rotating lines, which keeps significantly more geometric information than ADM. ALM is capable of resolving tip vortices, whereas ADM cannot due to the force averaging. Therefore, the actuator line model with LES should be utilized if the structures near the wake is of interest, even though ALM needs much more computational power [32, 34, 40]. For example, typical grid points across the rotor disk for ADM is about 15 while ALM is about 80 [39, 41]. Figure 1.3 illustrates the levels of details which ALM and ADM are able to provide. As can be seen in the regions close to the rotors, tip vortices are absent when modelling with ADM. Another significant advantage of ALM over full-geometry representation is that it may be coupled with aeroelastic codes easier, allowing fluid-structure interaction of wind turbines to be conducted at a reasonable computational cost. NREL (National Renewable Energy Laboratory), for example, combined SOWFA (Simulator for Wind Farm Application) and FAST (Fatigue, Aerodynamics, Stress, and Turbulence), where the former is the toolbox for ALM and the latter is the toolbox for aeroelastic codes [42]. Numerous research studies have been undertaken with ADM and ALM with various kind of turbulence model, both bottom-mounted wind turbines and FOWTs in motions, as it can be found in Table 1.1.

Table 1.1: Partial list of publications related to the current research. Here entry FM stands for force model for the turbines and MT is for whether the study consider cases with multiple turbines. LLT and DWM is acronym for lifting-line theory and dynamic wake meandering model. Note that study of Mancini et al. [23] did experimental studies and numerical studies with ALM, LLT, geometric resolved, and BEM method with engineering models.

Authors	**Year**	**TM/WM**	**FM**	**Motion**	**MT**	**Turbine/Airfoil**
Niels Troldborg [43]	2009	LES	ALM	fixed	O	Tjæreborg/NM80
Wu et al. [32]	2011	LES	ADM	fixed	X	GWS/EP-6030x3
Sebastian et al. [30]	2012	VM	LLT	various	X	NREL 5MW
Tran et al. [44]	2014	RANS	geometric resolved	pitching	X	NREL 5MW
Sarlak et al. [17]	2015	LES	ALM	fixed	O	NREL S826
Micallef et al. [45]	2015	RANS	ADM	surging	X	NREL 5MW
Tran et al. [10]	2016	RANS	geometric resolved	surging	X	NREL 5MW
Farrugia et al. [12]	2016	VM	LLT	complex	X	NREL 5MW
Cormier et al. [46]	2018	RANS	geometric resolved	surging	X	1/75 DTU 10MW
Draper et al. [47]	2018	LES	ALM	fixed	O	G1
Wang et al. [48]	2018	LES	ALM	pitching	O	G1
Sivalingam et al. [27]	2018	LES	geometric resolved	surging	X	1/126 NREL 5MW
Sedaghatizadeh et al.[33]	2018	RANS	geometric resolved	fixed	X	NREL phase VI
Johlas et al. [49]	2019	LES	ALM	complex	X	NREL 5MW
Cheng et al. [50]	2019	RANS	ALM	complex	X	NREL 5MW
Lee et al. [31]	2019	VM	LLT	complex	X	NREL 5MW
Thor Heine Snedkerg [51]	2020	LES	ADM	surging	O	GWS/EP-6030x3
Mancini et al. [23]	2020	various	various	surging	X	1/75 DTU 10MW
Wise et al. [52]	2020	DWM	FAST	complex	O	DTU 10MW
Revaz et al. [40]	2021	LES	ADM	fixed	X	WiRE-01
Johlas et al. [11]	2021	LES	ALM	complex	X	NREL 5MW
Rezaeiha et al. [20]	2021	RANS	ADM	surging	O	NREL 5MW
Xue et al. [53]	2022	LES	ALM	fixed	O	NREL 5MW
Chen et al. [21]	2022	IDDES	geometric resolved	surging	O	NREL S826

Table 1.1 is a partial list of relevant works on the numerical study of both bottom-mounted wind turbine and FOWT wakes with various methods and models. It can be seen that several investigations on FOWT in motion have been undertaken, including those with simple prescribed motion or hydrodynamic coupled (complex) motion. Even with minor amplitudes, the effects of platform motions on the aerodynamic performances (C_T and C_P) of FOWTs have been reported to be considerably [10, 44]. Moreover, theoretically, the time-averaged power converted by the surging turbines is expected to be greater than that of the bottom-mounted turbines, as the surging FOWT receives additional inputs of kinetic energy [1, 11]. Despite the fact that some studies have discovered a larger time-averaged C_P for surging FOWT [11, 12, 45, 51, 54], others have found that it is mostly unchanged [23].

In addition to affecting the performances of FOWTs, surging also alters the wake properties, which further influence the performances of the downstream turbines. Several studies have demonstrated that FOWT in motion will exhibit wake structures that are distinct from those of the bottom-mounted counterparts, such as the distances between the two subse-

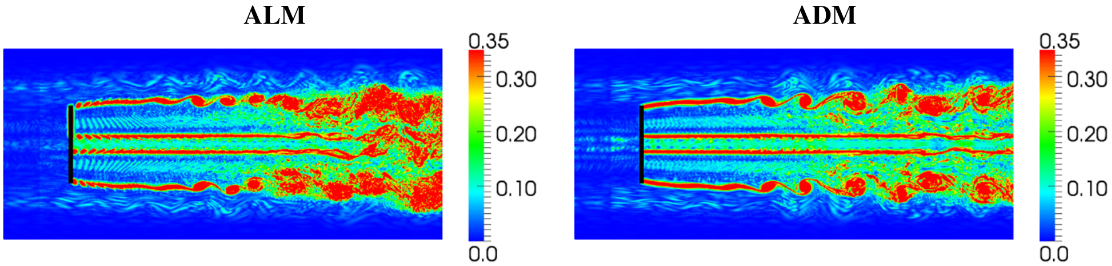

Figure 1.3: Comparison of instantaneous vorticity magnitude (s^{-1}) contours between ALM and ADM using LES, special focus should be placed at regions just behind the rotors. Taken form Martinez et al. [39].

quent tip vortices will vary as the platform moves (Figure 1.4) and the modes of interactions between the released tip vortices are different for fixed rotors and FOWT rotors in motion (Figure 1.5) [10, 12, 13, 31, 50, 55]. In addition, C_T of a sinusoidally surging FOWT varies [10, 23], which also influences the wake dynamics since the axial velocity of wake (axial induction) is directly related to C_T [21, 29, 56, 57]. These all suggest that the wake interaction among FOWTs in motion is different from the bottom-mounted ones. Moreover, in the circumstances of sinusoidally surging, it is hypothesized that the wakes of the surging FOWTs will have faster wake recovery rates compare to the fixed ones due to the additional instabilities introduced to the wakes resulting form the time-varying thrust force, and thus the turbines operate under wake conditions of surging FOWTs will likely to have bigger C_P. Indeed, Kopperstad et al. [57] had found a faster wake recovery rate for FOWT in motions with ADM using LES, and Rezaeiha et al. [20] had found turbine operates in wake of surging FOWT generates slightly more power when comparing to operating in the wake of fixed turbine with ADM using URANS. Note that this idea is very similar to the dynamical axial induction control (DIC), which has been proven being able to increase overall power performances of multiple aligned wind turbines experimentally [58]. The main idea of DIC is to actively adjusting the thrust force of rotor to enhance the mixing process of wakes, and this may lead to faster wake recovery rates; notice that time-varying thrust force is one of the major feature of FOWTs in motions.

Though several works have indicated the wake interactions within floating wind farms may be very different to the bottom-mounted ones, very limited studies had looked into these topics [9], and most of them are not using models with very high-fidelity. For instance, Wise et al. [52] had utilized FAST.Farm with dynamic wake meandering model (DWN) to investigate wake meandering and fatigue loading of two aligned FOWTs, while no comparison have been made between the fixed ones. On the other hand, Rezaeiha et al. [20] focused on comparing C_T and C_P for a fixed turbine operating under the wake of fixed or surging turbine using CFD (ADM with URANS), showing that surging motions may slightly increase the outputted power of the downstream turbine. It should be notice that none of these model can capture the dynamics of tip-vortices and neither able to resolute the transient flow fields well. In light of this, this thesis project is aimed to provide additional insight and knowledge about wake interactions between FOWTs with a higher fidelity model, namely LES with

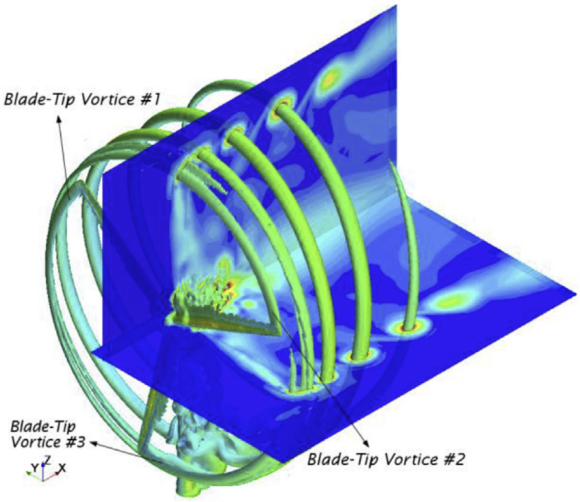

Figure 1.4: Isosurface of vorticity and vorticity contour obtained through simulation using blade resolve with URANS (surging FOWT). Taken from Tran et al. [10].

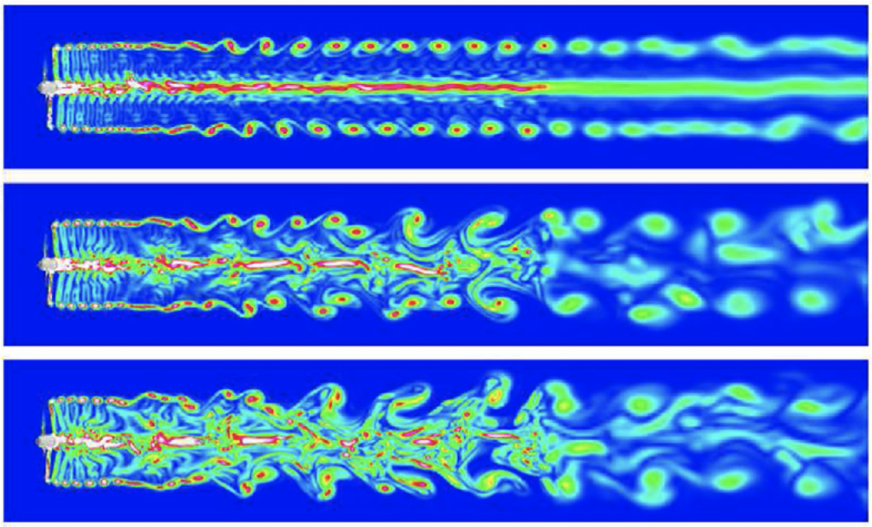

Figure 1.5: Contours of vorticity magnitude showing different interaction modes between tip-vorticies with FOWTs subjected to different surging motions. The rotor in top panel is fixed, while the middle and the bottom are surging with same frequency, and the surging amplitude of the bottom is twice of the middle one. Results are obtained through simulations using improved delayed detached eddy simulation (IDDES) with geometric resolved rotor. Taken from Chen et al. [55].

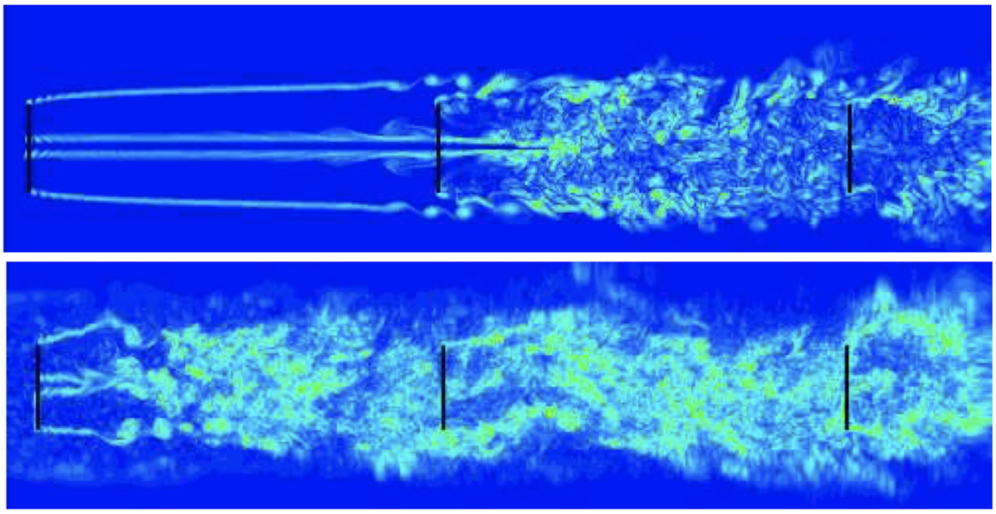

Figure 1.6: Effect of background turbulence on wake structures of wind turbine (vorticity contour), the inflow conditions for upper figure is laminar while lower figure is turbulent. Taken from Troldborg [43].

ALM, which has been described previously.

Note that there are very few studies about FOWT wakes using LES or IDDES (improved delay detached eddy simulation), and most of them either imposed a laminar inflow conditions [21, 55, 59, 60] or only focus on the rotor performances [11]. It should be noted that Troldborg has already reported that wakes of bottom-mounted wind turbines are very different when under laminar or turbulent inflow conditions using LES with AL (Figure 1.6) [43], and Sarlak also pointed out the length for wind turbine wake to breakdown will be unrealistic when under laminar inflow conditions [61]. Johlas et al. [49] used LES with ALM to investigate FOWT subject to different environmental conditions, including inflow wind speed and turbulence intensities. And they showed that motions of FOWTs may slightly increase turbulence intensity when compared to the fixed ones. On the other hand, Kopperstad et al. [57] used LES with ADM to model the wake of FOWT, they discovered that FOWTs in motions accelerated the wake recovery process both under laminar and turbulent inflow conditions, and they have discovered distinct wake structures (low-frequency modulation) with the snapshots of the instantaneous wake velocity contours; however, since ADM was deployed, information about tip-vorticies were not obtained. Regarding this, this work is going to study wakes of FOWTs both under laminar and turbulent conditions with high-fidelity numerical model able to capture tip vorticies (ALM), and report their instantaneous data as well as their statistics.

1.3 Objectives and Research Questions

Using CFD tools, particular actuator line model (ALM) with large eddy simulation (LES), this thesis project explored how several parameters affect the wake and wake interactions of sinusoidal surging full scale horizontal axis FOWTs (NREL 5 MW baseline turbine [62]). Moreover, for simplicity, the effects of tower, wind shear, and ground are neglected to better focus on the effects of surging; and most cases are implemented without rotor controlling, while some cases have simple torque controller. For cases with two rotors, their rotor centers are aligned in streamwise direction (in tandem). Note that barley no previous studies had used CFD tools with fidelity as high as this project to study wakes and wake interactions of FOWTs under turbulent inflow conditions as already stated in section 1.2.

One of the major goals is to find out whether the surging of FOWTs promotes the wake recovery and to see how the performances of rotors (especially the downstream ones) being influenced with different parameters. Parameters studied are ambient turbulence intensities, amplitudes of surging, frequencies of surging, streamwise separations (spacings) between the rotors, and phase differences of surging motions between FOWTs (Figure 1.7).

It had been expected that not all the parameters are equally influential, and this study will demonstrate the roles of the mentioned parameters when it comes to the wakes and wake interactions of FOWTs. Based on the prior studies, the two most important considered parameters are ambient turbulence intensities and surging frequencies. The former is based on the previous study with fixed turbines [43], and clearly the effect of ambient turbulence can be seen in Figure 1.6; while the latter is due to suggesting higher surging frequencies may shorten the inter-distances between the coherent structures introduced by surging, which lead to different interactions modes among them. As stated earlier, Kopperstad et al. had found special coherent structures (low-frequency modulation) in wakes of FOWT in motion [57], and they also showed this phenomenon would decay faster in turbulent inflow conditions (TI = 5%) compare to laminar. And thus, how wake structures of FOWT different from laminar and turbulent inflow conditions will also be a major focus.

The research questions of this thesis are listed below.

1. Will surge motions of FOWT significant alter its wake structures under both laminar and turbulent inflow conditions (with realistic turbulence intensity)? If yes, how are the wake structures related to surging amplitudes A_S and surging frequencies ω_S?

2. Will the effects of the surging motions on the wakes of FOWT facilitate the recovery rates of mean disk-averaged (area-averaged) velocity $\overline{u}_{\text{Disk}}$? If yes, how are the increasing rates related to related to inflow (ambient) turbulence intensities?

3. How do the surging motions affect the wake interactions between two wind turbine rotors (both with laminar and turbulent inflow conditions)? Will the performances of the downstream rotor be significantly affected by whether the upstream rotor is surging or fixed? Is the phase angle difference of surge motions $\Delta_{\phi_{S_0}}$ critical for the system?

4. Is it possible to improve the rotor performances of surging FOWT by implementing simple controlling strategies? For two aligned rotor, does the controller significantly affected the rotor performances and the modes of wake interactions?

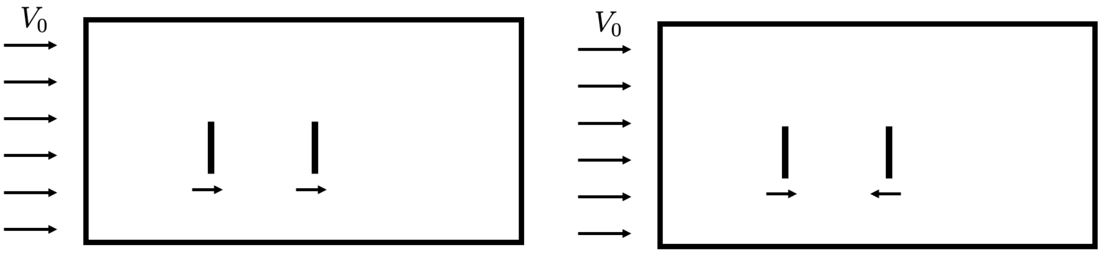

Figure 1.7: The schematic diagrams for two aligned FOWT rotors surging in-phase (left) and out-of-phase (right).

1.4 Thesis Outline

chapter 2 briefs over the methodologies used for the simulations, including large eddy simulation (LES), synthetic turbulent inlet conditions, and actuator line model (ALM). Also that the way of carrying out phase-locked averaging and the methods of the controller are explained in this chapter. chapter 3 describes the detail setups about the simulation framework, including the software & hardware used, discretization schemes, rotor models used, meshes, boundary conditions, and other input parameters such as turbulence intensities (TI) and operational parameters of rotors. Verifications and validations about the framework are also carried out.

In chapter 4, cases with single rotor (without controller) with different surging settings (A_S & ω_S) under laminar or turbulent (TI = 2.7, 5.3, or 11.6%) inflow conditions are conducted and analyzed. The repeating structures in wakes (periodic low-speed bubbles, PLSB) are found, and they are investigated. How C_T & C_P behave as well as angle of attack α when the rotor is surging are also looked into.

chapter 5 investigates the wake interactions between two rotors (without controller) in tandem with different fixed-surging conformations, different separation distances (spacings), different phase differences between the two surging motions, and different inflow turbulence intensities. Effects of surging on time averaged power performances of the two rotors are looked into, and angle of attack of the downstream rotor is also focused.

chapter 6 studies the cases with simple controller implemented. Effectiveness of the controller is overviewed, and time-averaged power performances are looked into. Cases with and without controller are compared, and the effects of surging on cases with controller are also visited.

chapter 7 concludes the works of this thesis projects and provides some recommendations and possible topics to study for future works.

Chapter 2

Methodology

In this chapter, a brief overview about the models, methods, and techniques used during the numerical simulations in this thesis project are presented.

2.1 Large Eddy Simulation

When solving the three-dimensional Navier-Stokes equations with LES, most turbulence motions are resolved explicitly, whereas the so-called subgird-scale (SGS) model only parameterizes those having scales smaller than the filtering length (which usually related to the grid size Δ) [32, 34]. SGS model enables LES to give dependable temporal information with significantly less computing effort than DNS, primarily by permitting a significantly larger mesh sizes and time steps [61, 63]. Despite being more computationally intensive than RANS, LES can provide sufficient instantaneous turbulence information for understanding the near wake structures of wind turbine rotors, whereas RANS hardly can. This is primarily due to the time-averaged nature of RANS and the fact that RANS parameterizes all turbulent effects [19, 32, 34]. Another major drawback when using (unsteady) RANS to model wake of rotor is that RANS is generally over dissipative, and will over smooth out the finest structures of the wake [61, 64]. Thus, LES is more desirable over than unsteady RANS for modelling wakes of wind turbines if detail flow structures are interested.

In most cases, LES is considered as dealing with low-pass filtered flow variables that vary spatially, such as velocity u_i and pressure p in Navier-Stokes equations. These values are decomposed as Equation 2.1, where $\tilde{u}_i$ represents the filtered (resolved) velocity and u_i^* represents the subgird-scale (unresolved) velocity. Here tilde denotes the filtering operator. The filtered Navier-Stokes equations are used to solve the flow field using only the resolved parts, while the SGS model handles the impacts of the unresolved parts which cannot be resolved explicitly (closing the closure problem). Equation 2.2 and 2.3 are the filtered momentum and continuity equations of the three-dimensional incompressible Navier-Stokes equations without taking into account the thermal effect (buoyancy) of the flow, where ρ, ν, and $\tilde{f}_{\text{body},i}$ represent the density of the flow, kinematic molecular viscosity, and the filtered external body force.

$$u_i = \tilde{u}_i + u_i^*, \qquad p = \tilde{p} + p^* \tag{2.1}$$

$$\frac{\partial \tilde{u}_i}{\partial t} + \frac{\partial (\tilde{u}_i \tilde{u}_j)}{\partial x_j} = -\frac{1}{\rho}\frac{\partial \tilde{p}}{\partial x_i} + \frac{\partial}{\partial x_j}\left[\nu\left(\frac{\partial \tilde{u}_i}{\partial x_j} + \frac{\partial \tilde{u}_j}{\partial x_i}\right)\right] - \frac{\partial \tau_{ij}}{\partial x_j} + \frac{\tilde{f}_{\text{body},i}}{\rho} \tag{2.2}$$

$$\frac{\partial \tilde{u}_i}{\partial x_i} = 0 \tag{2.3}$$

Note the term τ_{ij} (Equation 2.4) in Equation 2.2 represent the subgrid-scale stress tensor, and it is not possible to obtain the actual values of τ_{ij} solely with the resolved quantities ($\tilde{u}_i$). To overcome this, the term in often modelled through eddy viscosity ν_T by employing Boussinesq hypothesis in the form of Equation 2.6. Since incompressible flow is considered for this project, the isotropic part of τ_{ij}, $1/3\delta_{ij}\tau_{kk}$, in Equation 2.2 can be neglected, and only the deviatoric part is needed to be considered [65], which is τ^r_{ij} in Equation 2.5. After substituting τ_{ij} with τ^r_{ij} and utilizing ν_T to model τ^r_{ij} in Equation 2.6, Equation 2.3 can be rewritten as Equation 2.7 in a simplified form [34, 41, 61].

$$\tau_{ij} = \widetilde{u_i u_j} - \tilde{u}_i \tilde{u}_j \tag{2.4}$$

$$\tau^r_{ij} = \tau_{ij} - \frac{1}{3}\delta_{ij}\tau_{kk}, \qquad \tau_{ij} \simeq \tau^r_{ij} \tag{2.5}$$

$$\tau^r_{ij} \underbrace{=}_{\text{modelling}} -2\nu_T \tilde{S}_{ij}, \qquad \tilde{S}_{ij} = \frac{1}{2}\left(\frac{\partial \tilde{u}_i}{\partial x_j} + \frac{\partial \tilde{u}_j}{\partial x_i}\right) \tag{2.6}$$

$$\frac{\partial \tilde{u}_i}{\partial t} + \tilde{u}_j \frac{\partial \tilde{u}_i}{\partial x_j} = -\frac{1}{\rho}\frac{\partial \tilde{p}}{\partial x_i} + \frac{\partial}{\partial x_j}\left[(\nu + \nu_T)\left(\frac{\partial \tilde{u}_i}{\partial x_j} + \frac{\partial \tilde{u}_j}{\partial x_i}\right)\right] + \frac{\tilde{f}_{\text{body},i}}{\rho} \tag{2.7}$$

Smagoransky model [66] is one of the most prevalent SGS models, and it is renowned for its simplicity and robustness. It assumes that the turbulence energy generated by large-scale flow structures is in equilibrium with the energy drain caused by the small-scale turbulence through energy cascade, with the (molecular) dissipation would occur exclusively at the subgrid-scale. It models ν_T with Equation 2.8 which depends on the filtering (grid) length Δ. Note that C_k and C_ε are the model constants and their values used in this thesis are $C_k = 0.094$ and $C_\varepsilon = 1.048$, which are based on assuming the turbulence being homogeneous isotropic turbulence (HIT). Note that k_{sgs} is the sub-grid scale turbulence kinetic energy (Equation 2.9), which is the turbulence kinetic energy modeled by SGS model. Although there are other more sophisticated SGS model being utilized [17, 34, 41], such as Lagrangian dynamic scale dependent model which adjust values of model constants (C_k & C_ε) locally through Germano identity and test filters [67, 68]; however, it was shown that that the choice of SGS model and model coefficients are not deterministic factors for wake and load profiles when simulating wind turbines using LES with ALM, so long as the resolutions of the grids and the actuator lines are adequate ($\geq$ 35 points per radius) [17, 69, 70]. And thus, due to its simplicity and resiliency, standard Smagoransky model is selected for the current work.

$$\nu_T = C_k \Delta \sqrt{k_{\text{sgs}}} = C_k \sqrt{\frac{C_k}{C_\varepsilon}} \Delta^2 \sqrt{2\tilde{S}_{pq}\tilde{S}_{pq}} \tag{2.8}$$

$$k_{\text{sgs}} = \frac{1}{2}\left(u_i^* u_i^*\right) \tag{2.9}$$

One should notice that that other than this section in this thesis, the "velocity" is referred to the "filtered (resolved) velocity". That is, u_i outside this section is referred to $\tilde{u}_i$ (unless mentioned otherwise), and purpose of this is to make notations simpler.

2.2 Synthetic Turbulent Inlet

For the turbulent inlet conditions, it is fulfilled by divergence-free synthetic eddy method (DFSEM) [71]. This synthetic turbulent inlet is able to introduce inflow with desirable turbulence intensities, length scales, and anisotropy with much less computational efforts compare to the precursor method. For more information about DFSEM, please refer to Poletto et al. [71].

2.3 Actuator Line Model with Surging Motions

As previously stated, the complex geometry of the wind turbine rotor can be parameterized using the rotating lines of body force fields known as the actuator line model (ALM). It is done by replacing the effects of the no-slip boundary conditions imposed by the geometry shapes of wind turbines with desired body force fields ($\tilde{f}_{\text{body},i}$ in Equation 2.7). By doing so, the solutions of the boundary layers around the wind turbines are avoided, dramatically reducing the computational demand due to allowing much bigger time steps and much larger grid sizes. The calculations of the body force fields $\tilde{\boldsymbol{f}}_{\text{body}}$ are done with blade element approach, and it can be visualized with the well known velocity triangle (Figure 2.1). The blade element approach starts with solving the local lift and drag forces $\tilde{\boldsymbol{f}}_{2D}(r)$ (radial forces are assumed to be negligible) with the given local flow velocity and tabulated airfoil polar data at each actuator line position, as outlined in Equation 2.10 to 2.13. Here, V_{rel}, ϕ, and α represent the local flow velocity magnitude, the flow angle, and the angle of attack at the blade element sections (actuator line points), which are typically measured at the position of aerodynamic center. ρ, c, γ, and r represent the flow density, chord length, twist (plus pitch) angle local to the blade, and radial position, respectively. $\boldsymbol{L}$ & $\boldsymbol{D}$ are the local lift & drag forces per unit span. $C_L(Re_c, \alpha)$ & $C_D(Re_c, \alpha)$ are the local lift & drag coefficients, and their values are determined using the tabulated airfoil polar data in accordance with the chord based Reynolds number Re_c and angle of attack α. As for V_n & V_θ and $\tilde{f}_n$ & $\tilde{f}_\theta$, they are normal & tangential velocities and normal & tangential force components, and Ω is the rotational speed of the rotor. After calculating $\tilde{\boldsymbol{f}}_{2D}(r)$, the force distributions of the actuator lines are then projected onto the computational grids of CFD [17, 34, 38, 72].

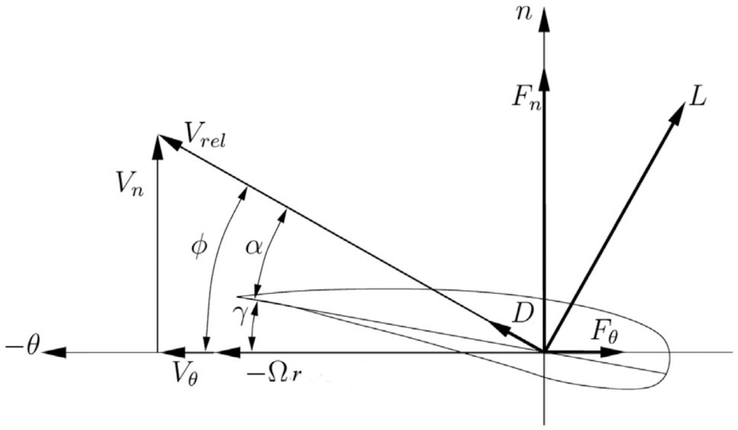

Figure 2.1: Velocity triangle of a typical blade element. Taken from Sarlak et al. [17].

$$\tilde{\boldsymbol{f}}_{2D}(r) = (\boldsymbol{L}, \boldsymbol{D}) = \frac{1}{2}\rho V_{\text{rel}}^2 c \Big(C_L(Re_c, \alpha)\boldsymbol{e}_L, C_D(Re_c, \alpha)\boldsymbol{e}_D \Big) \tag{2.10}$$

$$V_{\text{rel}} = \sqrt{V_n^2 + (-\Omega r + V_\theta)^2} \tag{2.11}$$

$$\phi = \arctan\left(\frac{V_n}{-\Omega r + V_\theta}\right), \qquad \alpha = \phi - \gamma \tag{2.12}$$

$$\tilde{f}_n = |\boldsymbol{L}|\cos\phi + |\boldsymbol{D}|\sin\phi, \qquad \tilde{f}_\theta = |\boldsymbol{L}|\sin\phi - |\boldsymbol{D}|\cos\phi \tag{2.13}$$

The force fields are projected from actuator lines onto the CFD computational grid through Equation 2.14, where $\boldsymbol{x}$ is the position vector of a cell centered grid point, B is number of the actuator lines (blades), R is the rotor radius, r_i is the radial distance of the ith line, $\boldsymbol{e}_i$ is the unit vector in the radial direction of the ith actuator line, and $\boldsymbol{p}_R$ is the position vector of the rotor center. Note that $\eta_\varepsilon(d)$ (Equation 2.15) is the Gaussian regularization kernel to smear out $\tilde{\boldsymbol{f}}_{2D}(r)$ into 3D space in order to avoid numeric instabilities, with d being the distance between cell centered grid point and the point of considered actuator line point, while ε is the smoothing factor [17, 34]. Also notice that before projecting the force to the computational grid with the Gaussian regularization kernel, Glauert tip correction f_{tip} was applied to ensure the loading at the blade tips drop to zero, as shown in equation Equation 2.16. This empirical correction is needed since ALM will over predict the loads around the tip (root) regions due to the coarse grid and the force smearing process with $\eta_\varepsilon(d)$ in Equation 2.15 [73, 74]. After the calculation of $\tilde{\boldsymbol{f}}_{\text{body}}(\boldsymbol{x})$, Equation 2.7 is then solved.

$$\tilde{\boldsymbol{f}}_{\text{body}}(\boldsymbol{x}) = \sum_{i=1}^{B} \int_0^R f_{\text{tip}}(r_i)\tilde{\boldsymbol{f}}_{2D}(r_i)\eta_\varepsilon(\|\boldsymbol{x} - (r_i\boldsymbol{e}_i + \boldsymbol{p}_R)\|)\mathrm{d}r_i \tag{2.14}$$

$$\eta_\varepsilon(d) = \frac{1}{\varepsilon^3 \pi^{3/2}} \exp\left[-\left(\frac{d}{\varepsilon}\right)^2\right] \tag{2.15}$$

$$f_{\text{tip}}(r) = \frac{2}{\pi} \arccos\left[\exp\left(-\frac{B(R-r)}{2r\sin\phi)}\right)\right] \tag{2.16}$$

Note that the aforementioned ALM framework is for the traditional bottom-mounted wind turbines. Adjustments are needed for the surging FOWTs. In order to account for the surging effects, V_{rel} in Equation 2.10 and ϕ in Equation 2.12 will be adjusted to Equation 2.18. Here, V_{WT} is the surging velocity of the FOWT and $V_{n,\text{app}}$ is the apparent normal velocity seen by the actuator line points (Equation 2.17, note the sign). Another important change is $\boldsymbol{p}_R$ in Equation 2.14 becomes time dependent ($\boldsymbol{p}_R(t)$), due to the fact that the position of the rotor's center will shift as it surges.

$$V_{n,\text{app}} \triangleq V_n - V_{\text{WT}} \tag{2.17}$$

$$V_{\text{rel}} = \sqrt{V_{n,\text{app}}^2 + (-\Omega r + V_\theta)^2}, \qquad \phi = \arctan\left(\frac{V_{n,\text{app}}}{-\Omega r + V_\theta}\right) \tag{2.18}$$

2.4 Defining Surge Motions and Phase-Locking

In this thesis, the surge motions are sinusoidal and prescribed. The streamwise position (x-position) of the rotor $p_R(t)$ in surge motion are defined as Equation 2.19. Here A_S is the surging amplitude, ω_S is surging frequency, ϕ_S is the phase angle of surging, ϕ_{S_0} is the phase shift of surging, and p_{R_0} is the neutral x-position of the rotor. Note that $\phi_S = 0\pi$ and $p_{R_0} = 0$ are kept for the upstream rotor in this thesis if not mentioned otherwise for convenience (Equation 2.20).

$$p_R(t) = A_S \sin\left(\omega_S t + \phi_{S_0}\right) + p_{R_0} = A_S \sin\phi_S + p_{R_0} \tag{2.19}$$

$$p_R(t)\Big|_{\phi_{S_0}=0,\, p_{R_0}=0} = A_S \sin\omega_S t \tag{2.20}$$

In order to better analyze the wake system of surging FOWT, a phase-locking between the surging frequency ω_S and rotational frequency of the rotor Ω was introduced. This is realized by making Ω being a integer multiple of ω_S, and this ensures that for every specific ϕ_S in every surge cycle will correspond to a same rotational phase angle of the rotor ϕ_Ω; the criteria may be loosen to making 3Ω being a integer multiple of ω_S for the three bladed rotor due to the 120° symmetry. ϕ_Ω is described in Equation 2.21, with ϕ_{Ω_0} being the phase shift of rotor's rotation, and $\phi_{\Omega_0} = 0$ is kept for the cases here. And for this thesis, $\phi_\Omega = 0$ corresponds to one of the blade pointing in positive z-direction. When analyzing parameters with phase-locking technique, say u as $\phi_S = 0\pi$, it is denoted as $u_{0\pi}$. And $< u >_{0\pi}$ will be the averaged value of $u_{0\pi}$ in a time period, while $< \sigma_u >_{0\pi}$ is the standard deviation of

$u_{0\pi}$, as shown in Equation 2.22. Moreover, in analogy of the turbulence kinetic energy TKE, a phase-locked averaged TKE at ϕ_S (<TKE>$_{\phi_S}$) is introduced here to better understand the extent of velocity fluctuations with the effects of phase difference (ϕ_S & ϕ_Ω) removed. Definitions of TKE and <TKE>$_{\phi_S=0\pi}$ for this thesis are shown in Equation 2.23.

$$\phi_\Omega = \Omega t + \phi_{\Omega_0} \tag{2.21}$$

$$< u >_{0\pi} = \frac{\sum_{n=1}^{N} u_{0\pi,n}}{N}, \qquad < \sigma_u >_{0\pi} = \sqrt{\frac{\sum_{n=1}^{N} \left(u_{0\pi,n} - < u >_{0\pi}\right)^2}{N}} \tag{2.22}$$

$$\text{TKE} = \frac{1}{2}\left(\sigma_u^2 + \sigma_v^2 + \sigma_w^2\right) \qquad < \text{TKE} >_{0\pi} = \frac{1}{2}\left(< \sigma_u >_{0\pi}^2 + < \sigma_v >_{0\pi}^2 + < \sigma_w >_{0\pi}^2\right) \tag{2.23}$$

Two non-dimensional parameters are important when it comes to FOWT in surge motions, which are the ratio between the maximum surging velocity $V_{\mathrm{WT,max}}$ and inflow velocity V_0 denoted as $\mathbb{V}$ in Equation 2.24, and the reduced frequency $\mathbb{W}$ defined in Equation 2.25. More detail characterization and analysis of these two parameters can be found in [29]. Take example of $\omega_S = 0.63$ rad/s with $A_S = 4$ m for rated condition of NREL 5MW baseline wind turbine ($D = 126$ m, $V_0 = 11.4$ m/s, $\Omega = 1.27$ rad/s), it corresponds to $\mathbb{V} = 0.22$ and $\mathbb{W} = 7.00$ (this is the base case of this thesis). Together with Equation 2.19, the surging velocity of the rotor V_{WT} can be expressed with $\mathbb{V}$ in Equation 2.26.

$$\mathbb{V} \triangleq \frac{V_{\mathrm{WT,max}}}{V_0} = \frac{A_S \omega_S}{V_0} \tag{2.24}$$

$$\mathbb{W} \triangleq \frac{\omega_S D}{V_0} \tag{2.25}$$

$$V_{\mathrm{WT}} = \frac{\mathrm{d}p_R(t)}{\mathrm{d}t} = A_S \omega_S \cos\phi_S = V_0 \mathbb{V} \cos\phi_S \tag{2.26}$$

Figure 2.2 depicts the $p_R(t)$ and V_{WT} of the base case, with T_S and T_Ω being the period of surging and rotating. As can be seen, as $\phi_S = 0$, V_{WT} has the maximum value, while p_R is in its neutral position. Note that positive V_{WT} will result in a smaller apparent inflow velocity $V_{0,\mathrm{app}}$ seen by the rotor, as depicted in Equation 2.27.

$$V_{0,\mathrm{app}} \triangleq V_0 - V_{\mathrm{WT}} \tag{2.27}$$

2.5 Parameters for Rotor Performance

To analyze the performance of the wind turbine rotor in this thesis, thrust coefficient C_T and power coefficient C_P are the two upmost important parameters. Their definitions are given in Equation 2.28. Here T & P are the output thrust force & power from the rotor, ρ is

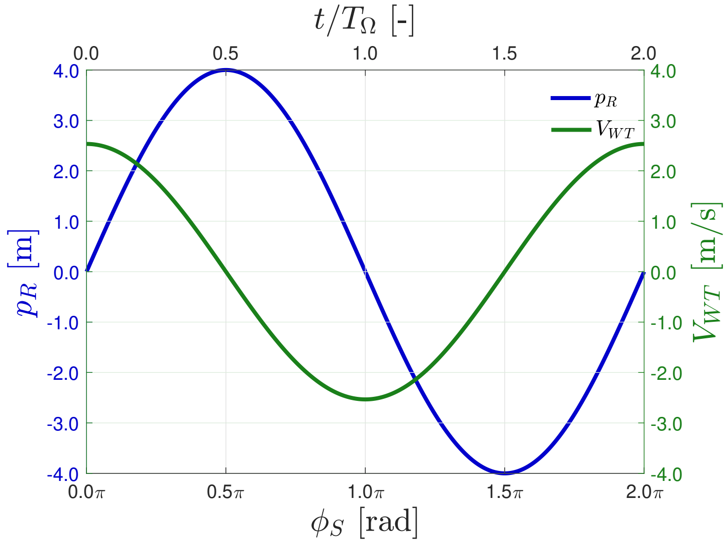

Figure 2.2: x-position of p_R and velocity of rotor V_{WT} of the surging FOWT rotor with $\omega_S = 0.63$ rad/s and $A_S = 4$ m.

the flow density, R is the rotor radius, and V_{ref} is the reference velocity. It should be noted that V_{ref} is usually the magnitude of mean inflow velocity V_0 of the specific case; however, for some cases, V_{ref} is not the value of V_0, and it is done for convenience (such as cases in Table 4.2 & G.1, V_{ref} is based on $V_{0,\mathrm{rated}}$, not V_0). Also it should be noted that the values of V_{ref} for C_T & C_P are kept constant even for surging rotor, even though the apparent inflow velocity $V_{0,\mathrm{app}}$ seen by the rotor is varying with time.

$$C_T \triangleq \frac{T}{\frac{1}{2}\rho V_{\mathrm{ref}}^2 \pi R^2}, \qquad C_P \triangleq \frac{P}{\frac{1}{2}\rho V_{\mathrm{ref}}^3 \pi R^2} \tag{2.28}$$

2.6 Analysis of Momentum Entertainment

To analyze time-averaged momentum entertainment along the streamwise direction, term $\partial\overline{u}\overline{u}/\partial x$ are looked into. $\partial\overline{u}\overline{u}/\partial x$ can be decomposed into several terms as presented in Equation 2.29. Note that Reynolds decomposition is applied at here, where overline indicates the time-averaged properties and prime represents the fluctuation part, as displayed in Equation 2.30. This thesis intend to analyze terms in Equation 2.29 on plane $y = 0$. However, since that the rotor considered in this thesis is circular and effects of floor & tower are not considered, $\partial/\partial y$ (azimuthal derivative) terms are assumed to be relatively small; together with the fact that terms involving molecular & eddy viscosity and term $\partial\overline{u'u'}/\partial x$ are not significant, Equation 2.29 can be simplified to Equation 2.31, leaving only 3 terms. For more detail derivations, see Appendix B.

$$
\begin{aligned}
\frac{\partial \overline{uu}}{\partial x} = 2\overline{u}\frac{\partial \overline{u}}{\partial x} + \frac{\partial \overline{u'u'}}{\partial x} = -2\overline{v}\frac{\partial \overline{u}}{\partial y} - 2\overline{w}\frac{\partial \overline{u}}{\partial z} - \frac{\partial \overline{u'u'}}{\partial x} - 2\frac{\partial \overline{u'v'}}{\partial y} - 2\frac{\partial \overline{u'w'}}{\partial z} - \frac{2}{\rho}\frac{\partial \overline{p}}{\partial x} \\
+2\overline{\frac{\partial}{\partial x}\left[(\nu+\nu_T)\left(\frac{\partial u}{\partial x}+\frac{\partial u}{\partial x}\right)\right]} + 2\overline{\frac{\partial}{\partial y}\left[(\nu+\nu_T)\left(\frac{\partial u}{\partial y}+\frac{\partial v}{\partial x}\right)\right]} + 2\overline{\frac{\partial}{\partial z}\left[(\nu+\nu_T)\left(\frac{\partial u}{\partial z}+\frac{\partial w}{\partial x}\right)\right]}
\end{aligned}
\tag{2.29}
$$

$$
u = \overline{u} + u' \tag{2.30}
$$

$$
\frac{\partial \overline{uu}}{\partial x} \simeq -2\overline{w}\frac{\partial \overline{u}}{\partial z} - 2\frac{\partial \overline{u'w'}}{\partial z} - \frac{2}{\rho}\frac{\partial \overline{p}}{\partial x} \tag{2.31}
$$

2.7 Simple Torque Controller

For most simulation cases in this thesis, there are no controlling system involved. While for cases in chapter 6 as well as Appendix G, a simple torque controller is implemented. Note that drive train efficiency are assumed to be 100% for this thesis, and low speed side (before the gear box) is focused.

The simple controller implemented in this thesis only involving adjusting rotor speed Ω (variable speed). That is, constant pitch angle θ_p is maintained. The idea is to introduce a simple torque controller that is commonly used for realizing maximum power point tracking (MPPT) when wind turbine rotors are operating under partial load (below rated) conditions (region 2 in Figure 2.3), and the way to do is making the rotors operate with certain tip speed ratio λ_{opt} which gives desired (optimal) C_P ($C_{P,\text{opt}}$) [75]. Note that C_P is function of λ. In real world, it is done by adjusting the generator torque τ_{Gen} based on the rotor rotational speed Ω, as shown from Equation 2.32 to 2.34 in a very briefly fashion. Here $P_{\text{Aero,opt}}$ is the desired aerodynamic power of the rotor, A stands for rotor swept area ($A = \pi R^2$), V is the magnitude of inflow wind speed, $C_{P,\text{opt}}$ is the desired power coefficient, P_{Gen} is the generator power, and K_τ is a coefficient. The main strategy is to adjust Ω to realize Equation 2.32, and $P_{\text{Aero,opt}} = P_{\text{Gen}}$ also has to hold to ensure the stability of the system. Note that these can be done by adjusting τ_{Gen}, and V here may vary depend on the inflow conditions.

$$
P_{\text{Aero,opt}} = \frac{1}{2}\rho A V^3 C_{P,\text{opt}} = \frac{\rho A R^3 C_{P,\text{opt}}}{2\lambda_{\text{opt}}^3}\Omega^3 \tag{2.32}
$$

$$
P_{\text{Gen}} = \tau_{\text{Gen}}\Omega \tag{2.33}
$$

$$
\text{for} \quad P_{\text{Gen}} = P_{\text{Aero,opt}}, \qquad \tau_{\text{Gen}} = \frac{\rho A R^3 C_{P,\text{opt}}}{2\lambda_{\text{opt}}^3}\Omega^2 = K_\tau \Omega^2, \qquad K_\tau = \frac{\rho A R^3 C_{P,\text{opt}}}{2\lambda_{\text{opt}}^3} \tag{2.34}
$$

After having the value of τ_{Gen}, Equation 2.36 is the additional equation of motion to

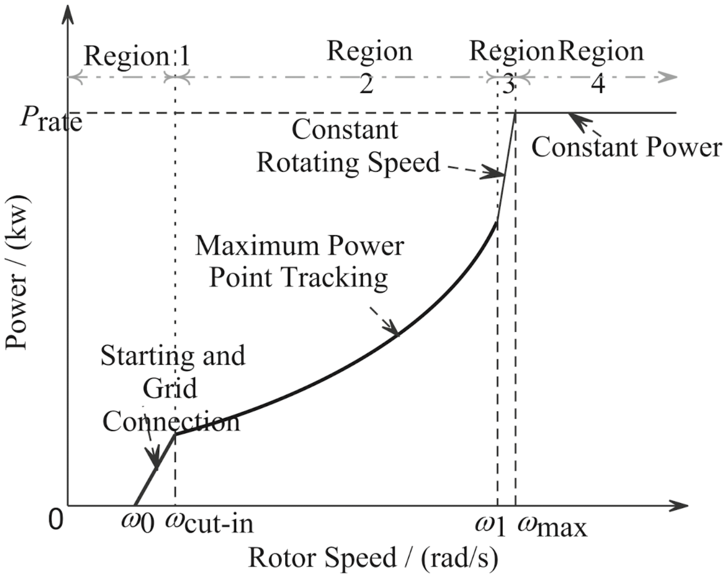

Figure 2.3: Wind turbine control modes in different control regions. Taken from Zhang et al. [75].

solve during simulations in order to implement the torque controller. Here I_R, I_{Gen}, I_B, and I_{hub} are the moment of inertia with respect to rotor center of the entire rotor, generator (drive-train), single blade, and hub, while their relation is described in Equation 2.35. τ_{Aero} is the aerodynamic torque of the rotor. Equation 2.36 are based on Newton's laws of motion, while the original tensor forms are simplified to scalar forms for simplicity, and the sign convention for τ_{Aero} and τ_{Gen} are based on the torque applied onto the rotor by wind and the torque applied onto the generator by rotor. Note that τ_{Aero} is output by modules of turbinesFoam.

$$I = I_R + I_{\text{Gen}} = (3I_B + I_{\text{hub}}) + I_{\text{Gen}} \tag{2.35}$$

$$I\frac{\mathrm{d}\Omega}{\mathrm{d}t} = \tau_{\text{Aero}} - \tau_{\text{Gen}} \tag{2.36}$$

As for updating $\Omega(t)$, Equation 2.37 is implemented.

$$\Omega(t + \Delta t) \simeq \Omega(t) + \frac{\mathrm{d}\Omega}{\mathrm{d}t}\Delta t \tag{2.37}$$

Note that the only input for the controller mentioned above is Ω, which is simple to measure in real case scenario. Also that τ_{Gen} can be adjusted by controlling the electric loads on the generator through power electronic system in reality. For more detail information about the controller described above, please refer to Manwell et al. [56], Zhang et al. [75], and Novak et al. [76]. And one should notice that cases without controller in this thesis are actually equivalent to always making $\tau_{\text{Aero}} = \tau_{\text{Gen}}$, which leads to $\mathrm{d}\Omega/\mathrm{d}t = 0\ \mathrm{rad/s^2}$.

Chapter 3

Simulation Setups and Validations

CFD simulations of this thesis project using LES with ALM were implemented with *OpenFOAM v2106*, a free open-source finite-volume based CFD software composed of C++ libraries. OpenFOAM is widely used for numerical studies of wind turbines utilizing LES with ALM in the research community [34, 73, 77].

Two wind turbines rotor models were implemented in this thesis, one being full scale NREL 5MW baseline turbine [62] and the other being 1/75 DTU 10MW RWT [78]. The former rotor was more focused and employed in most of the simulation cases, and the latter only served the validation purpose. Though NREL 5MW is the most used rotor model when it comes to numerical simulations of FOWT [9], it is a fiction turbine that have never been built, and thus lacking experimental data for validation. As for the 1/75 DTU 10MW RWT, which is a 1/75 down-scaled wind turbine of DTU 10MW RWT [79]. 1/75 DTU 10MW RWT was employed in the experimental campaigns of the UNAFLOW (UNsteady Aerodynamics for FLOating Wind) project, where the turbine model was tested with sinusoidal surging motions [13, 23]. Moreover, the data sets, including the turbine parameters & airfoil polars, and experimental results of UNAFLOW project were made public, making it a great source for this thesis project to validate and bench-mark. The simulation setups for these two models are kept very similar (in none-dimensional sense), as being described later in this section.

3.1 General Setups

Setups described in this subsection are common for the cases using both rotor models, namely full scale NREL 5MW baseline turbine and 1/75 DTU 10MW RWT.

3.1.1 Flow Properties, Solvers, and Discretization Schemes

The flow in this thesis was considered to be air and assumed to be incompressible and Newtonian ($\rho = 1.225$ kg/m^3 & $\nu = 1.5 \times 10^{-5}$ m^2/s). The thermal effects as well as Coriolis force are neglected. One of the simplest and most used SGS model for LES, which is the standard Smagoranky model of OpenFOAM with $C_k = 0.094$ & $C_\varepsilon = 1.048$, was chosen, since the SGS model is not considered to be the deterministic factor for wind turbine modellings using LES with ALM [17, 69, 70]. The codes for modelling surging FOWTs with ALM is based on the modified codes of *turbinesFoam* developed by Bachant et al. [72]. The discritization schemes for the governing equations (Equation 2.3 and 2.7) will be based on finite-volume method. For spatial discretization, second-order central differencing (`Gauss linear`) is utilized, and Crank-Nicolson scheme (`CrankNicolson`, with coefficient of 0.9) [80] is selected for time discretization, same as some of the proceeding works about modeling wind turbine wakes using LES with ALM [17, 39]. Regarding the algorithm used to solve the governing equations, the PISO (Pressure-Implicit with Splitting of Operators) algorithm is implemented using OpenFOAM application `pimpleFoam` (setting `nOuterCorrectors = 1` & `nCorrectors = 2`). PISO algorithm (`nOuterCorrectors = 1`) was selected since the CFL (Courant-Friedrichs-Lewy) numbers is able to be safely kept below 1 for the entire field with the simulation framework used (going to be described). The `tolerance` for the residuals are set to be `1e-6` for `p`, `pFinal`, & `U` (pressure & velocity). As for the hardware, high performance computing clusters of DTU Computing Center (DCC) [81] were utilized. Generally, 600 s simulation time takes around 66 hours on 64 processors for all cases.

3.1.2 Rotor Parameterization with ALM

By referring previous studies [17, 39, 82], each actuator line (blade) was represented with 40 points with equidistant of Δ_r, and the grid size Δ is designed to be similar as Δ_r for the wake region ($\Delta = D/80$, level 4 in Figure 3.1, 3.2, and 3.12). Moreover, the smoothing factor ε here will be set to 2Δ as recommended by Troldborg [43] and Martinez et al. [39]. A tip correction factor f_{tip} with Glauert model was implemented, as shown in Equation 2.16. For modelling the hubs (and towers, if there is), additional actuator line elements with desired C_D (0.3 for hubs, 1.1 for towers) was introduced [83, 84]. Also, since that the concerned cord-based reduced frequency (with respect to the considered surging frequencies) is relatively small, no dynamic-stall model was implemented in this thesis for simplicity, and no aeroelastic codes were coupled for the all the cases in this thesis.

3.1.3 General Mesh Layout

The meshes for this project were consisted of hexahedral cells, and they were created through application `snappyHexMesh`. Figure 3.1 displays one of the mesh layouts, and *Level* indicates the refinement levels. With the level decreased by one, the grid size Δ doubled. As described previously, the grid size Δ near by the rotor (wake region) will be similar to the inter-distance of the actuator line points Δ_r, meaning that Δ of level 4 is $D/80$. Cartesian coordinate system was selected for this thesis, with positive x pointing to the downstream direction. The neutral position of the (upstream) rotor was placed at $x/D = 0$, with the rotor center located at origin.

3.1.4 Temporal Resolution

For temporal resolution, there are 360 time steps for the rotor to complete a revolution under its rated condition, the limiting factor is the tip of the blade should not travel more than one grid size with a given time step [39], and it is about 0.7 for this thesis project (for both NREL 5MW and UNAFLOW cases).

3.1.5 Boundary Conditions

OpenFOAM v2106 has already equipped with divergence-free synthetic eddy method (DFSEM, see section 2.2) [71] as one of its inlet conditions (`turbulentDFSEMInlet`). Note that DFSEM may introduce undesired pressure fluctuations near the inlet regions, and thus the inflow properties (mean velocity, turbulence intensity, length scale) were characterized at $2D$ upstream form the (upstream) rotor in this thesis. For the laminar cases, inlet with fixed value for velocity is implemented. As for the other boundary conditions for velocity, advective outlet ($\mathrm{D}/\mathrm{D}t = 0$) was adopted, and the other four sides were set as slip walls. While for the pressure, the four sides and the inlet were all assigned with symmetry boundary conditions, the outlet was set to be an uniform fixed value.

3.2 Simulation Setups and Validations with NREL 5MW Baseline Turbine

Rotor of NREL 5MW [62] was chosen in order to study full scale surging FOWTs numerically. However, for simplicity, floor effects, wind shear, and thermal stability were not considered, tower, tilt angle, and pre-coning were also removed. These settings made the system become close to axis-symmetric, which made quantifying effects of different parameters easier.

3.2.1 Operational Parameters of Rotor

The rotor diameter D of NREL 5MW baseline turbine is 126 m, and it consists of DU and NACA airfoil series. For this study, tower of NREL 5MW is neglected, so as the tilt angles and pre-coning. The rotational frequency of its rated condition (of the upstream rotor) is $\Omega_{\mathrm{rated}} = 1.27$ rad/s with tip speed ratio λ_{rated} being 7, and the mean inflow velocity $V_{0,\mathrm{rated}}$ is 11.4 m/s. The rotor rotates clockwise when viewing from the upstream. For this thesis, the blade pitch angle θ_p was kept always 0°, and none of the control strategies were implemented except in chapter 6 and Appendix G, where a simple torque controller was applied. As for the turbulence intensities, surging frequencies, and surging amplitudes, they will be set according to different cases. For cases with two rotors, the positions and operational conditions of the downstream rotors will also be characterized depend on different cases, which will be described in later chapters.

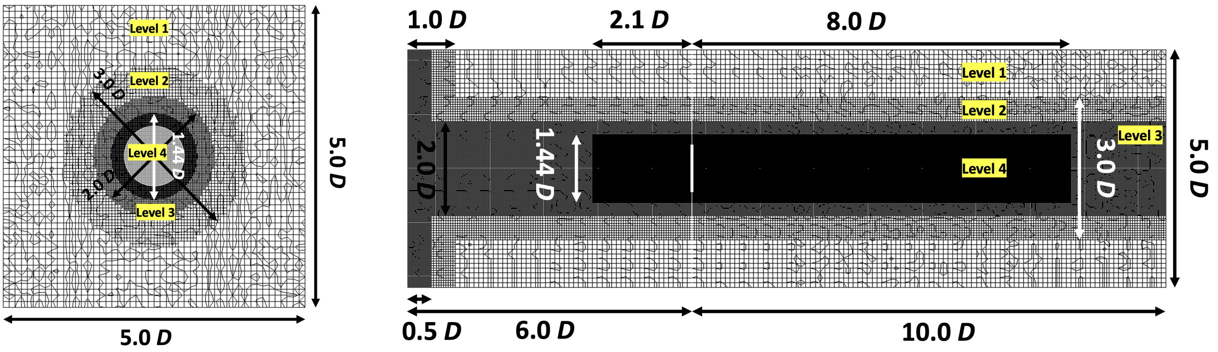

(a) yz plane

(b) xz plane

Figure 3.1: Schematic diagrams for mesh layouts of turbulent cases with NREL 5MW. Rotor disk is represented with disk or line.

3.2.2 Mesh Layouts

Figure 3.1 are the schematic diagrams of mesh layout used with turbulent cases. The upstream rotor is placed $6.0D$ downstream away from the synthetic turbulent inlet to allow the flow to develop and to damp out the undesired pressure fluctuations due to the synthetic turbulent inlet, and the refinements just after the inlet serve similar purpose [71]. The rotors are placed in the center of the yz-plane and towers are neglected, and the position of the most upstream rotor is set to be $x/D = 0$. The wake region is cylindrical (level 4), with a diameter of $1.44D$, starting form $2.1D$ upstream form the upstream-rotor to $8D$ downstream of the upstream-rotor. The separation distances investigated for the dual rotor cases are $3D$ and $5D$, which are well covered by the wake refined region. The domain size will be $16D \times 5D \times 5D$, with a blockage ratio of 3.14%. The total cell number is about 10.9M with Δ at level 4 being $D/80$.

As for the cases with laminar inflow conditions, a different but similar mesh layout was implemented, as shown in Figure 3.2. The differences are mainly removing refinement regions around the inlet and shorten the distance from inlet to rotor, while extending the wake region to the inlet. These changes were made to minimize the undesired turbulence generated with numerical errors related to mesh layouts. Cell number with this mesh layouts is about 10.4M. See Appendix A for more detail discussions.

3.2.3 Inflow Turbulence Characterization

Since that slip walls were applied in this thesis, implying that no turbulence would be generated around the domain boundaries; and thus with the setups adopted in this thesis, inflow turbulence modelled by LES with standard Smagoransky would decay along the streamwise direction [69]. Thus, instead of characterizing turbulence properties at the immediate inlet locations, they were measured at $2.0D$ upstream from the rotor by several probes, as shown in Figure 3.3 (all the probes are in the wake refined region).

Several mean and turbulence properties were measured for different turbulent inflow conditions in this thesis, including mean streamwise velocity $\overline{u}$, standard deviation of u

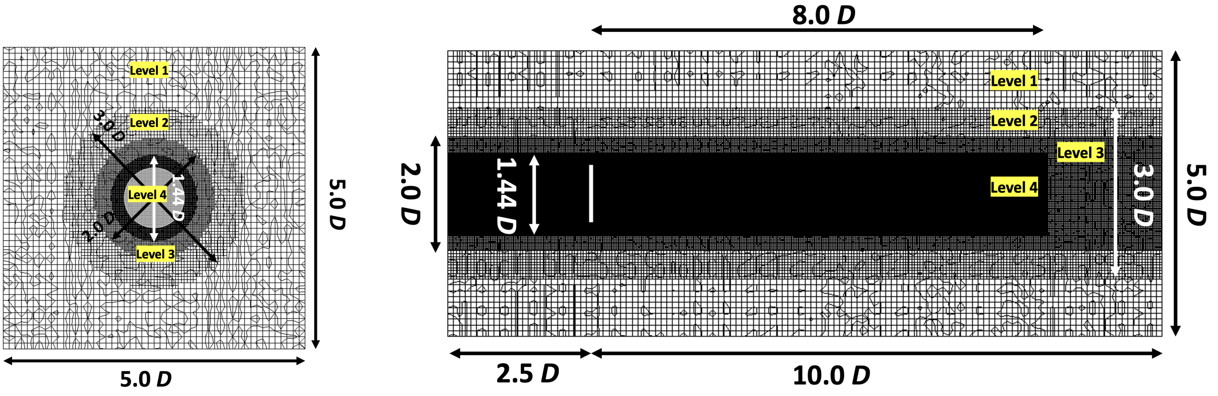

(a) yz plane

(b) xz plane

Figure 3.2: Schematic diagrams for mesh layouts of laminar cases with NREL 5MW. Rotor disk is represented with disk or line.

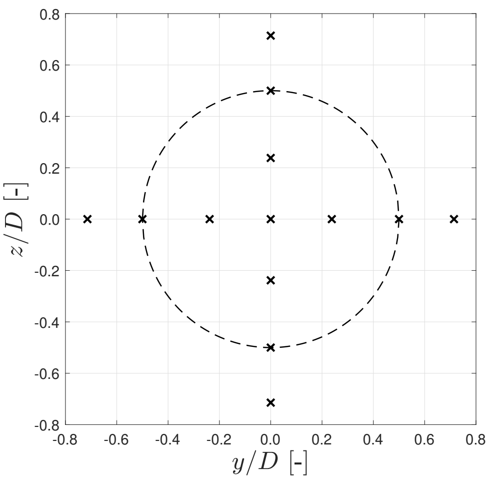

Figure 3.3: Positions of the probes used to characterize properties of inflow. The x-positions of the probes are $-2.0D$.

(σ_u or $\overline{u'u'}$, similar with v or w), turbulence intensity TI (Equation 3.1), autocorrelation function of u in x-direction ρ_{u_x}, integral length scale of u (in x-direction) L_u, and power spectrum of u ($S_u(f)$). Here the overline stands for the time-averaged (mean) operator and the superscript prime stands for the fluctuating part, note that this is the well known Reynolds decomposition; Equation 3.2 displays an example with u. L_u is defined as ρ_{u_x} first reaches zero, and ρ_{u_x} is obtained through Taylor's frozen-turbulence approximation [85] with time series data measured by the probe (Equation 3.3 and 3.4). Note that $\overline{u}$, σ_u, σ_v, σ_w, and TI are obtained through averaging (equally weighted) all probes presented in Figure 3.3, while ρ_{u_x}, L_u, and $S_u(f)$ are obtained through the single probe locate at the rotor center. Also notice that V_0 is the desired inflow velocity, which is 11.4 m/s for the turbulent cases with rotor of NREL 5MW.

$$\mathrm{TI} = \frac{\sqrt{\frac{1}{3}(\sigma_u^2+\sigma_v^2+\sigma_w^2)}}{V_0} \times 100\% = \frac{\sqrt{\frac{2}{3}\mathrm{TKE}}}{V_0} \times 100\% \tag{3.1}$$

$$\overline{u} = \frac{1}{T_2 - T_1}\int_{T_1}^{T_2} u\mathrm{d}t, \qquad u' = u - \overline{u} \tag{3.2}$$

$$\text{for} \quad \Delta x = \overline{u}(x_0)\Delta t, \qquad u(x_0+\Delta x, t_0) = u(x_0+\overline{u}(x_0)\Delta t, t_0) \simeq u(x_0, t_0 - \Delta t) \tag{3.3}$$

$$\begin{aligned}\rho_{u_x}(\Delta x) = \frac{\overline{u'(x_0,t_0)\, u'(x_0+\Delta x, t_0)}}{\sqrt{\overline{[u'(x_0)]^2}}\,\sqrt{\overline{[u'(x_0+\Delta x)]^2}}} &= \frac{\overline{u'(x_0,t_0)\, u'(x_0+\overline{u}(x_0)\Delta t, t_0)}}{\sqrt{\overline{[u'(x_0)]^2}}\,\sqrt{\overline{[u'(x_0+\overline{u}(x_0)\Delta t)]^2}}} \\ &\simeq \frac{\overline{u'(x_0,t_0)\, u'(x_0, t_0-\Delta t)}}{\overline{[u'(x_0)]^2}}\end{aligned} \tag{3.4}$$

Table 3.1 lists out the information of the turbulent inflow conditions adopted by this thesis, and ρ_{u_x} is showed in Figure 3.4. Note that since the random seeds fed into `DFSEM` inlet conditions are same, the turbulent inflow generated by it would be identical in space & time if other parameters remain the same, and this would be an advantage for comparing cases later in this thesis. According to the international standard IEC 61400-1 edition 4.0 (2019) [86], L_u should be 42 m (Equation 3.5, z is 90 m for this case, which is the hub height) and σ_v/σ_u should be bigger than 0.7 (when floor is considered, v is in lateral direction). Though σ_v and σ_w fulfill IEC 61400-1, L_u seems to be a bit larger. However, if consider some other standards in civil engineering realm (such as ASCE 7-16 & AIJ(2004)), L_u in this case should be around 150 to 250 m [87]. Thus, the L_u in Table 3.1 are considered to be realistic. Moreover, even though the three selected TI in Table 3.1 seems to be lower than the values which IEC 61400-1 suggested (for class C with normal turbulence model, σ_u/V_0 should be 0.149 as $V_0 = 11.4$ m/s), they are deemed to be valid since TI tends to be lower in offshore environments, while IEC standards are based on onshore conditions. Typically, TI for offshore conditions are around 5% to 8% [88].

Table 3.1: Turbulence characteristics measured at 2.0D upstream from rotor. Note that the length scales were measured only at the position of rotor center, and $V_0 = 11.4$ m/s.

TI [%]	$\overline{u}/V_0$	L_u [m]	σ_u/V_0	σ_v/σ_u	σ_w/σ_u
2.66	1.00	52.77	0.029	0.93	0.87
5.32	1.01	54.82	0.058	0.89	0.84
11.62	1.02	131.79	0.122	0.97	0.90

$$L_u = 0.7z, z \leq 60 \text{ m}, \qquad L_u = 42 \text{ m}, z > 60 \text{ m} \tag{3.5}$$

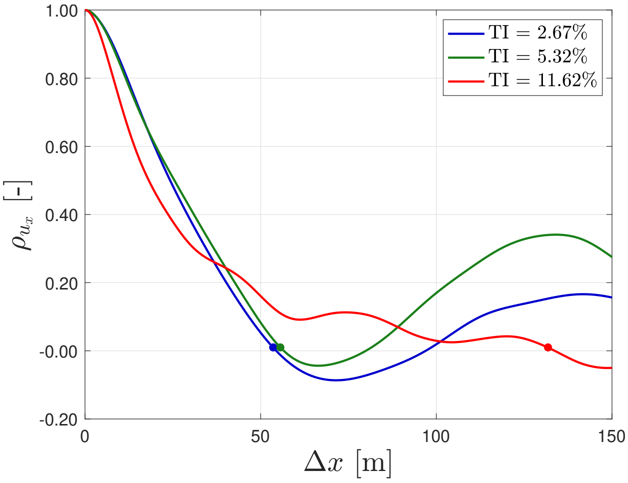

Figure 3.4: Autocorrelation function ρ_{u_x} with different turbulent inflow conditions. The dots label the integral length scale L_u.

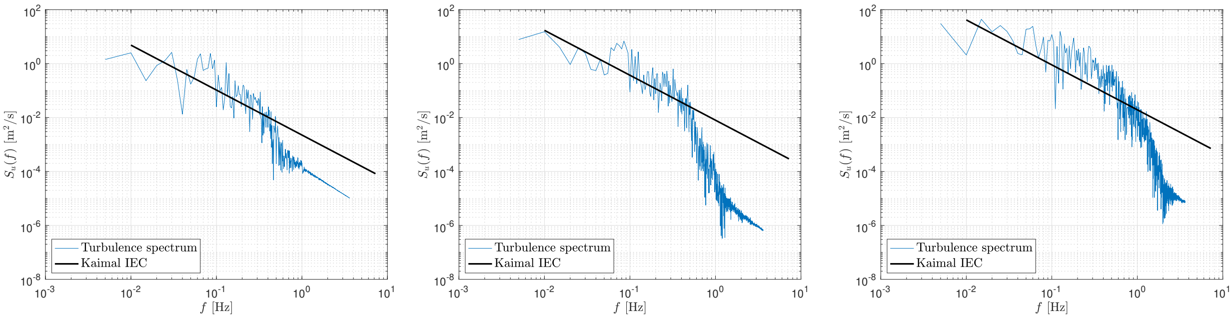

(a) TI = 2.66%

(b) TI = 5.32%

(c) TI = 11.62%

Figure 3.5: Turbulence and the corresponding Kamial spectrum of different turbulent inflow conditions.

Figure 3.5 shows the turbulence spectrum $S_u(f)$ measured by the probe at the center for different turbulent inflow conditions (parts with $f > V_0/2\Delta$ are truncated), the definition of the Kaimal spectrum adopted by IEC 61400-1 is in Equation 3.6 [86]. As can be seen, not only does the inertial ranges are clear visible, these spectrum also fit Kaimal spectrum well. With the above mentioned, it is confident to say that the turbulent inflow conditions of this thesis are reasonable and realistic. As for laminar inflow conditions, generally they have uniform fixed values of u at $x = -2.0D$, which is as expected. For more detail information about laminar inflow conditions, please see Appendix A.

$$S_u(f) = 0.05\sigma_u^2 \left(\frac{L_u}{V_0}\right)^{-2/3} f^{-5/3} \tag{3.6}$$

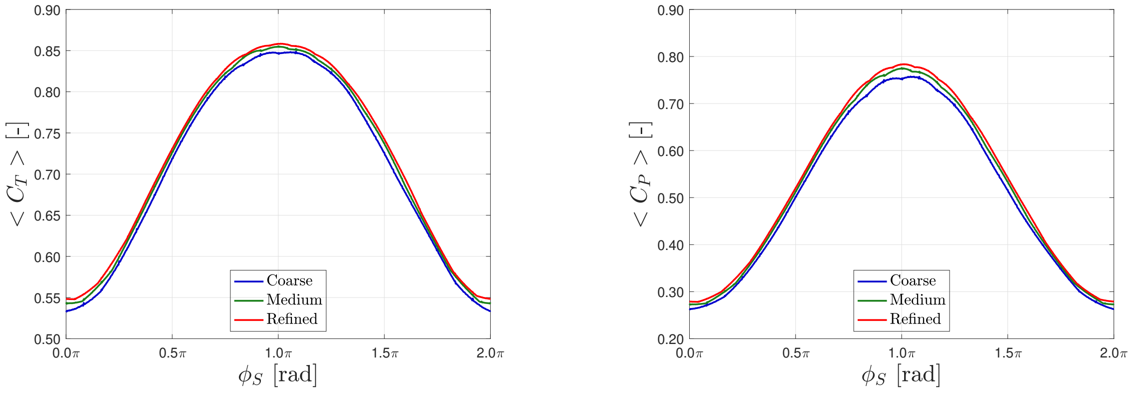

(a) $< C_T >$ (b) $< C_P >$

Figure 3.6: Cycle-averaged thrust and power coefficient based on the surging phase angle ϕ_S with different gird resolutions.

3.2.4 Model Verification

Grid Test

A brief grid independent test was carried out in this subsection with the setups of NREL 5MW baseline turbines mentioned previously in this section. Asides from Δ at wake region (level 4 in Figure 3.2) being $D/80$ (medium), setups with $\Delta = 1.25D/80$ (coarse) and $\Delta = 0.8D/80$ (refined) were also conducted to test the grid sensitivity. The inflow conditions were set to be laminar ($V_0 = 11.4$ m/s), while surging amplitude and surging frequency here were set to be $A_S = 4$ m and $\omega_S = 0.63$ rad/s. Note that even though Δ in level 4 was adjusted, $\Delta_r \simeq D/80$ and the absolute value of smearing factor for ALM $\varepsilon \simeq D/40$ were kept unchanged.

Table 3.2 listed out the time-averaged thrust and power coefficients with different grid sizes (with the reference velocity being 11.4 m/s). It can be found that even the cell number was almost quadrupled, the values of $\overline{C}_T$ and $\overline{C}_P$ remain relatively similar. Figure 3.6 displays the cycle averaged value of C_T and C_P based on the surging phase angle ϕ_S ($< C_T >$ and $< C_P >$). Once more, the three mesh setups output very similar values, despite their cell numbers different a lot.

Table 3.2: $\overline{C}_T$ and $\overline{C}_P$ with three different mesh resolutions for laminar inflow conditions with $A_S = 4$ m and $\omega_S = 0.63$ Hz.

	Δ in Level 4 [D]	Cell Number [M]	$\overline{C}_T$	$\overline{C}_P$
Coarse	1.25/80	5.6	0.708	0.511
Medium	1.00/80	10.9	0.715	0.523
Refined	0.80/80	18.8	0.720	0.531

Figure 3.7 presents information related to the mean streamwise velocity $\overline{u}$ with the three mesh setups. Similar as the case with C_T and C_P, the three setups agree with each other quite well.

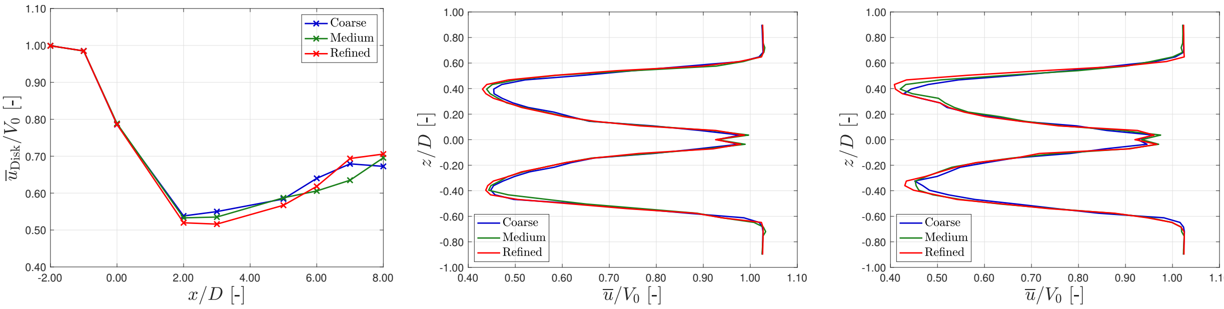

(a) $\overline{u}_{\text{Disk}}$ along x-direction. (b) Profile of $\overline{u}$ at $x/D = 2.0$. (c) Profile of $\overline{u}$ at $x/D = 3.0$.

Figure 3.7: Outputs related to the mean streamwise velocities $\overline{u}$ with different gird resolutions with rotor of NREL 5MW under laminar inflow conditions.

In this subsection, it is shown that the three mesh setups, coarse, medium, and refined all share very similar results, both in sense of rotor performances and velocity deficits in the wake. And thus it could be said that results are not significantly depending with the grid size. Even though setup using $\Delta = 1.25D/80$ in the wake region (coarse) seemed to be already viable, it was not adopted. Rather, grid size with medium was chosen. This decision was made by regarding the best practices suggested by the previous studies related to the current work, such as $\Delta_r \leq D/70$ & $\Delta \simeq \Delta_r$ [17, 39, 43], and also that cases with 10.9M cells is rather affordable with the available resources.

Ratios of the Unresolved Turbulent Kinetic Energy

For the large eddy simulation (LES), it is widely agreed that the ratio between the resolved turbulent kinetic energy (TKE) and total turbulent kinetic energy $\text{TKE}_{\text{total}}$ (TKE + TKE_{sgs}) should be more than 80% [89]. Since the sub-grid scale (SGS) model adopted in this thesis is the standard Smagoransky model [66] provided by OpenFOAM v2106, sub-grid scale turbulence kinetic energy TKE_{sgs} (k_{sgs}) could be recovered with the calculated ν_T fields using Equation 2.8. Contour plots of the ratios between TKE_{sgs} and $\text{TKE}_{\text{total}}$ of the selected cases are displayed in Figure 3.8 (instantaneous) and 3.9 (time-averaged), while the contours of TKE is in Figure 3.10. The four selected cases are fixed cases and surging cases ($A_S = 4$ m, $\omega_S = 0.63$ rad/s) with laminar and turbulent inflow conditions (TI = 5.3%), which correspond to cases **1**, **6**, **3**, and **11** in Table 4.1 displayed in later chapter. It can be seen that except for the regions with TKE/V_0^2 approach to 0, the ratios between TKE_{sgs} and $\text{TKE}_{\text{total}}$ are quite low, especially after time-averaging (the scratchy contours may related to the discussions in Appendix A). Therefore, together with with the power spectrum of u in Figure 3.5, it can be concluded that the setup with $\Delta = D/80$ in wake region is sufficient enough to resolved most of the turbulence.

Pressure Fluctuations Near the Inlet Regions for Turbulent Inflow Conditions

Figure 3.11 shows the fields of $\sigma_{\Delta p}$ (standard deviation of pressure) for the cases with single fixed rotor with different inflow conditions (TI). The four presented cases are cases

1-4 in Table 4.1 going to be displayed in later chapter. The undesired pressure fluctuations introduced by DFSEM mentioned in subsection 3.1.5 can be seen in the plots, and they are more significant with bigger TI. However, with the refinements just after the inlet mentioned in subsection 3.2.2, the fluctuations are damped and the fluctuation fields are deemed to be acceptable considering the $\sigma_{\Delta p}$ fields are mostly dominated by the rotor around its nearby regions.

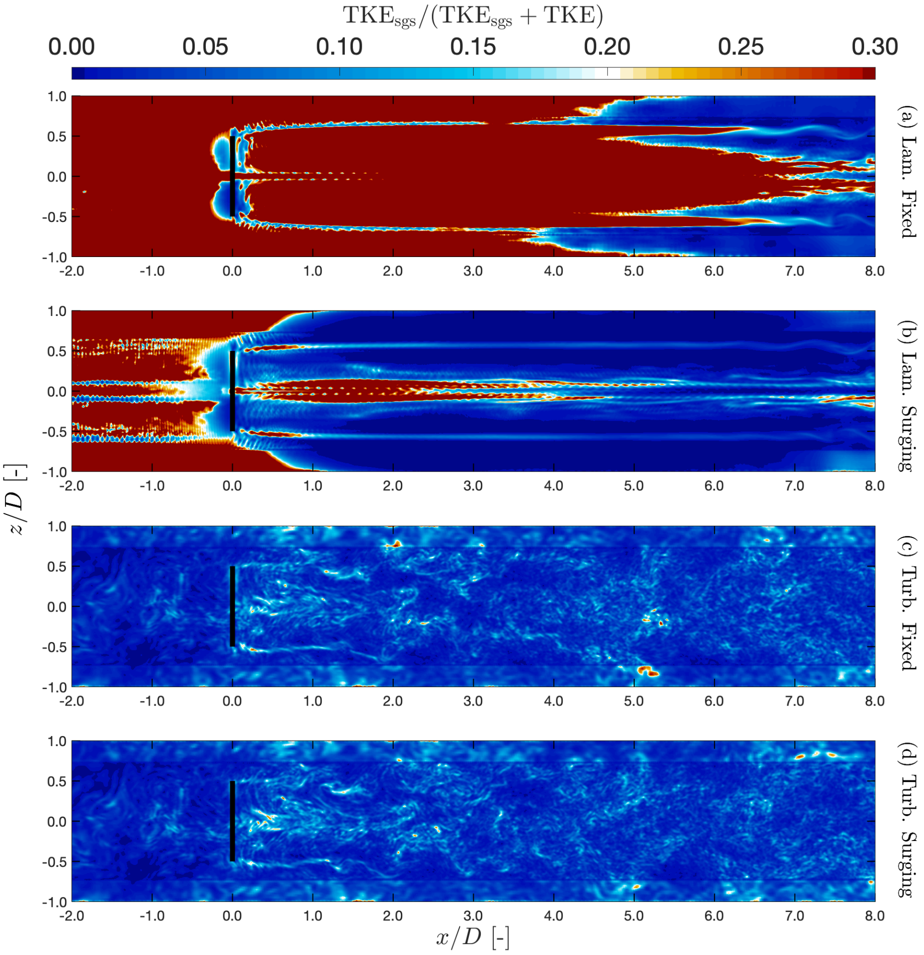

Figure 3.8: Contours of instantaneous ratios between TKE_{sgs} and $\text{TKE}_{\text{total}}$ ($\text{TKE} + \text{TKE}_{\text{sgs}}$) at $\phi_S = 0\pi$.

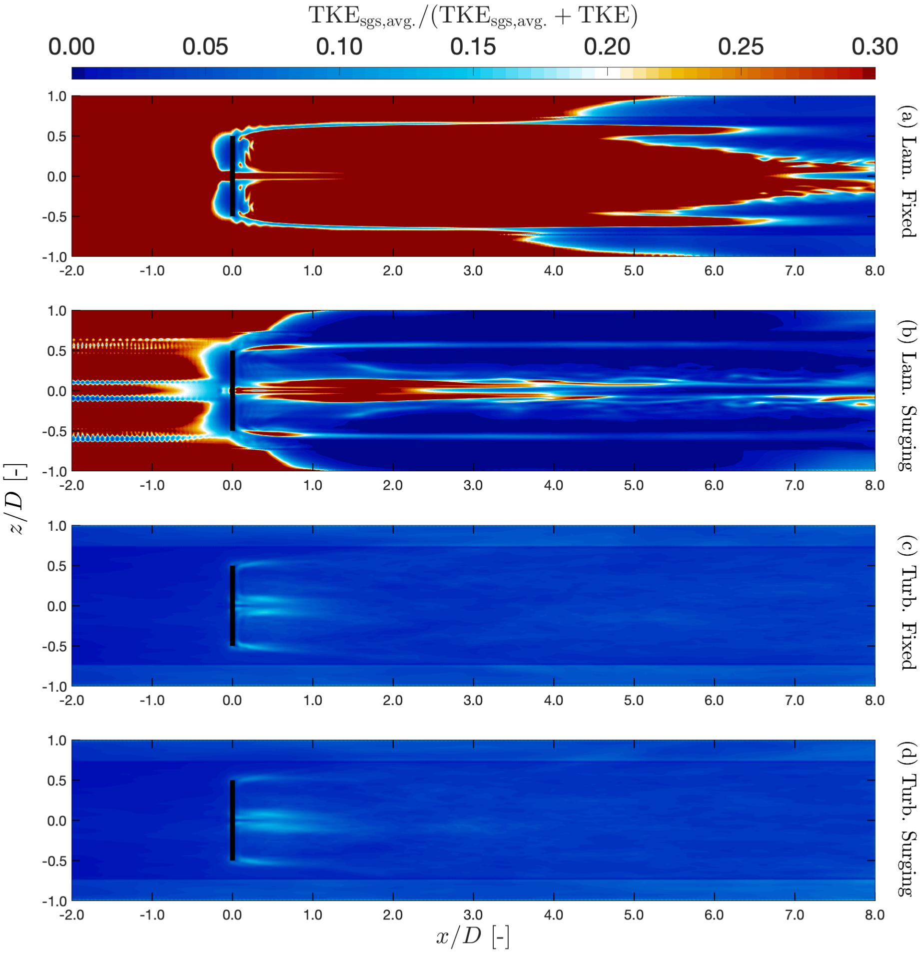

Figure 3.9: Contours of time-averaged ratios between TKE_{sgs} and $\text{TKE}_{\text{total}}$ ($\text{TKE} + \text{TKE}_{\text{sgs}}$) at $\phi_S = 0\pi$. The maximum values in (c) and (d) are 0.1678 and 0.1488.

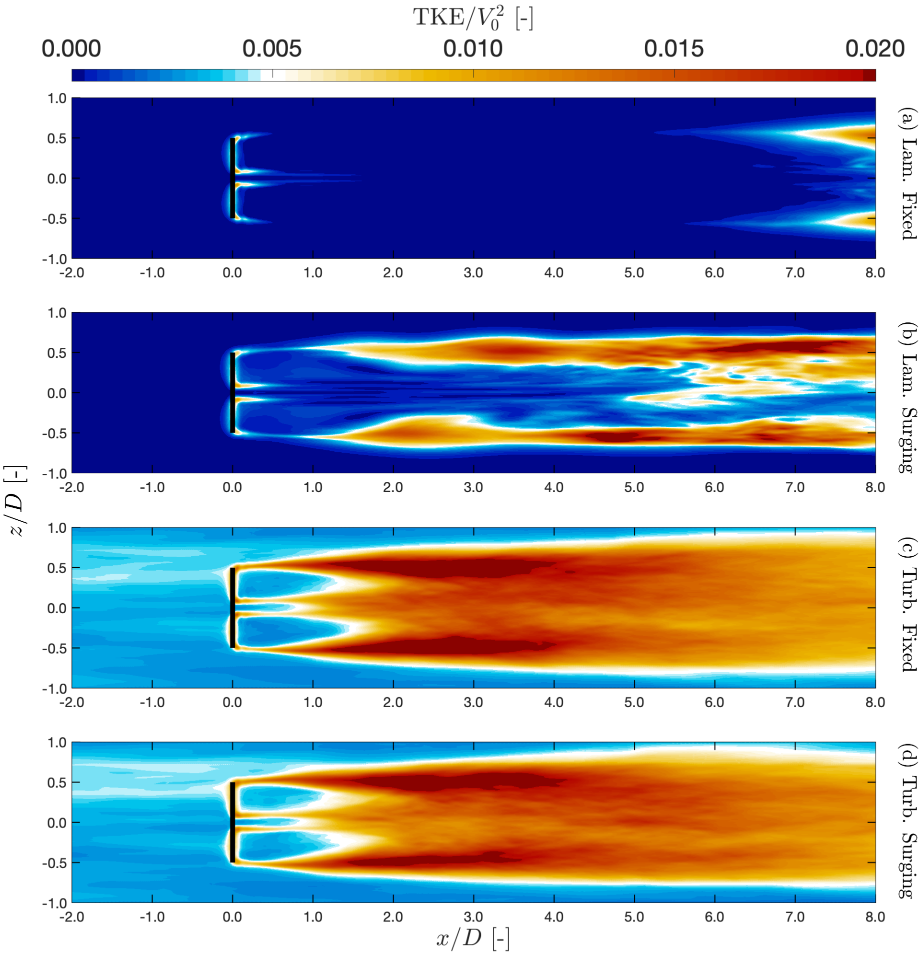

Figure 3.10: Contours of (resolved) TKE. Presented to better understand Figure 3.8 and 3.9.

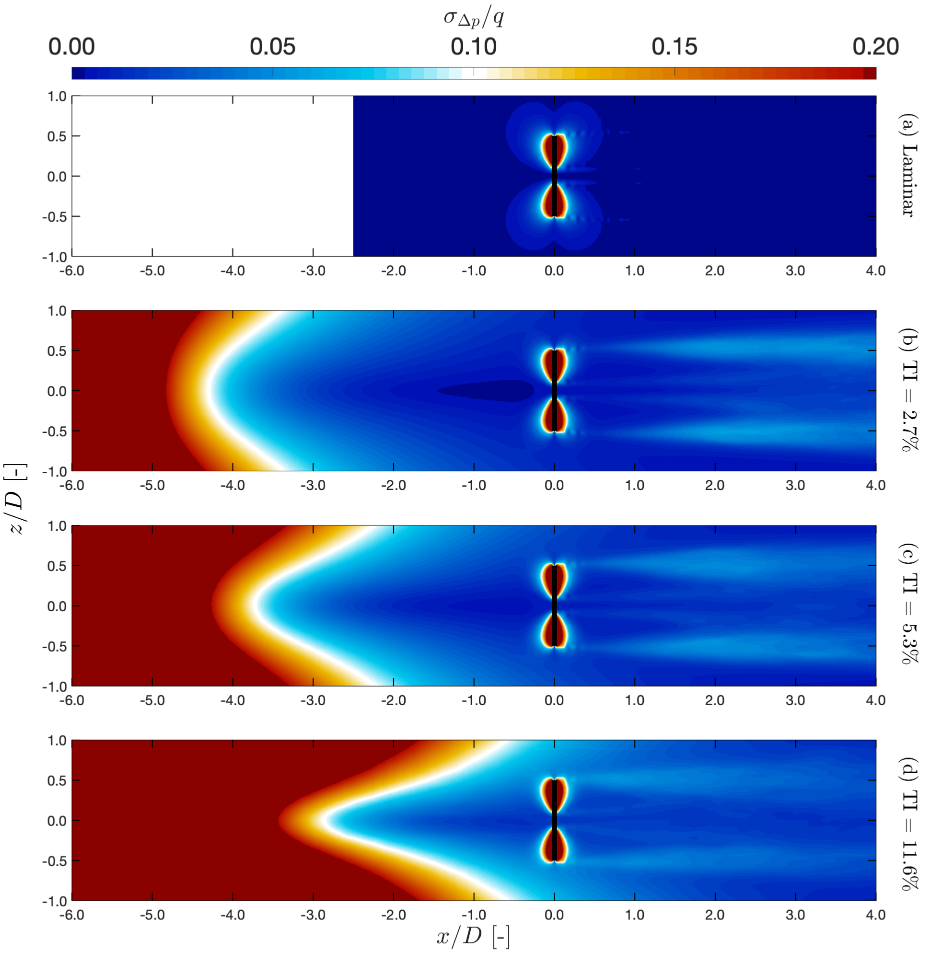

Figure 3.11: Contours of standard deviation of pressure fields $\sigma_{\Delta p}$ for the cases of single fixed rotor with different inflow conditions.

3.2.5 Model Validation

Since no NREL 5MW baseline turbine was built in reality, experimental results are not available. However, plenty of numerical studies had been carried out, thus providing data for this work to compare. Table 3.3 displayed the values of $\overline{C}_T$ and $\overline{C}_P$ from other studies and current work for the fixed cases under rated conditions ($\lambda_{\text{rated}} = 7.00$ and $V_{0,\text{rated}} = 11.4$ m/s). Even though the values of $\overline{C}_T$ and $\overline{C}_P$ from current works deviate quite away from the original design of Jonkman et al. [62], it falls into the range as comparing to other works with various numeric methods. Moreover, considering the parameter study about using LES with ALM & ADM carried out by Martinez et al. [39], as $\lambda = 7.55$ and $V_0 = 8.0$ m/s, $\overline{C}_P$ varied from 0.46 to 0.59 depending on grid size (around the rotor) Δ and values of smearing factor ε in Equation 2.15. Considering these facts, it was concluded that the setups presented in this thesis are able to capture the rotor performances of NREL 5MW baseline turbine reasonably well, and the outcomes are inline with other studies in the literature.

Table 3.3: Comparing $\overline{C}_T$ and $\overline{C}_P$ for fixed NREL 5MW rotor at its rated condition with other previous numeric works.

Source	Turbulence model	Force model	TI [%]	$\overline{C}_T$	$\overline{C}_P$
Current work	**LES**	**ALM**	**Laminar**	**0.723**	**0.510**
Current work	**LES**	**ALM**	**5.3**	**0.727**	**0.519**
Jonkman et al. [62]	-	FAST	-	0.81	0.47
Johlas et al. [49]	LES	ALM	4.1	0.752	-
Xue et al. [53]	LES	ALM	Laminar	0.75	0.52
Li et al. [90]	RANS	ALM	-	0.77	0.49
Yu et al. [91]	RANS	ALM	-	0.728	0.472
Rezaeiha et al. [20]	RANS	ADM	5	0.715	0.567

3.3 Simulation Setups and Validations with 1/75 DTU 10MW RWT

In order to confidently validate the simulation frame work of this thesis, it would be ideal to bench-mark against experimental results. However, since no NREL 5MW baseline turbine was built in real world, it is decided to validate the frame work with a different rotor model. Experimental results of UNAFLOW project was thus selected for validation purpose. UNAFLOW project had conducted experimental campaigns with 1/75 DTU 10MW RWT subjected to sinusoidal surging motions, which match the conditions studied in this thesis. Moreover, Mancini et al. had also done several numerical simulations with different numeric frameworks but similar configurations, including CFD method using LES with ALM [23]. In order to better mimic the experimental setups, the tower and floor (slip-wall) are introduced, and thus the system is not axis-symmetric, unlike the previous cases with NREL 5MW rotor.

3.3.1 Operational Parameters of Rotor

The rotor diameter of 1/75 DTU 10MW RWT is 2.38 m and it adopted SD7032 airfoil. And the twist & chord distributions as well as airfoil polar are all available [13]. Following with the experimental conditions conducted by UNAFLOW, mean inflow velocity, turbulence intensity, and rotational frequency are set to be 4.0 m/s, 2%, and 8π rad/s, and these conditions correspond to the rated condition of 1/75 DTU 10MW RWT ($\lambda = 7.5$) [23]. Here $\theta_p = 0°$ was maintained and no controlling systems were employed. As for the surging amplitude A_S and the surging frequency ω_S, $A_S = 0.008$ m and $\omega_S = 2$ Hz (4π rad/s) were focused, which correspond to $\mathbb{V} = 0.025$ and $\mathbb{W} = 7.48$. Note that comparison of the fixed case was also conducted.

3.3.2 Mesh Layout

Figure 3.12 displays the mesh layout used for UNAFLOW cases. Even though using different rotor model, its general setups remain very similar with the turbulent cases of NREL 5MW baseline turbine. Since the inflow turbulent intensity of 2% was introduced, the inlet refinement regions are retained. The major changes are the dimension of the inflow section, position of the rotor (centered at height $z = 2.05$ m), and the re-introduced of the tower (Figure 3.12). These adjustments are made to mimic the experimental conditions of UNAFLOW, which utilized the Polimi's wind tunnel (GVPM, 13.84 m wide and 3.84 m high) [13].

3.3.3 Inflow Turbulence Characterization

Similar with subsection 3.2.3, inflow turbulent conditions are characterized $2.0D$ upstream from the rotor with several probes displayed in Figure 3.3. The major difference is that now $D = 2.38$ m and $V_0 = 4.0$ m/s. Since that experiments carried out by UNAFLOW were all characterized with $V_0 = 4.0$ m/s and TI = 2%, only one turbulent inflow conditions

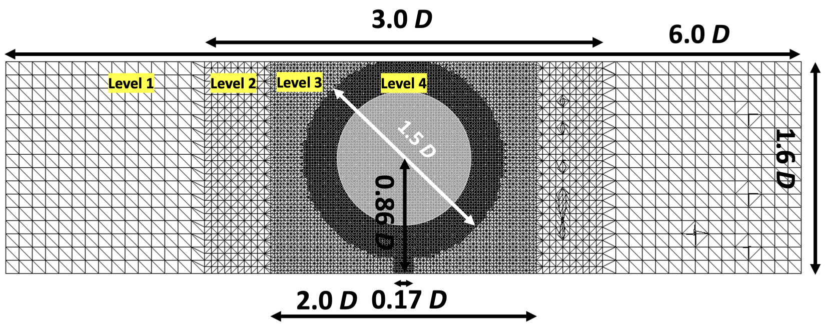

(a) yz plane

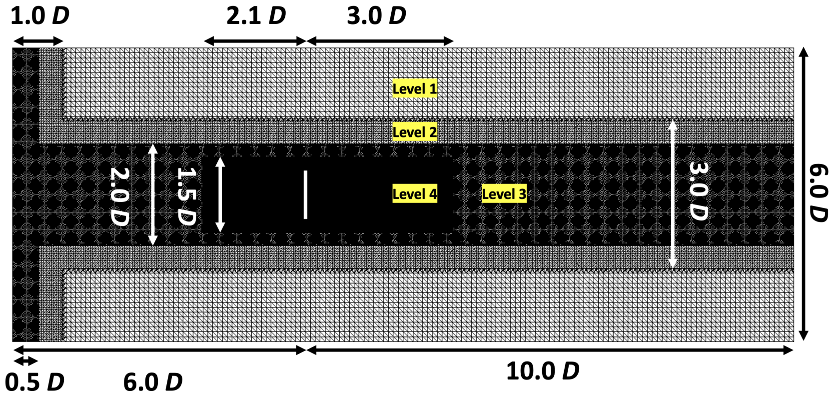

(b) xz plane

Figure 3.12: Schematic diagrams for mesh layouts of cases with 1/75 DTU 10MW RWT. Rotor disk is represented with disk or line.

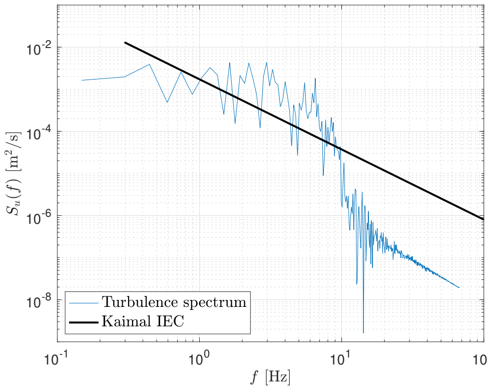

Figure 3.13: Turbulence and the corresponding Kaimal spectrum of simulated turbulent inflow for UNAFLOW cases.

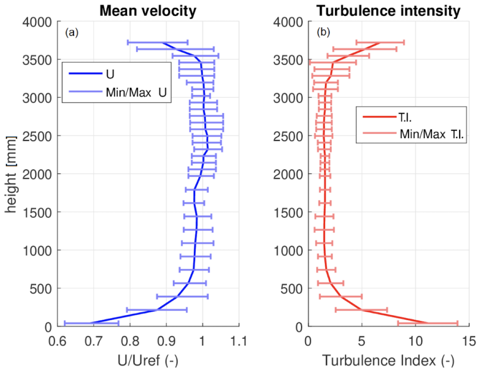

Figure 3.14: Mean inflow velocities and TI at different height measured by UNAFLOW project. Taken from Mancini et al. [23].

were adopted for the simulations, and it is characterized in Table 3.4 and Figure 3.13. The sampling methods are same as described in subsection 3.2.3. Figure 3.14 displays the measured inflow conditions of UNAFLOW project, they were measured at 5 m upstream from the rotor.

Table 3.4: Turbulence characteristics measured at 2.0D upstream from rotor for UNAFLOW simulation cases. Note $V_0 = 4.0$ m/s.

TI [%]	$\overline{u}/V_0$ [-]	L_u [m]	σ_u/V_0	σ_v/σ_u	σ_w/σ_u
1.95	0.99	0.53	0.022	0.80	0.79

3.3.4 Model Validation

The simulated rotor performances and wake properties are compared with the results of UNAFLOW projects. Other than experimenting with surging 1/75 DTU 10MW RWT, UNAFLOW projects also conducted numerical studies with various numeric frameworks, and two of them, LES with ALM & RANS with the full turbine representation, are used to compare with the current work.

Table 3.5 compares the time averaged thrust $\overline{T}$ and power $\overline{P}$ of a fixed 1/75 DTU 10MW RWT with different method. As can be seen, $\overline{T}$ and $\overline{P}$ predicted by current framework are comparable with the experimental results of UNAFLOW project, with both being slightly under estimated.

Figure 3.15 presents the time-averaged normal and tangential load distributions along the blade ($\overline{F}_n$ and $\overline{F}_t$) of a fixed 1/75 DTU 10MW RWT. Note that UNAFLOW project did not measured them during the experiments. However, their load distributions obtained by LES with ALM are quite comparable to the results obtained with the current framework.

Figure 3.16 compared the averaged fluctuation thrust based on the surging phase angle ϕ_S ($\Delta T = T - \overline{T}$). Generally speaking, results obtained with current framework agree with

Table 3.5: Time averaged thrust $\overline{T}$ and power $\overline{P}$ of a fixed 1/75 DTU 10MW RWT.

Case	$\overline{T}$ [N]	$\overline{P}$ [W]
Current work	34.27	76.39
UNAFLOW Experiment	35.91	83.79
UNAFLOW LES ALM	36.60	87.07
UNAFLOW Full CFD	36.57	84.29
UNAFLOW BEM	34.65	73.95

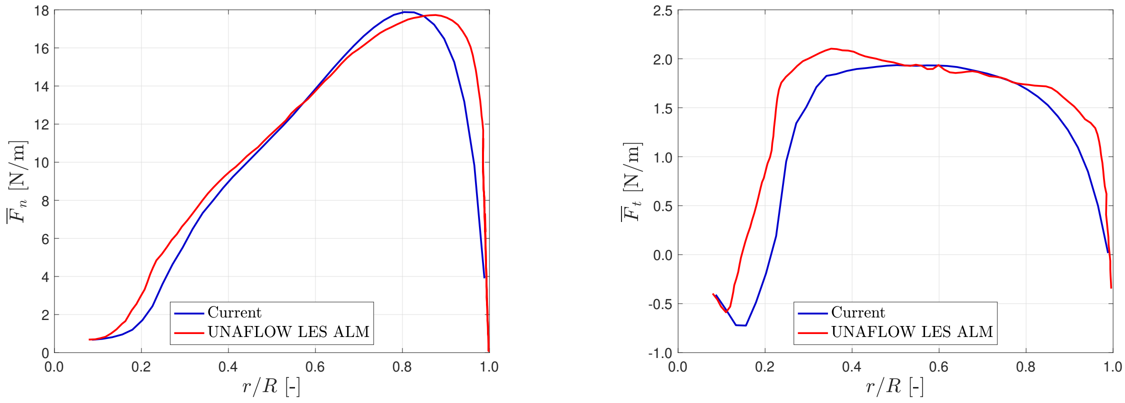

(a) $\overline{F}_n$ (b) $\overline{F}_t$

Figure 3.15: Time averaged normal and tangential load distributions along the blade ($\overline{F}_n$ & $\overline{F}_t$) of a fixed 1/75 DTU 10MW RWT.

the experimental results of UNAFLOW project. Note that current framework kept the tower during the simulations for 1/75 DTU 10MW RWT, and thus the effects of tower shadow can be observed. Moreover, there is a phase-locked relation between the rotation of the rotor and surging, and thus the the effects of tower shadow always happen at certain ϕ_S. As can be seen, simulation with full turbine representation conducted by UNAFLOW project had displayed very similar behaviour; behaviour of tower shadow was removed from the experimental results due to the applied low-pass filter [23].

Figure 3.17 shows the profiles of time-averaged streamwise velocity $\overline{u}$ at $2.3D$ downstream form the rotor of 1/75 DTU 10MW RWT. The simulation results of current work shared very similar profiles with the ones of UNAFLOW experiments (both surging and fixed), except around the rotor center (hub). Notice that the profiles of $\overline{u}$ for fixed and surging cases almost collapse together for the simulation results. Though this is not the case for the results of UNAFLOW experiments displayed in Figure 3.17, it is the case for some other A_S and ω_S, and some of those cases even have a larger $\mathbb{V}$ compare to the case $A_S = 0.008$ m and $\omega_S = 2$ Hz [13, 92].

With the results presented in this section, it is concluded that the results obtained with the current frameworks agree with the experimental results of UNAFLOW project to a good degree.

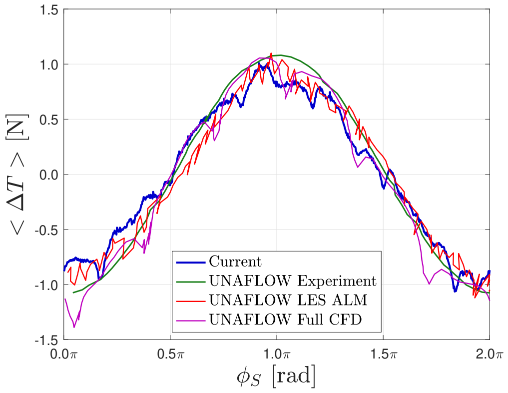

Figure 3.16: Comparison of the thrust fluctuations of 1/75 DTU 10MW RWT with $A_S = 0.008$ m and $\omega_S = 2$ Hz.

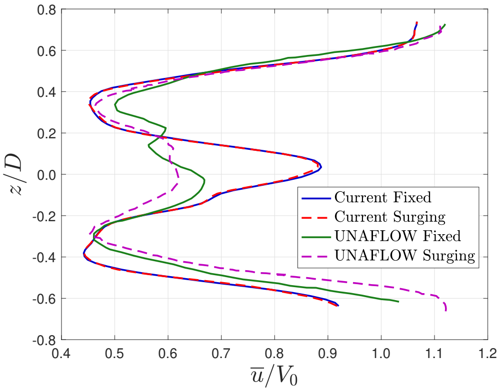

Figure 3.17: Profiles of time-averaged streamwise velocity profiles $\overline{u}$ at $2.3D$ downstream for 1/75 DTU 10MW RWT.

3.4 Conclusion

The simulation framework for studying surging FOWT is described in details in this chapter, and special focus is placed on the characteristics of flows generated by the synthetic turbulent inlet conditions (DFSEM), which are deemed being able to represent realistic offshore environments. Some verifications & validations are also done in this chapter, and they are deemed to perform well. The results obtained with the simulation framework are insensitive to the grid resolutions, and the ratios of the resolved turbulence are higher than the recommended value based on the common practices of LES (80%). Moreover, the obtained results match the experimental results well (section 3.3), and they also match with the results from other numerical studies. Thus, it is confident that the current simulation framework is able to provide reliable results for studying surging FOWT.

Chapter 4

Results and Discussions of Single Rotor Cases

4.1 Introduction

This chapter investigates the wake systems and rotor performances of a single surging FOWT rotor numerically with different surging frequencies ω_S, surging amplitudes A_S, and ambient turbulence intensities TI using the framework described in chapter 3. The rotor used in this chapter is the one of NREL 5MW baseline turbine, and it was set to be operated under its rated condition (see subsection 3.2.1). Note that the center of the rotor was placed at the origin and the mean flow blows from negative to positive x-direction, while the rotational direction of the rotor is clock wise when seen from upstream. Special focuses were placed on the mean disk-averaged velocity $\overline{u}_{\text{Disk}}$ of wakes and coherent structures induced by sinusoidal surging motions.

In order to understand the system dynamics with different ω_S, A_S, and TI comprehensively, the cases were organized into six groups and compared with each other. The six groups (S.1 − S.6) are listed below. Note that some cases appear in multiple groups, and cross comparisons between groups were also made.

S.1 Fixed cases with different TI (cases **1-4**)

S.2 Surging cases with different TI (cases **6** and **10-12**)

S.3 Laminar cases with different A_S (cases **1** and **5-7**)

S.4 Laminar cases with different ω_S (cases **1**, **6**, **8**, and **9**)

S.5 Turbulent cases with different A_S (cases **3**, **11**, **13**, and **14**)

S.6 Turbulent cases with different ω_S (cases **3**, **11**, **15**, and **16**)

$A_S = 4$ m and $\omega_S = 0.63$ rad/s were chosen to be the base settings for the surging cases when comparing with different TI, and TI$= 5.3\%$ was selected for the turbulent cases when comparing with different surging settings. Moreover, $T_\Omega = 4.96$ s, which is the period for the NREL 5MW rotor to complete a revolution under its rated condition, was chosen to be the main time scale for this chapter.

With the available metocean data sets [93] and analysis of the previous studies [10, 11, 94], the base settings for surging mentioned in previous paragraph should occur commonly (if the platform type being TLP, semisubmersible, or barge), and all the surging settings adopted in Table 4.1 should be realistic, while some of them will be quite rare. Notice that having surging settings (aero-hydro coupled) that occur in real cases will be nice, but it is not among the top priorities for this thesis. Nevertheless, surging motions are mainly dominated by hydrodynamic loading and relatively insensitive to aerodynamic loading [50], and that emphasis of this thesis is placed on studying aerodynamic responses and wake dynamics of the FOWT systems. As for the focused ambient turbulence intensity, 5.3% can be considered as common case for the offshore enviorments as stated in subsection 3.2.3.

For the flow fields, instantaneous, time-averaged, and phase-locked averaged quantities such as velocity, pressure, and vorticity fields were investigated. Fields of (specific) turbulent kinetic energy (TKE) and several second-order statistics related to momentum entertainment (Appendix B) were also looked into. For the rotor performances, time-averaged and cycle-averaged of thrust and power coefficients ($\overline{C}_T$ & $\overline{C}_P$ and $< C_T >$ & $< C_P >$) were investigated. The cycle-averaged were based on surging phase angles ϕ_S (or rotational phase angle ϕ_Ω when comparing with the fixed cases or comparing cases with different ω_S). In short, the averaging windows are $20T_\Omega$ and $50T_\Omega$ (10 and 25 complete surge cycles of base surging settings) for laminar and turbulent cases. With these windows, the statistics obtained were deemed to be converged enough for investigations. Check Appendix C for detail information about the sampling methods, the ways to obtain statistics, and convergence tests.

Since that the turbulent inflow was realized with synthetic turbulence (DFSEM), indicating the turbulent flows generated are repeatable as long as the mesh-setups, inflow conditions, and random seeds are kept the same. Thus, when comparing the instantaneous flow properties, as long as the snapshots were taken at the same time instant, they are comparable. The statement also holds for comparing statistics as long as the window selected for calculation are identical. Regarding this, all the instantaneous properties for turbulent cases were sampled at $t = 110T_\Omega$ and the averaging windows all started from $t = 60T_\Omega$ and ended at $t = 110T_\Omega$ (for laminar cases, instantaneous fields are sampled at $t = 70T_\Omega$).

In total, there are 22 cases conducted in this chapter (16 + 6), and their results are summarized in Table 4.1 and Table 4.2. $\mathbb{V}$ is the ratio of the maximum surging velocity and the inflow velocity (11.4 m/s for the cases here), and $\mathbb{W}$ is the reduced frequency. Their definitions can be found in Equation 2.25 and 2.26. $< C_T >^+$ & $< C_T >^-$ are the maximum & minimum $< C_T >$ of that case, similar notations were used for $< C_P >$. $\overline{u}^{3D}_{\text{Disk}}$ & $\overline{u}^{5D}_{\text{Disk}}$ are the time-averaged of the disk-averaged velocity at $x/D = 3$ & $x/D = 5$. The six cases listed in Table 4.2 are the auxiliary cases, they are used to study the dynamic inflow (hysteresis) effects (Figure 4.19). The six auxiliary cases have different inflow velocities V_0 with laminar inflow conditions, and those V_0 correspond to the maximum and minimum $V_{0,\text{app}}$ that the cases in Table 4.1 may have experienced. Notice that the reference wind speed of C_T & C_P for all cases in Table 4.1 & 4.2 are all based on $V_{0,\text{rated}} = 11.4$ m/s in order to make comparisons simpler.

Table 4.1: The basic settings and results for the cases conducted with single fixed or surging rotor of NREL 5MW baseline wind turbine ($V_0 = 11.4$ m/s, $\lambda = 7$).

Case	TI [%]	A_S [m]	ω_S [rad/s]	$\mathbb{V}$	$\mathbb{W}$	$\overline{C}_T$	$< C_T >^+$	$< C_T >^-$	$\overline{C}_P$	$< C_P >^+$	$< C_P >^-$	$\overline{u}^{3D}_{\text{Disk}}/V_0$	$\overline{u}^{5D}_{\text{Disk}}/V_0$
1	Lam.	Fixed	Fixed	–	–	0.727	0.728	0.727	0.517	0.519	0.517	0.493	0.494
2	2.7	Fixed	Fixed	–	–	0.724	0.727	0.722	0.514	0.518	0.509	0.610	0.710
3	5.3	Fixed	Fixed	–	–	0.726	0.731	0.723	0.518	0.526	0.510	0.666	0.739
4	11.6	Fixed	Fixed	–	–	0.725	0.741	0.718	0.520	0.546	0.508	0.711	0.794
5	Lam.	2	0.63	0.11	7.0	0.719	0.800	0.647	0.519	0.643	0.394	0.517	0.556
6	Lam.	4	0.63	0.22	7.0	0.715	0.855	0.542	0.523	0.776	0.272	0.535	0.587
7	Lam.	8	0.63	0.44	7.0	0.673	0.873	0.346	0.516	0.857	0.097	0.582	0.609
8	Lam.	4	0.32	0.11	3.5	0.724	0.800	0.642	0.518	0.648	0.392	0.510	0.540
9	Lam.	4	1.27	0.44	14.0	0.671	0.871	0.339	0.515	0.856	0.094	0.575	0.604
10	2.7	4	0.63	0.22	7.0	0.714	0.853	0.539	0.522	0.772	0.269	0.615	0.720
11	5.3	4	0.63	0.22	7.0	0.716	0.853	0.541	0.526	0.773	0.274	0.664	0.760
12	11.6	4	0.63	0.22	7.0	0.713	0.845	0.543	0.525	0.761	0.276	0.719	0.799
13	5.3	2	0.63	0.11	7.0	0.725	0.799	0.640	0.522	0.651	0.392	0.664	0.746
14	5.3	8	0.63	0.44	7.0	0.673	0.867	0.345	0.516	0.853	0.098	0.686	0.764
15	5.3	4	0.32	0.11	3.5	0.725	0.800	0.641	0.522	0.656	0.393	0.667	0.748
16	5.3	4	1.27	0.44	14.0	0.672	0.864	0.342	0.516	0.850	0.099	0.698	0.766

Table 4.2: The basic settings and results for the auxiliary cases with different V_0 but identical rotational frequency ($\Omega = 1.26$ rad/s) of a single fixed NREL 5MW rotor. Note that V_{ref} for calculating $\overline{C}_T$ & $\overline{C}_P$ are based on $V_{\text{ref}} = V_{0,\text{rated}} = 11.4$ m/s.

Case	TI [%]	V_0/ [m/s]	$V_0/V_{0,\text{rated}}$	$\overline{C}_T$	$\overline{C}_P$
17	Lam.	6.33	0.56	0.330	0.076
18	Lam.	8.67	0.78	0.538	0.264
19	Lam.	10.13	0.90	0.640	0.388
20	Lam.	12.67	1.11	0.801	0.651
21	Lam.	13.93	1.22	0.859	0.783
22	Lam.	16.47	1.44	0.856	0.846

Figure 4.1 is the histogram of $\overline{C}_P$ & $\overline{C}_T$ for cases in Table 4.1. Fixed case with inflow TI being 5.3% (case **3**) is selected to be the reference case since its conditions are considered to match the common offshore conditions well, and fixed rotor is what the wind energy industry commonly has. It can be seen that, except for the severe surging cases (cases with $\mathbb{V}$), surging motions generally make $\overline{C}_P$ slightly bigger while making slightly $\overline{C}_T$ smaller. Also that $\overline{C}_T$ & $\overline{C}_P$ are less sensitive to inflow TI than to the surging settings. These phenomena will be discussed more in the later sections.

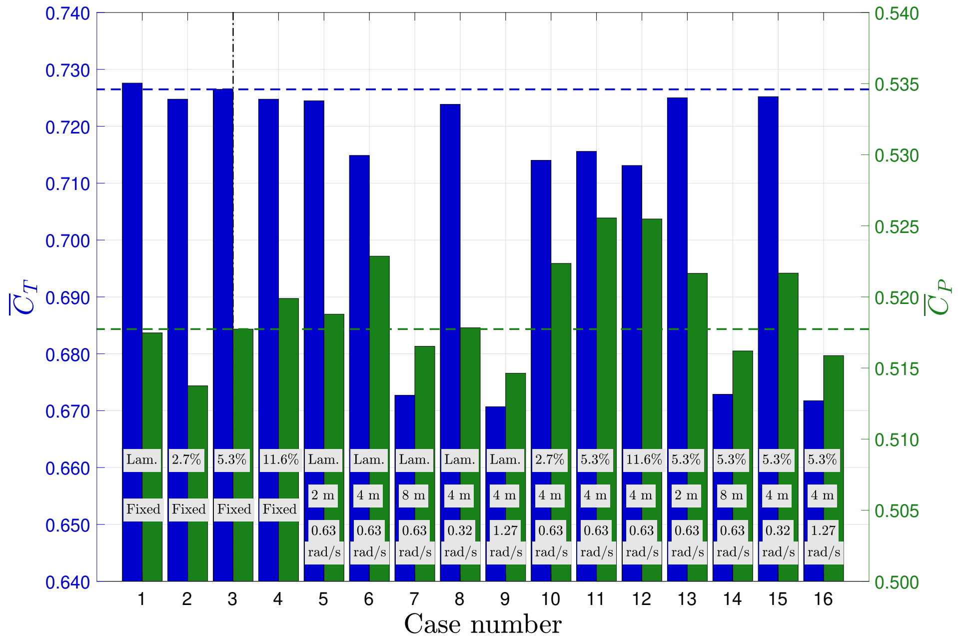

Figure 4.1: Histogram of $\overline{C}_T$ & $\overline{C}_P$ for single rotor cases listed in Table 4.1. The three entries on each bar stand for the values of TI, A_S, and ω_S for each case. The values of the fixed case with TI = 5.3% (case **3**) is chosen to be the reference values for comparison, they are indicated with horizontal dashed lines.

4.2 Different Inflow TI with Single Fixed or Surging Rotor

This section compare cases with single fixed or surging ($A_S = 4$ m & $\omega_S = 0.63$ rad/s) NREL 5MW rotor with different ambient turbulent intensities (TI), which are laminar, 2.7%, 5.3%, and 11.6%. In total there are eight cases, with four having a fixed rotor and the other having a surging rotor, and they correspond to cases **1-4**, **6** & **10-12** in Table 4.1 (groups S.1 & S.2). Note that additional information for this section (such as fields of $< w >_{0\pi}$ & $\overline{w}$, p & $< p >_{0\pi}$, and $< \omega_x >_{0\pi}$ & $< \omega_z >_{0\pi}$) can be found in section E.1.

4.2.1 Summarizing Wake Characteristics and Rotor Performances

Figure 4.2 and 4.3 plot out the results of time-averaged streamwise velocity $\overline{u}$ and its disk-averaged values $\overline{u}_{\text{Disk}}$.

Focusing on the two cases with laminar inflow conditions, it can be found that the $\overline{u}$ profiles in Figure 4.3 for the fixed case retains almost the same from $x/D = 3$ to 8, suggesting mixing and recovery of $\overline{u}$ are weak; while for the surging case, $\overline{u}_{\text{Disk}}$ grows as traveling downstream, suggesting recoveries happened. However, it is worth noting that the $\overline{u}$ profiles of the surging case are not Gaussian-shaped.

As considering the turbulent cases, it is clear that $\overline{u}$ and $\overline{u}_{\text{Disk}}$ recover faster with stronger ambient turbulence for both surging and fixed cases, and the differences of $\overline{u}_{\text{Disk}}$ between different TI become less as going more downstream, especially for cases with TI = 2.7% & 5.3%. For all the six turbulent cases, they all recover faster than the laminar cases, and their $\overline{u}$ profiles all eventually appear in Gaussian-shape. Moreover, for the area within the projection zone of the rotor ($|z/D| \leq 0.5$), obviously $\overline{u}$ becomes larger as going downstream. And for regions just outside the projection of the rotor ($|z/D| \geq 0.5$), $\overline{u}$ becomes smaller as going downstream. These hint there were momentum exchanges happening between the core of wake and its peripheral regions for the considered turbulent cases.

As looking for the effects of surging on the wake recovery rates with different TI, Table 4.3 lists the ratios of $\overline{u}_{\text{Disk}}$ for the fixed and surging cases. The differences of $\overline{u}_{\text{Disk}}$ profiles between the fixed and surging cases with laminar inflow conditions are pronounced, where $\overline{u}_{\text{Disk}}$ for surging case at $x/D = 5$ is 18.8% more than the fixed cases. As for the turbulent cases, $\overline{u}_{\text{Disk}}$ becomes much more similar for the fixed and surging cases. In general, there are still about 1% gains of $\overline{u}_{\text{Disk}}$ at $x/D = 3$ and $x/D = 5$.

Another interesting thing with $\overline{u}_{\text{Disk}}$ if looking very closely in Figure 4.2 is that the profiles of $\overline{u}_{\text{Disk}}$ (induction fields) just before the rotor ($x/D \simeq 0$) are more dominated by whether the rotor is surging or fixed. While after the rotor, profiles of $\overline{u}_{\text{Disk}}$ are much more influenced by inflow TI.

Figure 4.4 displays cycle-averaged C_T & C_P ($< C_T >$ & $< C_P >$) for the eight cases. Note that for the fixed cases, the reference period for cycle averaging is set to be $2T_\Omega$, which is same as the T_S of the considered surging cases here. For the four fixed cases, since that $< C_T >$ and $< C_P >$ are resulted from averaging C_T and C_P for several periods (25 periods for the turbulent cases) and that the simulation setups here ignored the floor and tower,

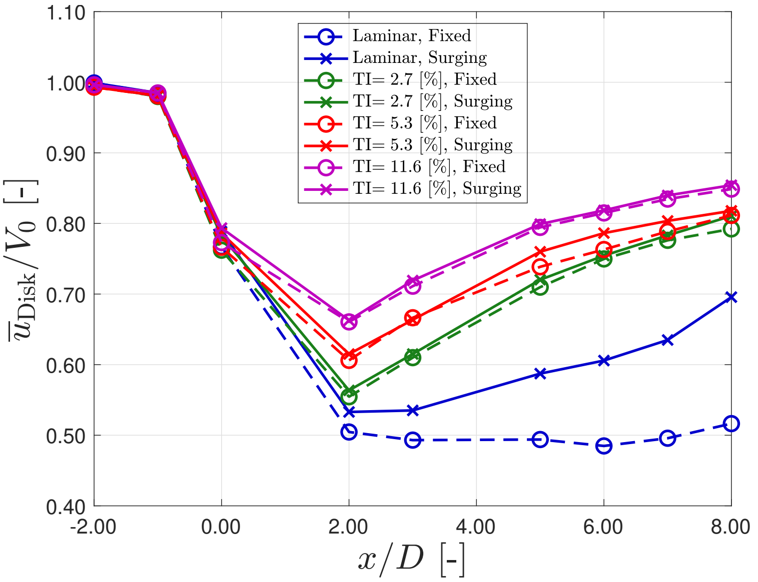

Figure 4.2: $\overline{u}_{\text{Disk}}$ along x-direction for cases of single fixed or surging rotor with different inflow TI.

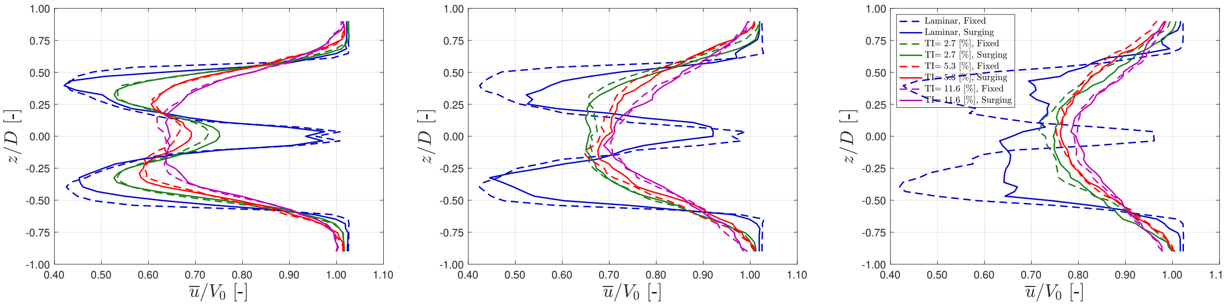

(a) $x/D = 3.0$ (b) $x/D = 5.0$ (c) $x/D = 8.0$

Figure 4.3: Profile of $\overline{u}$ at different x/D for cases of single fixed or surging rotor with different inflow TI.

Table 4.3: The ratios of $\overline{u}_{\text{Disk}}$ for the fixed and surging cases under different inflow TI at $x/D = 3$ and $x/D = 5$.

	Laminar	TI = 2.7%	TI = 5.3%	TI = 11.6%
$\overline{u}^{3D}_{\text{Disk,surging}}/\overline{u}^{3D}_{\text{Disk,fixed}}$	108.52%	100.82%	99.70%	101.13%
$\overline{u}^{5D}_{\text{Disk,surging}}/\overline{u}^{5D}_{\text{Disk,fixed}}$	118.83%	101.41%	102.84%	100.63%

their values are almost constants and being very close to their time averaged values ($\overline{C}_T$ & $\overline{C}_P$) displayed in Table 4.1. Furthermore, values of $\overline{C}_T$ and $\overline{C}_P$ showed here are not sensitive to inflow TI, due to the fact that their values for the four cases are very similar.

As for the four surging cases, both C_T and C_P vary periodically according to the phase angle of surging ϕ_S, and they are not sensitive to inflow TI as well (Notice the period of surging T_S is exactly twice of T_Ω, and $< t = 0 >$ corresponds to $\phi_S = 0$). Since that the displacement of the surging for these four cases can be written as $A_S \sin \omega_S < t >$ (Equation 2.19), the surging velocity of the rotor V_{WT} will be $\omega_S A_S \cos \omega_S < t >$. Thus at $< t = 0 >$, the rotor is moving along with the free-stream (V_0), making the apparent inflow velocity perceived by the rotor $V_{0,\mathrm{app}}$ smaller (Equation 2.18), and this results in relatively smaller values for $< C_T >$ and $< C_P >$ at $< t >= 0$.

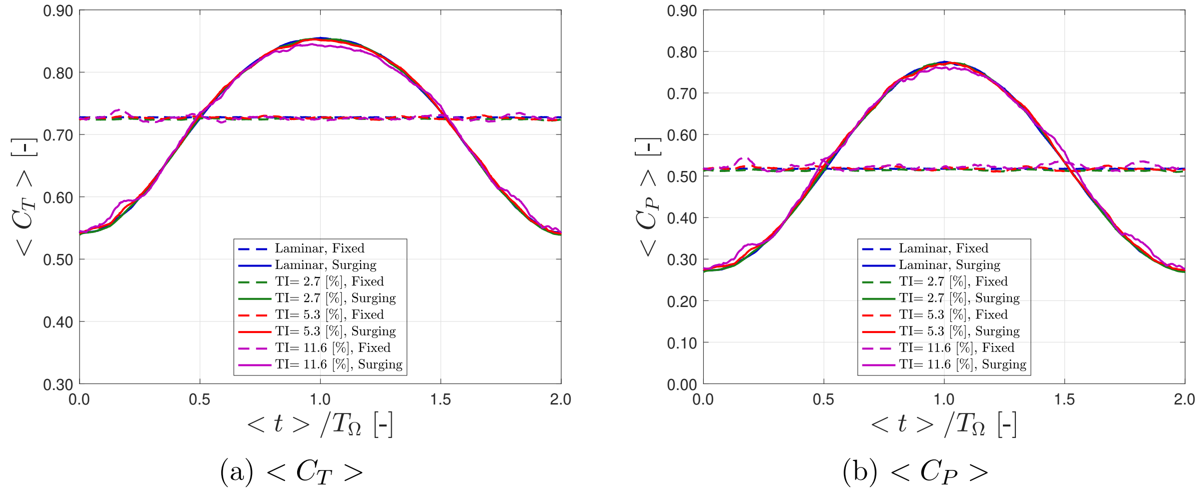

(a) $< C_T >$

(b) $< C_P >$

Figure 4.4: $< C_T >$ and $< C_P >$ for cases of single fixed or surging rotor with different inflow TI.

4.2.2 Velocity and TKE Fields

The instantaneous contours of streamwise velocity u for the eight cases of single NREL 5MW rotor with different inflow TI (cases **1-4**, **6** & **10-12**) are displayed in Figure 4.5. It is clear that cases with higher TI have more prominent fluctuations with u. As for the two laminar cases, the wake structure of the fixed case are relatively stable, and the breakdown process seems to be began around $x/D = 6.5$ to 8.0; while some periodic structures in the wake of the surging case are clearly visible. Moreover, although surging motion seems to alter the wake system significantly for the laminar cases, the instantaneous wake systems for turbulent cases with fixed rotor seem to be similar with the surging cases as comparing u fields in Figure 4.5 (at least for $x/D \leq 4$), especially for TI $= 5.3\%$ and 11.6%. This comparison is deemed valid since the other than the rotor being fixed or surging, other settings, including the random seeds for DFSEM and the time instant which the snapshots were taken, are exactly identical. The presence of the mentioned resemblance indicates that instantaneous wake structures are primarily influenced by the inflow turbulence, rather than whether or not the rotor is surging.

The phase-locked averaged streamwise velocity fields as $\phi_S = 0\pi$, or $\phi_\Omega = 0\pi$ for the eight cases ($< u >_{0\pi}$) are displayed in Figure 4.6. The way of phase-locked averaging is described in section 2.4. One should note that the phase-locked properties are both applicable for the rotational phase ϕ_Ω and the surging phase ϕ_S of the rotor. Comparing

$< u >_{0\pi}$ fields in Figure 4.6 with the u fields in Figure 4.5, the effects of tip and root vorticies for the turbulent cases become more observable and more similar to the laminar ones for both fixed and surging cases. Moreover, for the surging cases, not just the tip and root vorticies become visible for turbulent cases, they also display similar periodic structures as laminar cases. Pairs of periodic low speed regions are observed in the wakes, and they become more clear with lower inflow TI. The author called them *periodic low speed bubbles* (PLSB), and Kleine et al. [22] had also reported these structures. More details about PLSB will be displayed and discussed together with other surging cases in later sections and subsection 4.5.2.

The fields of time averaged streamwise velocity $\overline{u}$ are displayed in Figure 4.7 displayed. Wake recoveries and expansions (for $x/D > 3$) can be clearly observed for the six turbulent cases, and they seem to be related to turbulent intensity while insensitive to whether the rotors are surging. Moreover, for the turbulent cases, the far wake regions ($x/D > 5$) for the phase-locked averaged fields in Figure 4.6 are very similar with field of $\overline{u}$, indicating the wakes lose the *memory* about the detail geometries of the wind turbine rotors and gain randomness. As for the two laminar cases, the fixed case shows no to little wake expansions and wake recoveries; while wake recoveries are clearly observable for the surging case.

The phase-locked turbulent kinetic energy $<\text{TKE}>_{0\pi}$ fields are shown in Figure 4.8. The definition of $<\text{TKE}>_{0\pi}$ is in section 2.4, and the main purpose for introducing it is to measure the extent of the repeatability of flow fields with the specific periods (for surging cases is T_S, while for fixed cases is $2T_\Omega$). Regarding the very low $<\text{TKE}>_{0\pi}$ fields for the two laminar cases (even at the very near wake), it is shown that the flow field for laminar flow is highly periodic and repeatable. It is quite surprising that values of $<\text{TKE}>_{0\pi}$ are very low even with surging rotor under laminar inflow conditions, indicating the system is periodic and highly repeatable. Moreover, if compare the u fields and the $< u >_{0\pi}$ fields of the two laminar cases in Figure 4.5 and 4.6 closely, one can find they are almost identical, which supports the very low values of $<\text{TKE}>_{0\pi}$. As for the turbulent cases, periodic structures can be once more observed for the cases with surging rotor, where cases with fixed rotor do not have.

The fields of turbulent kinetic energy TKE are shown in Figure 4.9. Unlike $<\text{TKE}>_{0\pi}$ only considers certain time steps with relative large intervals, TKE considers all of the available time steps (see Appendix C), and thus is an indicator for flow fluctuations. For the turbulent cases with fixed rotor, the patterns of TKE and $<\text{TKE}>_{0\pi}$ are very alike, except for the regions just behind the rotor, where the geometry information of the rotor is still *remembered* by the wake. As for the laminar case with fixed rotor, regarding the very low value for TKE (except at the region just behind the rotor), the flow is not just highly repeatable, it is essentially without fluctuations. This suggests that the released tip vorticies are smeared out and a vortex tube (cylinder) with uniform vorticity magnitude was formed for the fixed case with laminar inflow conditions, and this agrees with the results reported in other studies which also used LES with ALM to study wake of fixed wind turbine rotors [43, 61]. While for the TKE fields of the turbulent cases with surging rotor, they are very similar to the fixed rotor cases for the same inflow TI. As for the laminar case with surging rotor, there are two strips of regions having higher TKE after the tip of the rotor; they are related to the convection of the vortical structures which will be discussed later in subsection 4.2.3.

4.2.3 Pressure and Vorticity Fields

The time-averaged pressure fields $\Delta\overline{p}$ of the eight cases are displayed in Figure 4.10, where Δp stands for the pressure difference between the ambient pressure (the fixed value set for the boundary conditions of outlet). Note that here q stands for dynamic pressure ($q = 0.5\rho V_0^2$). Here surging and fixed cases again share very similar contours for turbulent cases. While for the laminar case, surging case depicts two strips of lower values at the similar positions with higher TKE in Figure 4.9, which the case with fixed rotor do not. Moreover, higher pressure is featured at upstream side of the rotor, and lower pressure appears at the other side, which is as expected. Additionally, $\Delta\overline{p}$ almost completely recovers around $x/D = 8$, suggesting pressure fields can be considered fully recovered at the end of the computational domain ($x/D = 10$).

The instantaneous and phase-locked averaged y-component (out-of-plane) vorticity fields (ω_y & $< \omega_y >_{0\pi}$) are in Figure 4.11 and 4.12. The distributions of ω_y & $< \omega_y >_{0\pi}$ for the fixed cases are as expected, mainly concentrating at the regions behind the tips and roots, accounting for the released trailing (tip and root) vorticies, and they remain quite obvious even with the highest inflow TI considered. While for the surging cases, clearly that they have distinct ω_y & $< \omega_y >_{0\pi}$ fields compare to the fixed cases, especially for the laminar cases. Unlike the vortex tube (cylinder) formed in fixed case with laminar inflow, $< \omega_y >_{0\pi}$ for the surging case has periodic vortical structures, and their repeating frequencies are as same as the ω_S, just as the PLSB appear in the u fields. Every pair (ring) of a vortical structure in $< \omega_y >_{0\pi}$ field for the laminar case here is formed by the merge of the tip vorticites released within a completed surging cycle. The merging process of the tip vorticies are triggered by their interaction, since surging motions altered the inter-distance between them and make the inter-distance no longer constant. Kleine et al. [22] had reported the merging process as well, and subsection 4.5.1 & 4.5.2 will discuss more details about this. As for the turbulent cases with surging rotor, periodic structures with frequency of ω_S also can be found in $< \omega_y >_{0\pi}$ fields, but the patterns become more blurry with bigger TI. Note that with the sign of $< \omega_y >_{0\pi}$, these vortical structures indicate the flows get in and come out of wakes regions through their induction fields (see $< w >_{0\pi}$ fields in Figure E.1). Moreover, for the surging cases, the high magnitude cores of $< \omega_y >_{0\pi}$ are aligned with the low pressure cores of $< \Delta p >_{0\pi}$ fields (see Figure E.4). Furthermore, notice that even though field of $< \omega_y >_{0\pi}$ for laminar case with surging rotor seems to be a bit chaotic after $x/D = 5$, the very low <TKE>$_{0\pi}$ at the regions still suggest the flow being highly repeatable. As for the turbulent cases with surging rotor, the periodic structures of $< \omega_y >_{0\pi}$ fields once again are less obvious with higher inflow TI. Note that $< \omega_y >_{0\pi}$ could served as $\overline{\omega}_y$ with rather small sample size for the turbulent cases in the far wake regions. Also notice the vortex tube for the laminar case with fixed rotor mentioned previously are clearly observed with both ω_y & $< \omega_y >_{0\pi}$ fields.

4.2.4 Momentum Entrainment

With the analysis in section 2.6 and Appendix B, streamwise momentum entrainment (recovery) $\partial\overline{u}\overline{u}/\partial x$ was investigated with the terms of time-averaged pressure gradients $-\partial\overline{p}/\partial x$, vertical transport of streamwise momentum $-\overline{w}(\partial\overline{u}/\partial z)$, and one of the fluctuation (Reynolds Stress) terms $-\partial\overline{u'w'}/\partial z$. Their contour plots are displayed in Figure 4.13, 4.14, and 4.15. In short, it is found that the pattern of the three considered terms for the turbulent cases are not significantly affected by whether the rotor was surging.

In the fields of $\partial\overline{p}/\partial x$, clearly that all eight cases experienced momentum loss to overcome the adverse pressure gradients due to the presence of rotor. However, after $x/D > 1.5$, its effects on momentum are negligible, and the term did not aid momentum recovery at all.

For the contours of $\overline{w}(\partial\overline{u}/\partial z)$, all eight cases have strips of negative values just behind the rotors, indicating the streamwise velocity of the flows become smaller as x become bigger. Together with the information of $\overline{w}$ (see Figure E.2), contours of $\overline{w}(\partial\overline{u}/\partial z)$ show the wake expansions and the flows with lower streamwise momentum were transported outward from the core of wake, and this can be also expected with the contour plots of $\overline{u}$ in Figure 4.7. Other than the negative strips just behind the rotors, the six turbulent cases also feature positive strips in contours of $\overline{w}(\partial\overline{u}/\partial z)$ after the negative strips. Again together with the information of $\overline{w}$, it can be shown that flows with higher momentum were brought from outer free-stream to the positive regions. Note that since the positive regions did not really go into area shaded by the rotor ($|z/D| \leq 0.5$), Term $\overline{w}(\partial\overline{u}/\partial z)$ is not the main source for the wake recoveries for these cases. For the laminar case with surging rotor, very interestingly, distinct contour is found. This is due to that the system is highly deterministic (repeatable) for the laminar case with surging rotor; also that asymmetry can be observed, and this is further explained in subsubsection 4.5.2.

As for the contours of fluctuating term $\partial\overline{u'w'}/\partial z$, it is clear that $\partial\overline{u'w'}/\partial z$ is the main source term for momentum recoveries of the turbulent cases, since their values are much more significant compare to the other terms. Together with the contours of $\overline{u}$ in Figure 4.7, it can be seen momentum was transported from the flows in regions containing higher momentum (regions outside the projection area of the rotor disk and the very center) to the flow in regions with lower momentum. Note that momentum recoveries occur earlier in more upstream regions with bigger TI, and also in bigger extents. Not surprisingly, the $\partial\overline{u'w'}/\partial z$ field for laminar case with fixed rotor has a value of zero almost everywhere, this is expected since that no recovery on $\overline{u}$ and very low values for TKE field was observed in the previous investigation. However, once again, laminar case with surging rotor has distinct pattern of $\partial\overline{u'w'}/\partial z$ field; in general, seems that there is a net positive momentum gain for the case, but its patterns are not as smooth as the turbulent cases. The pattern for the laminar case with surging rotor is not easy to explain and asymmetry can be once observed; this is further investigated in subsubsection 4.5.2.

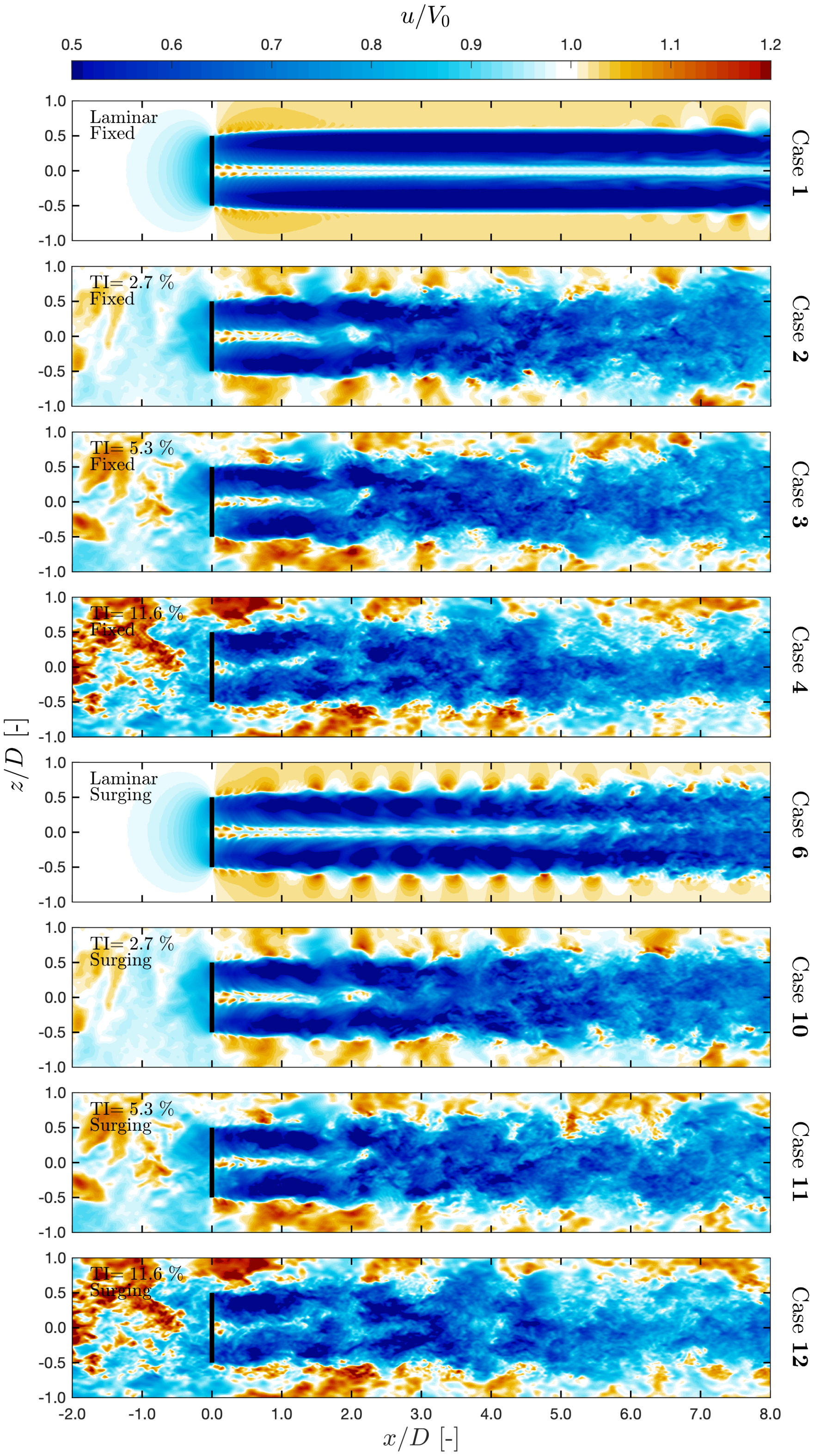

Figure 4.5: Fields of instantaneous streamwise velocity u for single fixed or surging rotor with different inflow TI.

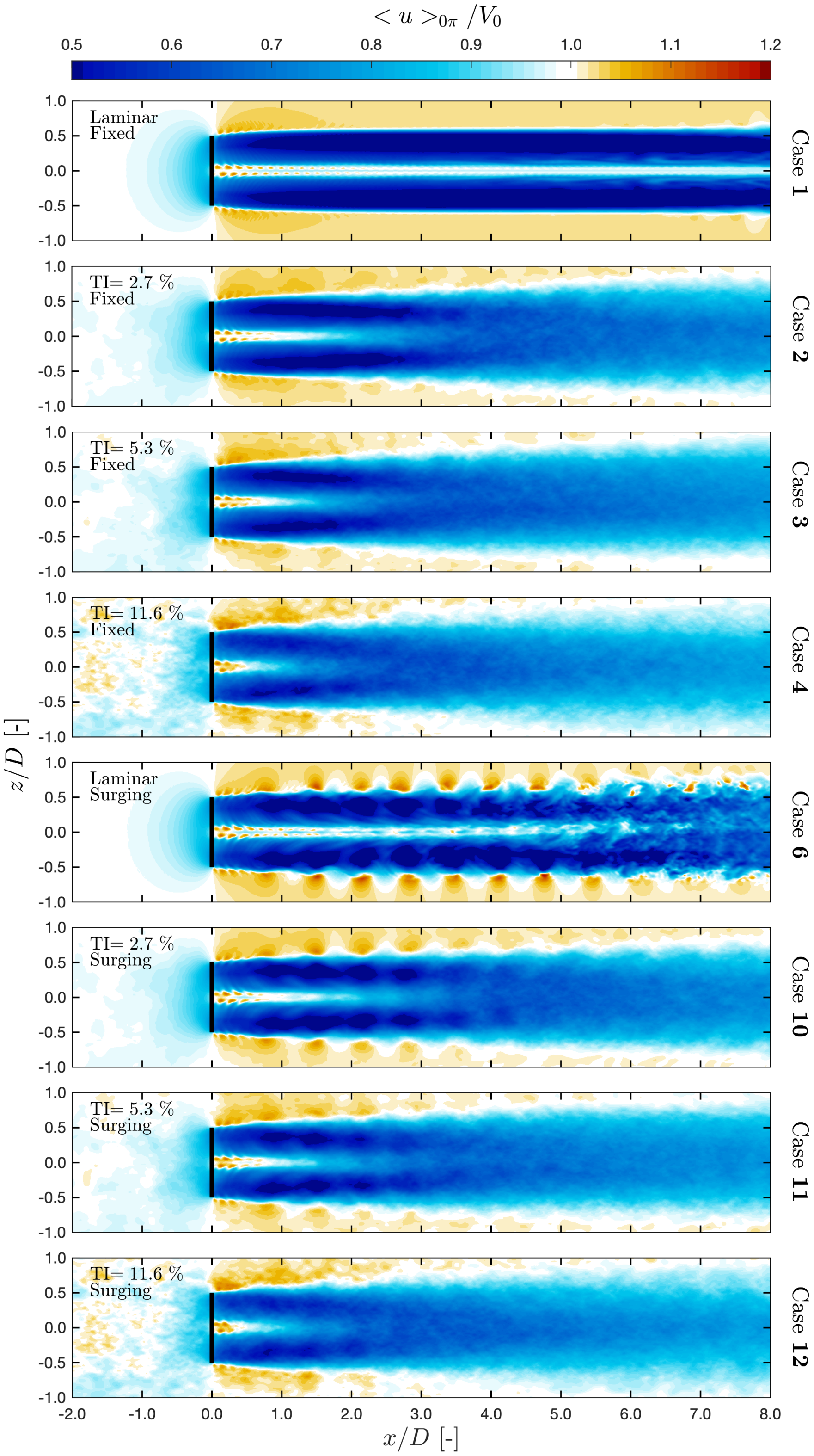

Figure 4.6: Fields of phase-locked averaged streamwise velocity $< u >_{0\pi}$ for single fixed or surging rotor with different inflow TI.

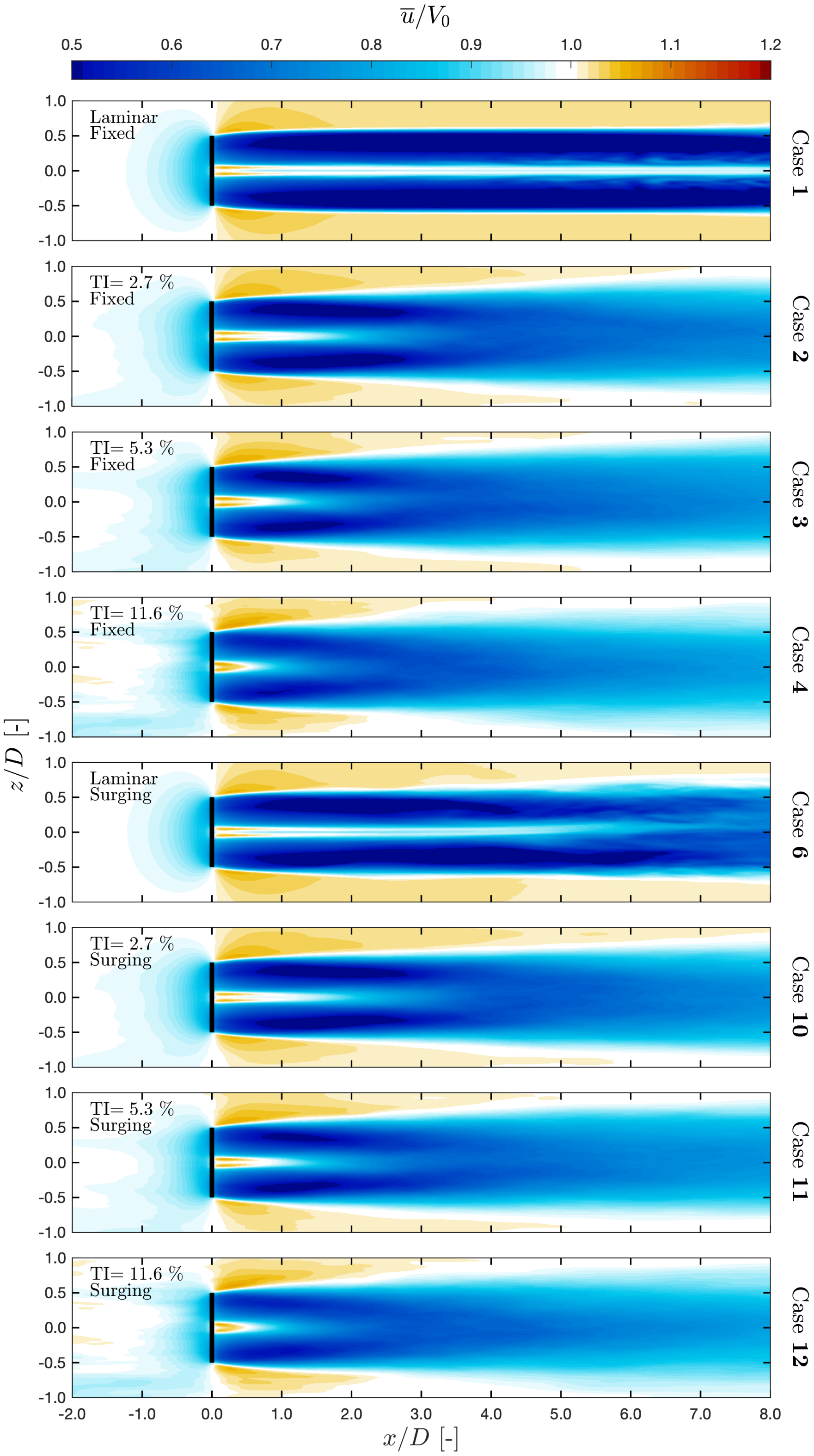

Figure 4.7: Fields of time-averaged streamwise velocity $\overline{u}$ for single fixed or surging rotor with different inflow TI.

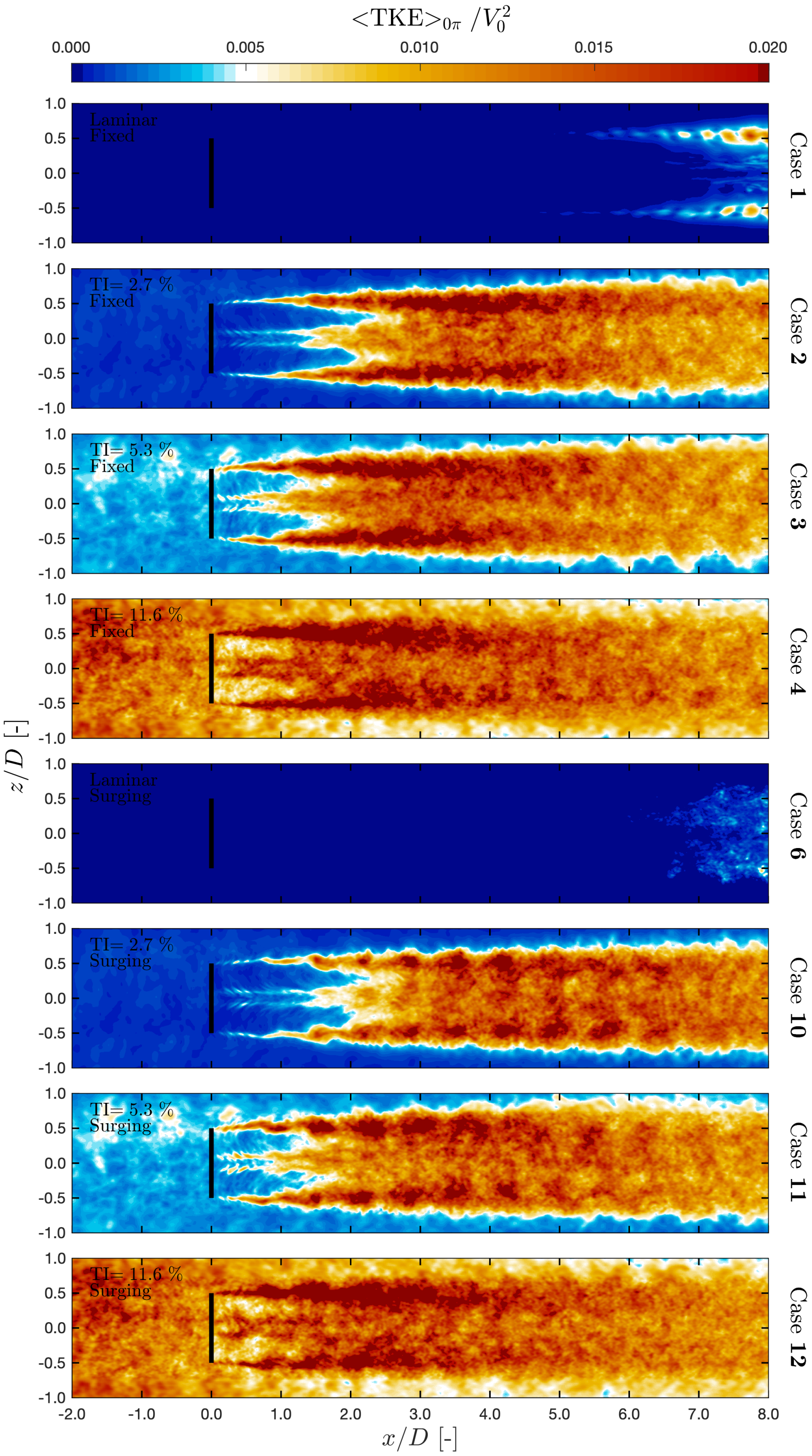

Figure 4.8: Fields of phase-locked averaged turbulent kinetic energy <TKE>$_{0\pi}$ for single fixed or surging rotor with different inflow TI.

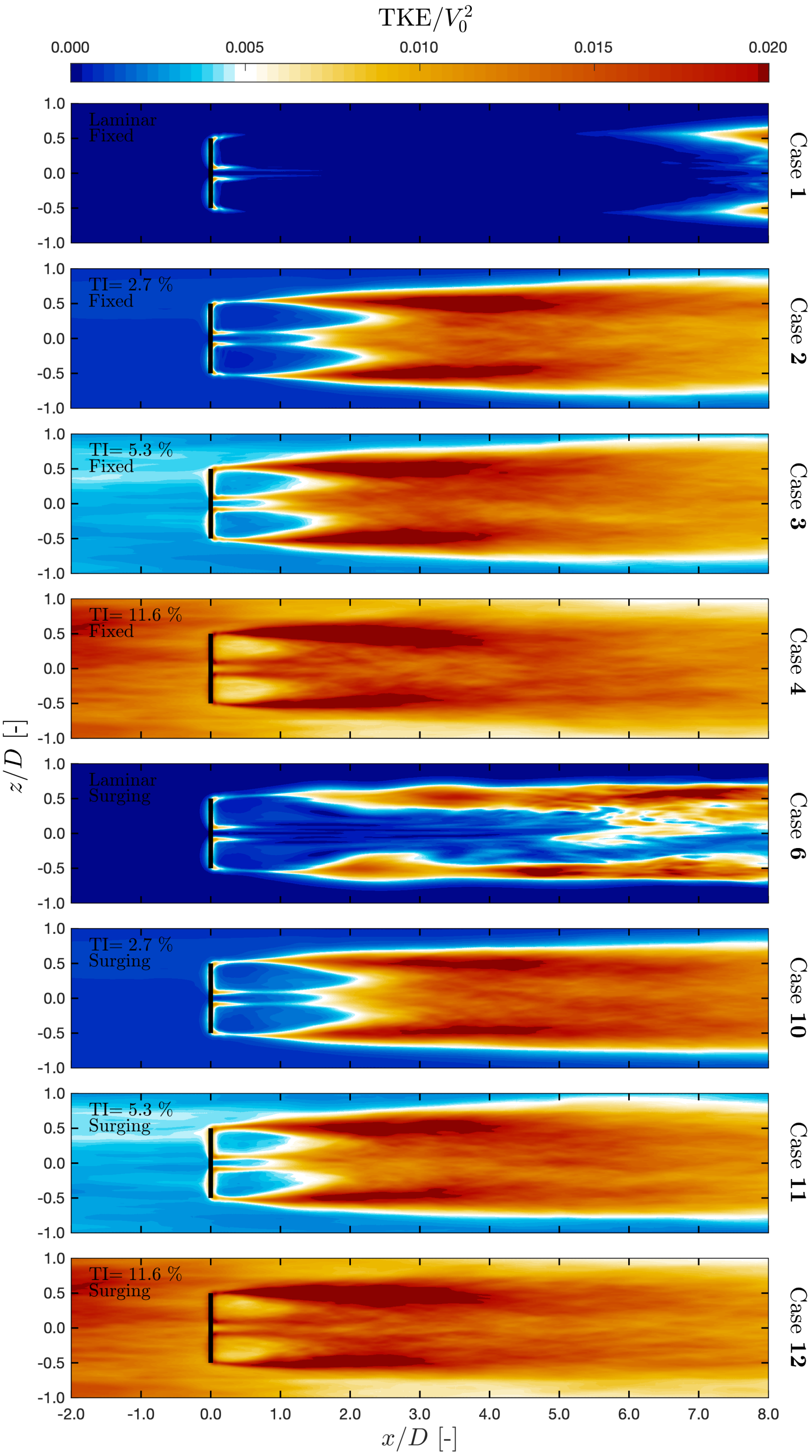

Figure 4.9: Fields of turbulent kinetic energy TKE for single fixed or surging rotor with different inflow TI.

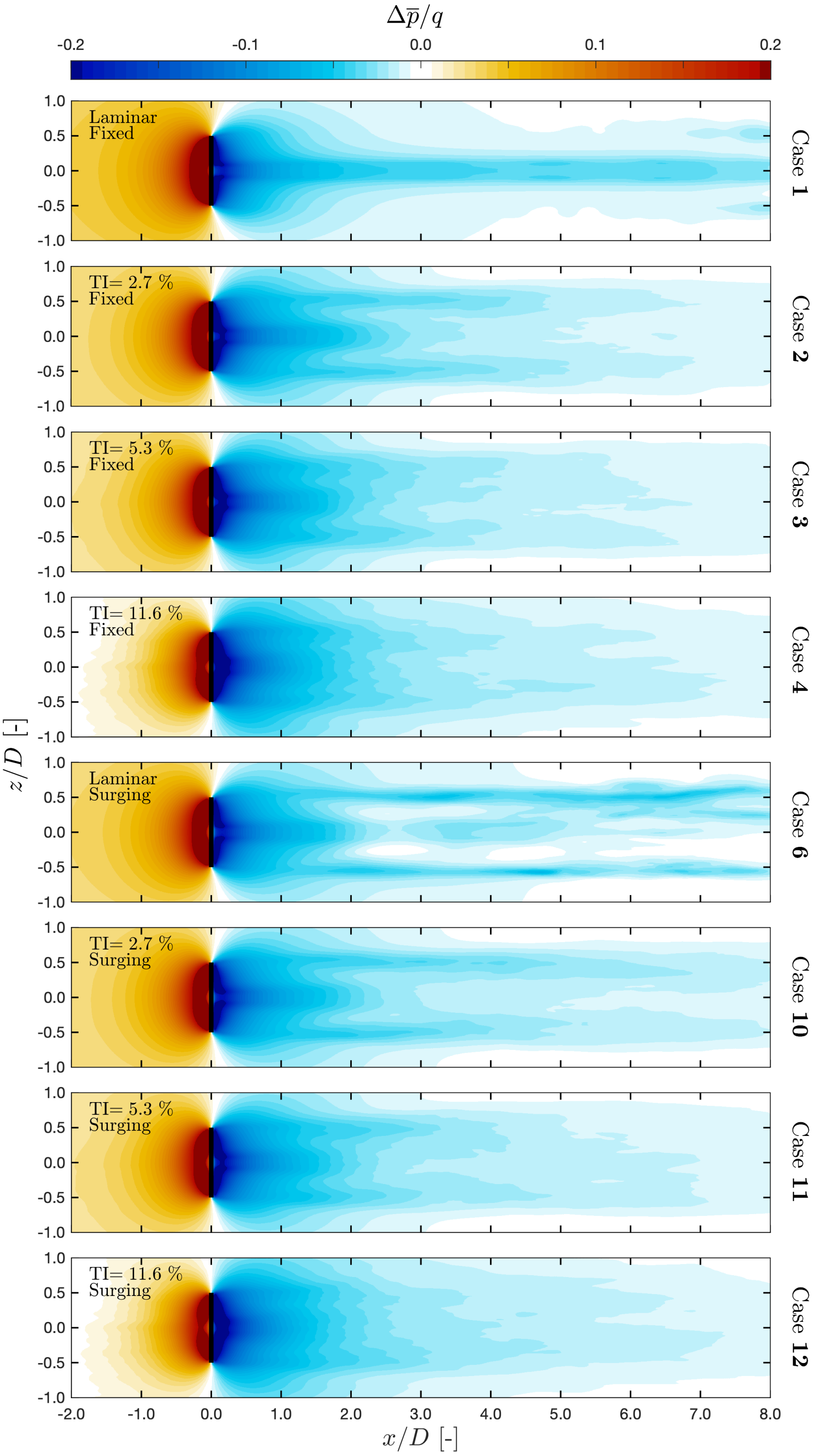

Figure 4.10: Fields of time-averaged pressure $\Delta\overline{p}$ for single fixed or surging rotor with different inflow TI.

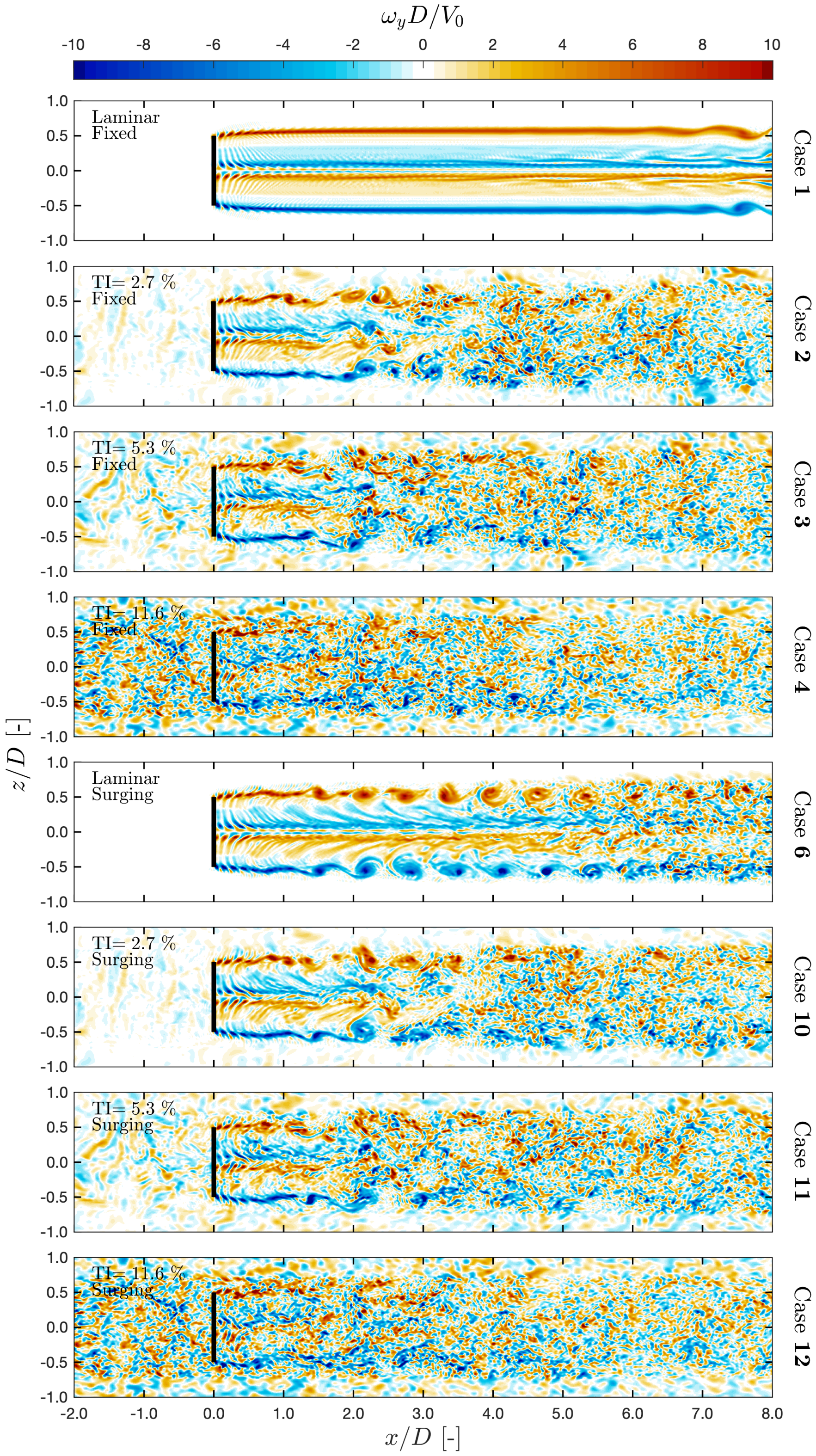

Figure 4.11: Fields of instantaneous y-component vorticity ω_y for single fixed or surging rotor with different inflow TI.

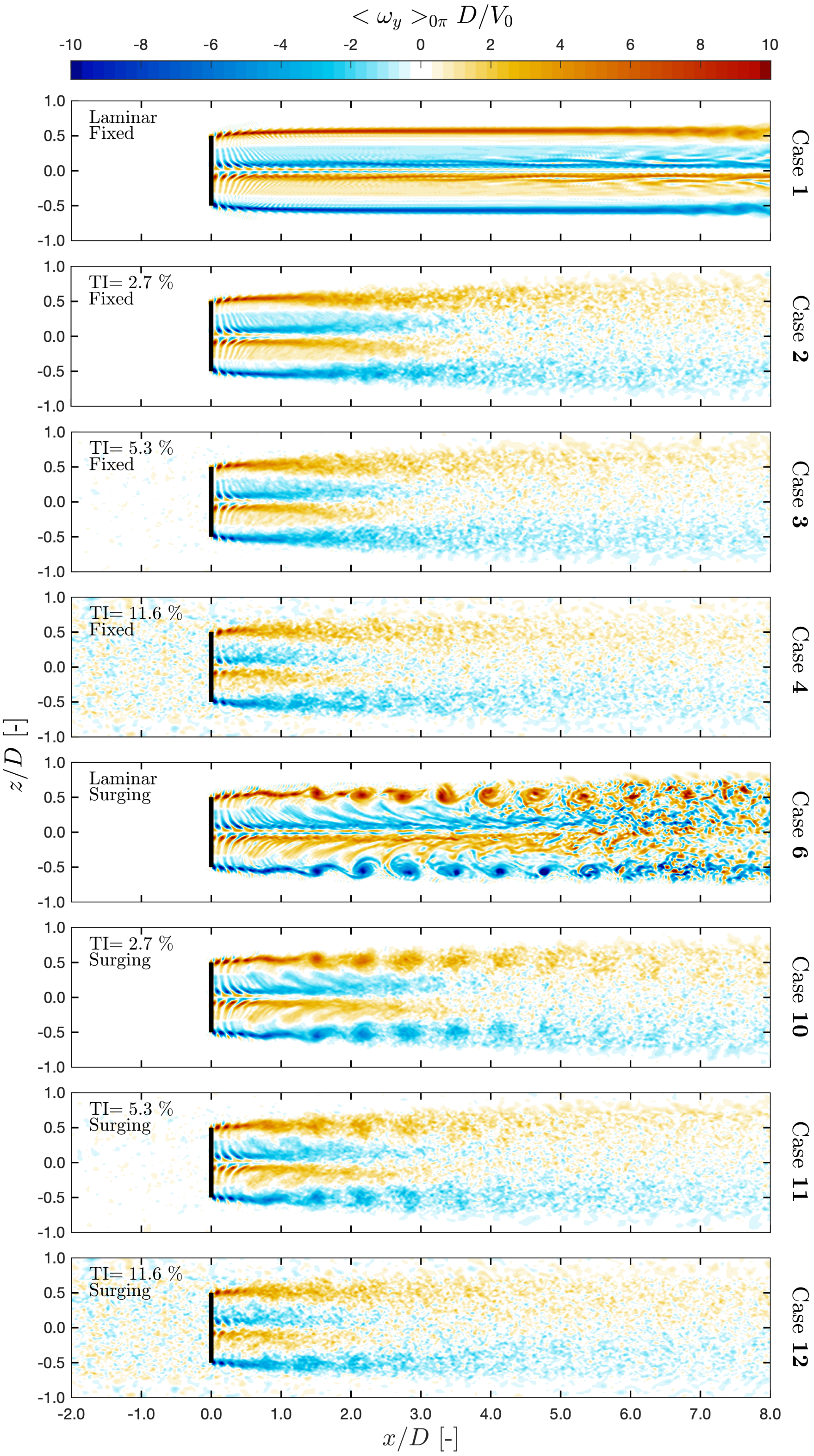

Figure 4.12: Fields of phase-locked averaged y-component vorticity $< \omega_y >_{0\pi}$ for single fixed or surging rotor with different inflow TI.

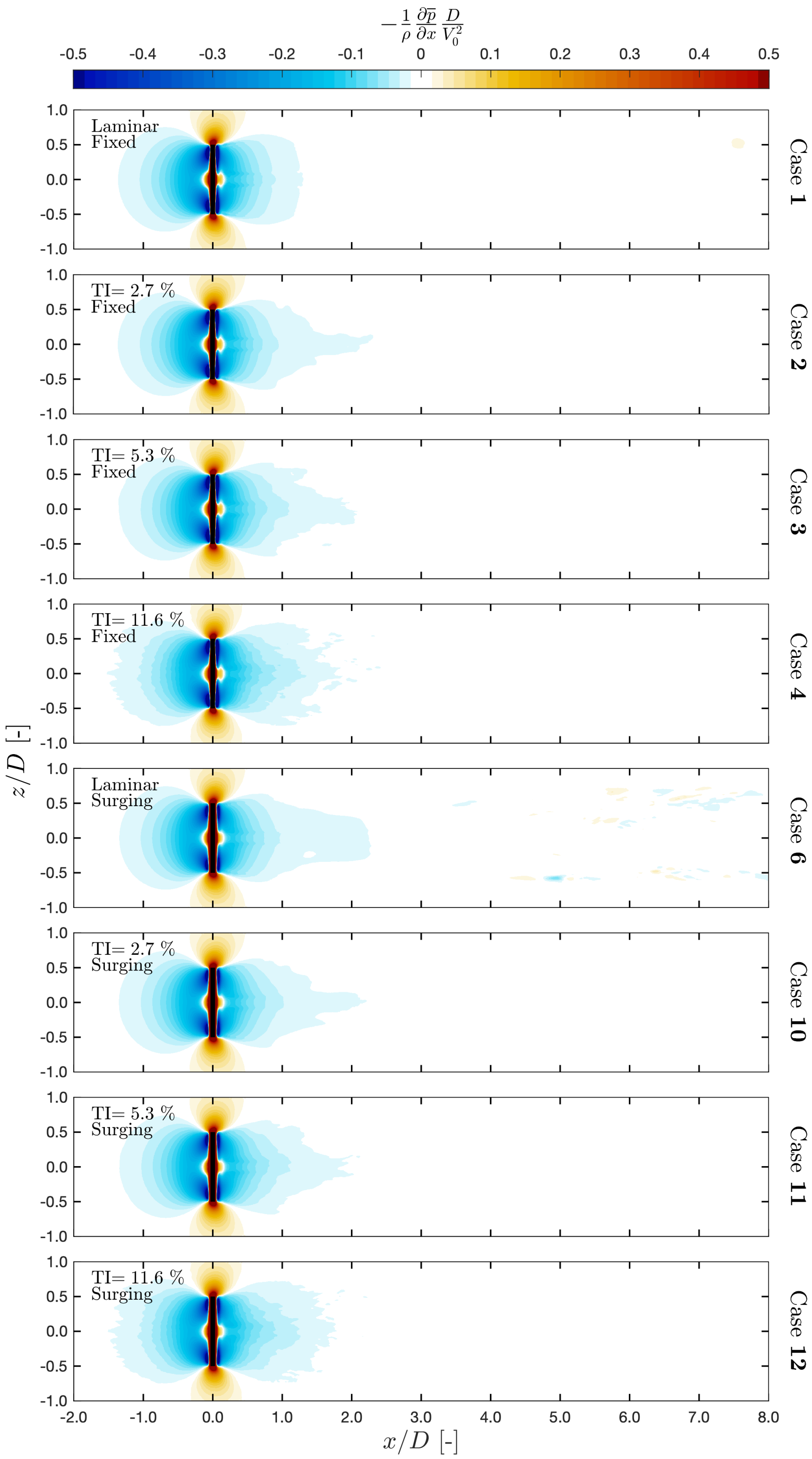

Figure 4.13: Fields of pressure gradients $-(1/\rho)(\partial\overline{p}/\partial x)$ for single fixed or surging rotor with different inflow TI.

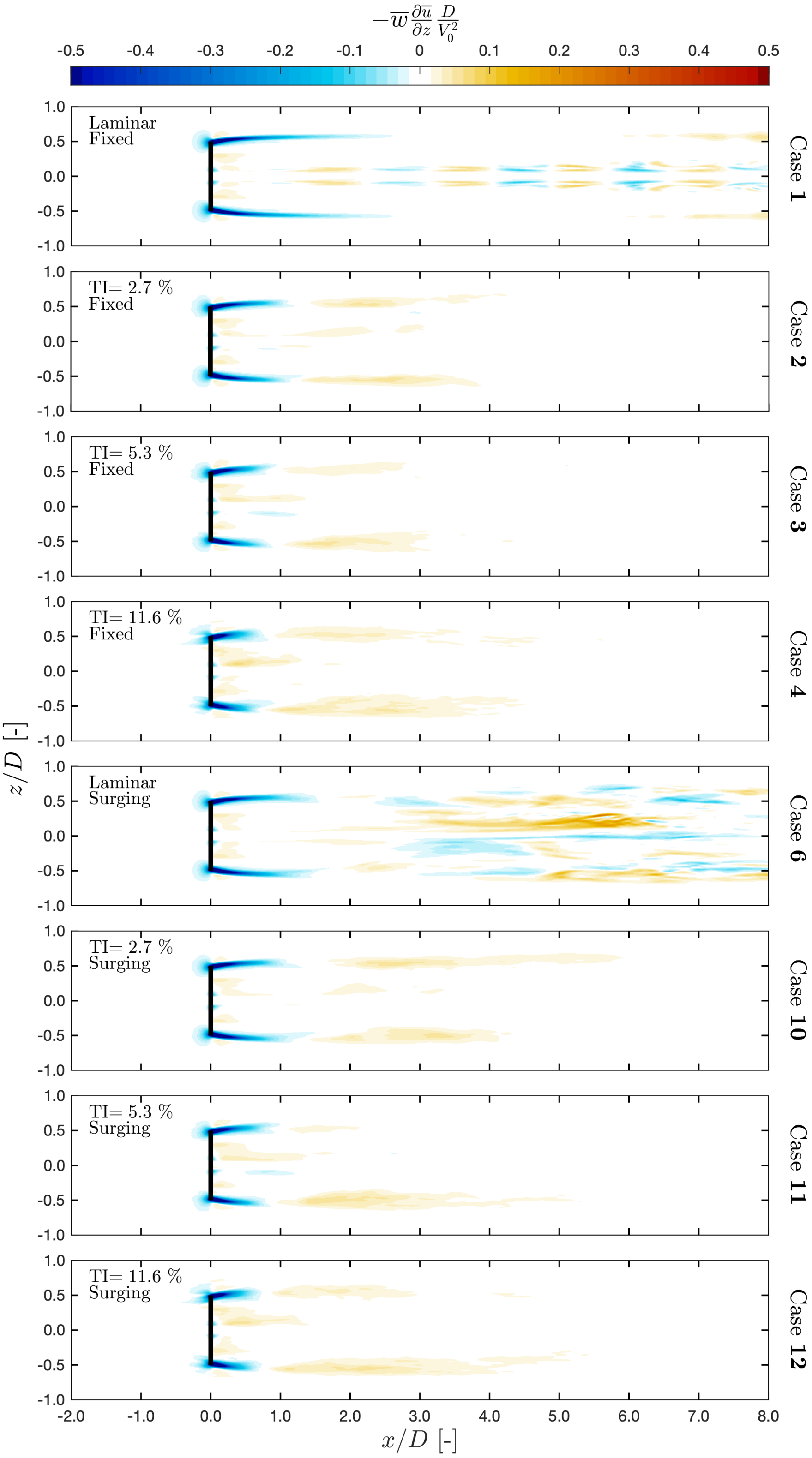

Figure 4.14: Fields of $-\overline{w}(\partial \overline{u}/\partial z)$ for single fixed or surging rotor with different inflow TI.

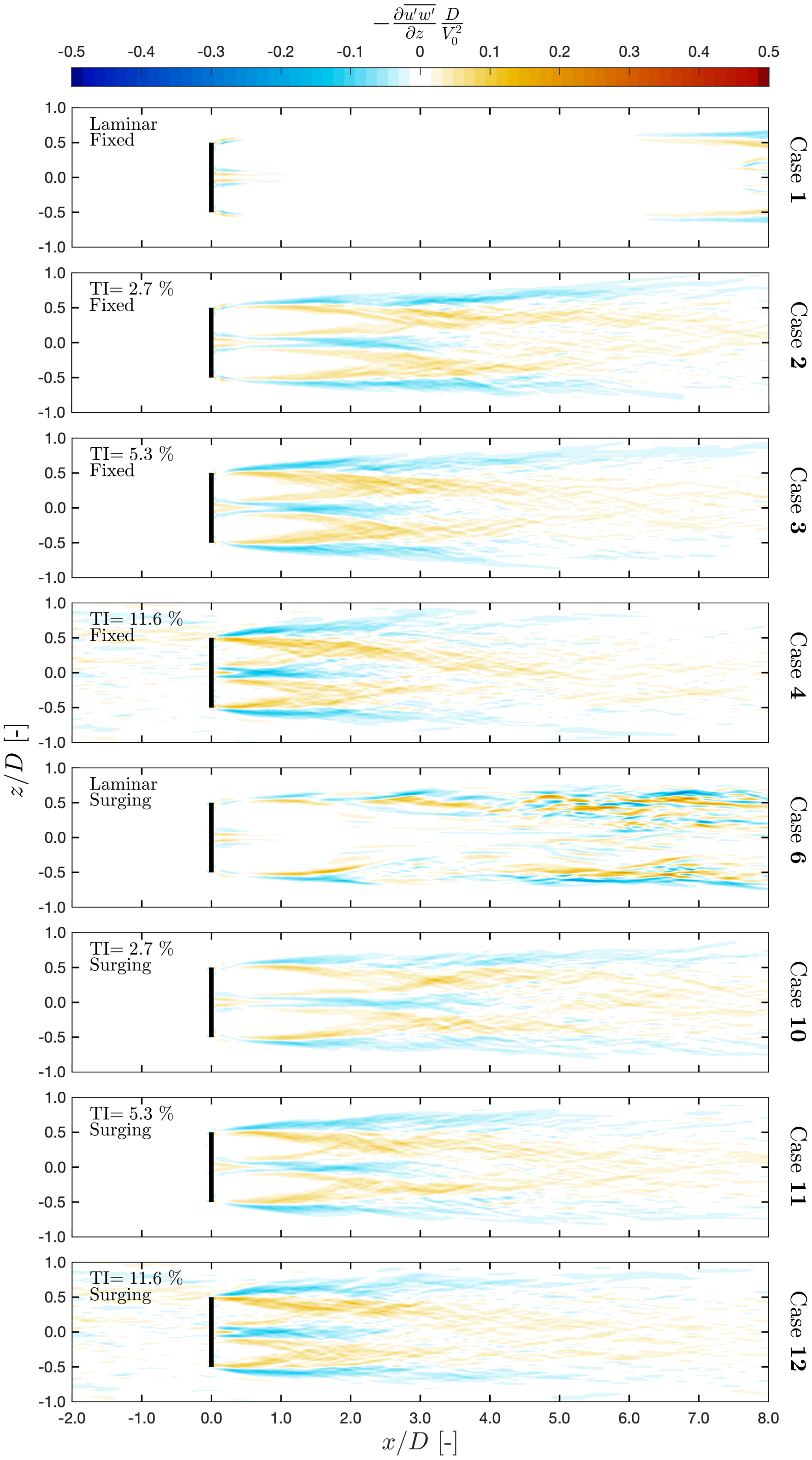

Figure 4.15: Fields of $-\partial\overline{u'w'}/\partial z$ for single fixed or surging rotor with different inflow TI.

4.3 Laminar Inflow Conditions with Different A_S and ω_S

This section compare cases of single NREL 5MW rotor with different surging amplitudes A_S and surging frequencies ω_S along with a fixed case under laminar inflow conditions. The selected settings for A_S & ω_S are 2 m & 0.63 rad/s, 4 m & 0.63 rad/s, 8 m & 0.63 rad/s, 4 m & 0.32 rad/s, 4 m & 1.27 rad/s, and a fixed case. The six cases correspond to cases **1** and **5-9** in Table 4.1 (groups S.3 & S.4). Note that additional information for this section can be found in section E.2. Also it should be noted that laminar inflow conditions are unrealistic for wind energy industry, thus the results in this section are not likely to happen in the real world.

4.3.1 Summarizing Wake Characteristics and Rotor Performances

Figure 4.16 and 4.17 present the overall results about $\overline{u}_{\text{Disk}}$ and $\overline{u}$. It can be observed that surging do facilitate recoveries of $\overline{u}$, and cases with bigger A_S & ω_S have higher $\overline{u}_{\text{Disk}}$ up until $x/D = 6$. In general, it shows that the trends for $\overline{u}_{\text{Disk}}$ profiles are related to $\mathbb{V}$ (see Table 4.1), and higher $\mathbb{V}$ results in larger values for $\overline{u}_{\text{Disk}}$ (Table 4.4). While interestingly, for $x/D \geq 7$, they tend to converge to a similar value. Chen et al. [55] had reported similar results. However, since the wake systems of these cases are very complex (and highly repeatable with frequency being ω_S), more cases with different surging settings should be tested before drawing solid conclusions. As for profiles of $\overline{u}$ in Figure 4.17, unlike the turbulent cases analyzed in section 4.2, the $\overline{u}$ profiles here are not in Gaussian-shape, though the recoveries of $\overline{u}$ can be clearly observed. Note the sharp kinks of $\overline{u}$ profiles for the surging cases, since they imply the effects of mixing (diffusion) are weak for these cases. More detail discussions are in subsubsection 4.5.2.

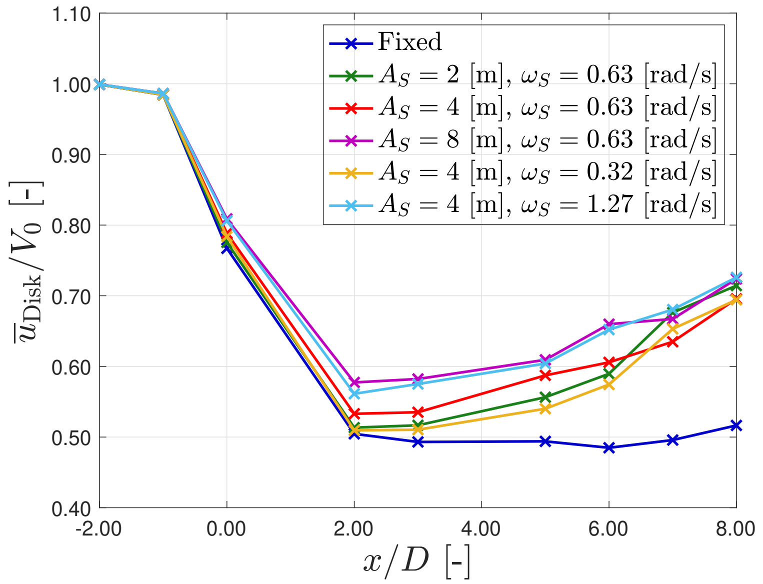

Figure 4.16: $\overline{u}_{\text{Disk}}$ along x-direction for cases of single rotor with different A_S and ω_S under laminar inflow conditions.

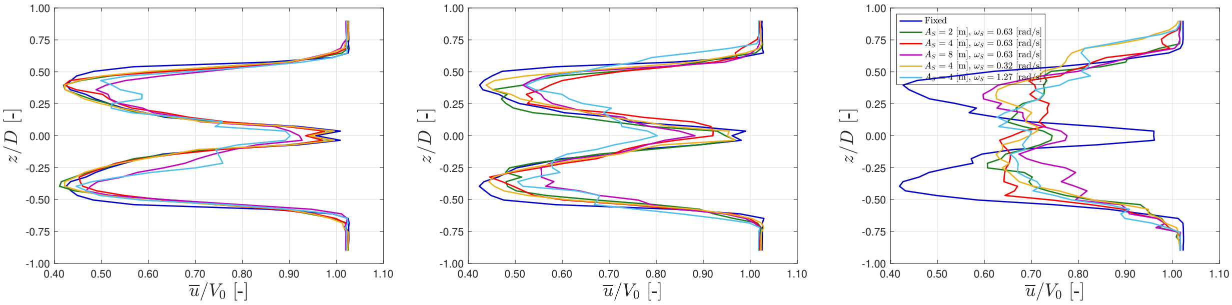

(a) $x/D = 3.0$ (b) $x/D = 5.0$ (c) $x/D = 8.0$

Figure 4.17: Profile of $\overline{u}$ at different x/D for cases of single rotor with different A_S and ω_S under laminar inflow conditions.

Table 4.4: The ratios of $\overline{u}_{\text{Disk}}$ for the fixed and surging cases under laminar inflow conditions at $x/D = 3$ and $x/D = 5$.

	$A_S = 2$ m $\omega_S = 0.63$ rad/s	$A_S = 4$ m $\omega_S = 0.63$ rad/s	$A_S = 8$ m $\omega_S = 0.63$ rad/s	$A_S = 4$ m $\omega_S = 0.32$ rad/s	$A_S = 4$ m $\omega_S = 1.27$ rad/s
$\overline{u}^{3D}_{\text{Disk,surging}}/\overline{u}^{3D}_{\text{Disk,fixed}}$	104.78%	108.53%	118.07%	103.52%	116.63%
$\overline{u}^{5D}_{\text{Disk,surging}}/\overline{u}^{5D}_{\text{Disk,fixed}}$	112.65%	118.91%	123.37%	109.35%	122.31%

Figure 4.18 displays $< C_T >$ and $< C_P >$ for the six cases, and $\overline{C}_T$ and $\overline{C}_P$ can be found in Table 4.1. Here clearly can see that both C_T and C_P vary periodically according to the surging frequency ω_S of their case, and their amplitudes are related to $\mathbb{V}$, which is related to both A_S & ω_S, where larger $\mathbb{V}$ brings larger varying amplitudes. However, there are upper limits for both C_T and C_P, and they are related to stalling, which will be more elaborated in subsection 4.5.3. Moreover, if focusing around the values of $< C_T >$ for the fixed case, one can find out that the extents of under-shoots are more significant compare to the over-shoots for the surging cases, and the differences are become larger with larger $\mathbb{V}$. This is clearly documented with $< C_T >^+$ and $< C_T >^-$ in Table 4.1, and it is also reflected with $\overline{C}_T$, from which cases with bigger $\mathbb{V}$ have smaller $\overline{C}_T$ for the considered surging settings here. As for $\overline{C}_P$, seems that surging cases with lower $\mathbb{V}$ ($\mathbb{V} = 0.11$ or 0.22) have slightly bigger values compare to the fixed case, while the opposite happen for the cases with bigger $\mathbb{V}$ ($\mathbb{V} = 0.44$). It is suggested that the velocity triangle and stalling can be used to explain these behaviours of $\overline{C}_T$ & $\overline{C}_P$. More detail discussions about stalling and the causes of lower $\overline{C}_T$ for surging rotor can be found in subsection 4.5.3.

Further observing the curves of $< C_T >$ and $< C_P >$, one can find that they are almost in-phase with the surging motions, and this agrees with most of the findings in literature [10, 21, 29]. It can be seen that curves of $< C_T >$ and $< C_P >$ cross the values of fixed case at around $< t > /T_\Omega = 0.5$ and 1.5, which are the timing when surging velocity of rotor is 0.0 m/s ($\phi_S = 0.5\pi$ or 1.5π, $V_{0,\text{app}} = V_0$). However, slight hysteric effects still appear after plotting $< C_T >$ against surging velocity of rotor V_{WT} in Figure 4.19. Notice that V_{WT} reflects the phase of surging (Equation 2.26). While the hollow marks in Figure 4.19 represent the minimums and maximums of $< C_T >$ a case should get according to quasi-steady solutions form the auxiliary simulation cases in Table 4.2 together with their values. Notably in

Figure 4.19, cases with $A_S = 8$ m & $\omega_S = 0.63$ rad/s and $A_S = 4$ m & $\omega_S = 1.27$ rad/s (cases with $\mathbb{V} = 0.44$) have more significant hysteresis effects, and it is more pronounced for cases with higher ω_S. That is, the extents of hysteresis effects depend on both $\mathbb{V}$ and $\mathbb{W}$ (ω_S), and larger values of $\mathbb{W}$ will end up in stronger hysteresis effects. Moreover, for all cases, hysteresis effects are more pronounced when the rotor moves along the free stream direction, which the rotor moves into its wake.

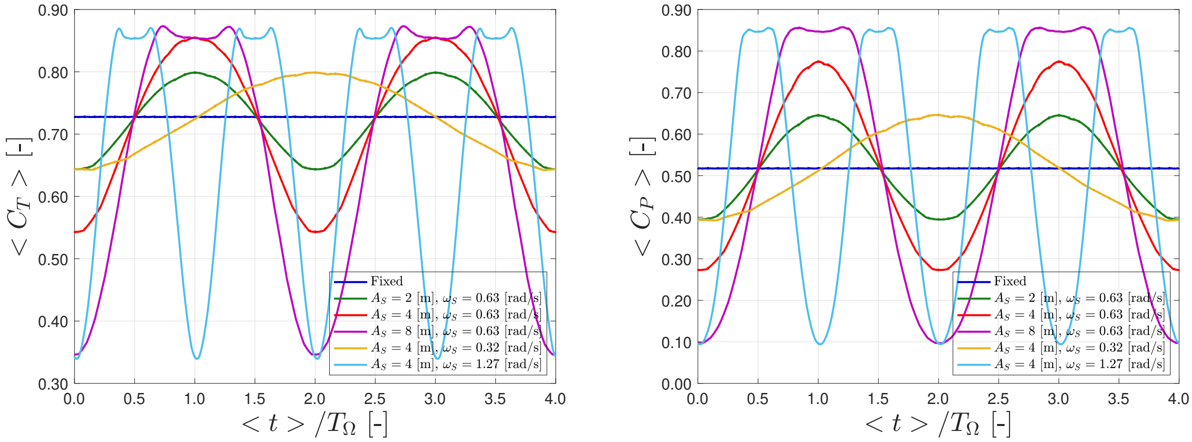

(a) $< C_T >$ (b) $< C_P >$

Figure 4.18: $< C_T >$ and $< C_P >$ for cases of single rotor with different A_S and ω_S under laminar inflow conditions.

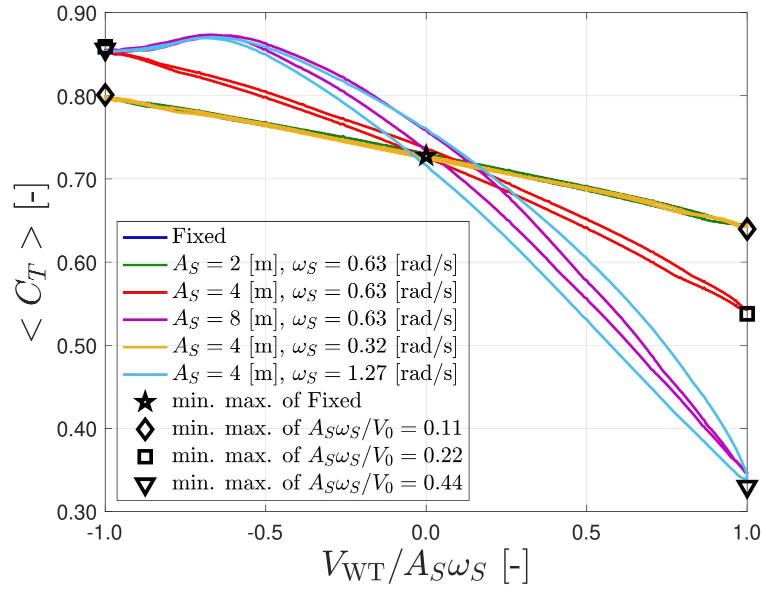

Figure 4.19: $< C_T >$ against V_{WT} with with different A_S and ω_S under laminar inflow conditions. All the curves travel in clockwise direction.

4.3.2 Velocity and TKE Fields

The fields of $< u >_{0\pi}$ for the six cases of single NREL 5MW rotor with different surging amplitudes A_S and surging frequencies ω_S under laminar inflow conditions are displayed in Figure 4.20 (cases **1** & **5-9**). Instantaneous contours of u are not displayed since they are very similar to $< u >_{0\pi}$ fields due to the very low values $<$TKE$>_{0\pi}$ fields which will be displayed later. Clearly that except for the fixed case, all the other five show periodic structures in their wakes, which are the periodic low speed bubbles (PLSB) introduced in section 4.2. Note it can be seen that the repeating frequencies of PLSB are exactly the values of the cases' ω_S; and even with the different frequencies, the PLSB basically shares same characteristics, having slower regions in the wakes but faster at just outside the wakes. Also, one should be aware of the 3D nature of the wakes and actually PLSB are more like rings. More detail descriptions and analysis can be found in subsection 4.5.1 & 4.5.2, where PLSB will be more explored.

The fields $<$TKE$>_{0\pi}$ are shown in Figure 4.21. Once again, values for $<$TKE$>_{0\pi}$ fields are very low, even at the vicinity of the rotors. As being stated in the previous sections, this indicates the flow is highly repeatable and deterministic, and this seems to be the theme for the laminar inflow cases with the simulation framework employed in this thesis. And very interesting phenomenon is that with bigger A_S, the fields of $<$TKE$>_{0\pi}$ seems to be smaller (Figure 4.21), and the fixed case has the most pronounced values. Fang et al. [60] had reported similar phenomena using IDDES with geometric resolved rotor, stating that tip-vorticity related structures actually breakup earlier while the rotor is fixed compare to a surging one. The above phenomenon implies that with bigger A_S, the flow fields actually become more repeatable, or in other words, more predictable. And this may be the reason why for $x/D \geq 6$, recovery rate of $\overline{u}_{\text{Disk}}$ for case $A_S = 2$ m are greater than cases with larger A_S (same ω_S), since the flow structures are more chaotic with smaller A_S. As for varying ω_S, the flow fields are still seemed to be more repeatable compared to the fixed case with the three considered ω_S. While the trend with ω_S is not as clear as A_S, since they have quite different patterns of $<$TKE$>_{0\pi}$ at the downstream regions.

Fields of TKE for the three surging cases under laminar inflow conditions are very similar, and thus they are not displayed. One can find the TKE contour for surging case with $A_S = 4$ m & $\omega_S = 0.63$ rad/s under laminar inflow conditions in case **6** of Figure 4.9.

4.3.3 Pressure and Vorticity Fields

The field of $\Delta\overline{p}$ for the eight cases are displayed in Figure 4.22. In these contours, two strips of lower pressure regions appear in the five surging cases. Moreover, an important finding is that cases with smaller $\mathbb{V}$ have more noticeable high and low pressure regions in front and after the neutral positions of the rotor, and the fixed cases having the biggest pressure jump. And for the case with $\mathbb{V} = 0.44$ ($A_S = 8$ m & $\omega_S = 0.63$ rad/s and $A_S = 4$ m & $\omega_S = 1.27$ rad/s), their pressure bubbles are significantly smaller compared to the other cases, which should be related to the curves in Figure 4.18a. This is reasonable together with the findings that $\overline{C}_T$ drops as $\mathbb{V}$ becomes bigger in Table 4.1. More detail discussions are in subsection 4.5.3. As for fields of Δp and $< \Delta p >_{0\pi}$, since they are similar with the laminar cases in last section (section 4.2), they are not displayed.

The fields of $< \omega_y >_{0\pi}$ are in Figure 4.23. Contours of ω_y fields are not displayed since they are almost identical to $< \omega_y >_{0\pi}$ fields. Periodic structures once again can be observed in fields of $< \omega_y >_{0\pi}$; and once again, these vortical structures indicate the flow get in and come out from the wake region (see Figure E.8). For cases with $\omega_S = 0.63$ rad/s and 1.27 rad/s, it is obvious that periods of the vortical structure are exactly the same with ω_S, since these vortical structures are results of the merges of the tip vorticites released within a completed surging cycle. However, for $\omega_S = 0.32$ rad/s, during the formation of the vortical structures, tip vorticies within a complete surging cycle did not form together as one vortex structure, but rather two, with one stronger (eg. the one at x/D between 2.8 and 3.2) and the other weaker (eg. the one at x/D between 3.5 and 3.8). This is the result of different varying rates for the inter-distances between the tip vorticies. Moreover, for the cases considered here, the ones with higher ω_S would form their vortical structures at more upstream positions. Furthermore, for the three cases with $\omega_S = 0.63$ rad/s but with different A_S, magnitudes of their vortical structures are similar; this is mainly due to that these vortical structures are results of the merges of the tip vorticites released within a completed surging cycle, together with the rotational speed being kept unchanged during the simulations and the fact that both $\overline{C}_T$ and $\overline{C}_P$ for the three cases are similar (implying the release tip vorticies have similar magnitudes). See subsection 4.5.1 for more details about the merging process of the vortical structures.

4.3.4 Momentum Entrainment

Fields of $-\partial\overline{p}/\partial x$, $-\overline{w}(\partial\overline{u}/\partial z)$, and $-\partial\overline{u'w'}/\partial z$ are similar for the five surging settings concerned here and thus they are not shown. Check case **6** in subsection 4.2.4 to see the contours of three fields for surging rotor under laminar inflow conditions.

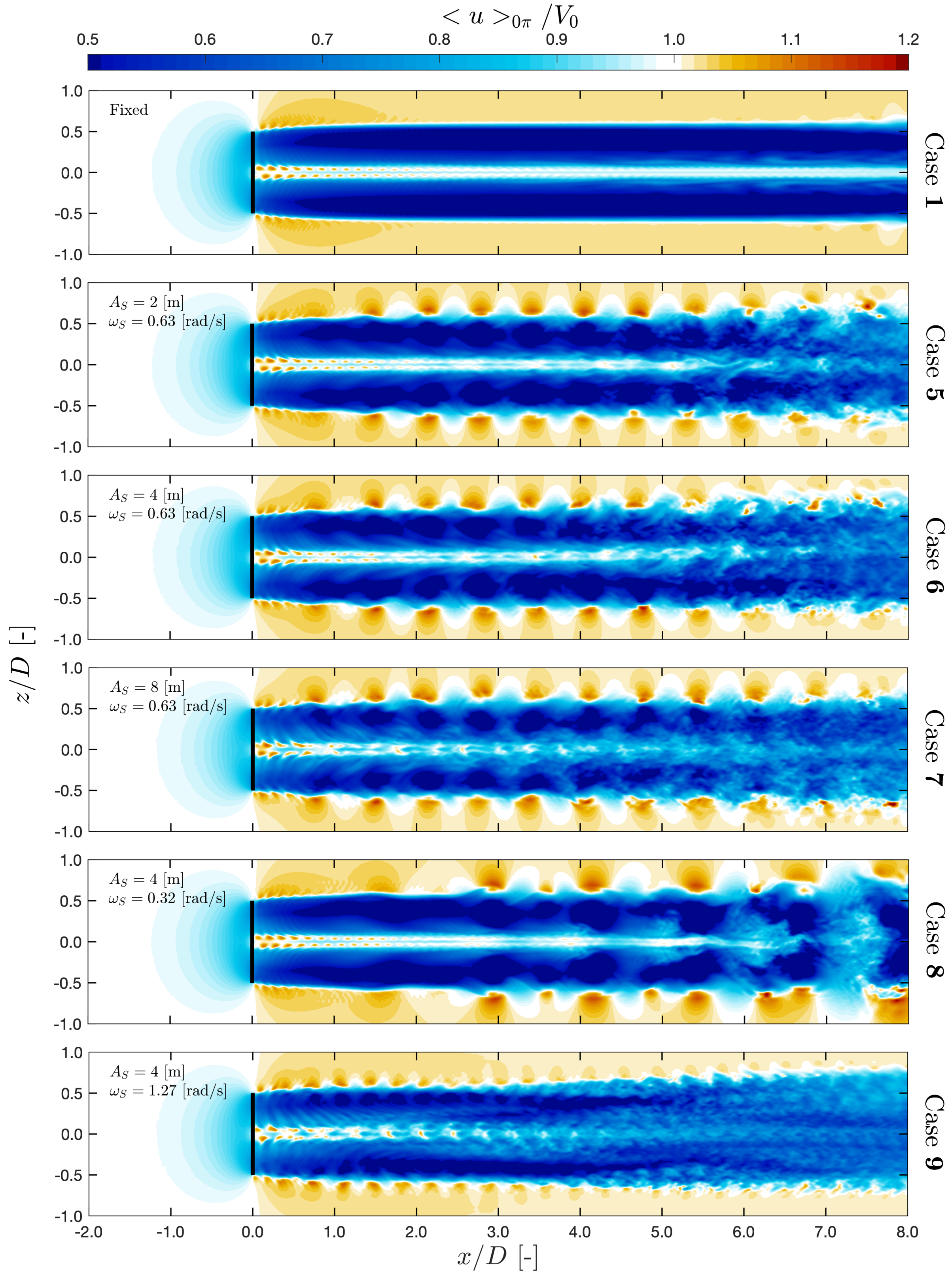

Figure 4.20: Fields of phase-locked averaged streamwise velocity $< u >_{0\pi}$ for single rotor with different A_S and ω_S under laminar inflow conditions.

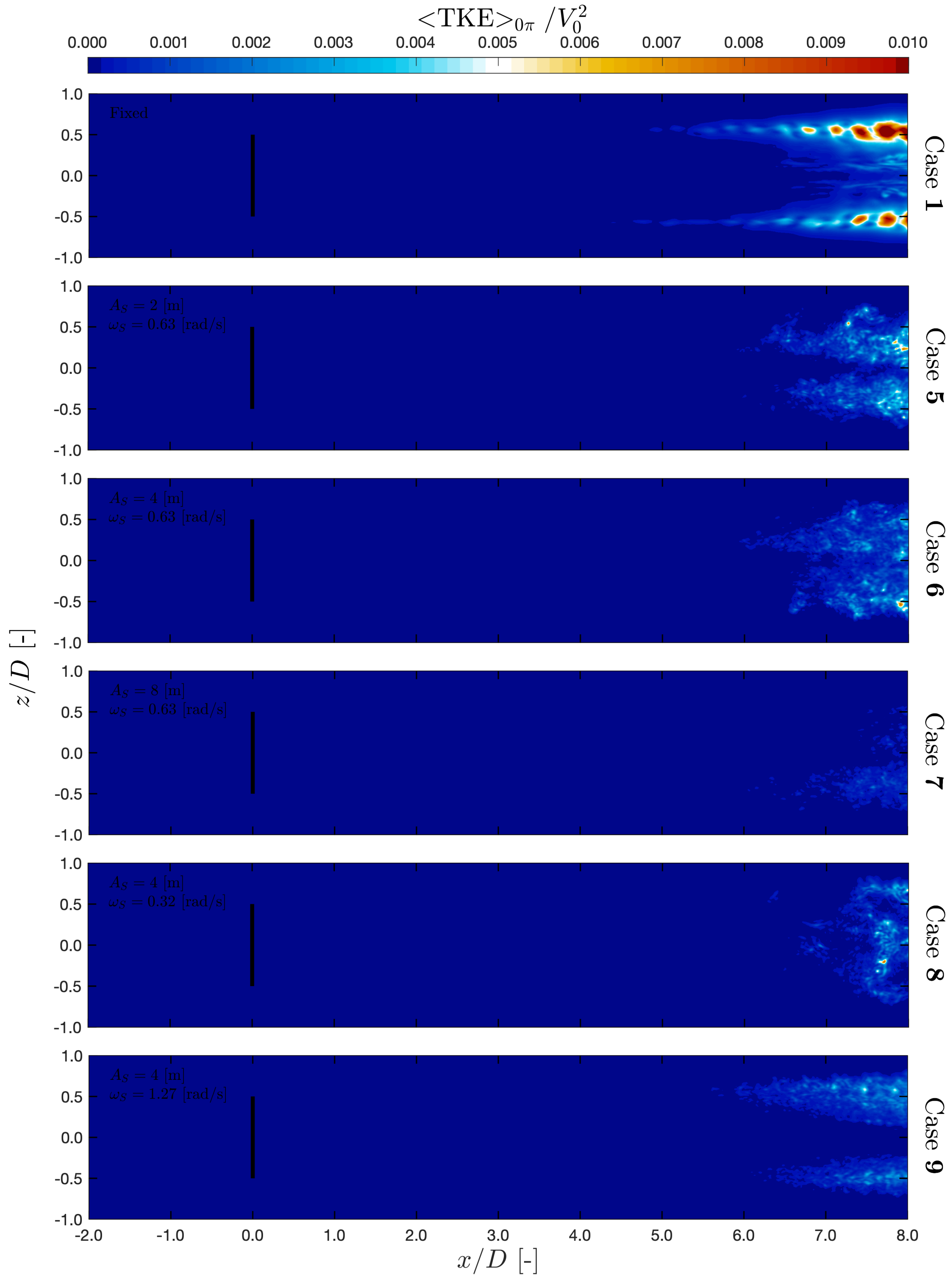

Figure 4.21: Fields of phase-locked averaged turbulent kinetic energy <TKE>$_{0\pi}$ for single rotor with different A_S and ω_S under laminar inflow conditions.

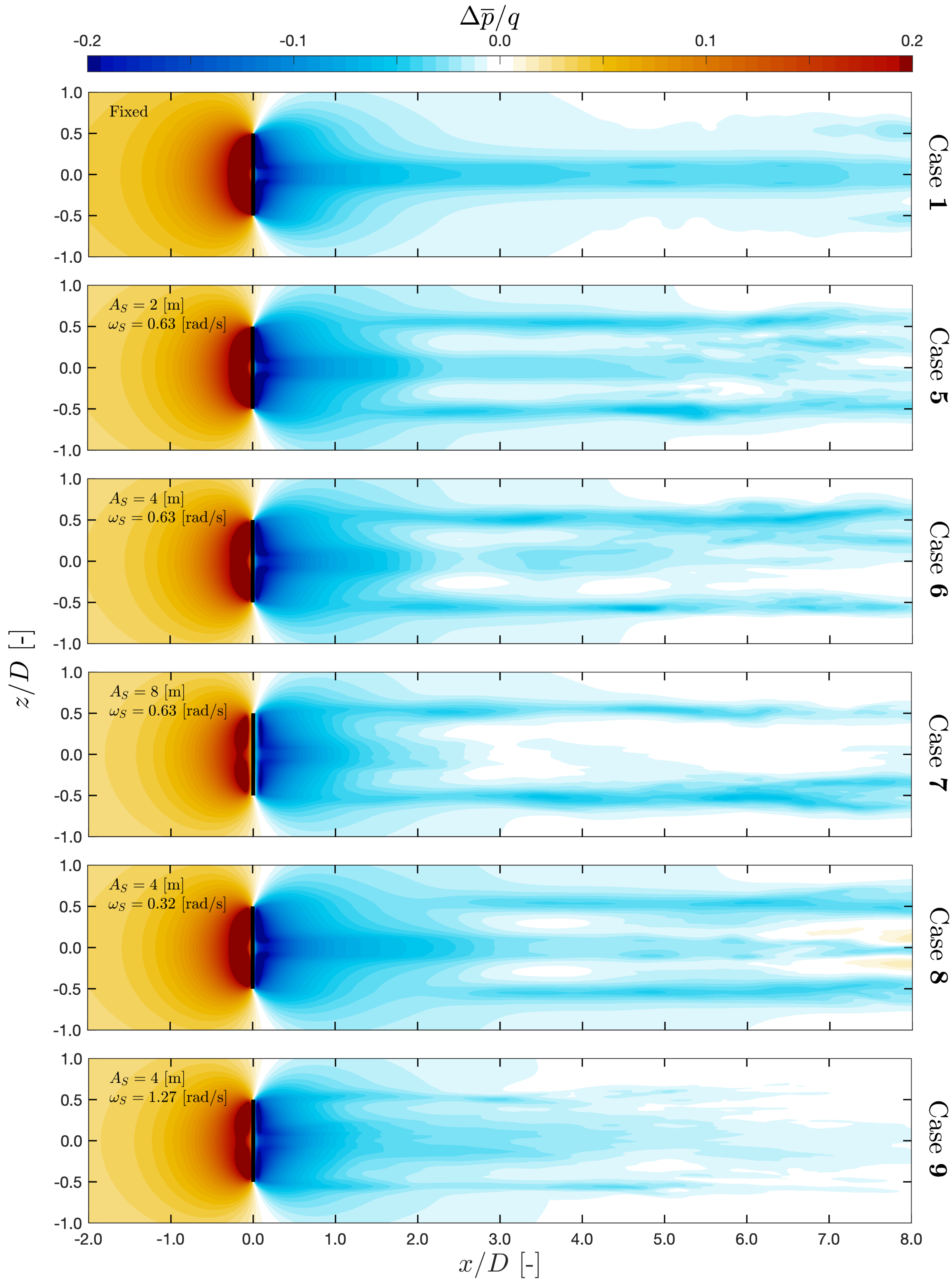

Figure 4.22: Fields of time-averaged pressure $\Delta\overline{p}$ for single rotor with different A_S and ω_S under laminar inflow conditions.

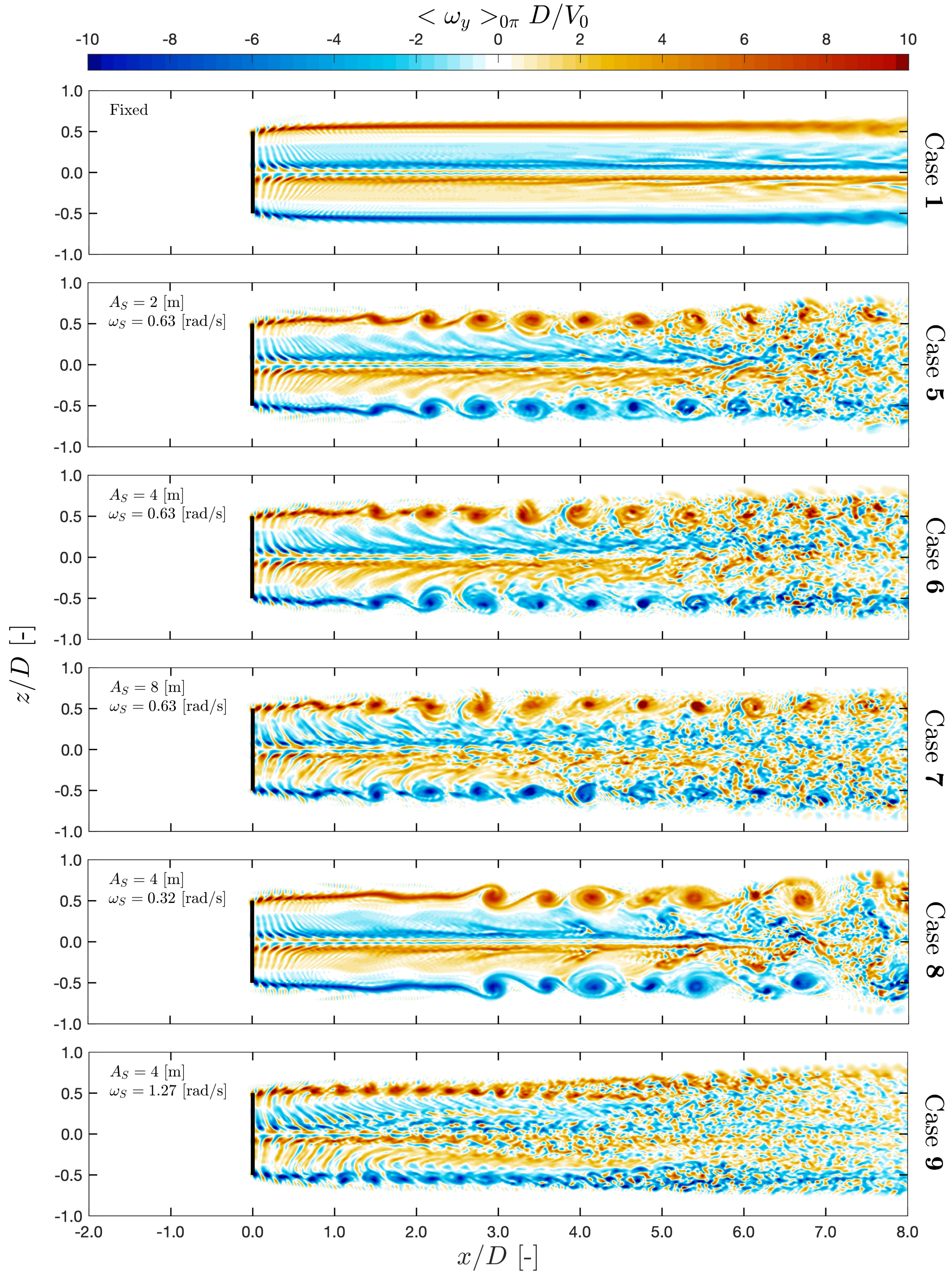

Figure 4.23: Fields of phase-locked averaged y-component vorticity $< \omega_y >_{0\pi}$ for single rotor with different A_S and ω_S under laminar inflow conditions.

4.4 Turbulent Inflow Conditions with Different A_S and ω_S

This section compare cases of single NREL 5MW rotor with different surging amplitudes A_S and surging frequencies ω_S along with a fixed case under a turbulent inflow of TI = 5.3%. The selected A_S and ω_S are same as section 4.3. The six cases correspond to cases **3**, **11**, & **13-16** in Table 4.1 (groups S.5 & S.6). Note that TI = 5.3% are considered to be a common situation for offshore environment [88]. Additional information for this section can be found in section E.3.

4.4.1 Summarizing Wake Characteristics and Rotor Performances

Figure 4.24 and 4.25 present the overall results about $\overline{u}$. Unlike cases with laminar inflow conditions in section 4.3, differences $\overline{u}_{\text{Disk}}$ between fixed case and surging cases are not very pronounced. However, it still can be seen that $\overline{u}_{\text{Disk}}$ for surging cases are slightly larger compare to the fixed case, and $\overline{u}_{\text{Disk}}$ seems to have faster recovery rates with bigger A_S and ω_S, suggesting larger $\mathbb{V}$ may have positive effects on wake recovery under the conditions of realistic turbulent inflows; however, it should be noted that this may also relate to the smaller $\overline{C}_T$ for the surging cases, which result in milder blockage (see subsection 4.5.5). Table 4.5 shows the ratios of $\overline{u}_{\text{Disk}}$ between the surging cases and the fixed case at $x/D = 3$ & 5, and it shows that the correlation of bigger $\mathbb{V}$ with larger $\overline{u}_{\text{Disk}}$ under turbulent inflow conditions is maintained at least up to $x/D = 8$. Moreover, the profiles of $\overline{u}$ became Gaussian-shape for $x/D \geq 5$, similar as the previous analysis in section 4.2.

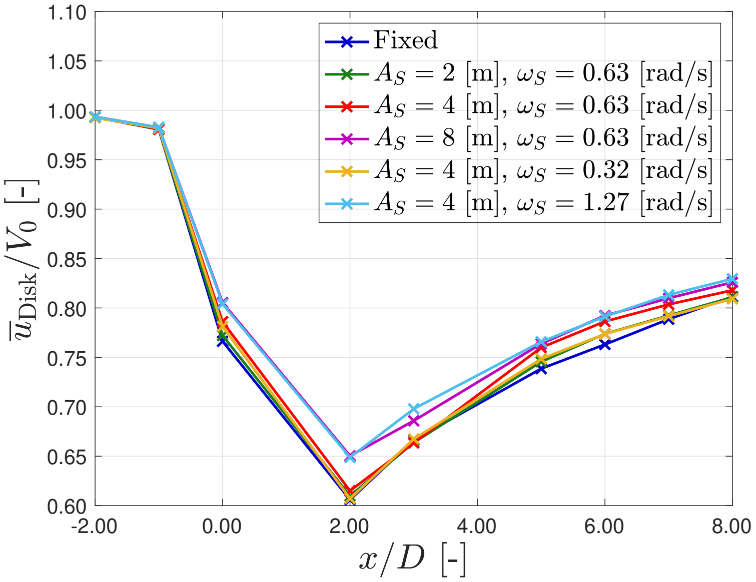

Figure 4.24: $\overline{u}_{\text{Disk}}$ along x-direction for cases of single rotor with different A_S and ω_S under turbulent inflow conditions of TI = 5.3% of TI = 5.3%.

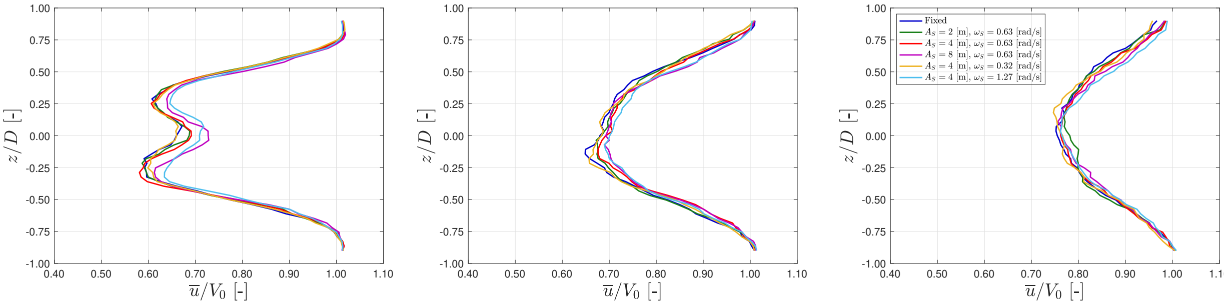

(a) $x/D = 3.0$ (b) $x/D = 5.0$ (c) $x/D = 8.0$

Figure 4.25: Profile of $\overline{u}$ at different x/D for cases of single rotor with different A_S and ω_S under turbulent inflow conditions of TI = 5.3%.

Table 4.5: The ratios of $\overline{u}_{\text{Disk}}$ for the fixed and surging cases under turbulent inflow conditions (TI 5.3%) at $x/D = 3$ and $x/D = 5$.

	$A_S = 2$ m $\omega_S = 0.63$ rad/s	$A_S = 4$ m $\omega_S = 0.63$ rad/s	$A_S = 8$ m $\omega_S = 0.63$ rad/s	$A_S = 4$ m $\omega_S = 0.32$ rad/s	$A_S = 4$ m $\omega_S = 1.27$ rad/s
$\overline{u}^{3D}_{\text{Disk,surging}}/\overline{u}^{3D}_{\text{Disk,fixed}}$	99.61%	99.56%	102.92%	100.14%	104.72%
$\overline{u}^{5D}_{\text{Disk,surging}}/\overline{u}^{5D}_{\text{Disk,fixed}}$	100.95%	102.89%	103.41%	101.34%	103.68%

Figure 4.26 displays $< C_T >$ and $< C_P >$ for the six cases, and $\overline{C}_T$ and $\overline{C}_P$ can be found in Table 4.1, and they are essentially the same with the ones for the laminar cases in section 4.3. Stalling and asymmetries about the fixed case are once again presented with curves of $< C_T >$ and $< C_P >$. And with the curves of $< C_T >$ and $< C_P >$, seems that cases with larger $\mathbb{V}$ are less susceptible to the fluctuations due to inflow turbulence.

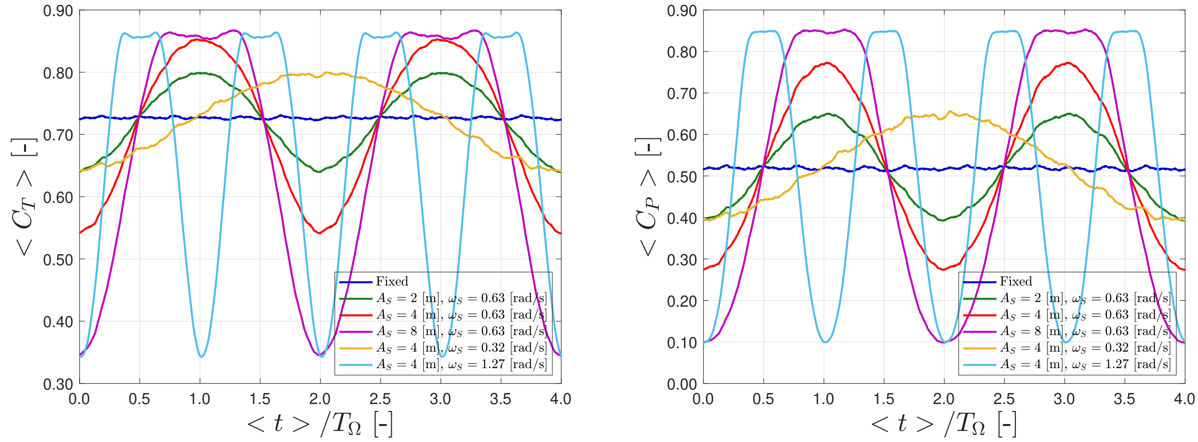

(a) $< C_T >$ (b) $< C_P >$

Figure 4.26: $< C_T >$ and $< C_P >$ for cases of single rotor with different A_S and ω_S under turbulent inflow conditions of TI = 5.3%.

4.4.2 Velocity and TKE Fields

The instantaneous contours of u for the six cases of single NREL 5MW rotor with different A_S and ω_S under turbulent inflow conditions of TI $= 5.3\%$ are displayed in Figure 4.27 (cases **3**, **11**, & **13-16**). Note that since the flow fields of the six cases are identically generated by synthetic turbulent inflows, their instantaneous fields can be directly compared. Note that snapshots for the four cases are all taken at $t = 110T_\Omega$, where the rotor is moving along the free stream with $\phi_S = 0\pi$. It can be seen the instantaneous wake structures for the surging cases are quite alike with the fixed case and PLSB are hardly identified, which is unlike with the laminar cases discussed in section 4.3, where the instantaneous wake structures of fixed and surging cases are dramatically different.

The fields of $< u >_{0\pi}$ are displayed in Figure 4.28. After the phase-locked averaging, PLSB are revealed in the fields of $< u >_{0\pi}$ for surging cases. Moreover, cases with bigger A_S (with the same ω_S) have clearer structures and persist downstream further. This indicates surging cases with bigger A_S affect their wakes more. Additionally, the repeating rates of PLSB display in Figure 4.28 are directly linked to the ω_S, and that the cases with lower ω_S seems to have PLSB more persist into the regions more downstream.

Note that the six cases share very similar patterns for $\overline{u}$ fields, and two of the cases (cases **3** & **11**) have already been shown in section 4.2; thus they are not shown here (see section E.3).

The fields <TKE>$_{0\pi}$ are shown in Figure 4.29. Periodic structures with similar distribution of $< u >_{0\pi}$ fields can be seen. As one may have already expected, their repeating rates are related to ω_S and cases with bigger A_S has sharper structures.

Fields of TKE for the six cases under turbulent inflow conditions are very similar, and thus they are not displayed. One can find the TKE contour for fixed case and surging case with $A_S = 4$ m & $\omega_S = 0.63$ rad/s under the same turbulent inflow conditions in case **3** & **11** of Figure 4.9.

4.4.3 Pressure and Vorticity Fields

The fields of $< \omega_y >_{0\pi}$ are in Figure 4.30. Again, effects of surging can be characterized, and their repeating rates are once more directly linked to ω_S. Also, it can be seen that periodic structures in fields of $< \omega_y >_{0\pi}$ become more visible with bigger A_S, indicating surging effects become more prominent with larger A_S.

4.4.4 Momentum Entrainment

Fields of $-\partial\overline{p}/\partial x$, $-\overline{w}(\partial\overline{u}/\partial z)$, and $-\partial\overline{u'w'}/\partial z$ are not displayed here once more due to the fact that they are quite similar for the five surging settings concerned here. Check case **11** in subsection 4.2.4 to see the contours of three fields for surging rotor under turbulent inflow conditions (TI= 5.3 %).

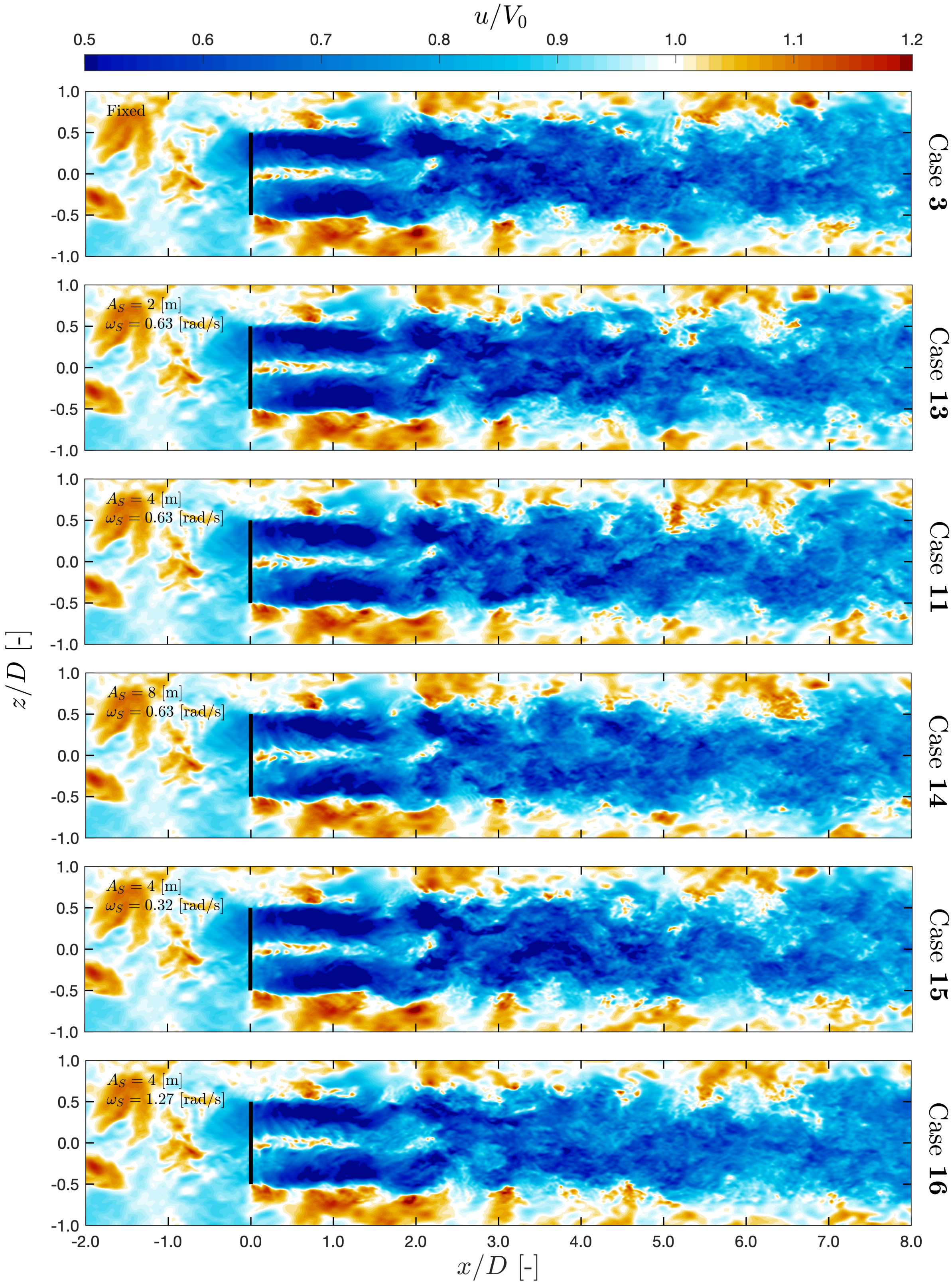

Figure 4.27: Fields of instantaneous streamwise velocity u for single rotor with different A_S and ω_S under turbulent inflow conditions of TI = 5.3%.

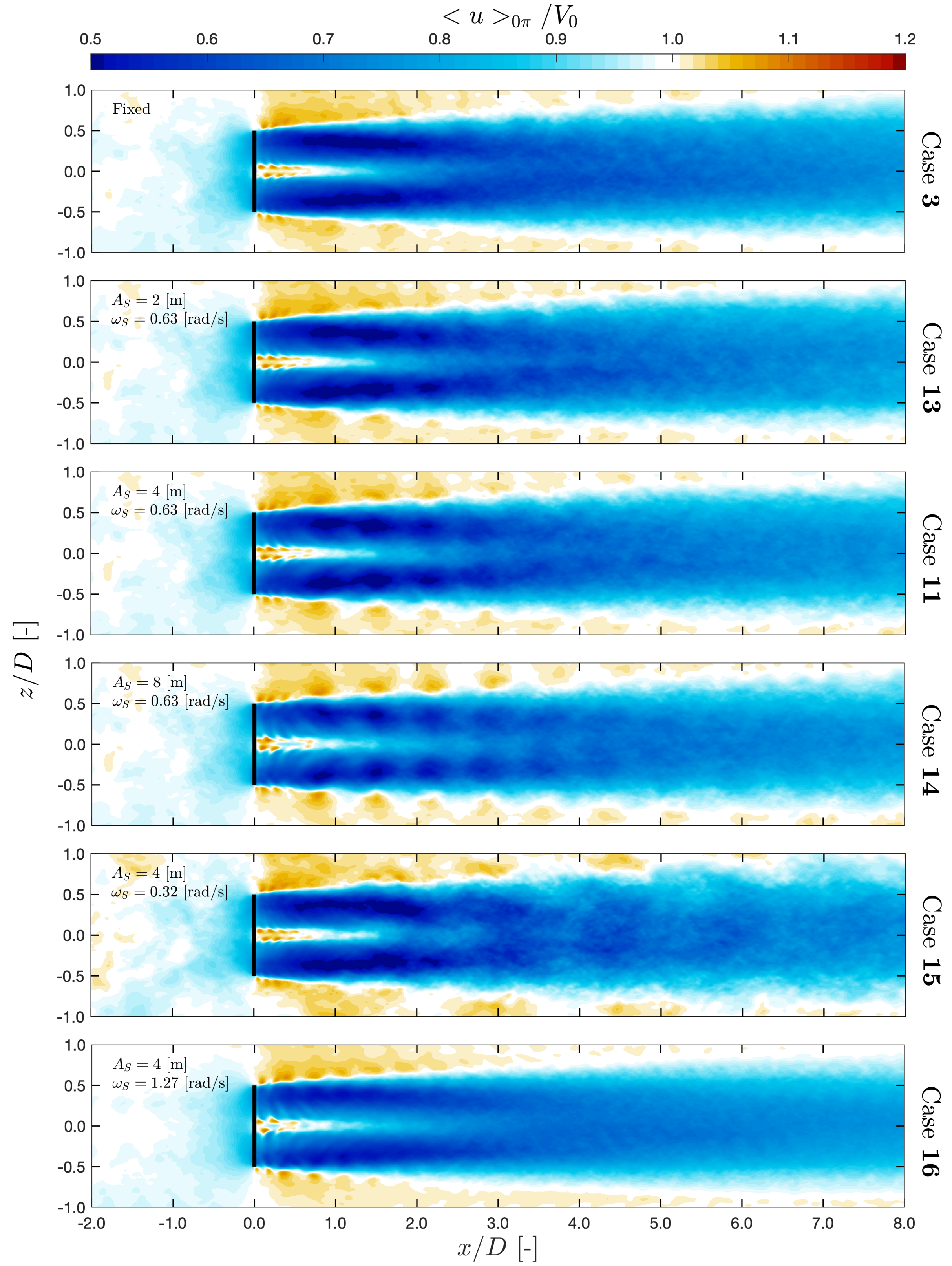

Figure 4.28: Fields of phase-locked averaged streamwise velocity $< u >_{0\pi}$ for single rotor with different A_S and ω_S under turbulent inflow conditions of TI = 5.3%.

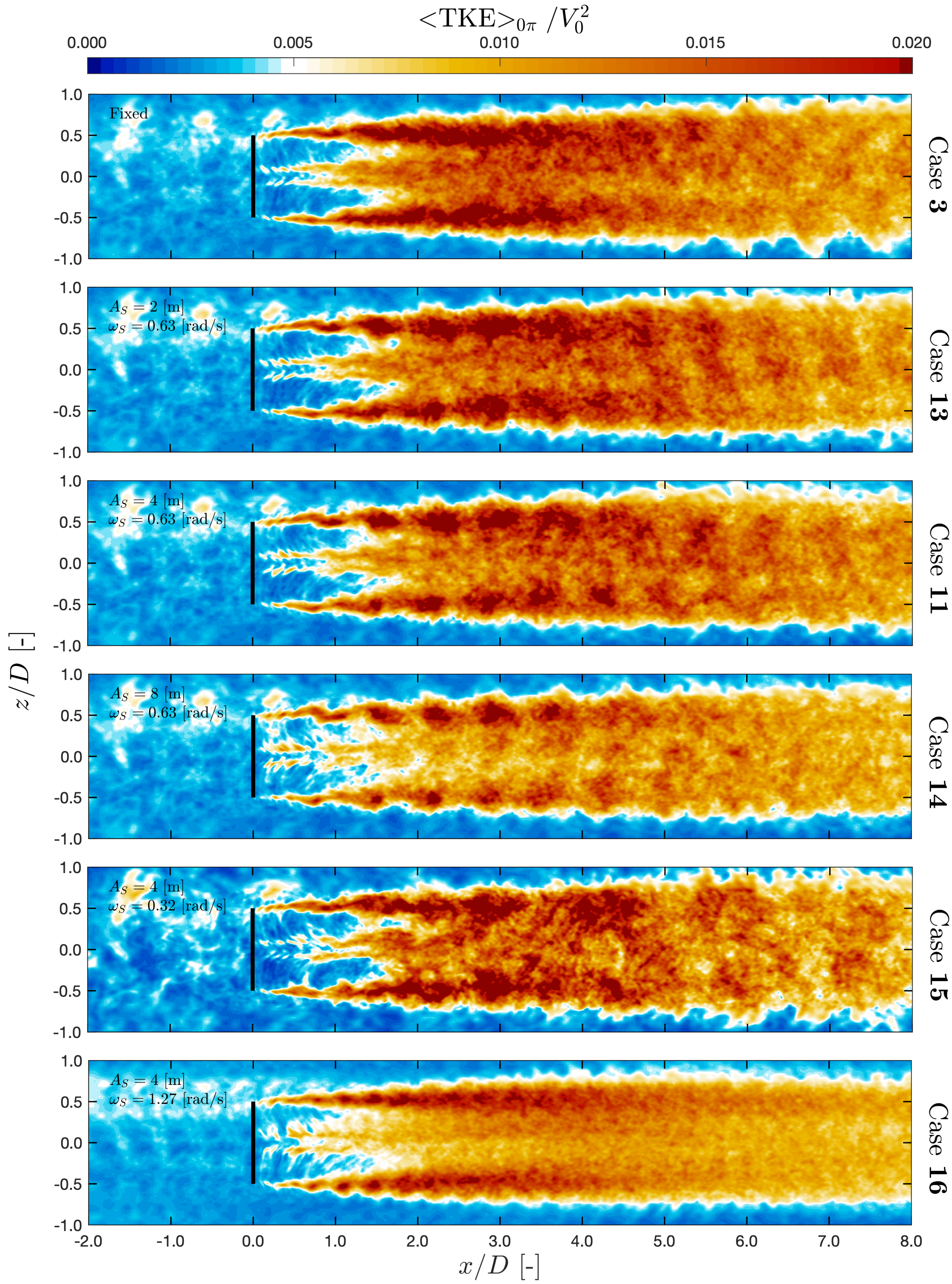

Figure 4.29: Fields of phase-locked averaged turbulent kinetic energy <TKE>$_{0\pi}$ for single rotor with different A_S and ω_S under turbulent inflow conditions of TI = 5.3%.

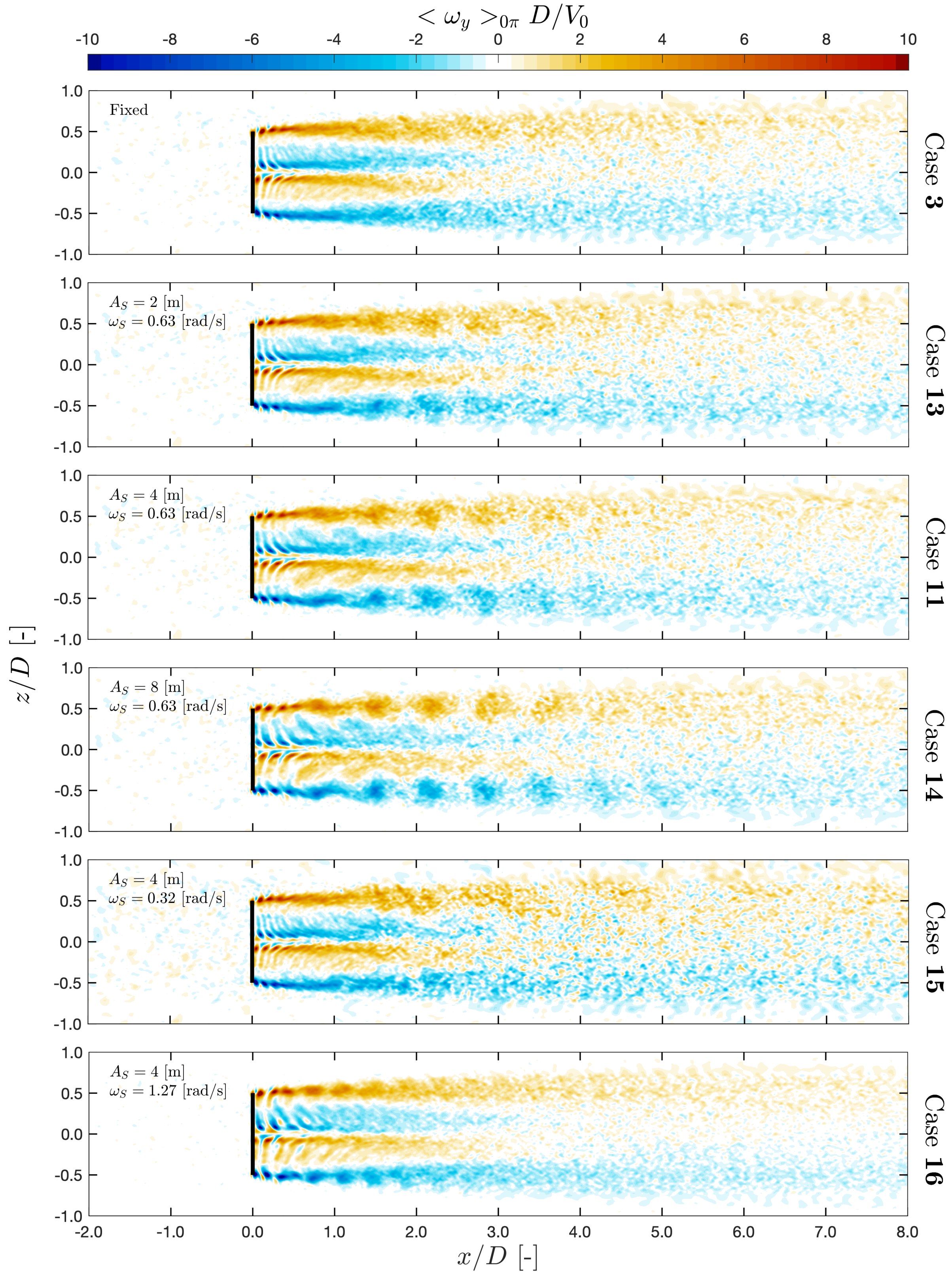

Figure 4.30: Fields of phase-locked averaged y-component vorticity $< \omega_y >_{0\pi}$ for single rotor with different A_S and ω_S under turbulent inflow conditions of TI $= 5.3\%$.

4.5 Further Discussions

4.5.1 Interactions of Tip Vorticies Within a Surging Cycle

As displayed in the previous sections in this chapter, surging cases will result in distinct vortical structures in their wakes, especially for for the cases with laminar inflow conditions. As been shown in Figure 4.23, the modes of the vortical structures are mainly dominated by surging frequencies ω_S, while surging amplitudes A_S have less influences for the considered cases. Figure 4.31 to 4.33 depict how the vortical structures are generated and convected with series of sequential snapshots for cases with ω_S being 0.32, 0.63, and 1.27 rad/s (cases in section 4.3). In the three sets of plots, the boxes of red dashed-line indicate the vortical structures formed within a surging cycle, and it can be seen that the vortical structures for the three cases are formed through merging tip-vorticies through rolling up. The merging processes are triggered since the inter-distances between tip-vorticies are varied during a surging cycle, which brings up the imbalance of inductance forces among them. The differences of the inter-distances between tip-vorticies are the most pronounced as comparing $\phi_S = 0.5\pi$ with $\phi_S = 1.5\pi$ in Figure 4.31 to 4.33 (focus on the regions just after the rotors), especially for the cases with higher ω_S. It is worth noting again that each pair of the vortical structures appeared in the figures are actually a ring, and for cases of $\omega_S = 0.63$ rad/s and $\omega_S = 1.27$ rad/s, each pair of the vortical structures corresponds to a complete surging cycle; as for the case $\omega_S = 0.32$ rad/s, a completed surge cycle corresponds to two pairs (rings) of vortical structures, with a pair stronger and another weaker.

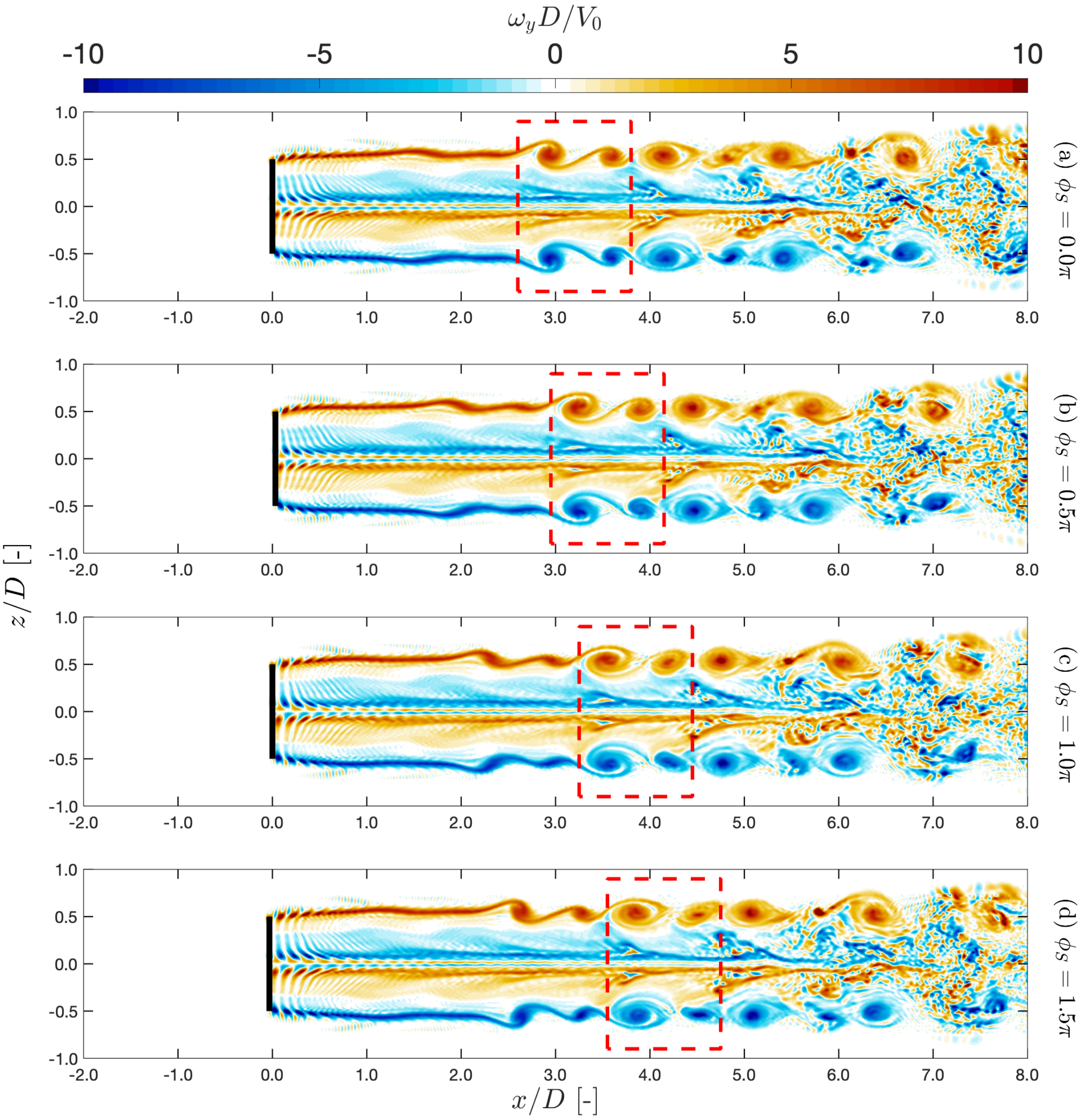

Figure 4.31: Time evolution of ω_y fields within a surging cycle for single surging rotor with $A_S = 4$ m & $\omega_S = 0.32$ rad/s under laminar inflow conditions (case **8**).

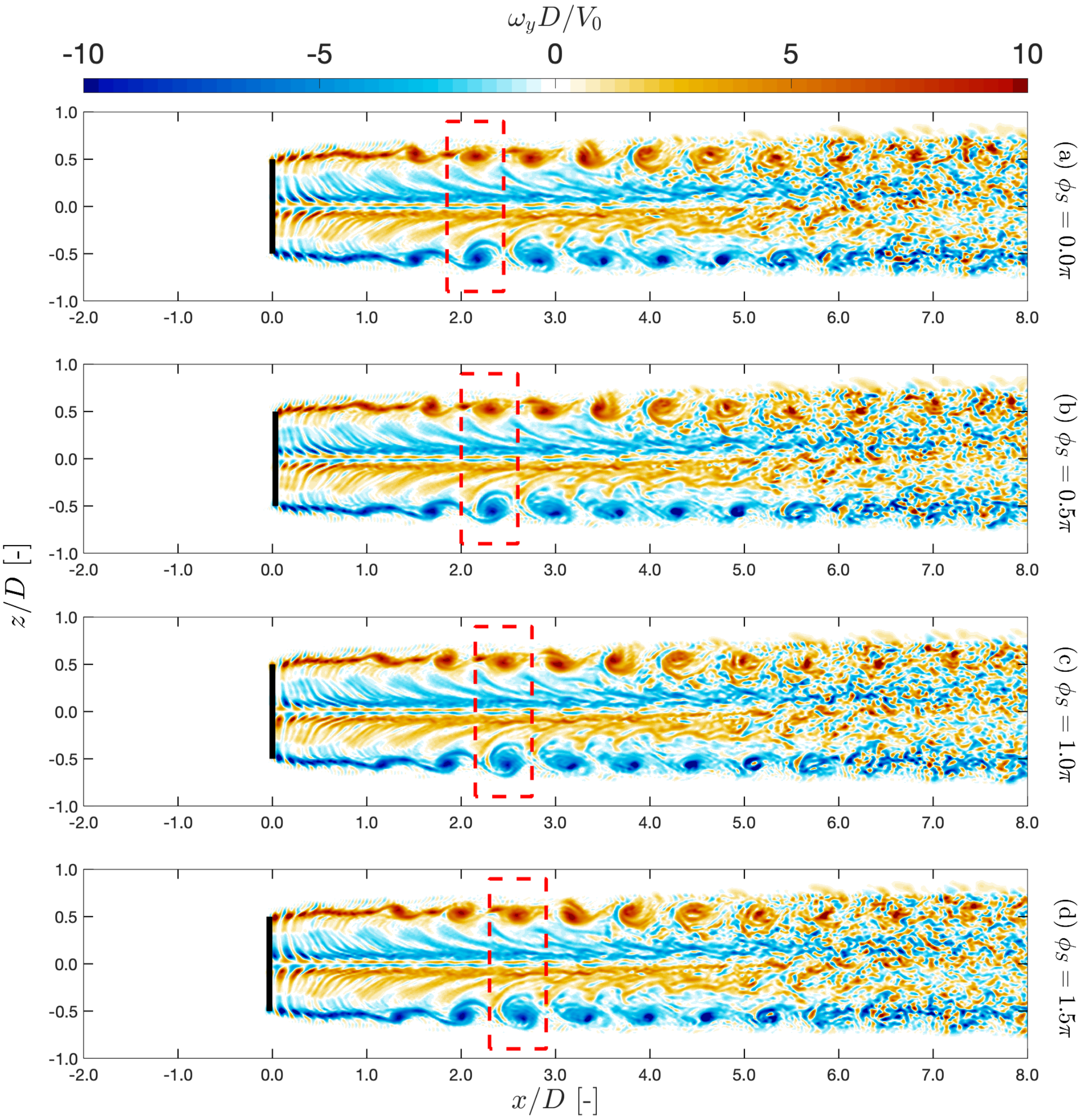

Figure 4.32: Time evolution of ω_y fields within a surging cycle for single surging rotor with $A_S = 4$ m & $\omega_S = 0.63$ rad/s under laminar inflow conditions (case **6**).

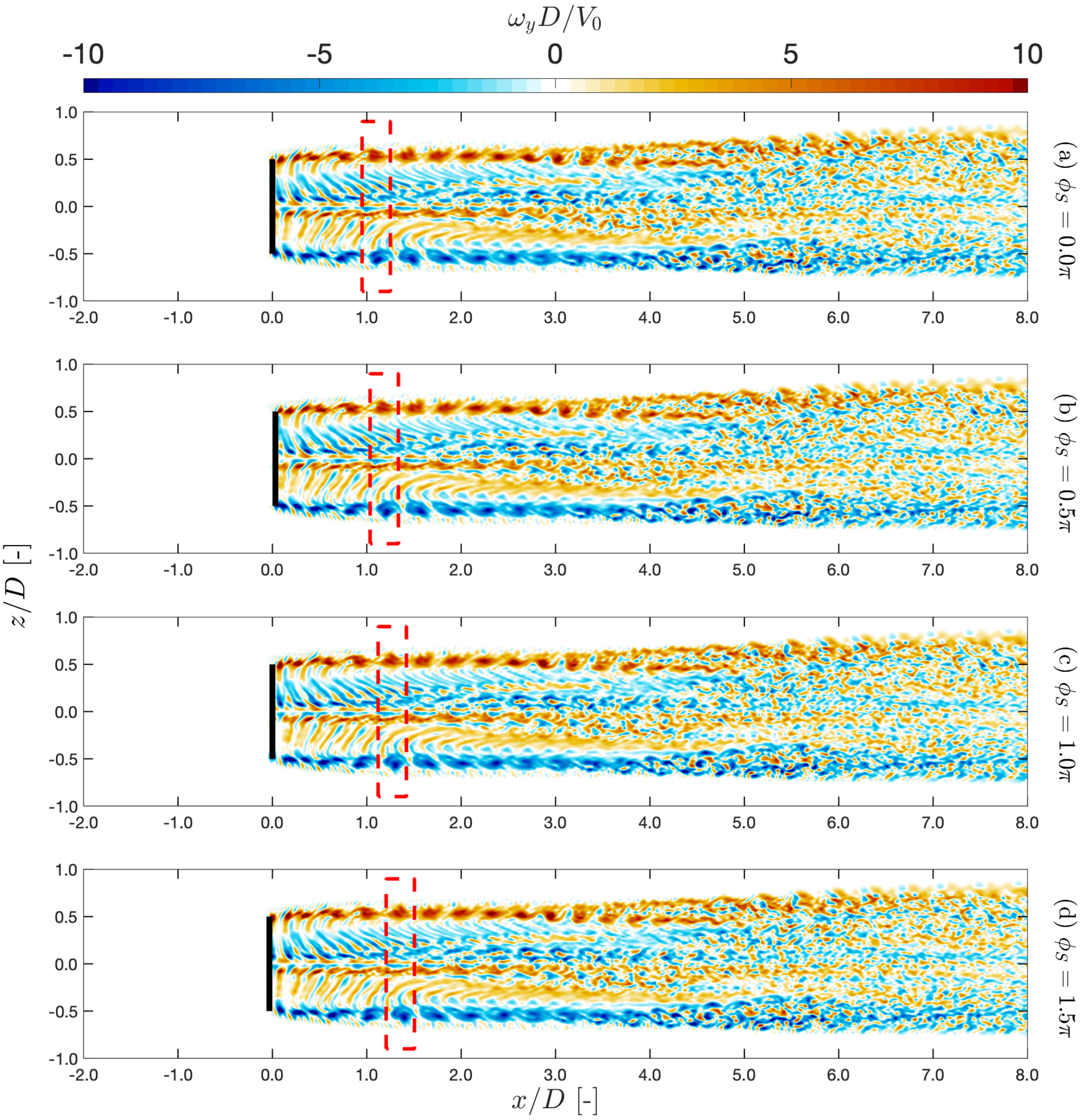

Figure 4.33: Time evolution of ω_y fields within a surging cycle for single surging rotor with $A_S = 4$ m & $\omega_S = 1.27$ rad/s under laminar inflow conditions (case **9**).

4.5.2 Detail Discussions about of PLSB

This section discusses about the periodic low speed bubbles (PLSB) presented in the previous sections. Other than the $y = 0$ planes, several selected cases and quantities are also analyzed with yz-planes at x/D being 3, 5, and 8. Note that for the laminar cases, since that the values of <TKE>$_{\phi_S}$ fields are generally very low, instantaneous fields and phase-locked averaged fields are treated interchangeably in this section, as long as the considered ϕ_S is same.

A brief analysis with *proper orthogonal decomposition* (POD) using the phase-locking fields of y-component vorticity $\omega_{y,0\pi}$ was conducted in Appendix D; cases with fixed and surging rotor under both laminar and turbulent inflow conditions are considered. However, not much additional information could be obtained besides the phase-locked averaged fields. Thus, simply displaying phase-locked averaged fields may be more suitable for this thesis project for the sake of brevity.

General Structures of PLSB

Figure 4.34 shows the corresponding u fields in the $y = 0$ plane with different ϕ_S, and Figure 4.35 to 4.38 presents the phase-locked averaged streamwise velocity based on different ϕ_S ($< u >_{\phi_S}$) on the yz-planes. The surging setting for the case being considered here are $A_S = 4$ m and $\omega_S = 0.63$ rad/s (case **6**). Note that the locations of red dashed-line boxes in Figure 4.34 are identical with the ones in Figure 4.32 (ω_y fields), and a pair (ring) of PLSB are enclosed in every boxes. Also, it is now very clear that PLSB is actually ring with the plots of $< u >_{\phi_S}$ on yz-planes; however, instead of being actual axis-symmetric, the structures of PLSB is only symmetry about every 120° (P3). Notice that fields of yz-planes with different ϕ_S depicts the convection of PLSB.

Figure 4.39 is the phase-locked averaged velocity fields for $\phi_S = 0\pi$ ($< u >_{0\pi}$) of the case $A_S = 4$ m & $\omega_S = 1.27$ rad/s (case **9**) on the yz-planes. In general, they share similar features with the case $A_S = 4$ m & $\omega_S = 0.63$ rad/s presented earlier.

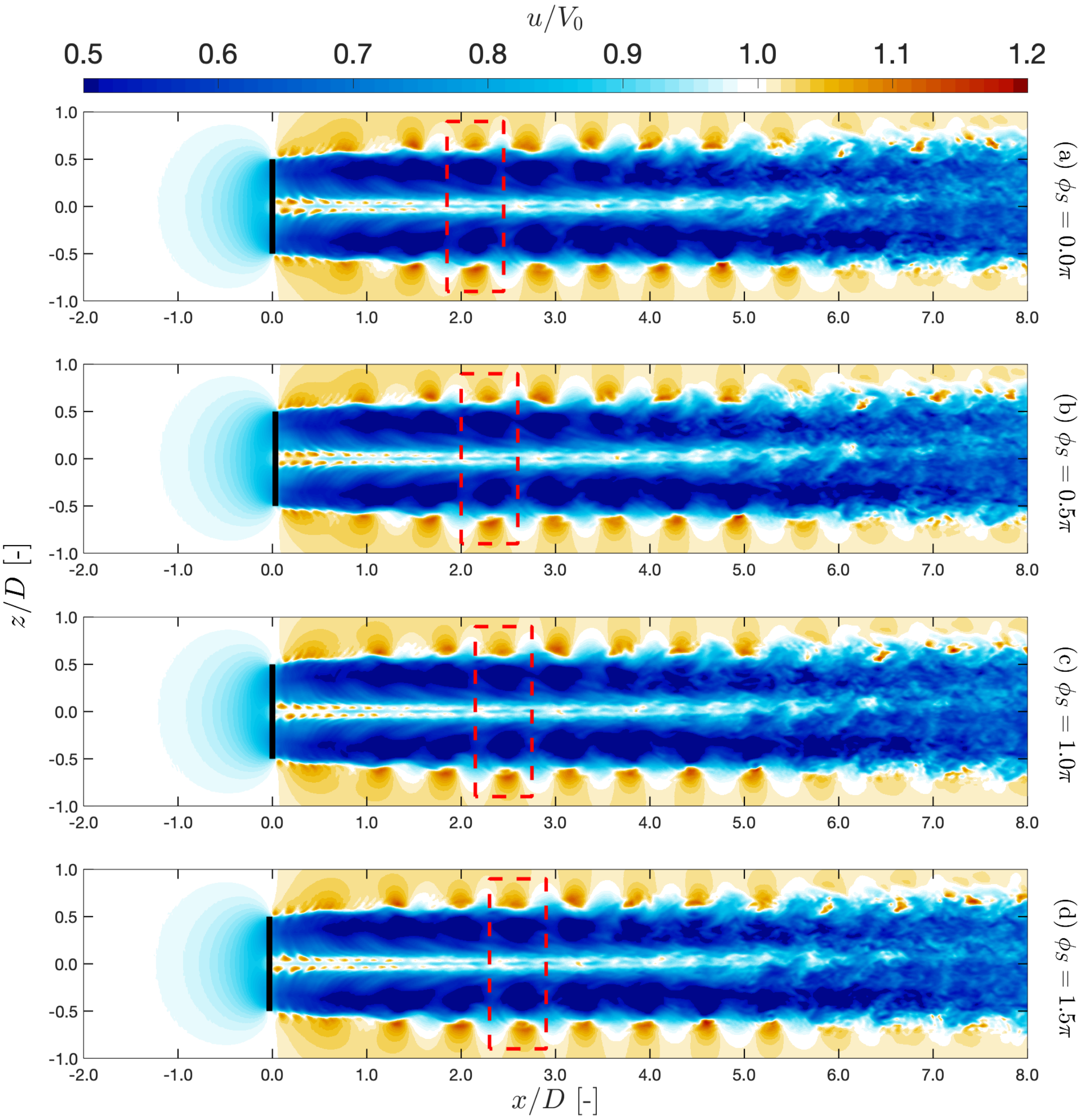

Figure 4.34: u fields correspond to different ϕ_S on plane $y = 0$ within a surging cycle for single surging rotor with $A_S = 4$ m & $\omega_S = 0.63$ rad/s under laminar inflow conditions (case **6**). Note that u fields here can be interpreted as $< u >_{\phi_S}$ fields, and the locations of the red dash-lined boxes are identical with Figure 4.32 (ω_y fields).

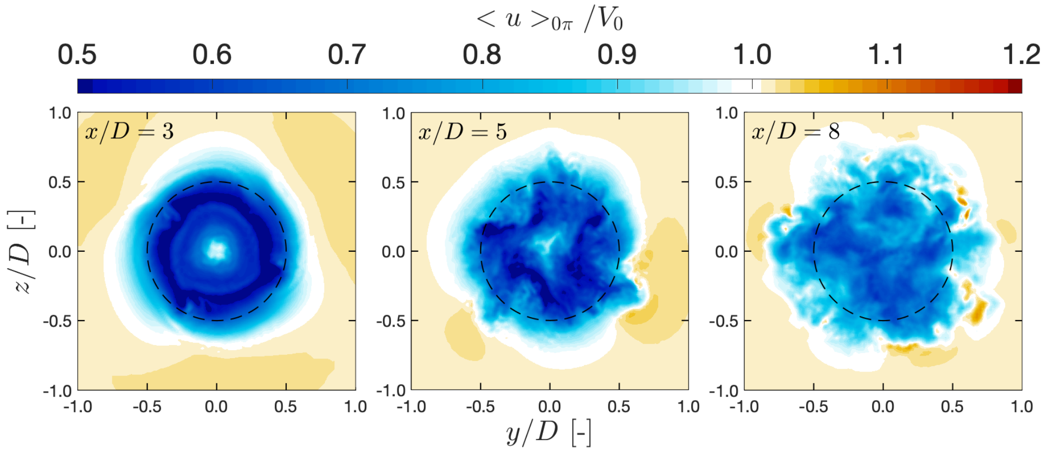

Figure 4.35: Phase-locked averaged velocity fields as $\phi_S = 0.0\pi$ on yz-planes for single surging rotor case with $A_S = 4$ m & $\omega_S = 0.63$ rad/s under laminar inflow conditions (case **6**).

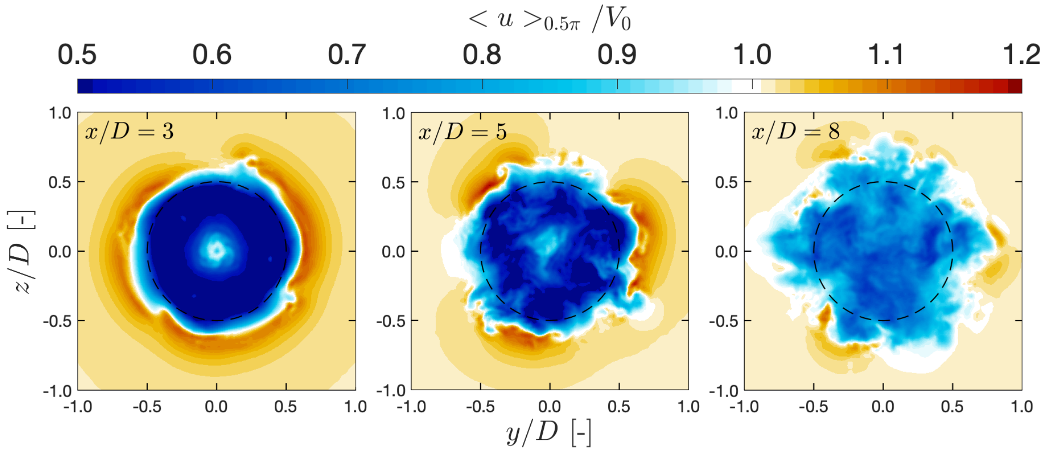

Figure 4.36: Same as Figure 4.35 but with $\phi_S = 0.5\pi$.

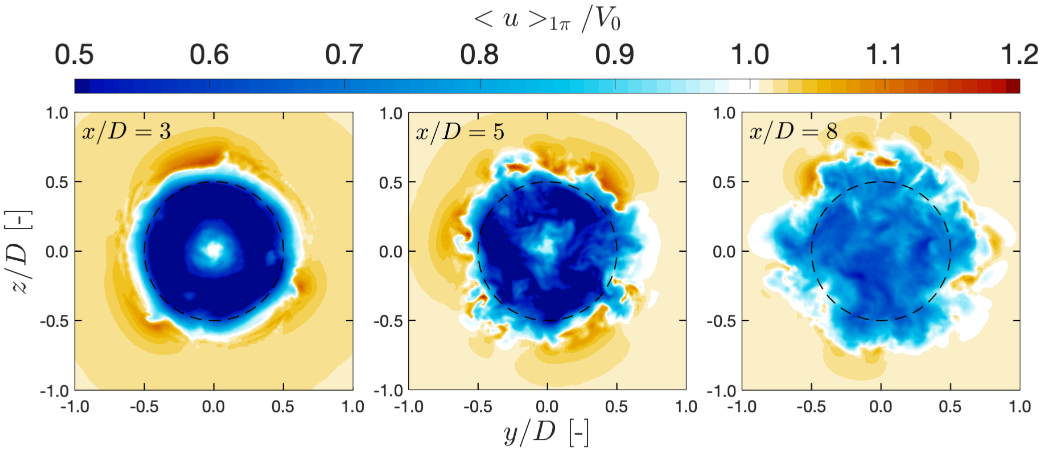

Figure 4.37: Same as Figure 4.35 but with $\phi_S = 1.0\pi$.

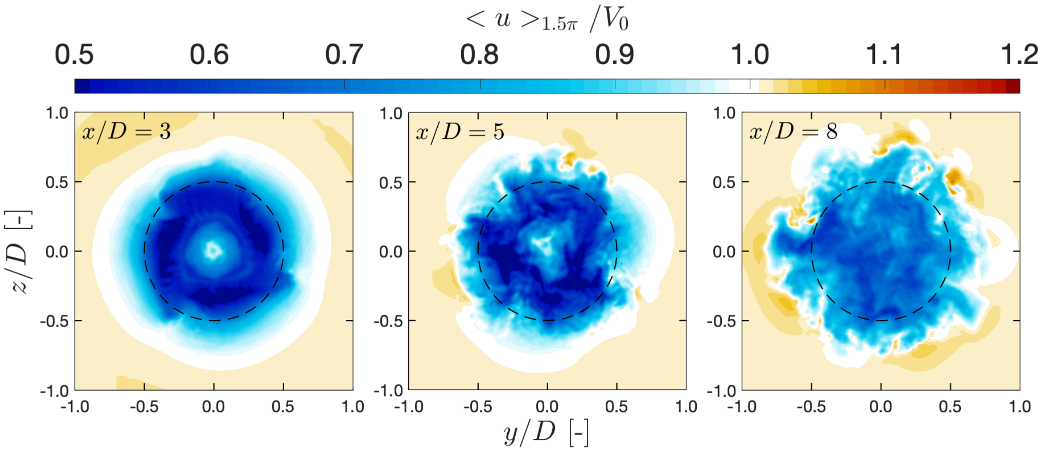

Figure 4.38: Same as Figure 4.35 but with $\phi_S = 1.5\pi$.

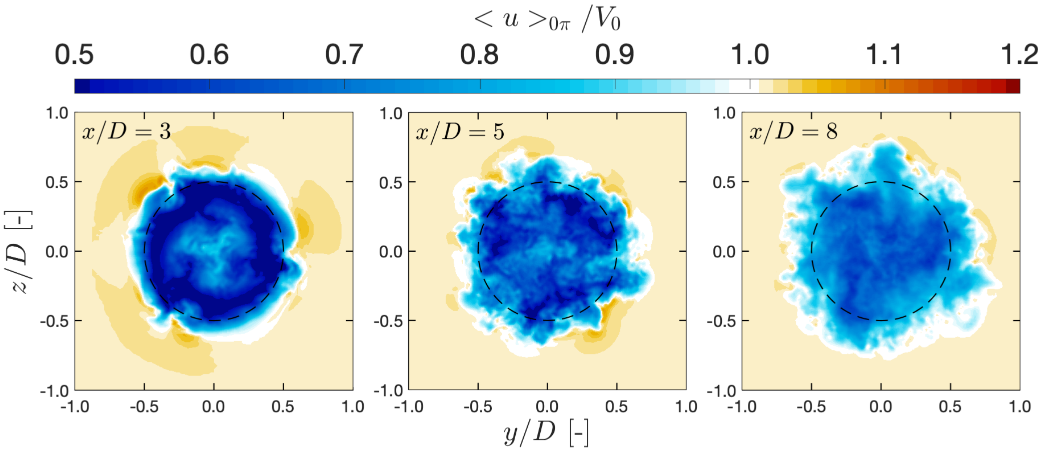

Figure 4.39: $< u >_{0\pi}$ fields on yz-planes for single surging rotor case with $A_S = 4$ m & $\omega_S = 1.27$ rad/s under laminar inflow conditions (case **9**).

Highly Complex but Highly Deterministic

Figure 4.40 and 4.41 displayed the fields of $< \omega_x >_{0\pi}$ for the cases $\omega_S = 0.63$ rad/s & $A_S = 4$ m and $\omega_S = 1.27$ rad/s & $A_S = 4$ m (cases **6** and **9**). Together with the $< u >_{0\pi}$ fields shown before, it can be said that the wake systems are highly complex. However, with the <TKE>$_{0\pi}$ fields (Figure 4.42, 4.43, & 4.29) for the two cases, the very low values indicate that the wakes are repeatable and highly deterministic, lacking randomness. And this is the reason which led to the profiles of $\overline{u}$ for laminar surging cases (eg. Figure 4.17) are not in Gaussian shapes as well. Also that highly repeatable process makes structures with highly localized characteristics (eg. vortical structures in Figure 4.32) pass through the exact same locations for every surging cycles, resulting in the kinks in the $\overline{u}$ profiles for the laminar cases with surging rotor.

Slight asymmetries about $z/D = 0$ of the $\overline{u}$ fields can be observed, especially for the case of $\omega_S = 1.27$ rad/s (case **9**, see Figure E.7). These asymmetries can be explained by the 120° symmetries displayed before. Figure 4.44 and 4.45 display the $\overline{u}$ fields on yz-planes for the two cases ($\omega_S = 0.63$ & 1.27 rad/s) with laminar inflow conditions, and clearly that 120° symmetries still occurs with the time-averaged quanties. The 120° symmetries become less obvious as traveling to more downstream positions. However, full axis-symmetric is not arrived. This may relate to the decay of the coherent structures and numeric errors of using hexahedral grids to simulate semi-axis-symmetric system. However, further investigation about this is not conducted in this thesis.

Figure 4.46 to 4.48 display the fields of $< u >_{0\pi}$, $< \omega_x >_{0\pi}$, and $\overline{u}$ for the case $A_S = 4$ m and $\omega_S = 0.63$ rad/s under turbulent inflow conditions (TI 5.3%). It is clear that the wake structures are much more axis-symmetric as compare to the cases with laminar inflows. This indicates the randomness introduced by the ambient turbulence homogenizes the wakes in azimuthal direction.

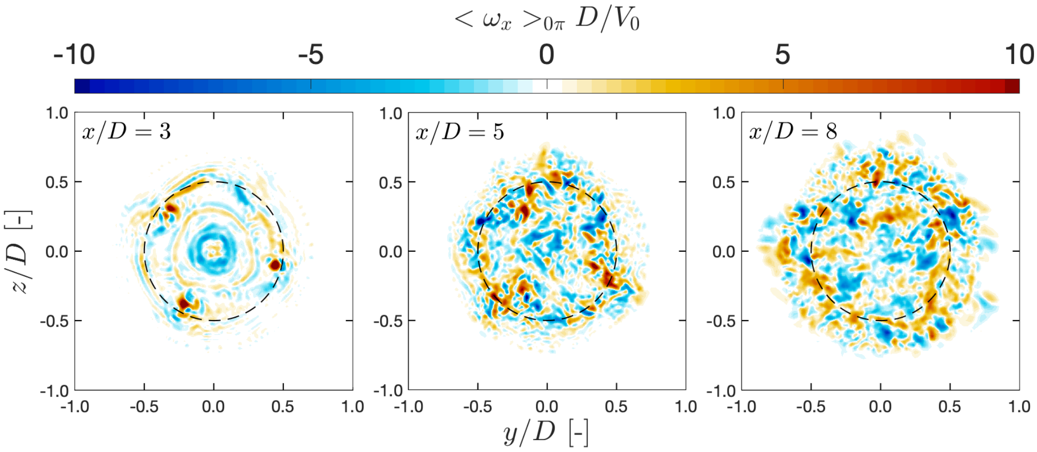

Figure 4.40: $< \omega_x >_{0\pi}$ fields on yz-planes for single surging rotor case with $A_S = 4$ m & $\omega_S = 0.63$ rad/s under laminar inflow conditions (case **6**).

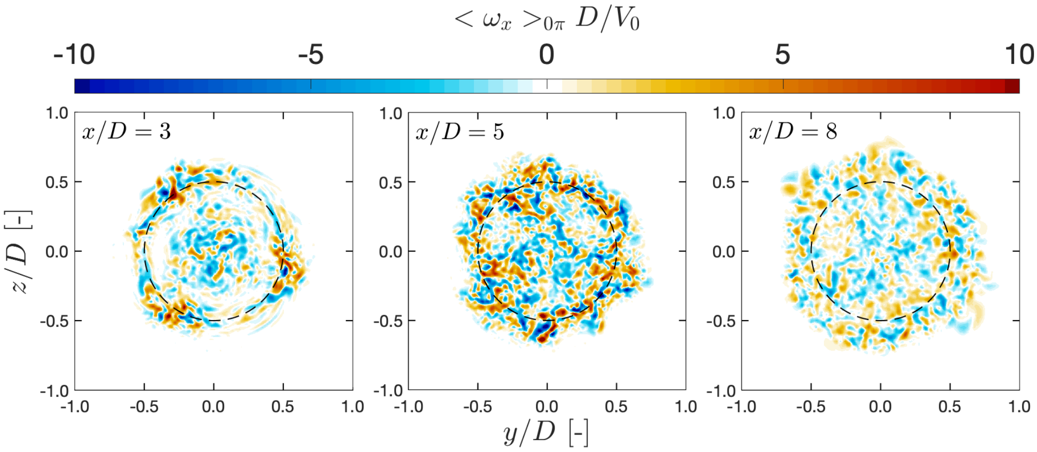

Figure 4.41: $< \omega_x >_{0\pi}$ fields on yz-planes for single surging rotor case with $A_S = 4$ m & $\omega_S = 1.27$ rad/s under laminar inflow conditions (case **9**).

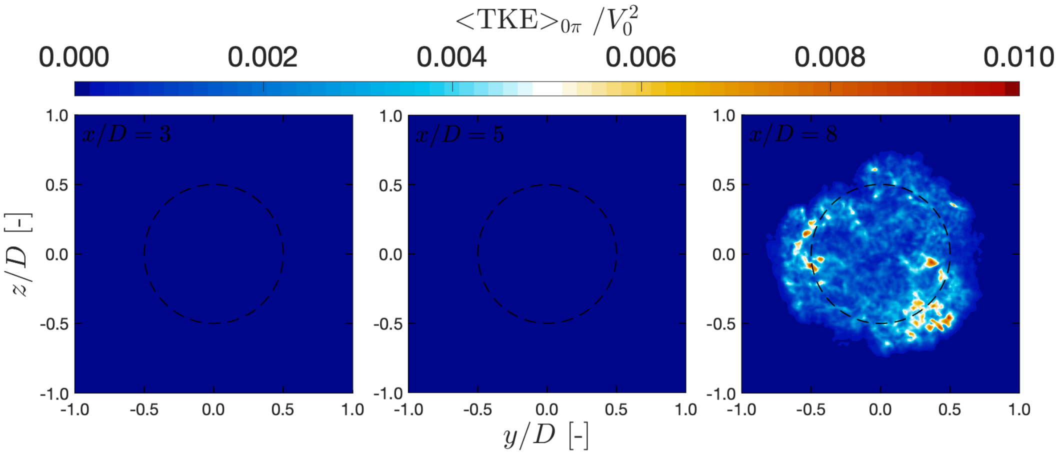

Figure 4.42: Phase-locked averaged TKE fields on yz-planes for single surging rotor case with $A_S = 4$ m & $\omega_S = 0.63$ rad/s under laminar inflow conditions (case **6**).

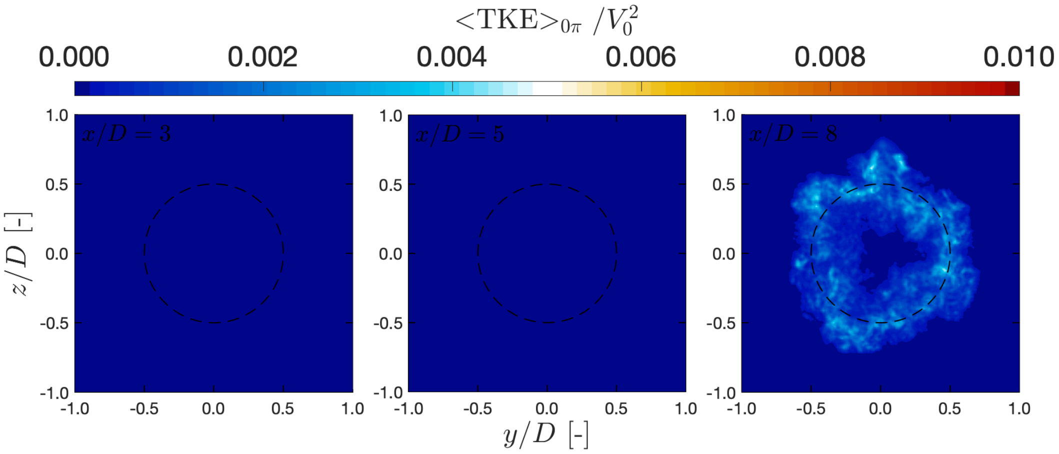

Figure 4.43: Phase-locked averaged TKE fields on yz-planes for single surging rotor case with $A_S = 4$ m & $\omega_S = 1.27$ rad/s under laminar inflow conditions (case **9**).

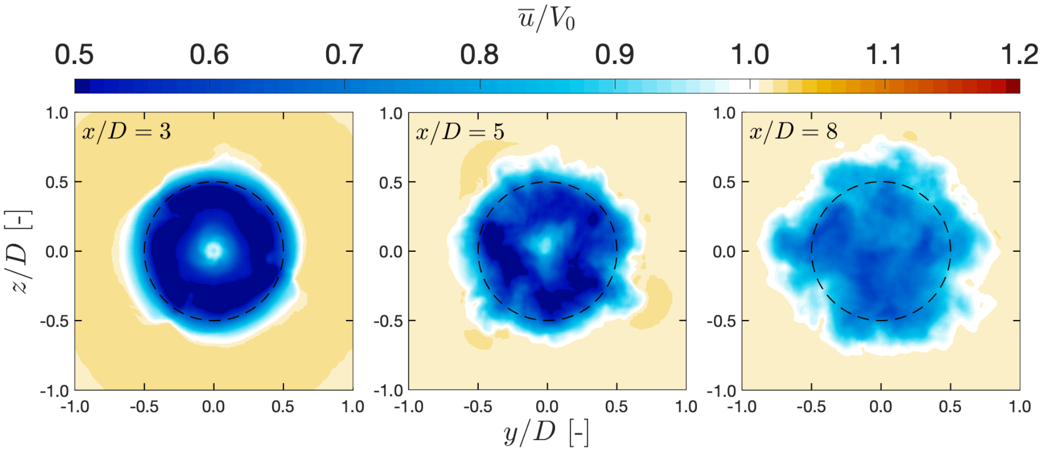

Figure 4.44: $\overline{u}$ fields on yz-planes for single surging rotor case with $A_S = 4$ m & $\omega_S = 0.63$ rad/s under laminar inflow conditions (case **6**).

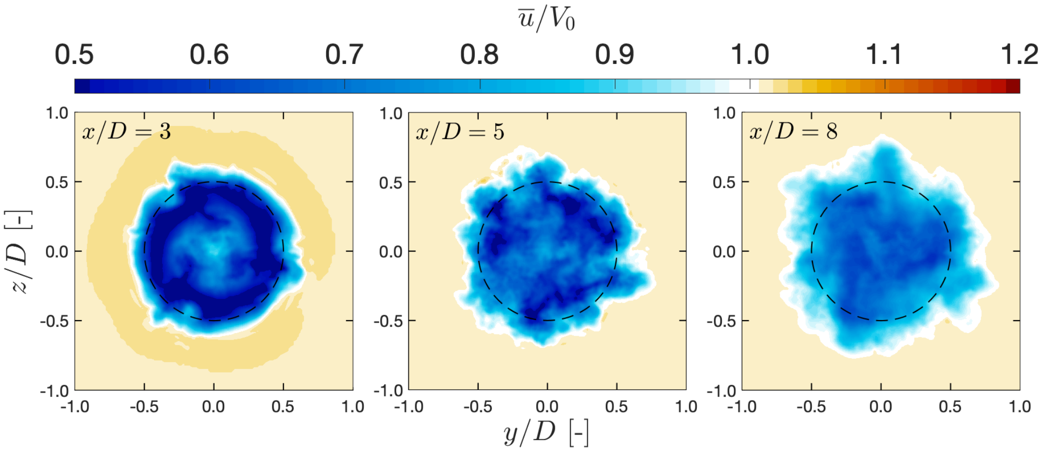

Figure 4.45: $\overline{u}$ fields on yz-planes for single surging rotor case with $A_S = 4$ m & $\omega_S = 1.27$ rad/s under laminar inflow conditions (case **9**).

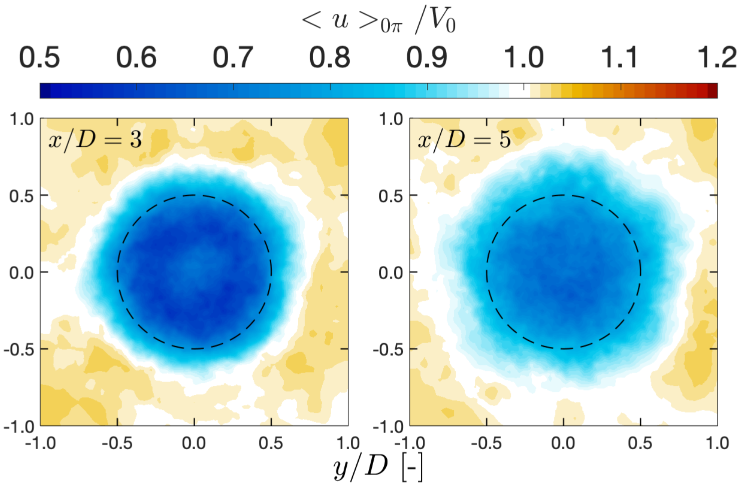

Figure 4.46: $< u >_{0\pi}$ fields on yz-planes for single surging rotor case with $A_S = 4$ m & $\omega_S = 0.63$ rad/s under turbulent inflow conditions of TI = 5.3% (case **11**).

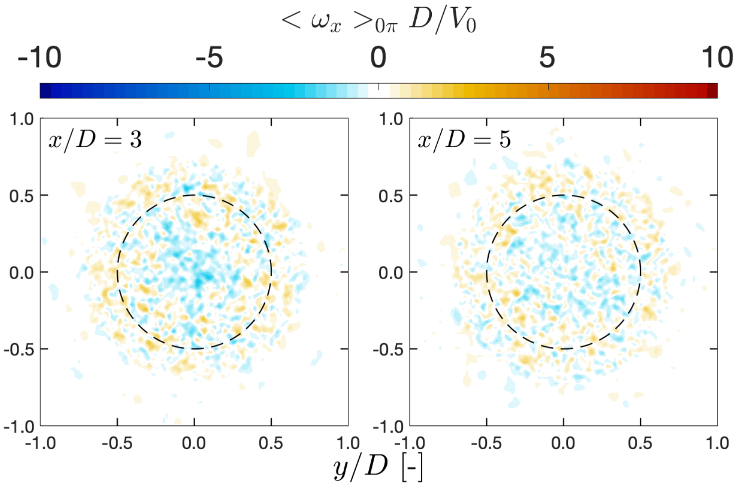

Figure 4.47: $< \omega_x >_{0\pi}$ fields on yz-planes for single surging rotor case with $A_S = 4$ m & $\omega_S = 0.63$ rad/s under turbulent inflow conditions of TI = 5.3% (case **11**).

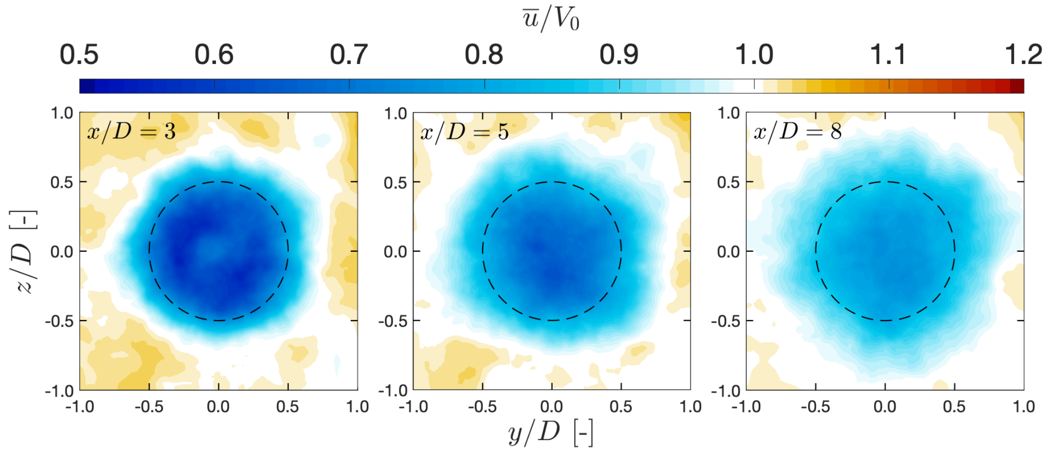

Figure 4.48: $\overline{u}$ fields on yz-planes for single surging rotor case with $A_S = 4$ m & $\omega_S = 0.63$ rad/s under turbulent inflow conditions of TI = 5.3% (case **11**).

4.5.3 Expected and Actual Behaviours of $< C_T >$ & $< C_P >$

This section discusses the expected and actual behaviour of $< C_T >$ & $< C_P >$ under different surging conditions; their time averaged values, asymmetries about the values of the fixed case, and stalling will be analyzed.

In section 4.3 to 4.4, it is shown that the curves of $< C_T >$ and $< C_P >$ seem to be very similar with simple harmonic functions (for the cases without significant stalling), their mechanisms behind are actually rather complicated and hard to come up with simple analytical solutions. To understand the behaviours of $< C_T >$ and $< C_P >$ for the full surging cycle, one should consider all the parameters that appeared in Equation 2.10 and 2.18, including surging velocity V_{WT}, apparent normal velocity seen by the surging rotor's airfoil sections (actuator line points) $V_{n,\mathrm{app}}$ (Equation 2.17), V_{rel}, ϕ, α, and airfoil polar data for C_l & C_d.

Expected Behaviours of $< C_T >$ & $< C_P >$

To begin with the analysis, instantaneous thrust and power conversion rates (ξ_{C_T} & ξ_{C_P}) are introduced. They are linked to the instantaneous rotor thrust & power (T & P) through the apparent inflow wind speed seen by the rotor $V_{0,\mathrm{app}}$ (Equation 2.27), as in Equation 4.1. Note that unlike ξ_{C_T} & ξ_{C_P}, C_T & C_P ($\overline{C}_T$ & $\overline{C}_P$) are linked to T & P ($\overline{T}$ & $\overline{P}$) through V_0, which is the free stream velocity without considering surging effects.

$$T = \xi_{C_T} V_{0,\mathrm{app}}^2, \qquad P = \xi_{C_P} V_{0,\mathrm{app}}^3 \tag{4.1}$$

If ξ_{C_T} & ξ_{C_P} are considered to be fixed (constants) and effects of dynamic inflow are negligible throughout the surging cycle, both the values for time-averaged thrust and power coefficients ($\overline{C}_T$ & $\overline{C}_P$) for the surging cases should be greater than the fixed case, due to the inequalities shown in Equation 4.2 and 4.3 (Johlas et al. [11] had done a similar analysis).

And with these facts, values of $\overline{C}_T$ and $\overline{C}_P$ should be bigger for cases with larger $\mathbb{V}$. However, both $\overline{C}_T$ and $\overline{C}_P$ do not comply the theory as can be seen in Table 4.1, where $\overline{C}_T$ even drops significantly as $\mathbb{V}$ becomes larger. This suggest that ξ_{C_T} and ξ_{C_P} are not constants during the surging cycle, and how f_n & f_θ are obtained for every actuator line points should be closely looked into (Equation 2.10 to 2.13). Nevertheless, as $V_{0,\text{app}}$ being influenced during surging in the simulations, the operational conditions (such as Ω) did not adjust accordingly, making the rotor operated in sub-optimal conditions, and thus affecting ξ_{C_T} and ξ_{C_P} (where ξ_{C_P} should be guaranteed to drop). Once again, note that the values of reference velocity for $\overline{C}_T$ & $\overline{C}_P$ are both bases on V_0 (fixed value) for this thesis, not $V_{0,\text{app}}$.

$$\frac{1}{T_S}\int_0^{T_S} \xi_{C_T} V_{0,\text{app}}^2 \text{d}t = \frac{1}{T_S}\int_0^{T_S} \xi_{C_T} V_0^2 (1-\mathbb{V}\cos\omega_S t)^2 \text{d}t \, > \, \xi_{C_T} V_0^2, \quad \text{for} \quad 0<\mathbb{V}<1 \tag{4.2}$$

$$\frac{1}{T_S}\int_0^{T_S} \xi_{C_P} V_{0,\text{app}}^3 \text{d}t = \frac{1}{T_S}\int_0^{T_S} \xi_{C_P} V_0^3 (1-\mathbb{V}\cos\omega_S t)^3 \text{d}t \, > \, \xi_{C_P} V_0^3, \quad \text{for} \quad 0<\mathbb{V}<1 \tag{4.3}$$

Actual Behaviours of $<C_T>$ & $<C_P>$

If looking closer to the the curves of $<C_T>$ and $<C_P>$ for the surging cases, for example in Figure 4.18, one can find that as $V_{\text{WT}} = 0$ m/s, both $<C_T>$ and $<C_P>$ have values which are very close of the fixed case (neutral values), suggesting hysteresis (dynamic inflow) effects are weak (see Figure 4.19 for more details about hysteresis effects). Moreover, even though the curves looks quite like sinusoidal, their fluctuations are not symmetry about the value for fixed rotor, especially for the $<C_T>$. Clearly that with the neutral values as the base points, the under-shoots of $<C_T>$ are larger than the over-shoots, and this also reflects in lower values of $\overline{C}_T$ (Table 4.1). As for $\overline{C}_P$, its values for fixed and surging cases considered in this chapter are similar (slightly bigger for cases with $\mathbb{V} = 0.11$ & 0.22 but smaller for cases with $\mathbb{V} = 0.44$).

The different behaviours of $\overline{C}_T$ and $\overline{C}_P$ as comparing to the neutral values could be explained by the inflow angle ϕ and angle of attack α are varying during a surging cycle simultaneously. As can be seen in Equation 2.18, larger apparent normal velocity seen by the surging rotor $V_{n,\text{app}}$ (Equation 2.17) will result in a larger ϕ and thus lager α, and higher α will lead to larger lift force $\boldsymbol{L}$ in general (if stalling does not occur). Moreover, usually bigger $\boldsymbol{L}$ will end up in larger thrust and larger power, since they both directly related to $\boldsymbol{L}$ (Equation 2.13). However, ϕ is also changing as $V_{n,\text{app}}$ varies, and note that $\boldsymbol{L}$ can be decomposed into $\hat{\boldsymbol{n}}$ & $\hat{\boldsymbol{\theta}}$ (Equation 4.4), where they are the normal (thrust) component and tangential component. With basic trigonometry, bigger ϕ will lead to smaller $\cos\phi$ but bigger $\sin\phi$, projecting $\boldsymbol{L}$ less to the thrust (normal) component but more to the tangential component. And thus, risings of C_T are less than C_P while $V_{n,\text{app}} > V_n$. While as $V_{n,\text{app}} < V_n$, opposite situations occurs, C_T drops less while C_P drops more. However, according to Equation 4.2 and 4.3, it is reasonable that periods of $V_{n,\text{app}} > V_n$ are more important when it comes to the time-averaged values of $\overline{C}_T$ and $\overline{C}_P$ due to the weighting of $V_{0,\text{app}}^2$. And thus the results of $\overline{C}_T$ for surging cases being smaller than the fixed cases while $\overline{C}_P$ remain for fixed and surging cases are reasonable.

$$\boldsymbol{L} = |\boldsymbol{L}| \cos\phi \, \hat{\boldsymbol{n}} + |\boldsymbol{L}| \sin\phi \, \hat{\boldsymbol{\theta}} \tag{4.4}$$

4.5.4 Stalling and $< C_T >$ & $< C_P >$

The dips in $< C_T >$ and $< C_P >$ curves for cases with higher $\mathbb{V}$ (Figure 4.18) can be explained with stalling. As the surging velocity V_{WT} becomes large enough to make the angle of attack α of a blade section in Equation 2.12 to exceed the stalling angle α_{stall} through the enlarged inflow angle ϕ in Equation 2.18, that blade section will experience stalling and making C_l to drop while C_d to rise, causing both C_T and C_P dropping. Note that since ALM is implemented here, stalling behaviours are modelled through the input polar data; only the values of C_l and C_d are concerned, and no additional effects such as extra turbulence from the boundary layer development nor leading edge vortex generated due to stalling are modelled. Also one should note that polar data used in this thesis are static polar data and no dynamic-stall model was applied.

Figure 4.49 presents the stalling angle of attack α_{stall} for NREL 5MW baseline turbine along its blade span, and α_{stall} is defined at the α which it gives the (first local) maximum C_l. Note that since NREL 5MW has different airfoils along the blade, α_{stall} is not constant. Figure 4.50 to 4.52 present the cycle-averaged α along the blade during a surging cycle based on ϕ_S for the surging cases, and $< \alpha >$ for the fixed case are also presented for comparison. Note that cases presented here are all under laminar inflow conditions. It is clear that $< \alpha >$ for the fixed case can be considered as constants, and stalling did not occur. While for the surging cases, it is clear that patterns of $< \alpha >$ for cases with same $\mathbb{V}$ are almost identical, and stalling effects are more prominent with higher $\mathbb{V}$. Together with with Equation 2.26, it is clear that stalling effects occur the most when the rotor is moving against the inflow, as $V_{0,\mathrm{app}}$ & $V_{n,\mathrm{app}}$ has bigger values. Note that stalling mostly occurs at the sections closer to the root, this is as expected since α close to the root is more subjected to $V_{n,\mathrm{app}}$ due to the fact that Ωr is smaller (Equation 2.18). Moreover, since that timings of stalling are aligned with the dips of $< C_T >$ and $< C_P >$ for the surging cases (Figure 4.18), it can be conclude that stalling is the cause of the dips on the curves.

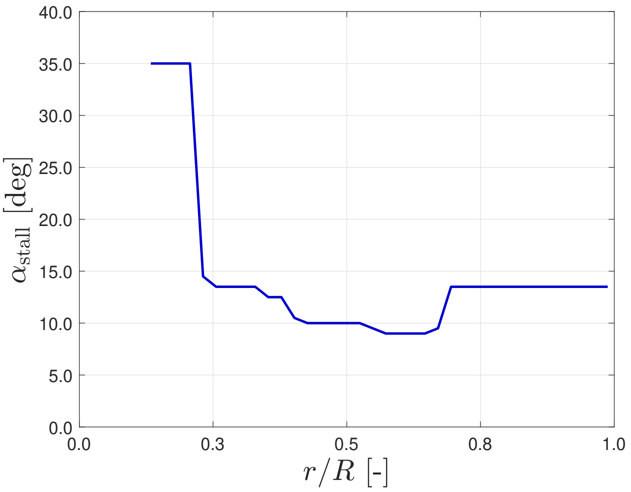

Figure 4.49: Stalling angles α_{stall} along the blade span of NREL 5MW baseline turbine rotor.

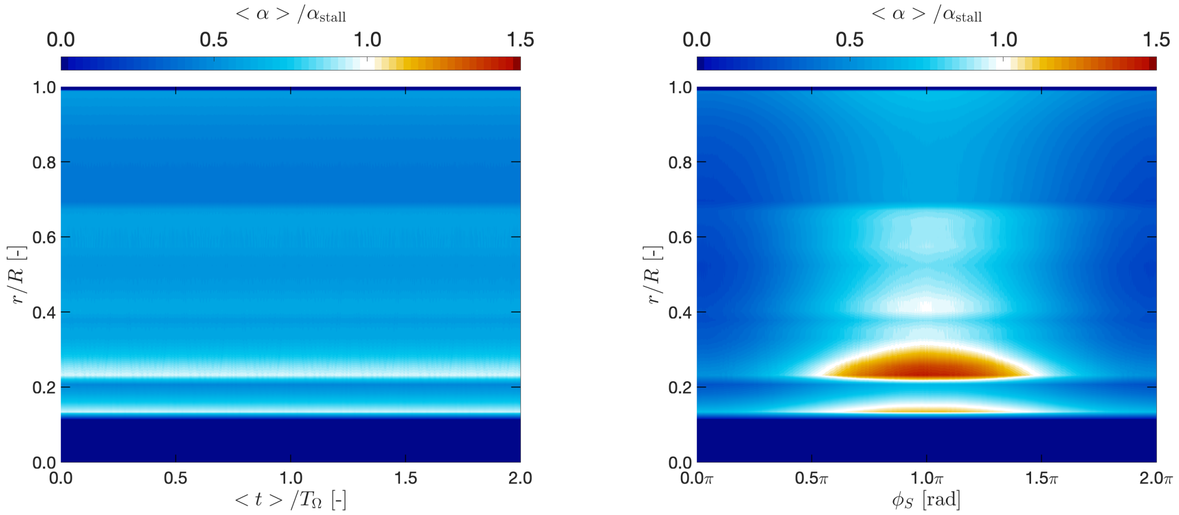

(a) Fixed.

(b) $A_S = 4$ m & $\omega_S = 0.63$ rad/s ($\mathbb{V} = 0.22$).

Figure 4.50: Cycle-averaged angle of attack $< \alpha >$ for fixed case and surging case with $A_S = 4$ m & $\omega_S = 0.63$ rad/s under laminar inflow conditions (cases **1** & **6**).

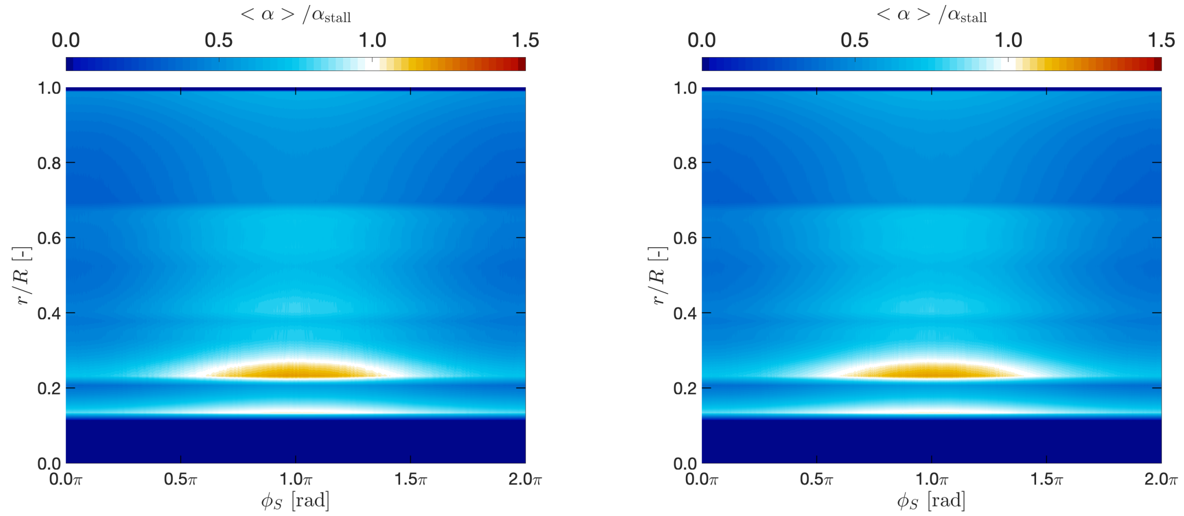

(a) $A_S = 2$ m & $\omega_S = 0.63$ rad/s ($\mathbb{V} = 0.11$). (b) $A_S = 4$ m & $\omega_S = 0.32$ rad/s ($\mathbb{V} = 0.11$).

Figure 4.51: Cycle-averaged angle of attack $< \alpha >$ for surging cases with $A_S = 2$ m & $\omega_S = 0.63$ rad/s and $A_S = 4$ m & $\omega_S = 0.32$ rad/s under laminar inflow conditions (cases **5** & **8**).

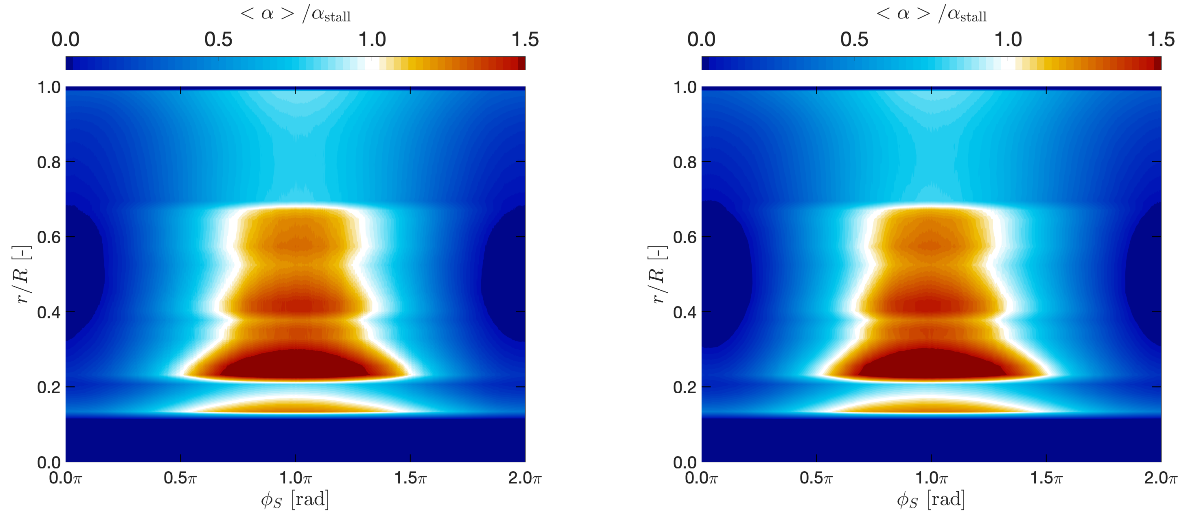

(a) $A_S = 8$ m & $\omega_S = 0.63$ rad/s ($\mathbb{V} = 0.44$). (b) $A_S = 4$ m & $\omega_S = 1.27$ rad/s ($\mathbb{V} = 0.44$).

Figure 4.52: Cycle-averaged angle of attack $< \alpha >$ for surging cases with $A_S = 8$ m & $\omega_S = 0.63$ rad/s and $A_S = 4$ m & $\omega_S = 1.27$ rad/s under laminar inflow conditions (cases **7** & **9**).

4.5.5 Blockage Effects of Different Surging Settings

Figure 4.53 and 4.54 show the streamwise profiles of $\overline{u^3w}$ at $y/D = 0$, $z/D = 0.5$ for cases with different A_S and ω_S under both laminar and turbulent (TI = 5.3%) inflow conditions (groups S.3-S.6). $\overline{u^3w}$ indicates the time-averaged vertical transports of the aerodynamic power that the flows contain. And here, positive indicates losses of aerodynamic power from the wake regions, while negative indicates gains. It can be seen that the power loss due to the blockages effects are most pronounced for the case with fixed rotor, and become less for the cases with bigger $\mathbb{V}$. This has already been hinted by the behaviours of $\overline{C}_T$ for different surging settings, and the significant drops about $\overline{u^3w}$ for cases with $\mathbb{V} = 0.44$ may be related to the stalling behaviours discussed previously. Milder blockage effects may have also contribute for the bigger $\overline{u}_{\text{Disk}}$ of wake. Moreover, both Figure 4.53 and 4.54 shows that turbulent cases have a negative profiles of $\overline{u^3w}$ after the rotor, indicating aerodynamic power is entrained to the wake regions. While for the laminar cases, profiles of $\overline{u^3w}$ are a bit irregular, but generally negative for surging cases. This may also related to the highly repeatable wake systems and the asymmetries for the laminar cases discussed previously.

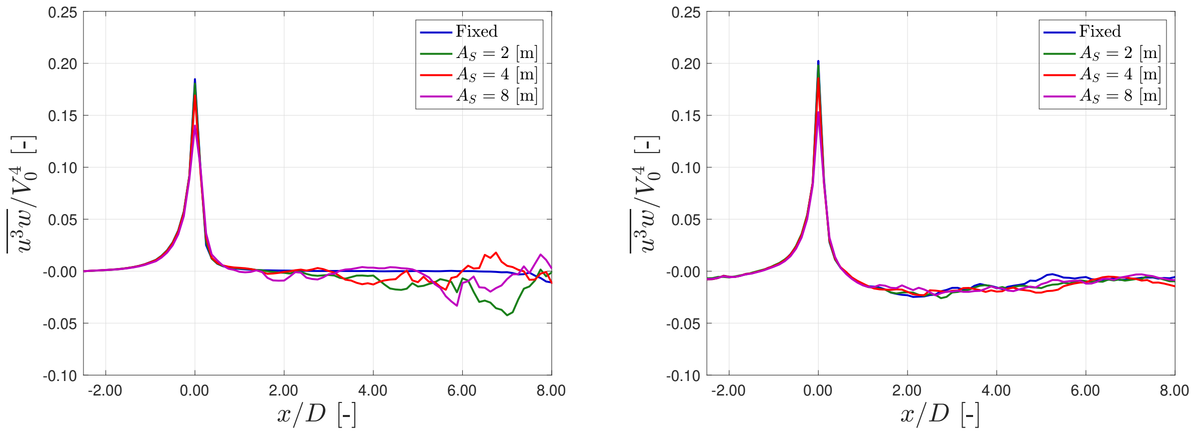

(a) Laminar inflow conditions (b) Turbulent inflow conditions (TI = 5.3%)

Figure 4.53: Streamwise profiles of $\overline{u^3w}$ at $z/D = 0.5$ for cases with different A_S while $\omega_S = 0.63$ rad/s (cases **1**, **3**, **5-7**, **11**, **13**, & **14**).

4.6 Summary and Conclusions

In this chapter, comprehensive investigations about the influences of inflow turbulence intensities TI, surging amplitudes A_S, and surging frequencies ω_S on a surging horizontal-axis wind turbine rotor had been conducted. In total, 22 cases using LES with ALM had been carried out and summarized in Table 4.1 & 4.2. Major discoveries and conclusions are listed below.

1. For cases with laminar inflow conditions, distinct coherent structures were found in the wakes (PLSB). Moreover, periodic vortical structures were formed through the

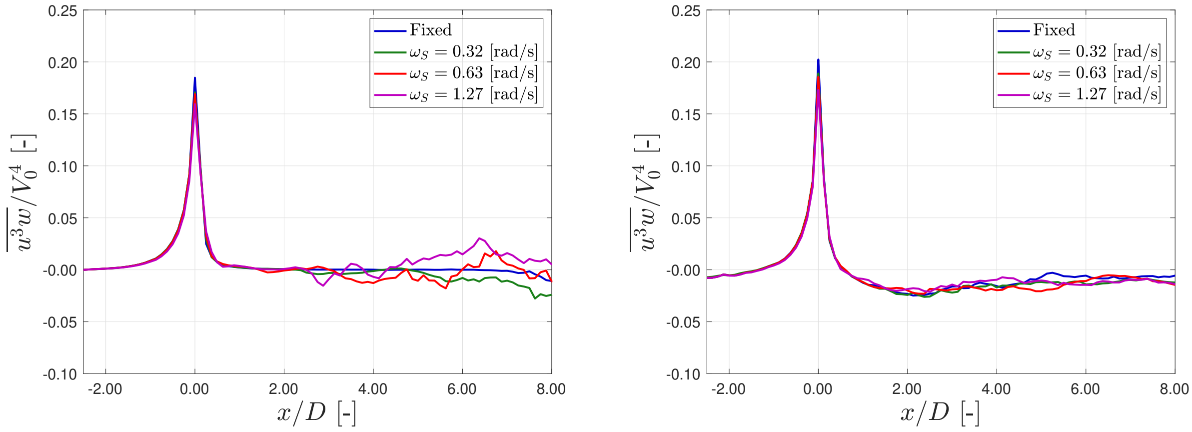

(a) Laminar inflow conditions

(b) Turbulent inflow conditions (TI = 5.3%)

Figure 4.54: Streamwise profiles of $\overline{u^3w}$ at $z/D = 0.5$ for cases with different ω_S while $A_S = 4$ m (cases **1**, **3**, **6**, **8**, **9**, **11**, **15**, & **16**).

interactions and merging of tip-vorticies. The flows get in and come out of wakes regions by circulating these vortical structures, which facilitate the momentum exchange of wake and has positive effects on recovering $\overline{u}_{\text{Dsik}}$ of wake.

2. For the laminar inflow cases, mean area-averaged wake velocities $\overline{u}_{\text{Disk}}$ for the surging cases may be 23% higher when compare to the fixed cases at $x/D = 5.0$, the increase was diminished to around $0.5\% \sim 2.0\%$ for turbulent inflow cases.

3. At this point, for the turbulent inflow cases, the increase of mean disk-averaged wake velocities $\overline{u}_{\text{Disk}}$ for the surging cases may be mainly related to the enhanced mixing (momentum entrainment) and milder blockage effects, and the extent of increments are mainly related to $\mathbb{V}$. However, contribution of the two effects are not investigated in great details in this thesis.

4. In general, inflow TI has little effects on $\overline{C}_T$ and $\overline{C}_P$. However, $\mathbb{V}$ considered in this chapter affects $\overline{C}_T$ noticeably and slightly affects $\overline{C}_P$. For the cases considered in this chapter, before severe stalling occur ($\mathbb{V} \leq 0.22$), higher $\mathbb{V}$ brings lower $\overline{C}_T$ with slightly higher $\overline{C}_P$. While for cases with severe stalling $\mathbb{V} = 0.44$, $\overline{C}_T$ is significantly lower than the fixed case while $\overline{C}_P$ is slightly lower.

5. With the current numerical frameworks, the wake system for surging cases with laminar inflow conditions are highly periodic and repeatable. That is, the instantaneous fields and phase-locked averaged fields are almost identical as long as the considered ϕ_S is same.

6. For cases with turbulent inflow conditions, the instantaneous fields are dominated by the inflow turbulence. However, distinct periodic structures (PLSB) are revealed if phase-locked averaging is conducted. That is, inflow turbulence dilutes the effects of surging on wake systems.

7. There is slight hysteresis (dynamic inflow) effects for surging cases, considering $< C_T >$ and $< C_P >$ follow similar curve while $V_{0,\mathrm{app}}$ (V_{WT}) grows and drops during a surge cycle (Figure 4.19); hysteresis effects are more noticeable with higher ω_S. Moreover, stalling affects the curves of $< C_T >$ and $< C_P >$, and the extent of stalling closely related to $\mathbb{V}$.

In the following chapter, another rotor will be added in the downstream, and analysis about wake interactions with different surging-fixed combinations will be conducted; and the effects of the slight increase about mean disk-averaged streamwise velocity on the downstream rotor will be tested.

Chapter 5

Results and Discussions of Dual Rotors Cases

5.1 Introduction

The wake interactions of two uncontrolled full scale wind turbine rotors operating in tandem with different surging settings, separation distances between the two rotors, and inflow turbulence intensities are examined in this chapter. It should be highlighted that complete knowledge of wake interactions between FOWT is still lacking in the literature, despite the fact that planning floating offshore wind farms will likely require through understanding of it [9].

Several key aspects of this chapter are described as follow. Firstly, studying the effects of surging on wake interactions of the two rotors, where cases from none of the rotors are surging to both being surging are investigated. Next, effects of phase differences between the two surging motions $\Delta_{\phi_{S_0}}$ for the two surging rotors are visited (Figure 1.7). Thirdly, effects of different turbulence inflow intensities on the wake interactions between the two fixed or two surging rotors are looked into. Note that all of the aspects mentioned above are tested with cases having different separation distances between the two rotors Δ_D in order to also understand the impacts of Δ_D on wake interactions.

In this chapter, the meshes used and the boundaries conditions applied are identical as the single rotor cases in chapter 4 (note turbulent cases and laminar cases use similar but different meshes), and rotor of NREL 5MW baseline turbine is again used, so as the settings for the upstream rotor (except for ϕ_{S_0}). That is, the neutral position of the upstream rotor $p_{R_0}^{\mathrm{up}}$ is kept at $x/D = 0$ and the rotational speed Ω^{up} is kept to be $\Omega_{\mathrm{rated}} = 1.27$ rad/s (the superscripts indicate whether the parameter is for the upstream rotor or the downstream rotor). The interested separation distances between the two rotors in tandem Δ_D are chosen to be $3D$ & $5D$. Though $3D$ & $5D$ are smaller or at the lower end of the typical Δ_D for realistic offshore wind farms ($\sim 7D$), they still fall into the interested range for the studies about wake interaction between wind turbines [17, 20, 95, 96, 97]; moreover, effects of surging conformations and other parameters on the rotors are likely to be larger with smaller Δ_D, and thus smaller Δ_D may help to identify their roles of wake interactions [20].

As for the rotational speed of the downstream rotor Ω^{down}, $\Omega^{\text{down}} = 2\Omega^{\text{up}}/3 = 0.84$ rad/s was set. Setting of Ω^{down} is based on keeping the phase-locked relations and attempting to maintain $\lambda^{\text{down}} = 7$ for the downstream rotor, since the estimated mean disk-averaged inflow wind speeds $\overline{u}_{\text{Disk}}$ at $x/D = 3$ and 5 are around 7.6 m/s ($2V_{0,\text{rated}}/3$), based on the the results in chapter 4 (see Figure 4.2, where TI = 5.3% is focused). Notice no controllers were implemented in this chapter just as the previous one. For all the surging rotors in this chapter, $A_S^{\text{up}} = A_S^{\text{down}} = 4$ m and $\omega_S^{\text{up}} = \omega_S^{\text{down}} = 0.63$ rad/s were chosen no matter the rotors are located at upstream or downstream, since that A_S & ω_S are mainly dominated by hydrodynamic loading [50]. Moreover, as in chapter 4, TI = 5.3% was focused for the turbulent cases since it is considered to be common for typical offshore conditions [88]. As for the positions of the rotors (p_R^{up} & p_R^{down}), they are described with Equation 5.1 and 5.2, which are in the same form of Equation 2.19. Note that if not mentioned otherwise, $\phi_{S_0}^{\text{up}}$ & $\phi_{S_0}^{\text{down}}$ are set to be 0.0π.

$$p_R^{\text{up}}(t) = A_S^{\text{up}} \sin\left(\omega_S^{\text{up}} t + \phi_{S_0}^{\text{up}}\right) + p_{R_0}^{\text{up}} = A_S^{\text{up}} \sin\phi_S^{\text{up}} + p_{R_0}^{\text{up}} \tag{5.1}$$
$$p_R^{\text{down}}(t) = A_S^{\text{down}} \sin\left(\omega_S^{\text{down}} t + \phi_{S_0}^{\text{down}}\right) + p_{R_0}^{\text{down}} = A_S^{\text{down}} \sin\phi_S^{\text{down}} + p_{R_0}^{\text{down}} \tag{5.2}$$
$$\Delta_{\phi_{S_0}} = \phi_{S_0}^{\text{up}} - \phi_{S_0}^{\text{down}} \tag{5.3}$$

In total, 36 cases were conducted in this chapter, and their basic settings and results are listed in Table 5.1; histograms of $\overline{C}_P^{\text{up}}$ & $\overline{C}_P^{\text{down}}$ for the cases are in Figure 5.1 & 5.2 for better visualization. $\phi_{S_0}^{\text{up}}$ is ϕ_{S_0} for the upstream rotor. $\overline{C}_T^{\text{up}}$, $\overline{C}_P^{\text{up}}$, $\overline{C}_T^{\text{down}}$, & $\overline{C}_P^{\text{down}}$ are the time averaged C_T & C_P for the upstream or downstream rotor, and note that the reference velocity for C_T & C_P adopted in this chapter is $V_{0,\text{rated}} = 11.4$ m/s for both upstream and downstream rotors to make the comparison simpler. $\overline{G}_{C_P}^{\text{up}}$, $\overline{G}_{C_P}^{\text{down}}$, & $\overline{G}_{C_P}^{\text{total}}$ are the gains of $\overline{C}_P$ due to the surging motions for the upstream rotor, downstream rotor, and the two rotors combined (see Equation 5.4). Note that the baselines for $\overline{G}_{C_P}^{\text{up}}$, $\overline{G}_{C_P}^{\text{down}}$, & $\overline{G}_{C_P}^{\text{total}}$ are the corresponding FF case in the specific set, and they are in bold font in Table 5.1.

$$\overline{G}_{C_P} = \frac{C_P \text{ of the interested case} - C_P \text{ of the } \textbf{reference case}}{C_P \text{ of the } \textbf{reference case}} \times 100\% \tag{5.4}$$

The cases in Table 5.1 are further classified into 12 groups for comparisons, and they are listed down below. Note that F stands for *Fixed* and S stands for *Surging*. While FF is the abbreviation of upstream rotor being fixed while downstream rotor being fixed as well (*Fixed* + *Fixed*). Similarly, FS, SF, and SS stand for *Fixed* + *Surging*, *Surging* + *Fixed*, and *Surging* + *Surging*.

D.1 Combinations of fixed and surging (FF, FS, SF, SS) with $\Delta_D = 3D$ under laminar inflow conditions (cases **31-34**)

D.2 Combinations of fixed and surging with $\Delta_D = 3D$ under turbulent inflow conditions (cases **38-41**)

D.3 Combinations of fixed and surging with $\Delta_D = 5D$ under turbulent inflow conditions (cases **45-48**)

D.4 Combinations of fixed and surging with $\Delta_D = 5D$ under turbulent inflow conditions (cases **52-55**)

D.5 Varying $\phi_{S_0}^{\mathrm{up}}$ with $\Delta_D = 3D$ under laminar inflow conditions (cases **34-37**)

D.6 Varying $\phi_{S_0}^{\mathrm{up}}$ with $\Delta_D = 3D$ under turbulent inflow conditions (cases **41-44**)

D.7 Varying $\phi_{S_0}^{\mathrm{up}}$ with $\Delta_D = 5D$ under laminar inflow conditions (cases **48-51**)

D.8 Varying $\phi_{S_0}^{\mathrm{up}}$ with $\Delta_D = 5D$ under turbulent inflow conditions (cases **55-58**)

D.9 Two fixed rotors with $\Delta_D = 3D$ and different inflow turbulent intensities (cases **31**, **38**, **59**, and **61**)

D.10 Two surging rotors with $\Delta_D = 3D$ and different inflow turbulent intensities (cases **34**, **41**, **60**, and **62**)

D.11 Two fixed rotors with $\Delta_D = 5D$ and different inflow turbulent intensities (cases **45**, **52**, **63**, and **65**)

D.12 Two surging rotors with $\Delta_D = 5D$ and different inflow turbulent intensities (cases **48**, **55**, **64**, and **66**)

For groups D.1 to D.4, combinations of fixed and surging are looked into, note that all combinations are looked into (FF, FS, SF, & SS), and thus how surging affects the wake interactions between two rotors can be studied thoroughly. It should be noted that comparisons between pairs of FF/SF & FS/SS should be prioritized in order to precisely analyze how surging motions affect the performances of the downstream rotor through wake interactions; it will be difficult to compare FF and SS directly since multiple variables are involved.

Effects of $\Delta_{\phi_{S_0}}$ on wake interactions of FOWTs are studied with the cases in groups D.5 to D.8. $\Delta_{\phi_{S_0}}$ is interested because motions of FOWT are not likely always being in-phase or out-of-phase, and thus whether $\Delta_{\phi_{S_0}}$ will affect wake interactions is important, as it may play a role when designing layouts for floating offshore wind farms.

Groups D.9 to D.12 look into the influences of inflow TI on wake interactions, both with fixed (FF) and surging (SS) rotors, and cases with $\Delta_D = 3D$ & $5D$ are considered.

For all the cases in this chapter, including cases with both laminar and turbulent inflow conditions, the time instant for the instantaneous snapshots of fields are all taken at $t = 110T_\Omega$, and the averaging windows all started from $t = 60T_\Omega$ and ended at $t = 110T_\Omega$. These are identical to the ones for single rotor cases with turbulent inflow conditions in chapter 4. It should be noticed that the statistics of the downstream rotors are less converged than the upstream ones. Again, see Appendix C for more details about the sampling and statistic methods and convergence tests.

Table 5.1: The basic settings and results for cases conducted with dual rotors without implementing controlling strategies.

Case	TI [%]	Up	Down	Δ_D/D	$\Delta_{\phi_{S_0}}$ [rad]	$\overline{C}_T^{\text{up}}$	$\overline{C}_P^{\text{up}}$	$\overline{C}_T^{\text{down}}$	$\overline{C}_P^{\text{down}}$	$\overline{G}_{C_P}^{\text{up}}$ [%]	$\overline{G}_{C_P}^{\text{down}}$ [%]	$\overline{G}_{C_P}^{\text{total}}$ [%]	$\overline{u}_{\text{Disk}}^{8D}/V_0$
31	**Lam.**	**F**	**F**	**3.0**	-	**0.726**	**0.515**	**0.254**	**0.076**	**-**	**-**	**-**	**0.452**
32	Lam.	F	S	3.0	-	0.726	0.515	0.249	0.086	0.0	13.7	1.8	0.483
33	Lam.	S	F	3.0	-	0.714	0.521	0.264	0.085	1.2	12.3	2.6	0.597
34	Lam.	S	S	3.0	0.0π	0.714	0.521	0.260	0.092	1.1	21.5	3.8	0.607
35	Lam.	S	S	3.0	0.5π	0.714	0.521	0.254	0.094	1.2	23.4	4.0	0.596
36	Lam.	S	S	3.0	1.0π	0.714	0.521	0.251	0.094	1.2	23.8	4.1	0.590
37	Lam.	S	S	3.0	1.5π	0.714	0.521	0.258	0.093	1.2	21.7	3.8	0.579
38	**5.3**	**F**	**F**	**3.0**	-	**0.726**	**0.516**	**0.306**	**0.138**	**-**	**-**	**-**	**0.739**
39	5.3	F	S	3.0	-	0.726	0.516	0.300	0.140	0.0	1.4	0.3	0.752
40	5.3	S	F	3.0	-	0.715	0.524	0.310	0.140	1.5	1.6	1.5	0.723
41	5.3	S	S	3.0	0.0π	0.715	0.524	0.299	0.141	1.5	2.5	1.7	0.725
42	5.3	S	S	3.0	0.5π	0.714	0.524	0.296	0.140	1.5	1.8	1.5	0.743
43	5.3	S	S	3.0	1.0π	0.715	0.524	0.299	0.142	1.5	3.5	1.9	0.748
44	5.3	S	S	3.0	1.5π	0.715	0.525	0.299	0.142	1.6	3.3	1.9	0.740
45	**Lam.**	**F**	**F**	**5.0**	-	**0.727**	**0.517**	**0.254**	**0.076**	**-**	**-**	**-**	**0.349**
46	Lam.	F	S	5.0	-	0.727	0.517	0.249	0.087	0.0	14.1	1.8	0.419
47	Lam.	S	F	5.0	-	0.715	0.523	0.283	0.108	1.1	42.2	6.3	0.599
48	Lam.	S	S	5.0	0.0π	0.715	0.523	0.278	0.114	1.1	49.8	7.3	0.597
49	Lam.	S	S	5.0	0.5π	0.715	0.523	0.274	0.113	1.1	49.2	7.3	0.596
50	Lam.	S	S	5.0	1.0π	0.715	0.523	0.271	0.114	1.1	49.8	7.3	0.571
51	Lam.	S	S	5.0	1.5π	0.715	0.523	0.275	0.114	1.1	50.4	7.4	0.579
52	**5.3**	**F**	**F**	**5.0**	-	**0.726**	**0.518**	**0.344**	**0.181**	**-**	**-**	**-**	**0.658**
53	5.3	F	S	5.0	-	0.726	0.518	0.330	0.176	0.0	-2.9	-0.7	0.664
54	5.3	S	F	5.0	-	0.716	0.525	0.347	0.184	1.5	1.6	1.5	0.668
55	5.3	S	S	5.0	0.0π	0.716	0.525	0.332	0.178	1.5	-1.8	0.7	0.667
56	5.3	S	S	5.0	0.5π	0.715	0.525	0.331	0.177	1.4	-2.1	0.5	0.687
57	5.3	S	S	5.0	1.0π	0.715	0.525	0.332	0.178	1.5	-1.5	0.7	0.679
58	5.3	S	S	5.0	1.5π	0.716	0.526	0.331	0.178	1.5	-1.7	0.7	0.665
59	**2.7**	**F**	**F**	**3.0**	-	**0.724**	**0.512**	**0.290**	**0.118**	**0.0**	**0.0**	**0.0**	**0.734**
60	2.7	S	S	3.0	0.0π	0.713	0.521	0.283	0.121	1.7	2.8	1.9	0.738
61	**11.6**	**F**	**F**	**3.0**	-	**0.724**	**0.519**	**0.322**	**0.159**	**0.0**	**0.0**	**0.0**	**0.769**
62	11.6	S	S	3.0	0.0π	0.712	0.524	0.314	0.160	1.1	1.0	1.1	0.788
63	**2.7**	**F**	**F**	**5.0**	-	**0.725**	**0.514**	**0.332**	**0.166**	**0.0**	**0.0**	**0.0**	**0.654**
64	2.7	S	S	5.0	0.0π	0.714	0.522	0.319	0.164	1.7	-1.3	0.9	0.661
65	**11.6**	**F**	**F**	**5.0**	-	**0.724**	**0.520**	**0.352**	**0.195**	**0.0**	**0.0**	**0.0**	**0.685**
66	11.6	S	S	5.0	0.0π	0.713	0.525	0.340	0.189	1.1	-3.1	-0.1	0.719

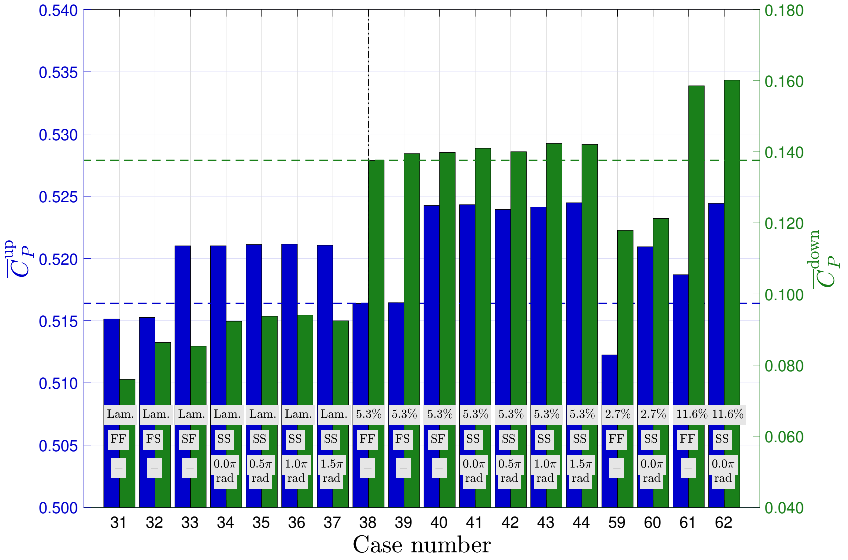

Figure 5.1: Histogram of $\overline{C}_P^{\mathrm{up}}$ & $\overline{C}_P^{\mathrm{down}}$ for dual rotor cases with $\Delta_D = 3D$ listed in Table 5.1. The three entries on each bar stand for the values of TI, surging-fixed conformations, and $\Delta_{\phi_{S_0}}$ for each case. Case FF with TI $= 5.3\%$ (case **38**) is chosen to be the reference case for comparison, its values are indicated with horizontal dashed lines.

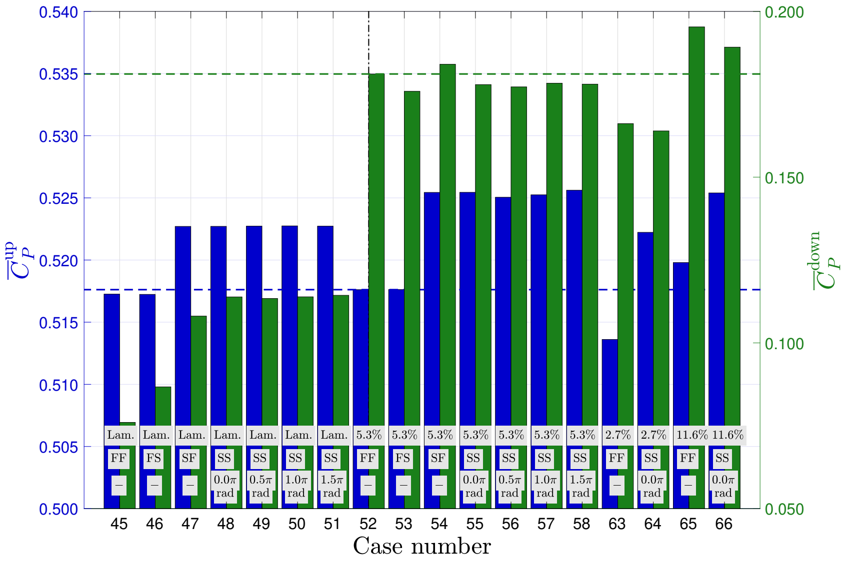

Figure 5.2: Histogram of $\overline{C}_P^{\mathrm{up}}$ & $\overline{C}_P^{\mathrm{down}}$ for dual rotor cases with $\Delta_D = 5D$ listed in Table 4.1. Other details are same with Figure 5.1, but the reference case changed to **52** (still being the FF case with TI $= 5.3\%$).

5.2 Combinations of Fixed and Surging with Δ_D being $3D$ Under Laminar and Turbulent Inflow Conditions

This section investigates how surging affects the wake interactions of two NREL 5MW rotor in tandem with Δ_D being $3D$ under both laminar and turbulent inflow conditions. That is, $p_{R_0}^{\text{down}}$ in Equation 5.2 is $3D$. Eight cases are analyzed, and they are cases **31-34** & **38-41** in Table 5.1, corresponding to groups D.1 & D.2 in section 5.1.

5.2.1 Summarizing Wake Characteristics

Characteristics of $\overline{u}_{\text{Disk}}$ for the eight cases (both laminar and turbulent cases) are summarized in Figure 5.3, while the $\overline{u}$ profiles are displayed in Figure 5.4 & 5.5 for the four laminar cases & the four turbulent cases. It is very clear that $\overline{u}_{\text{Disk}}$ do not experience any significant recovery before hitting the downstream rotor for all the eight cases. Furthermore, they show that the profiles of $\overline{u}_{\text{Disk}}$ and $\overline{u}$ for the laminar cases are mostly dominated by whether the upstream rotor is surging or fixed, while the roles of the downstream rotor are not as significant; but in general, $\overline{u}_{\text{Disk}}$ still recovers faster when the downstream rotor is surging for the cases with laminar inflow conditions. As for the turbulent cases, the four cases share very similar profiles for $\overline{u}_{\text{Disk}}$ and $\overline{u}$. While looking closer at $x/D = 5$, values of $\overline{u}_{\text{Disk}}$ will be slightly lower for the cases with fixed upstream rotor compare to the cases having surging upstream rotor. While as $x/D > 5$, trends of how $\overline{u}_{\text{Disk}}$ related to surging conformations become unclear for the turbulent cases as their differences are less pronounced. Moreover, if viewing Figure 5.3 together with Figure 5.31 in the later section, seems that $\phi_{S_0}^{\text{up}}$ also affects profiles of $\overline{u}_{\text{Disk}}$ with $\Delta_D = 3D$. Note that the wake systems of the two rotors are very complex, factors such as turbulence, stalling, and convection of PLSB affect the systems. As for the $\overline{u}$ profiles, laminar cases have irregular shapes while turbulent cases have Gaussian shape, just as the cases of single rotor in the previous chapter.

5.2.2 Summarizing Rotor Performances

Power coefficients for the upstream and downstream rotors under laminar inflow conditions are summarized in Figure 5.6, while the counterparts for the cases with turbulent inflow conditions are in Figure 5.7. Note that the calculations of C_P (and C_T as well) for the both rotor are based on reference wind speed being 11.4 m/s. Together with the $< C_P >$ curves for the single rotor (Figure 4.4), it can be easily concluded that the performances of $< C_P >$ are (almost) not affected by the rotor at downstream, and values for $\overline{C}_P$ & $\overline{C}_P^{\text{up}}$ in Table 4.1 & Table 5.1 also tell the same tale (still very slight blockages can be detected by comparing $\overline{C}_P^{(\text{up})}$, Figure 6.10 in the later chapter gives a better visualization). As for the downstream rotor, curves of $< C_P^{\text{down}} >$ for the four laminar cases are significantly different, while the turbulent cases share almost the same curves (only depending on the surging conformation of the downstream rotor). However, as looking $\overline{G}_{C_P}^{\text{down}}$ in Table 5.1 for the turbulent cases, one can find that $\overline{C}_P^{\text{down}}$ for the case SF is 1.6% higher comparing to case FF; this pointed

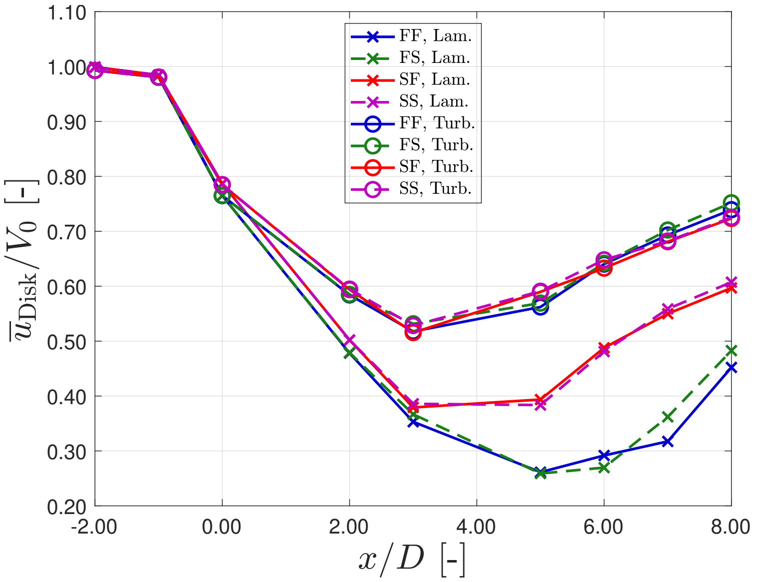

Figure 5.3: $\overline{u}_{\text{Disk}}$ along x-direction for cases of dual rotors with $\Delta_D = 3D$ and different surging-fixed combinations under laminar or turbulent (TI $= 5.3\%$) inflow conditions.

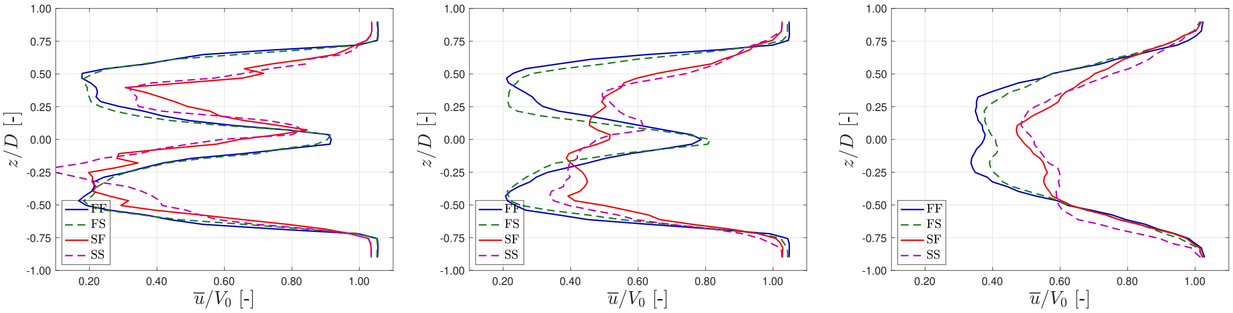

(a) $x/D = 5.0$

(b) $x/D = 6.0$

(c) $x/D = 8.0$

Figure 5.4: Profile of $\overline{u}$ at different x/D for cases of dual rotors with $\Delta_D = 3D$ and different surging-fixed combinations under laminar inflow conditions.

out the wake characteristics of a surging FOWT are likely to be more desirable for the downstream rotor in sense of outputting higher mean power. Moreover, $\overline{C}_P^{\text{down}}$ for the cases of SS (cases **41-44**) also out-performed FS for about 1% to 2%. It is worth noting that $\overline{C}_P^{\text{up}}$ for the turbulent cases with surging upstream rotor are already higher than the turbulent cases with fixed upstream rotor, together with the fact that C_P^{down} for the cases with surging upstream rotor are also higher, it may be concluded that surging do have positive effects on making the overall power converting rates of floating offshore wind farms higher even in the environments with realistic turbulent inflow conditions; and in general, $\overline{u}_{\text{Disk}}^{8D}$ is also comparable for the SS cases than the FF case.

Figure 5.8 shows the power spectrum of the power coefficients for the downstream rotor ($S_{C_P^{\text{down}}}(f)$) of the eight cases, where the laminar and turbulent cases are plotted separately. For the laminar cases (Figure 5.8a), it can be seen that the highest peaks locate at $f =$

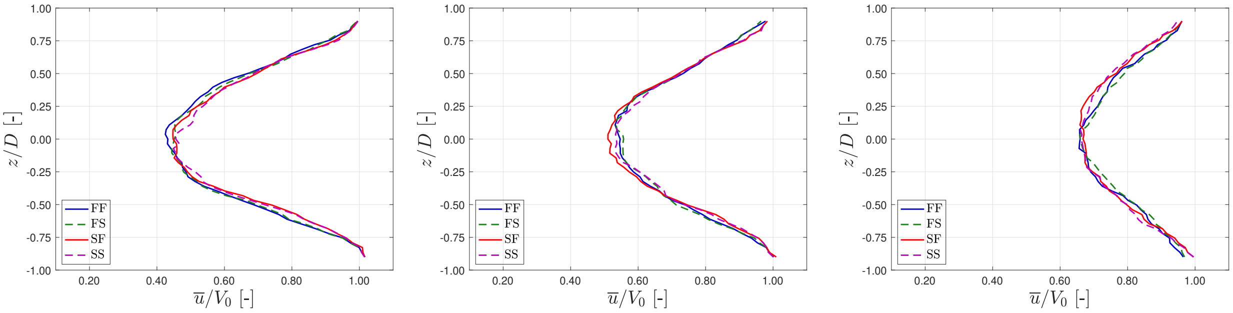

(a) $x/D = 5.0$ (b) $x/D = 6.0$ (c) $x/D = 8.0$

Figure 5.5: Profile of $\overline{u}$ at different x/D for cases of dual rotors with $\Delta_D = 3D$, different surging settings, and inflow TI being 5.3%.

$\omega_S/2\pi$ Hz for cases which the downstream rotor is surging (cases FS & SS), indicating C_P^{down} oscillates most significantly with ω_S; this is as expected with the curves $< C_P^{\text{down}} >$ plotted in Figure 5.6b. Note that there are several lower peaks at higher frequencies, which are the harmonics of ω_S. Interestingly, for case SF, even though the downstream rotor is not surging, it still has a peak at $f = \omega_S/2\pi$, while the magnitude is smaller compared to cases FS or SS; the peak is due to the wake structures (PLSB) generated by the upstream surging rotor, and notice that case FF do not have this feature. As for the range around 3P of the downstream rotor ($f = 3\Omega^{\text{down}}/2\pi = 4\omega_S/2\pi$), cases SF & SS have sharper peaks, while cases FF & FS have a relatively broadened peaks; these suggested the periodicity of wake structures is more stronger when the upstream rotor is surging, and this could be confirmed with the $<$TKE$>_{0\pi}$ fields (Figure 5.12) in the later section. As for the turbulent cases, peaks at $f = \omega_S/2\pi$ for cases FS & SS are still significant, while their harmonics are not as sharp as the laminar cases. And the peak at $f = \omega_S/2\pi$ for case SF has a much smaller magnitude, even making it difficult to tell whether it was due to the PLSB from upstream rotor or simply due to the turbulent fluctuations. As for the peak around 3P, all the four turbulent cases have rather broadened peak, and the higher harmonics of ω_S are much weaker.

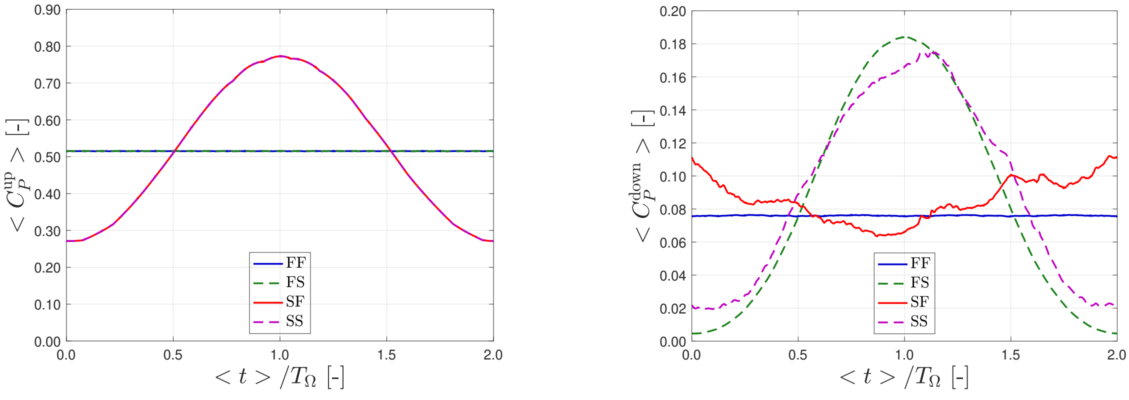

(a) $< C_P^{\mathrm{up}} >$ (b) $< C_P^{\mathrm{down}} >$

Figure 5.6: $< C_P^{\mathrm{up}} >$ and $< C_P^{\mathrm{down}} >$ for cases of dual rotors with $\Delta_D = 3D$ and different surging-fixed combinations under laminar inflow conditions.

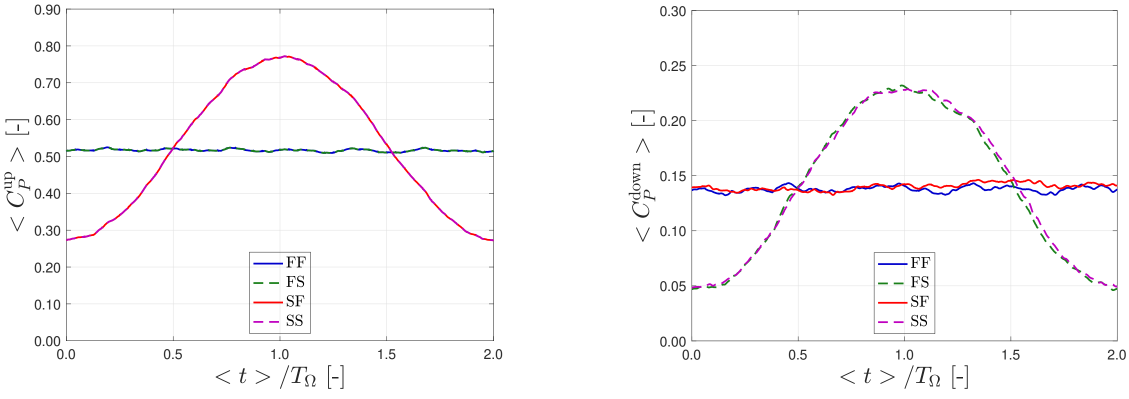

(a) $< C_P^{\mathrm{up}} >$ (b) $< C_P^{\mathrm{down}} >$

Figure 5.7: $< C_P^{\mathrm{up}} >$ and $< C_P^{\mathrm{down}} >$ for cases of dual rotors with $\Delta_D = 3D$ and different surging-fixed combinations under turbulent inflow conditions.

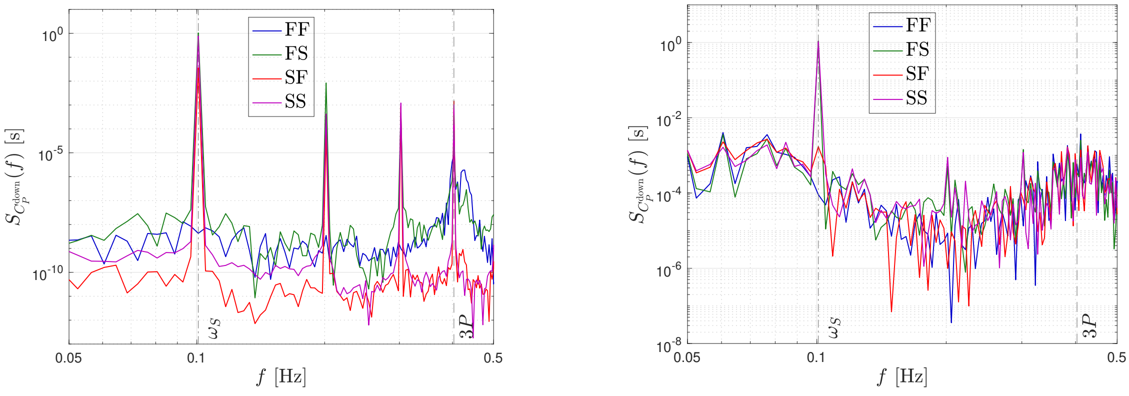

(a) Laminar cases (b) Turbulent cases (TI = 5.3%)

Figure 5.8: Power spectrum of C_P^{down} ($S_{C_P^{\mathrm{down}}}(f)$) for cases of dual rotors with $\Delta_D = 3D$ and different surging-fixed combinations under laminar or turbulent inflow conditions.

5.2.3 Velocity and TKE Fields

The instantaneous contours of u for the eight cases with two rotors separated with $\Delta_D = 3D$ are in Figure 5.9. For both the laminar and turbulent cases, the instantaneous fields are more dominated by the upstream rotor. For example, u fields after the second rotor of cases FF and FS with laminar inflow conditions (case **31** & **32**) are rather similar, which the effects of surging of downstream rotor are much less pronounced compared to the upstream rotor, and same can be said by comparing cases SF and SS with laminar inflow conditions (cases **33** & **34**). Moreover, similar with the cases of single rotor in chapter 4, the instantaneous fields of the turbulent cases are dominated by the inflow turbulence, as can be seen that the u fields for cases **38-41** share similar features. However, if looking closer, one can say that wake structure of cases **38** & **39** (FF & FS) share more detail features between themselves, and same can be said for cases **40** & **41** (SF & SS), and these suggest that the influences of the upstream rotor still exist and being more pronounced than the downstream one.

Figure 5.10 displays the $< u >_{0\pi}$ fields of the eight cases. Note that the phase-locked relationships are maintained even with the introduced of the downstream rotor, it is maintained with the rotational speed of the downstream rotor being $3\Omega^{\mathrm{down}} = 2\Omega^{\mathrm{up}} = \omega_S$ (note the 120° symmetry of the rotor (3P)) for all the eight cases. Similar with the single rotor cases, the fields of u and $< u >_{0\pi}$ for the four laminar cases are almost identical up until $x = 4.5D$, and this can also be explained with the $<\mathrm{TKE}>_{0\pi}$ fields presented later. As for the turbulent cases, surging effects of the upstream rotor can be easily identified by observing $< u >_{0\pi}$ fields. However, surging effects of the downstream rotor cannot be clearly detected by the phase-locked averaged streamwise velocity fields $< u >_{0\pi}$, and fields of $< \Delta p >_{0\pi}$ & $< \omega_y >_{0\pi}$ presented later also show similar things.

The fields of $\overline{u}$ are displayed in Figure 5.11. Clearly that $\overline{u}$ is further slowed down by the downstream rotor for all the eight cases. For the laminar cases, unlike with the cases of single fixed rotor in chapter 4, all the four cases have significant recovery of $\overline{u}$ after $x = 6D$, suggesting wake-wake interaction promotes recovery of $\overline{u}$ under laminar inflow conditions. Moreover, the recovery rates of $\overline{u}$ for the laminar cases are dominated by the surging conformations of the upstream rotor, and unsurprisingly, $\overline{u}$ recovered faster while upstream rotor is surging. As for the four turbulent cases, they share very similar $\overline{u}$ fields even the surging-fixed conformations are different, which is similar to that the $\overline{u}$ fields are similar for single rotor cases with different surging settings in the previous chapter (Figure E.7).

The fields $<\mathrm{TKE}>_{0\pi}$ for the eight cases are shown in Figure 5.12. For the laminar cases, even with the addition of the downstream rotor, low values of $<\mathrm{TKE}>_{0\pi}$ fields were still maintained at the vicinity of the downstream rotor, and this is still true with case SS. However, unlike with the single rotor cases (Figure 4.21), low values of $<\mathrm{TKE}>_{0\pi}$ did not persist to the far downstream for the four cases, significant fluctuations unrelated to surging nor rotations of rotors occurred around $x = 4.5D$, suggesting the breakdown of the wake structures. Once again, the patterns of $<\mathrm{TKE}>_{0\pi}$ fields are more dominated by the upstream rotor. Interestingly, just as the single rotor cases, values of $<\mathrm{TKE}>_{0\pi}$ fields are lower for the cases with the upstream rotor being surging, suggesting surging actually makes the wake systems more *orderly* (repeatable). As for the turbulent cases, other than the two different patterns around $0 \leq x/D \leq 3$ depending whether the upstream rotor is surging (related to the PLSB structures of upstream rotor), the four cases share similar features.

The fields of TKE are shown in Figure 5.13. For the laminar cases, similar with the $\overline{u}$ fields, TKE fields are mostly affected by whether the upstream rotor is surging. Furthermore, unlike the single rotor cases, where only at the tracks of the tip vorticies have significant TKE values, now most of the parts within the rotor projection areas ($-0.5 \leq z/D \leq 0.5$) have pronounced values, especially for cases FF and FS. As for the four turbulent cases, the addition of the downstream rotor increased TKE of the wakes, which is unsurprisingly. And just as the $\overline{u}$ fields, the four turbulent cases share very similar features.

5.2.4 Pressure and Vorticity Fields

Fields of $< \Delta p >_{0\pi}$ and $\Delta\overline{p}$ for the eight cases are displayed in Figure 5.14 and 5.15 (instantaneous fields Δp is in Figure F.1). The phase-locked averaged fields $< \Delta p >_{0\pi}$ show that upstream rotor influence $< \Delta p >_{0\pi}$ fields much more than the downstream rotor, especially for the turbulent cases where the effects of the downstream rotor are almost not observable. $\Delta\overline{p}$ fields show that although they are affected by the surging conformations for the laminar cases, they are almost the same for the turbulent cases.

The fields of $< \omega_y >_{0\pi}$ for the eight cases are in Figure 5.16, the fields depict the characteristics of the released tip vorticies of the two wind turbine rotors in tandem (fields of $< \omega_x >_{0\pi}$ & $< \omega_z >_{0\pi}$ are in Figure F.2 & F.3). For the laminar cases, case FF shows that the vortex tubes of the two rotor are separated around the vicinity of the downstream rotor, and they eventually merge together and smear out in the more downstream regions ($x \geq 5D$). Case FS with laminar inflow conditions shares very similar features with case FF, while the periodic structures due to surging of the downstream rotor exist, and those structures do make the stream tube of the upstream rotor interacts with the wake system of upstream rotor earlier. As for the cases SF and cases SS under laminar inflow conditions, the vortex tube or periodic structures result from the downstream rotor are not found, suggesting the strong induction fields due to the surging upstream rotor dominates over the one of the downstream rotor. Furthermore, an interesting phenomena is that after the interactions of the two wakes from upstream and downstream rotor, the values of $< \omega_y >_{0\pi}$ fields for the four laminar cases are smeared out, making them similar to the turbulent cases. For the four turbulent cases, the fields of $< \omega_y >_{0\pi}$ after the downstream rotor are almost indistinguishable, suggesting the effects of surging of the downstream rotor are weak; however, it is very clear that with $\Delta_D = 3D$, the downstream rotor situates at the region where the shapes of periodic structures (PLSB) of the surging upstream rotors are still quite sharp.

5.2.5 Momentum Entrainment

Fields of $-\partial\overline{p}/\partial x$, $-\overline{w}(\partial\overline{u}/\partial z)$, and $-\partial\overline{u'w'}/\partial z$ are displayed in Figure 5.17, 5.18, and 5.19. They are the three fields contribute the most to the momentum recovery ($\partial\overline{uu}/\partial x$) along the streamwise direction (Appendix B). With the fields of $-\partial\overline{p}/\partial x$, it can be seen that separation of $3D$ is close enough to make the mean pressure fields of the two rotors interact with each other, and this probably explains why the values of $\overline{C}_T^{\text{up}}$ are (very) slightly lower compared to the values of $\overline{C}_T$ with just a single rotor. While for the patterns of the fields, other than cases SF and SS with laminar inflow conditions have peculiar patterns right after the downstream rotor, they behave as one may have expected. While for the fields of convection term $-\overline{w}(\partial\overline{u}/\partial z)$, cases with laminar inflow conditions showcase that their momentum recovery due to convections are much more pronounced compared to the turbulent cases, which is similar to the cases with single rotor (Figure 4.14). As for the Reynolds stress term $-\partial\overline{u'w'}/\partial z$, cases FF & FS with laminar inflow conditions show that after the interactions of the wakes of upstream and downstream rotors, their patterns look more similar with the turbulent cases. While for the cases SS & SF with laminar inflow conditions, they once more showed the peculiar patterns just as the single rotor cases (Figure 4.15). These suggest that wake-wake interactions with laminar inflow conditions between bottom-mounted wind turbines may facilitate turbulent transitions (breakdown of the wake structures) more than the surging (upstream) rotor, and these might related to that the induction fields of surging rotor are much more persist. As for the turbulent cases, once again, differences for the four turbulent cases about $-\partial\overline{u'w'}/\partial z$ fields are not obvious.

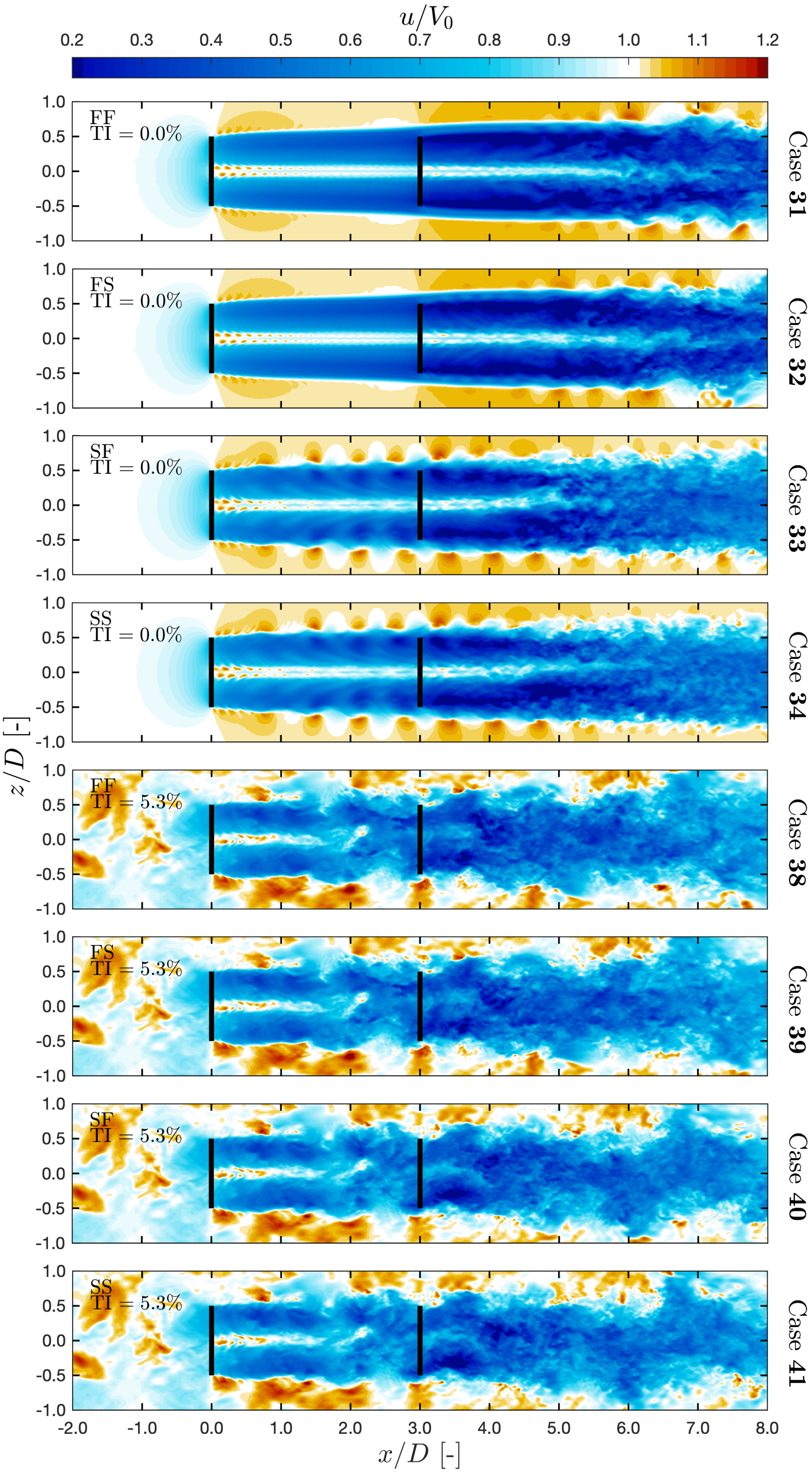

Figure 5.9: Fields of instantaneous streamwise velocity u for dual rotors with $\Delta_D = 3D$ and different surging-fixed combinations.

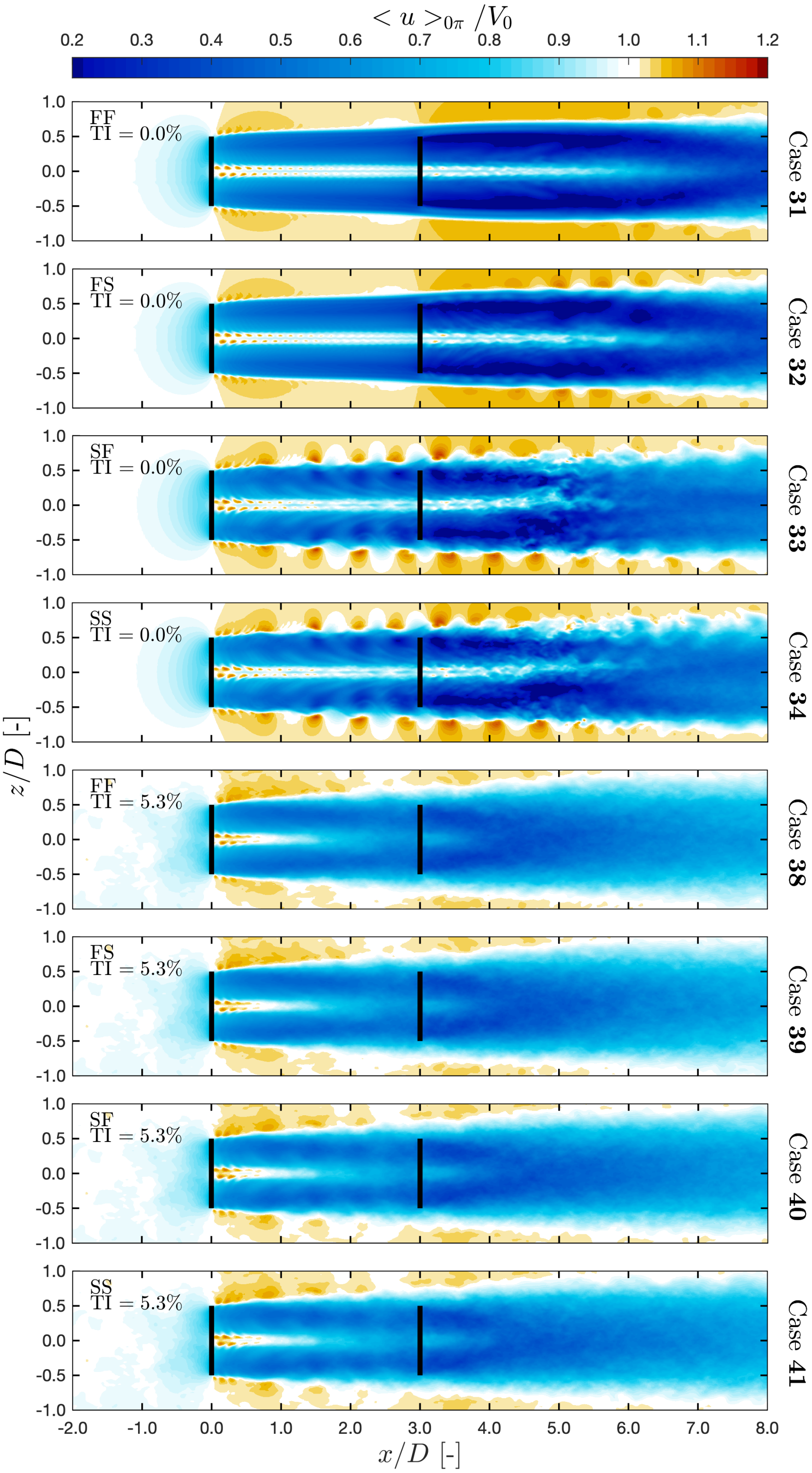

Figure 5.10: Fields of phase-locked averaged streamwise velocity $< u >_{0\pi}$ for dual rotors with $\Delta_D = 3D$ and different surging-fixed combinations.

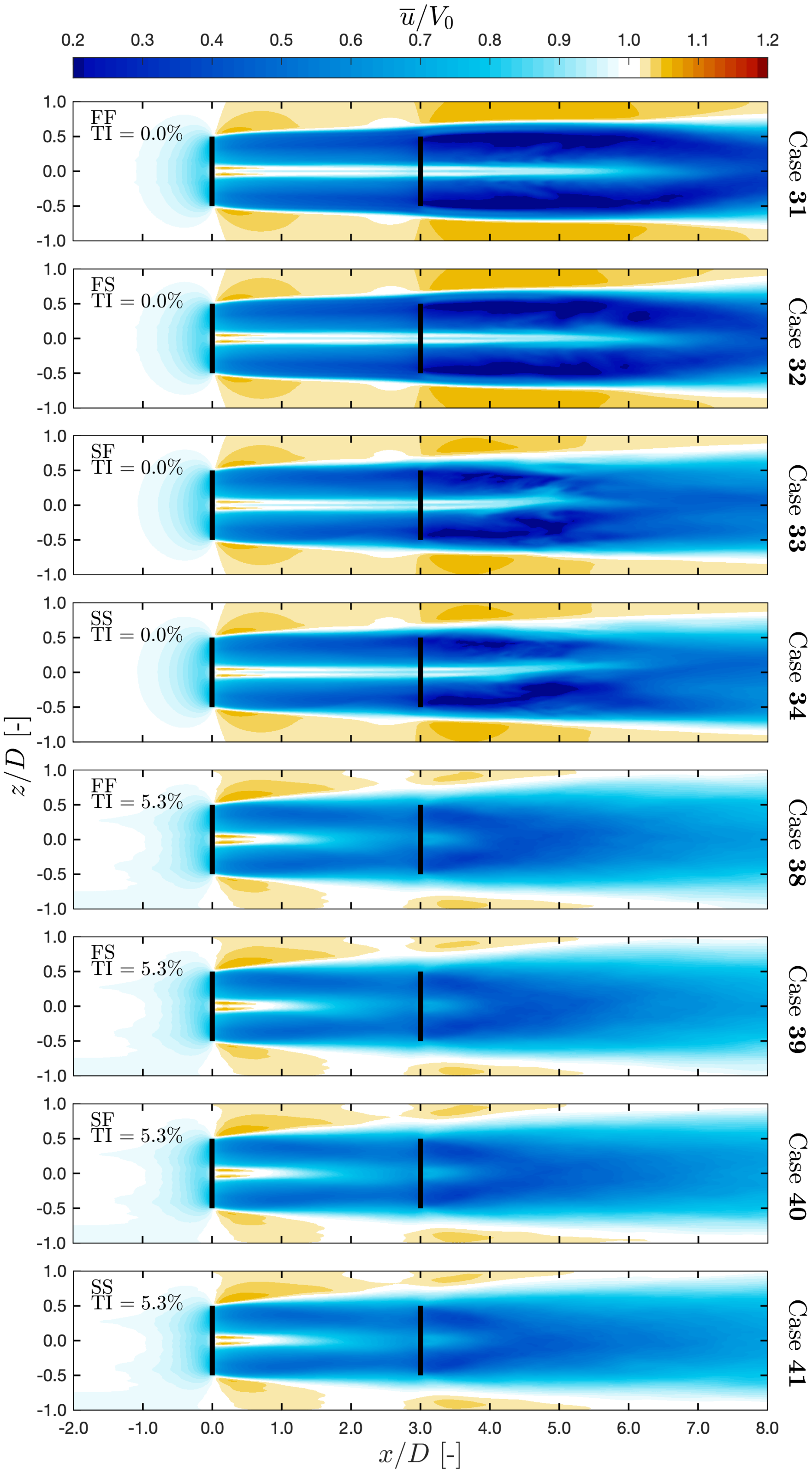

Figure 5.11: Fields of time-averaged streamwise velocity $\overline{u}$ for dual rotors with $\Delta_D = 3D$ and different surging-fixed combinations.

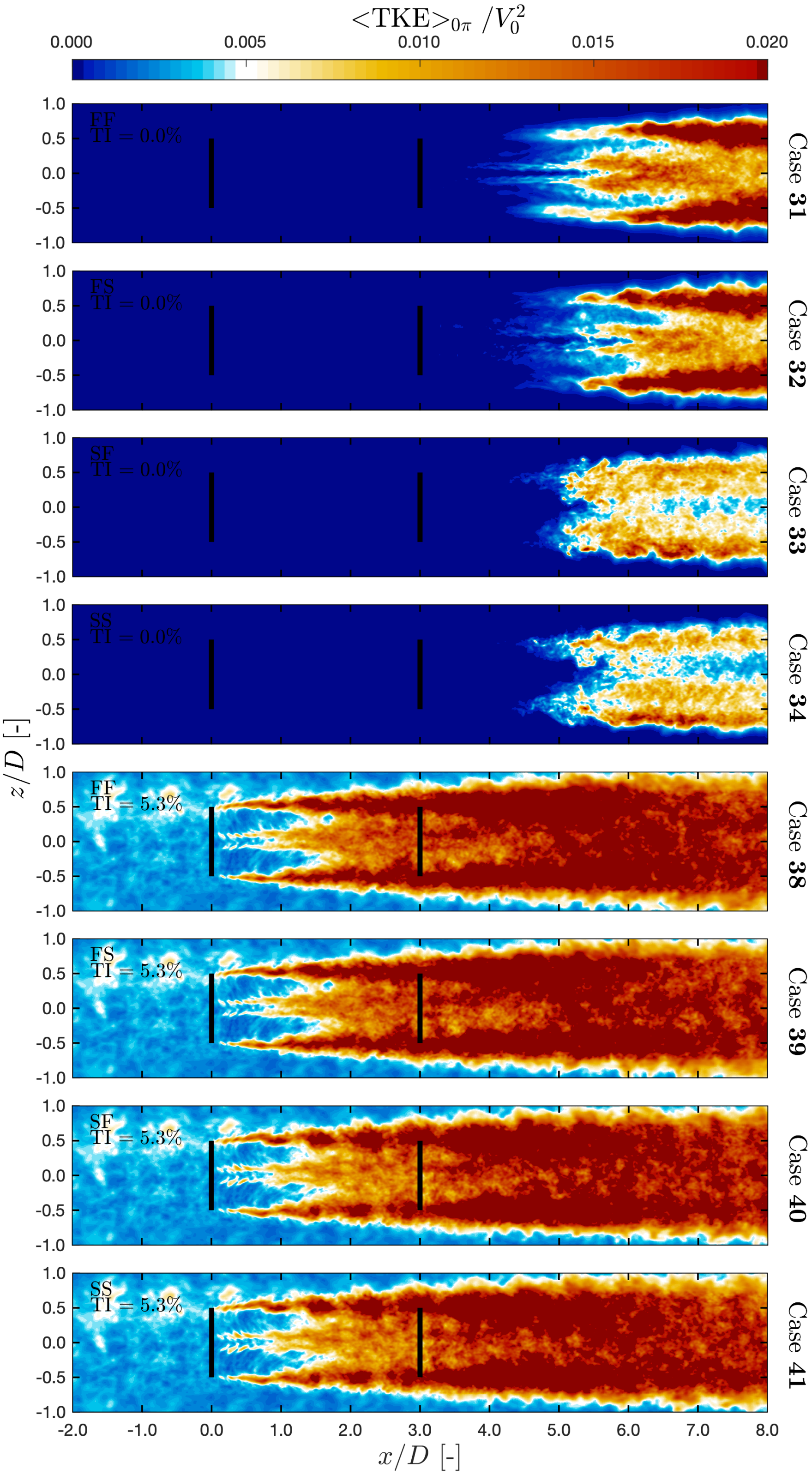

Figure 5.12: Fields of phase-locked averaged turbulent kinetic energy <TKE>$_{0\pi}$ for dual rotors with $\Delta_D = 3D$ and different surging-fixed combinations.

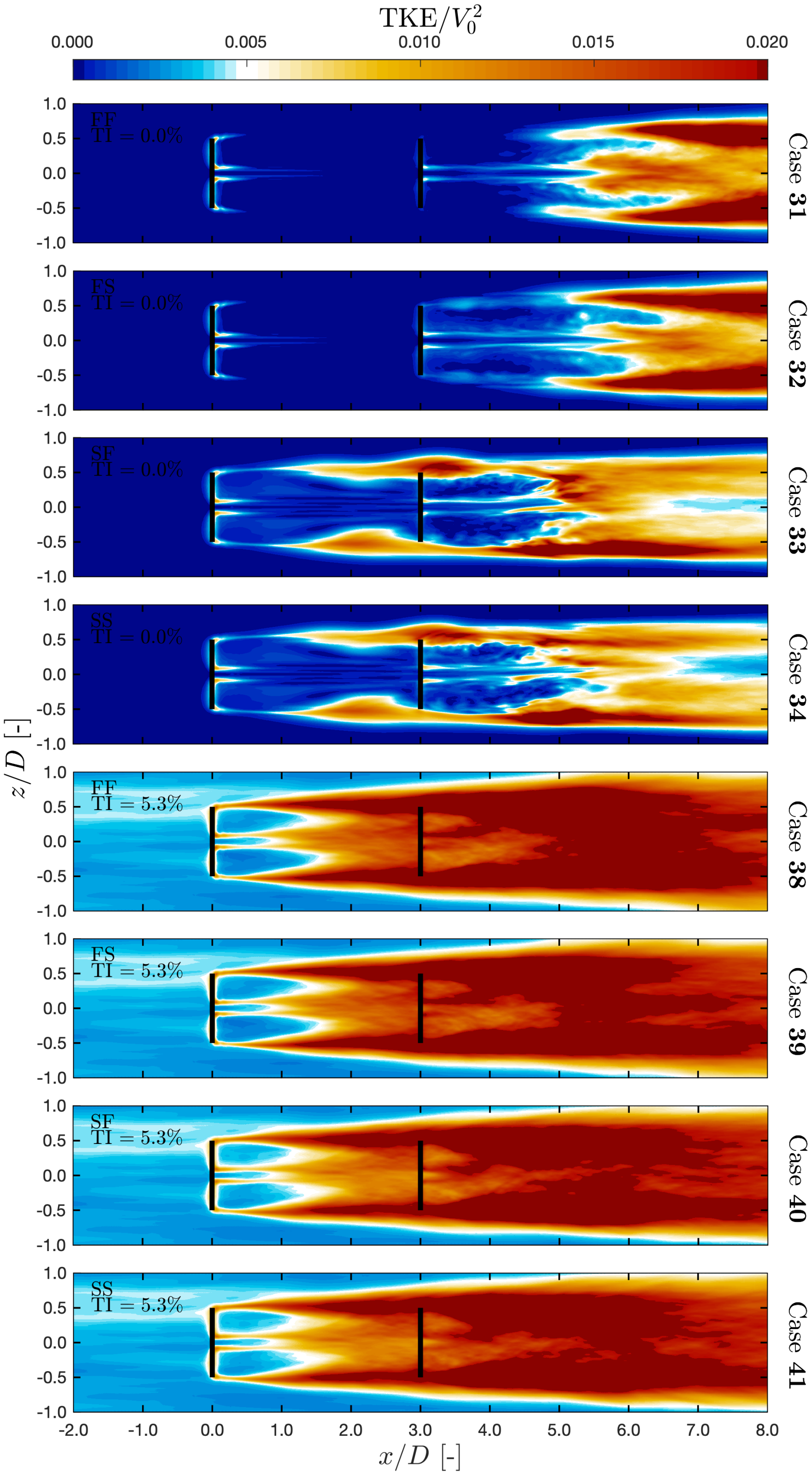

Figure 5.13: Fields of turbulent kinetic energy TKE for dual rotors with $\Delta_D = 3D$ and different surging-fixed combinations.

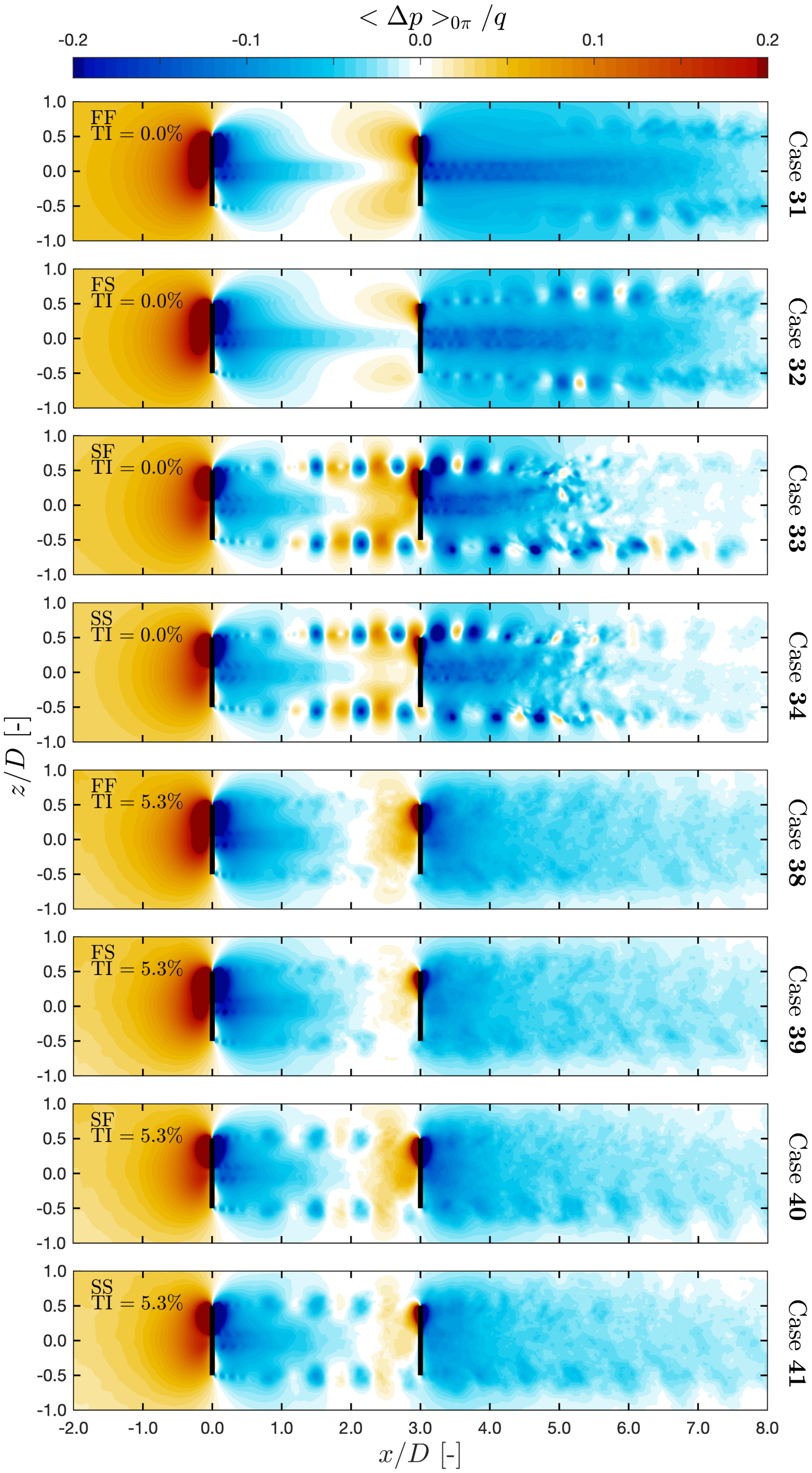

Figure 5.14: Fields of phase-locked averaged pressure $< \Delta p >_{0\pi}$ for dual rotors with $\Delta_D = 3D$ and different surging-fixed combinations.

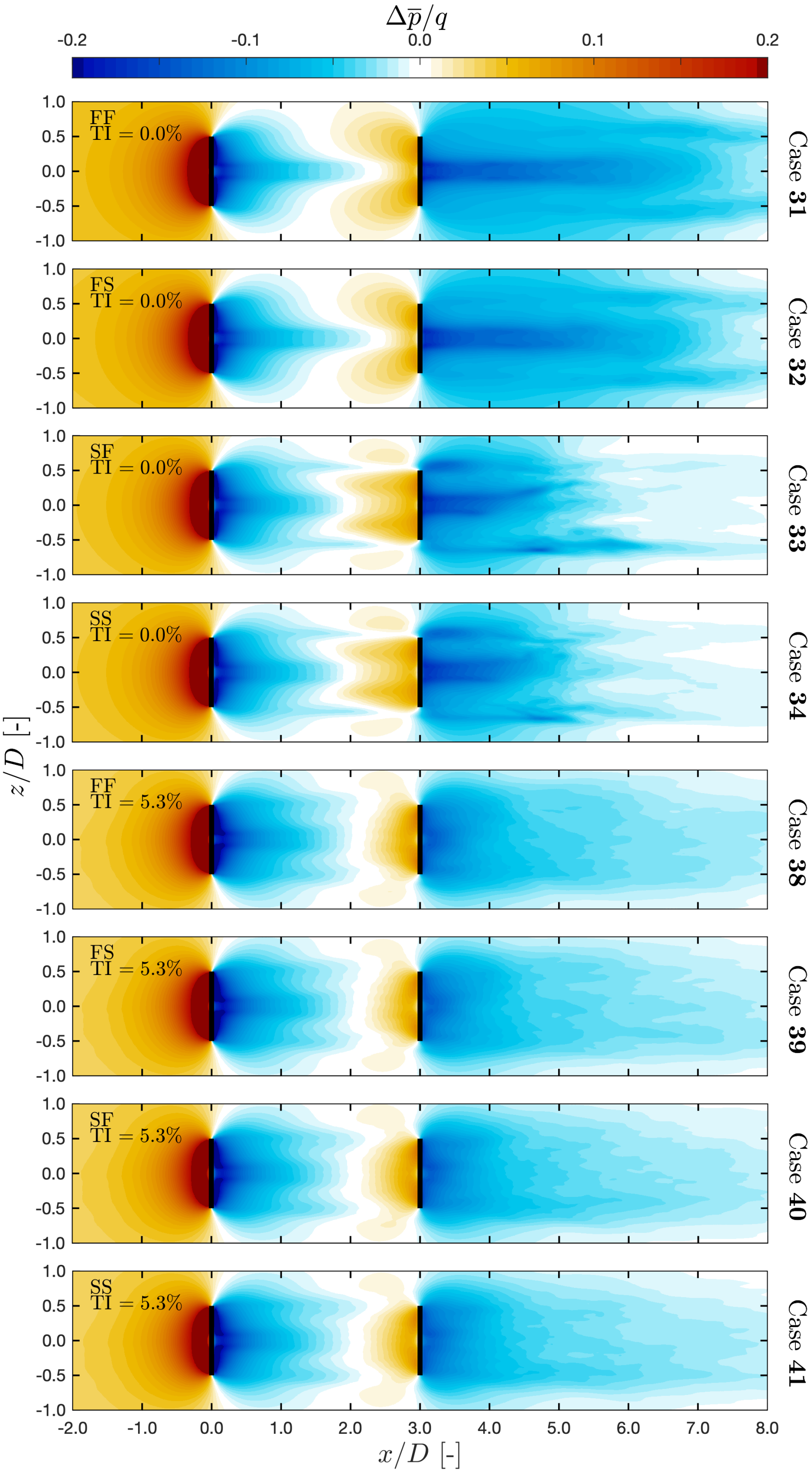

Figure 5.15: Fields of time-averaged pressure $\Delta\overline{p}$ for dual rotors with $\Delta_D = 3D$ and different surging-fixed combinations.

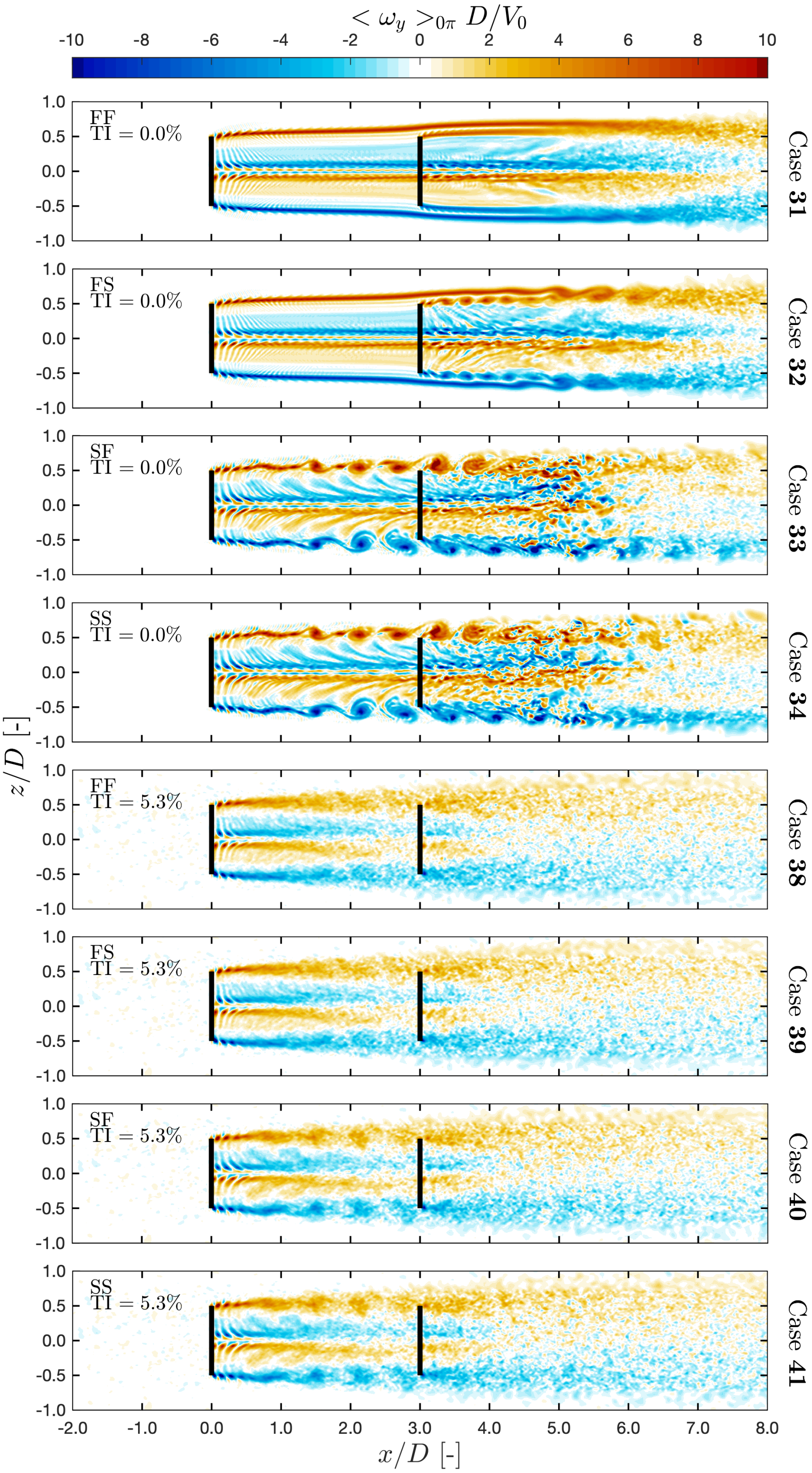

Figure 5.16: Fields of phase-locked averaged y-component vorticity $< \omega_y >_{0\pi}$ for dual rotors with $\Delta_D = 3D$ and different surging-fixed combinations.

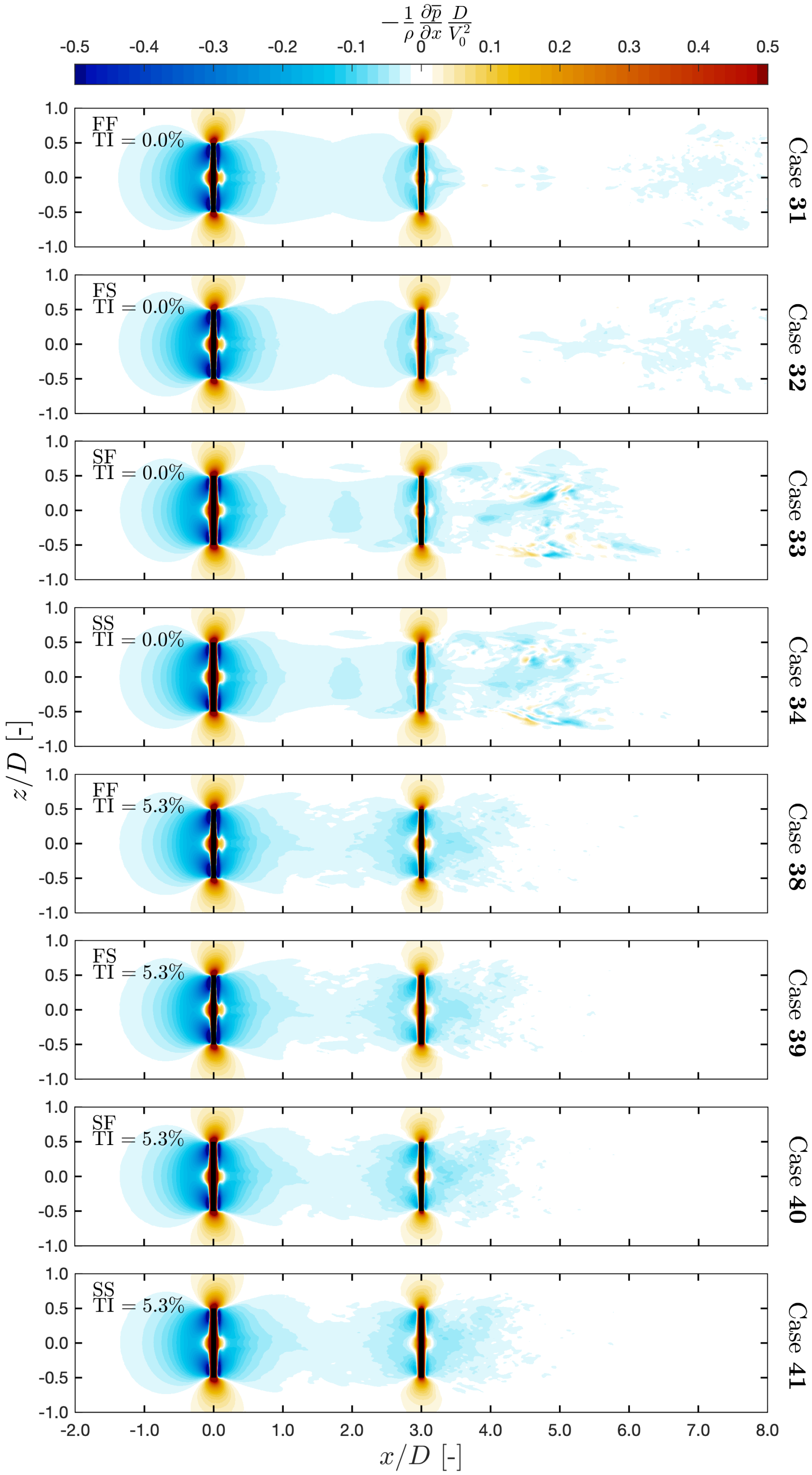

Figure 5.17: Fields of pressure gradients $-(1/\rho)(\partial\overline{p}/\partial x)$ for dual rotors with $\Delta_D = 3D$ and different surging-fixed combinations.

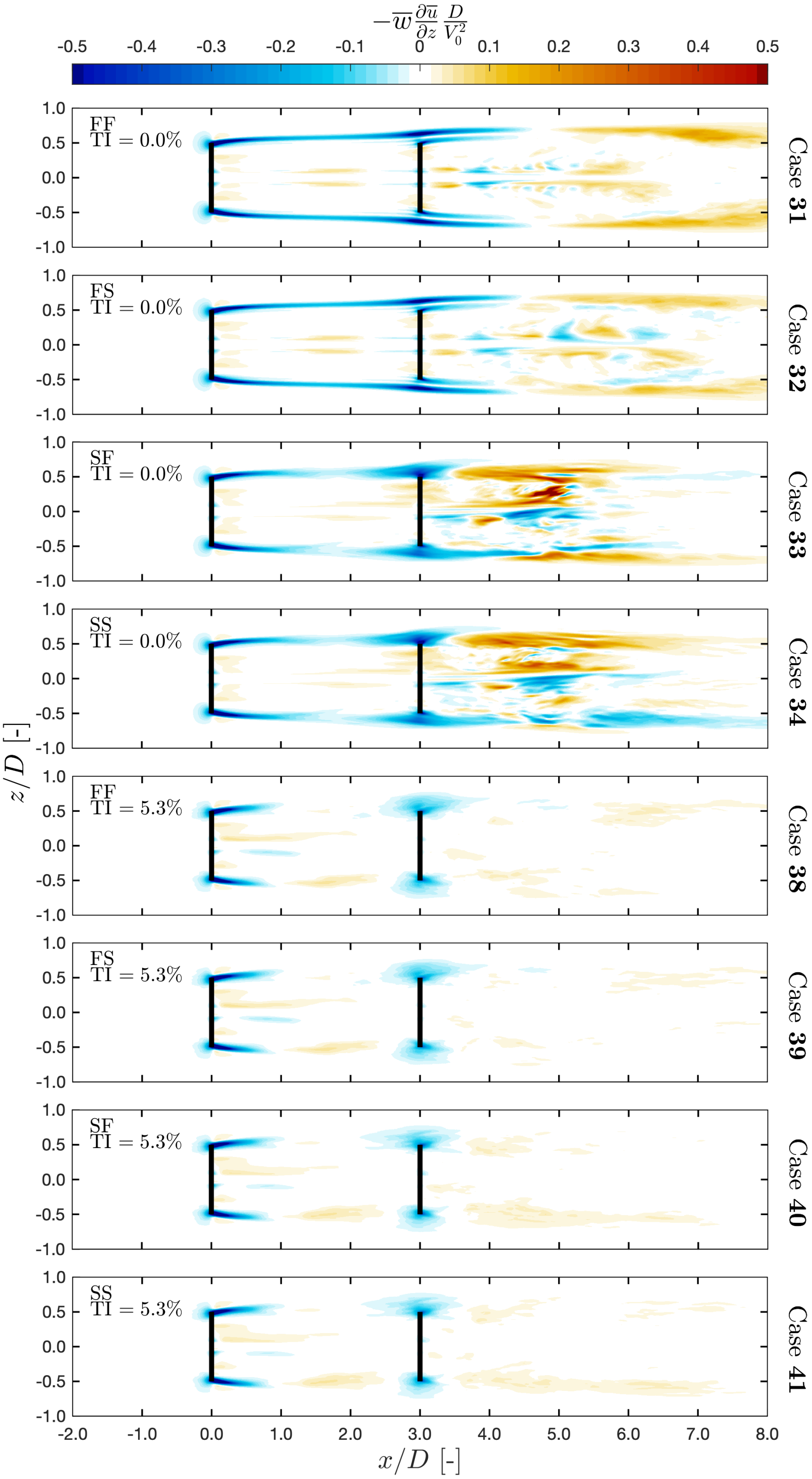

Figure 5.18: Fields of $-\overline{w}(\partial\overline{u}/\partial z)$ for dual rotors with $\Delta_D = 3D$ and different surging-fixed combinations.

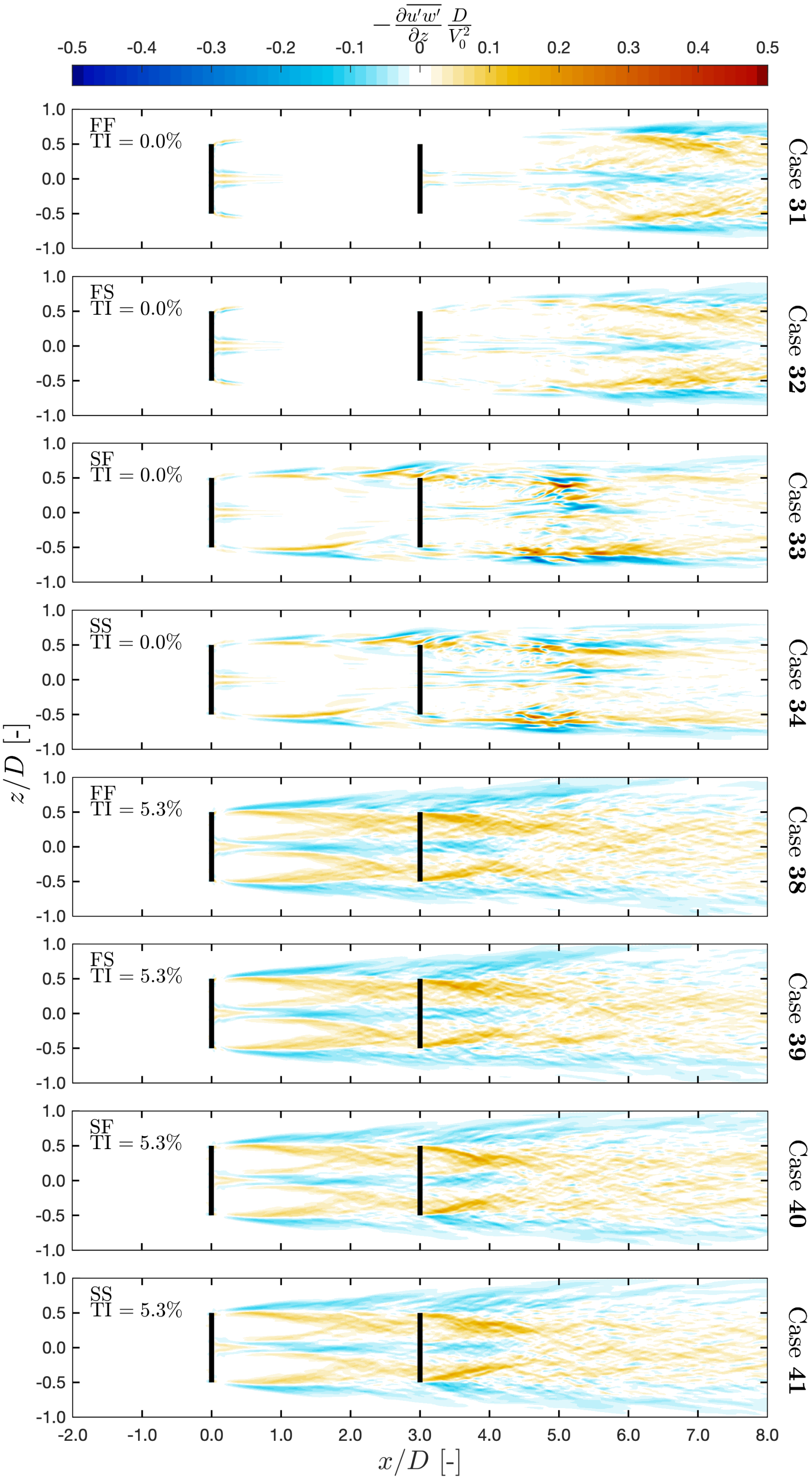

Figure 5.19: Fields of $-\partial\overline{u'w'}/\partial z$ for dual rotors with $\Delta_D = 3D$ and different surging-fixed combinations.

5.3 Combinations of Fixed and Surging with Δ_D being $5D$ Under Laminar and Turbulent Inflow Conditions

This section investigates how surging affects the wake interactions of two NREL 5MW rotor in tandem with Δ_D being $5D$ ($p_{R_0}^{\text{down}} = 5D$) under both laminar and turbulent inflow conditions. Eight cases are analyzed, which are cases **45-48** and **52-55** in Table 5.1, and correspond to groups D.3 and D.4 in section 5.1. In general, results in this section with $\Delta_D = 5D$ are very similar to results with $\Delta_D = 3D$ in section 5.2, with some minor differences.

5.3.1 Summarizing Wake Characteristics

Characteristics of $\overline{u}_{\text{Disk}}$ for the eight cases are summarized in Figure 5.20, while $\overline{u}$ for the four laminar cases are plotted in Figure 5.21 and the four turbulent cases are in Figure 5.22. It can be seen that other than $\overline{u}_{\text{Disk}}$ recovers a bit before reaching the downstream rotor, the behaviors of $\overline{u}_{\text{Disk}}$ and $\overline{u}$ are very similar to the cases with $\Delta_D = 3D$ in section 5.2. Another thing to notice is that for cases SS & SF with laminar inflow conditions, their $\overline{u}_{\text{Disk}}^{8D}$ are comparable to the counterparts with $\Delta_D = 3D$, and this can be observed by the relatively steep slopes between $6 \leq x/D \leq 8$ in Figure 5.20.

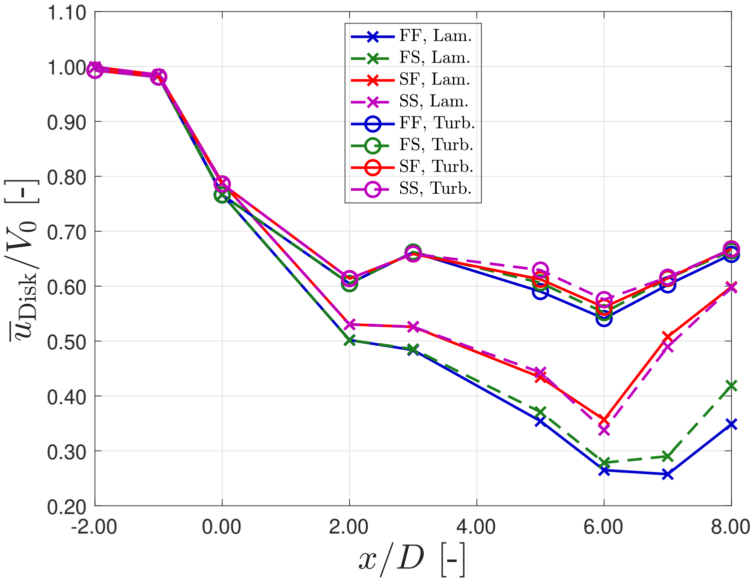

Figure 5.20: $\overline{u}_{\text{Disk}}$ along x-direction for cases of dual rotors with $\Delta_D = 5D$ and different surging-fixed combinations under laminar or turbulent (TI = 5.3%) inflow conditions.

5.3.2 Summarizing Rotor Performances

Power coefficients for upstream and downstream rotors under laminar inflow conditions are summarized in Figure 5.23, while the counterparts for the cases with turbulent inflow conditions are in Figure 5.24. Behaviours of $< C_P^{\text{up}} >$, and $< C_P^{\text{down}} >$ are very similar when

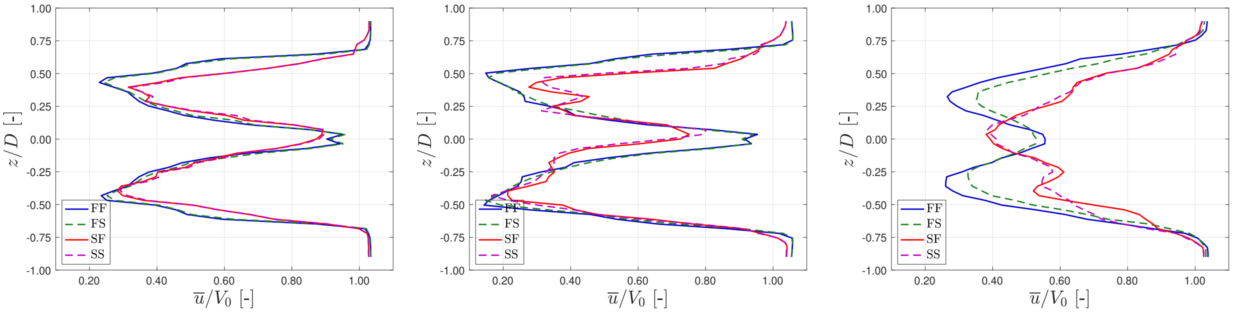

(a) $x/D = 5.0$ (b) $x/D = 6.0$ (c) $x/D = 8.0$

Figure 5.21: Profile of $\overline{u}$ at different x/D for cases of dual rotors with $\Delta_D = 5D$ and different surging-fixed combinations under laminar inflow conditions.

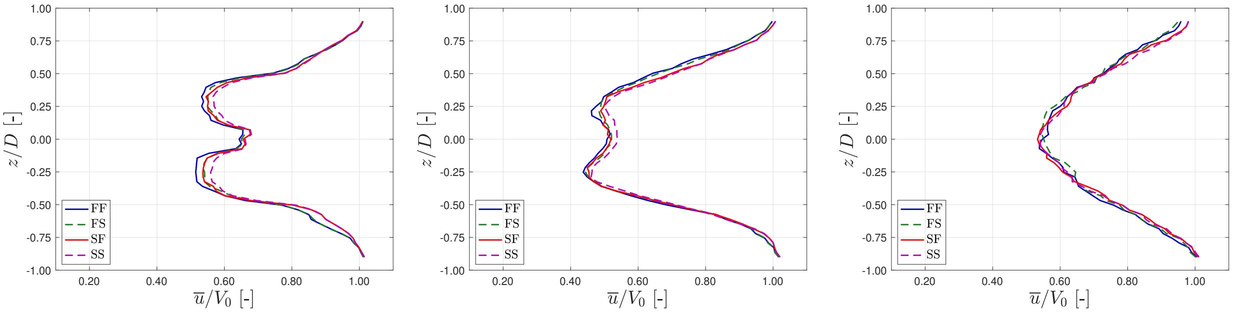

(a) $x/D = 5.0$ (b) $x/D = 6.0$ (c) $x/D = 8.0$

Figure 5.22: Profile of $\overline{u}$ at different x/D for cases of dual rotors with $\Delta_D = 5D$ and different surging-fixed combinations under turbulent (TI $= 5.3\%$) inflow conditions.

comparing to cases with $\Delta_D = 3D$ in section 5.2. The biggest difference is the discrepancy between cases FF & SF and cases FS & SS are more pronounced, since that the wakes had longer distances to develop. However, it is worth noting that again, with the realistic inflow TI, $\overline{C}_P^{\text{down}}$ for case SF (case **54**) out-performed case FF (case **52**) for about 1.5%, and cases SS (cases **55-58**) also out-performed case FS (case **53**) for about 1%; these demonstrate once more how a surging upstream rotor may improve the power performance of the downstream rotor, but this time with $\Delta_D = 5D$.

Figure 5.25 shows the power spectrum of the power coefficients for the downstream rotor ($S_{C_P^{\text{down}}}(f)$) of the eight cases. Their characteristics are very similar with the cases with $\Delta_D = 3D$ (Figure 5.8). The only significant difference is the the peak at $f = \omega_S/2\pi$ for case SF with turbulent inflow did not exist, suggesting with Δ_D becomes larger, the influences of PLSB from upstream rotor become smaller; which is as one may have expected since ambient turbulence would dilute the PLSB as it is convected (Figure 5.27).

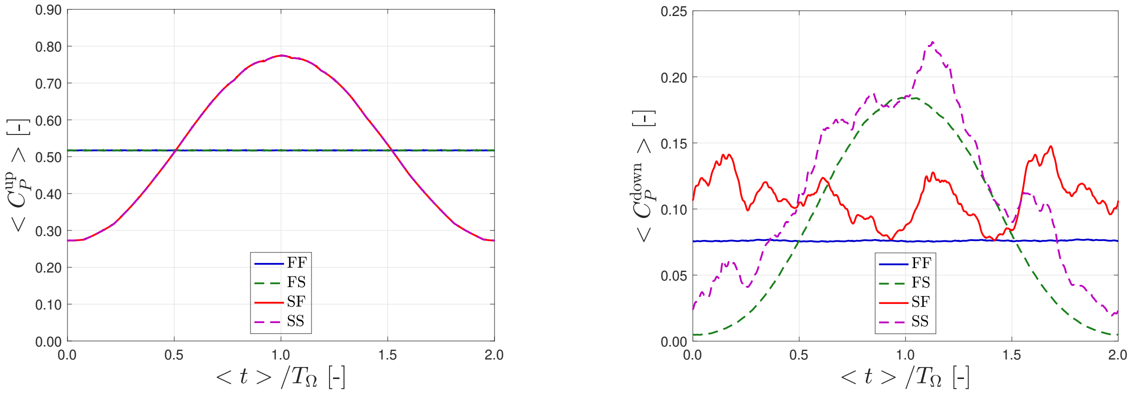

(a) $< C_P^{\text{up}} >$

(b) $< C_P^{\text{down}} >$

Figure 5.23: $< C_P^{\text{up}} >$ and $< C_P^{\text{down}} >$ for cases of dual rotors with $\Delta_D = 5D$ and different surging-fixed combinations under laminar inflow conditions.

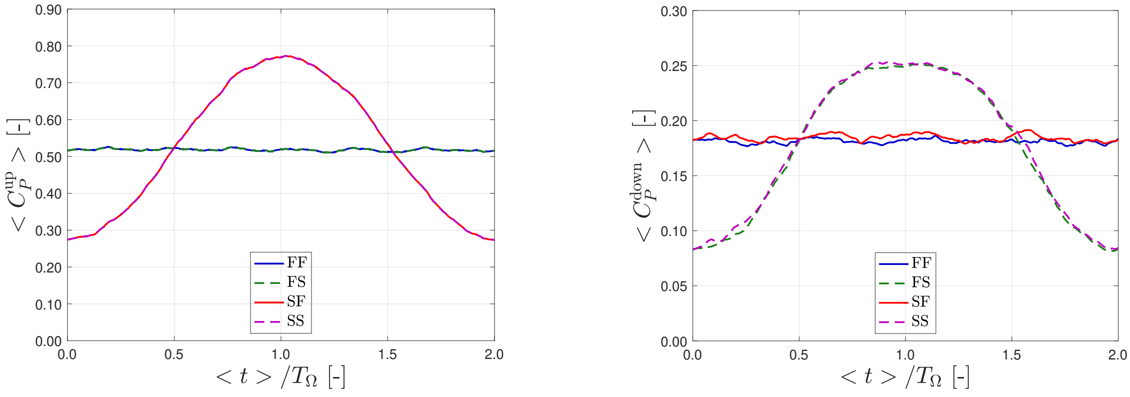

(a) $< C_P^{\text{up}} >$

(b) $< C_P^{\text{down}} >$

Figure 5.24: $< C_P^{\text{up}} >$ and $< C_P^{\text{down}} >$ for cases of dual rotors with $\Delta_D = 5D$ and different surging-fixed combinations under turbulent (TI $= 5.3\%$) inflow conditions.

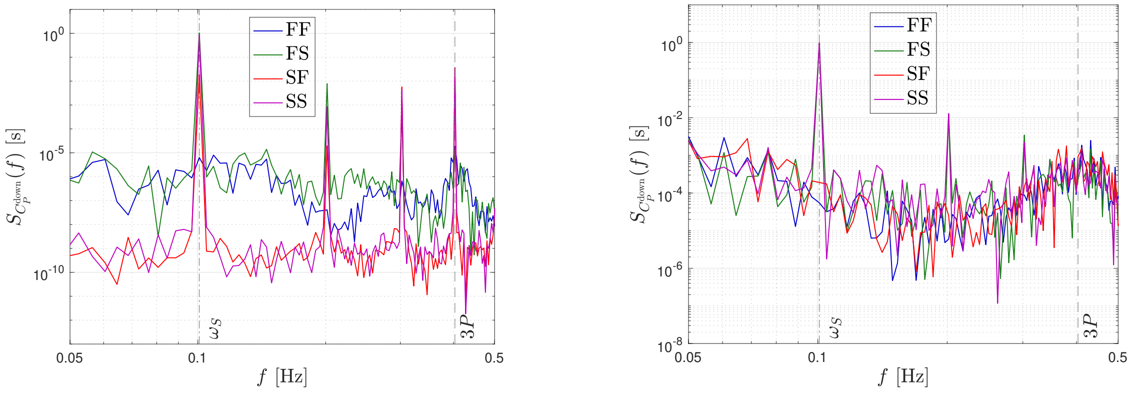

(a) Laminar cases

(b) Turbulent cases (TI $= 5.3\%$)

Figure 5.25: Power spectrum of C_P^{down} ($S_{C_P^{\text{down}}}(f)$) for cases of dual rotors with $\Delta_D = 5D$ and different surging-fixed combinations under laminar or turbulent inflow conditions.

5.3.3 Summarizing the Field Data

Since that the fields data in this sections share comparable features to the cases in section 5.2 with $\Delta_D = 3D$, only several selected fields are presented in this section. The selected fields are u, $< u >_{0\pi}$, $\overline{u}$, <TKE>$_{0\pi}$, & $< \omega_y >_{0\pi}$, and they are presented in Figure 5.26 to 5.30. Since the fields share very similar features with the cases in the previous section (section 5.2), descriptions and explanations for the fields can also be applied here. The shared features includes that the wake systems are more influenced by the upstream rotor's surging conformations, the wake systems are more influenced by the inflow turbulence, the flow is highly repeatable for the laminar cases, and surging of the upstream rotor seems to make the wake systems more repeatable for the laminar cases. While the most significant difference appears at cases SF & SS under turbulent inflow conditions, where the downstream rotor now is operating at regions where surging effects from the upstream rotor are much less pronounced judging by the facts that the periodic structures (PLSB) appeared in phase-locked averaged fields are much more smeared out at $x/D = 5$ compare to $x/D = 3$.

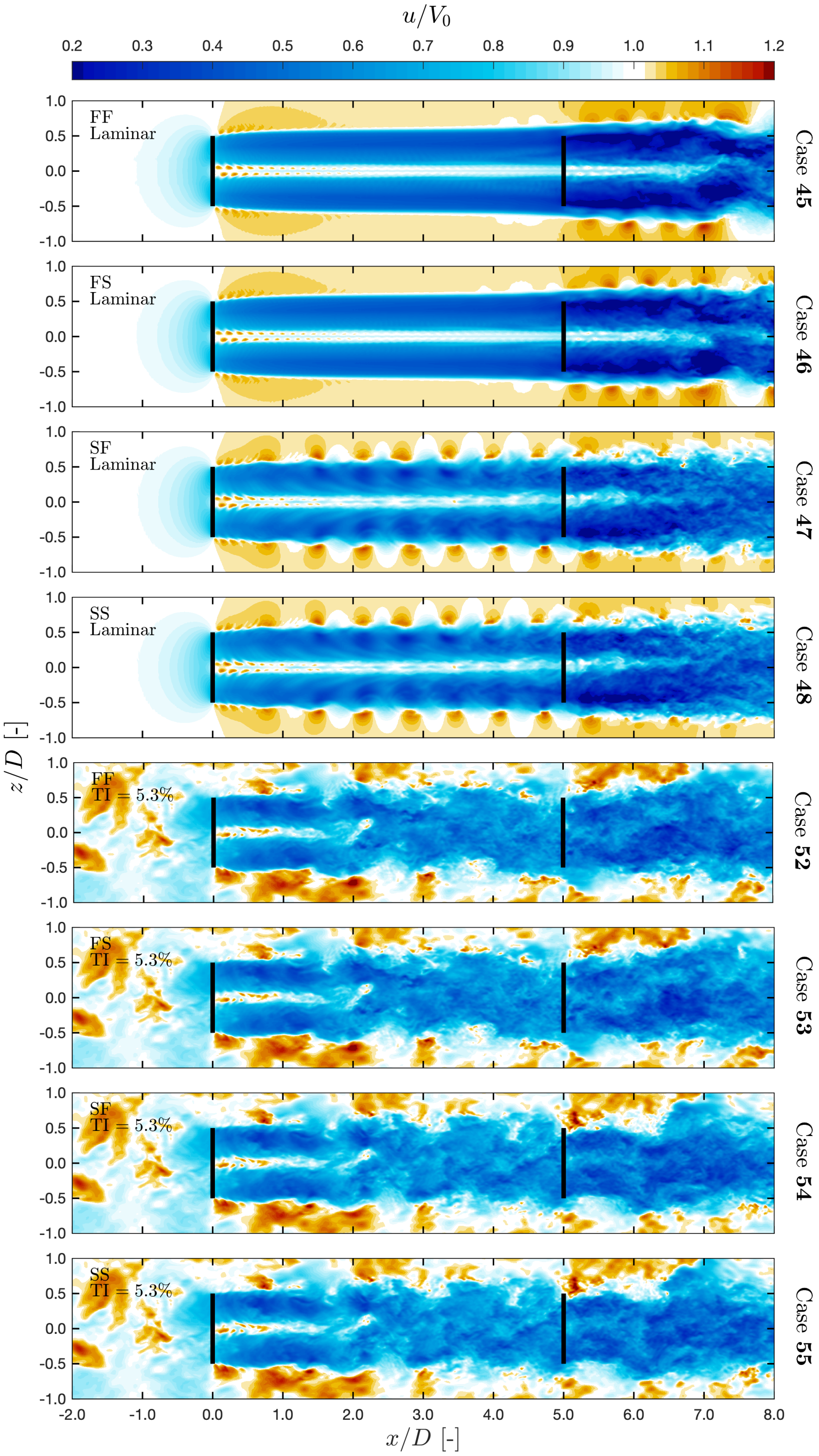

Figure 5.26: Fields of instantaneous streamwise velocity u for dual rotors with $\Delta_D = 5D$ and different surging-fixed combinations.

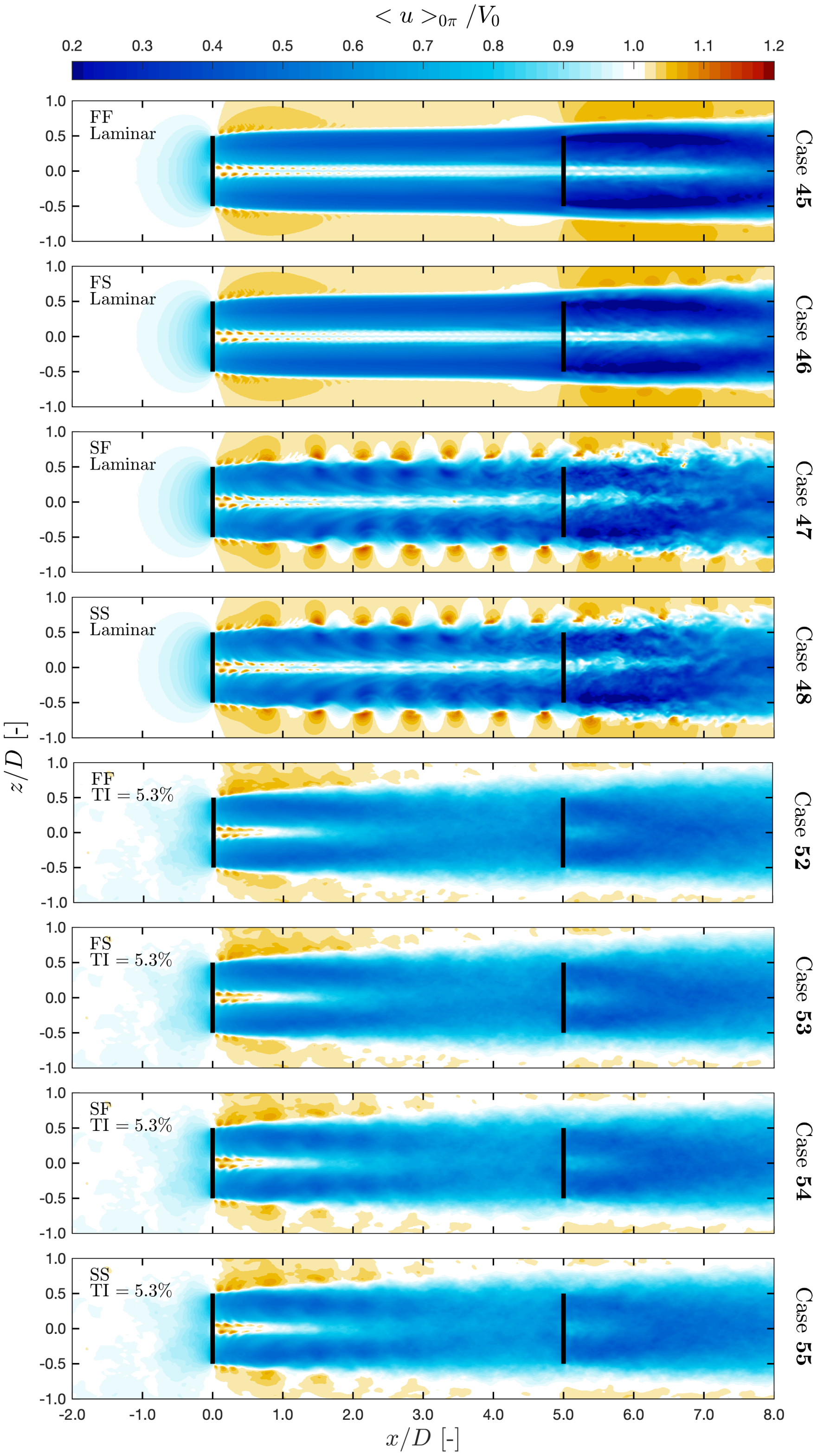

Figure 5.27: Fields of phase-locked averaged streamwise velocity $< u >_{0\pi}$ for dual rotors with $\Delta_D = 5D$ and different surging-fixed combinations.

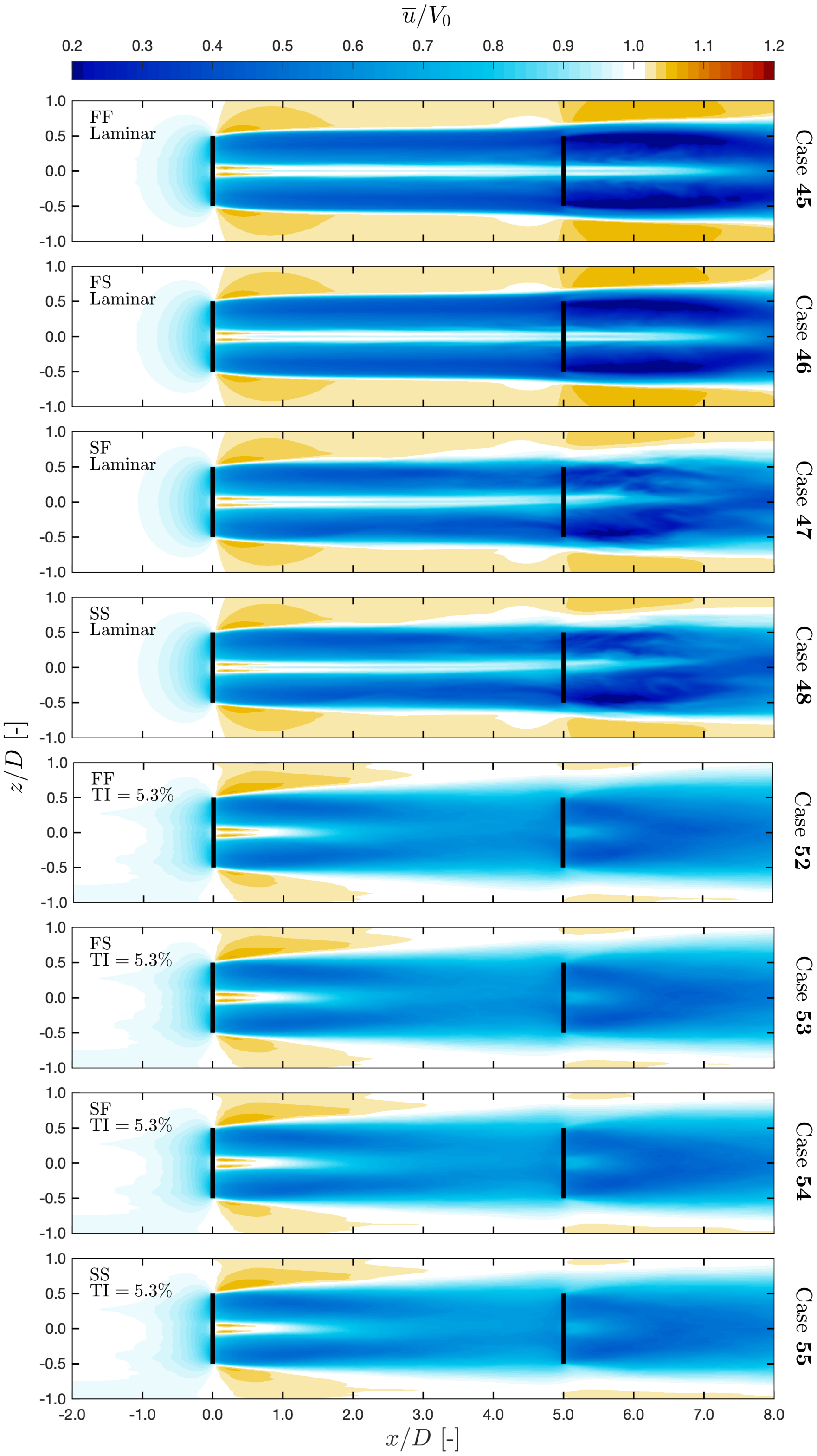

Figure 5.28: Fields of time-averaged streamwise velocity $\overline{u}$ for dual rotors with $\Delta_D = 5D$ and different surging-fixed combinations.

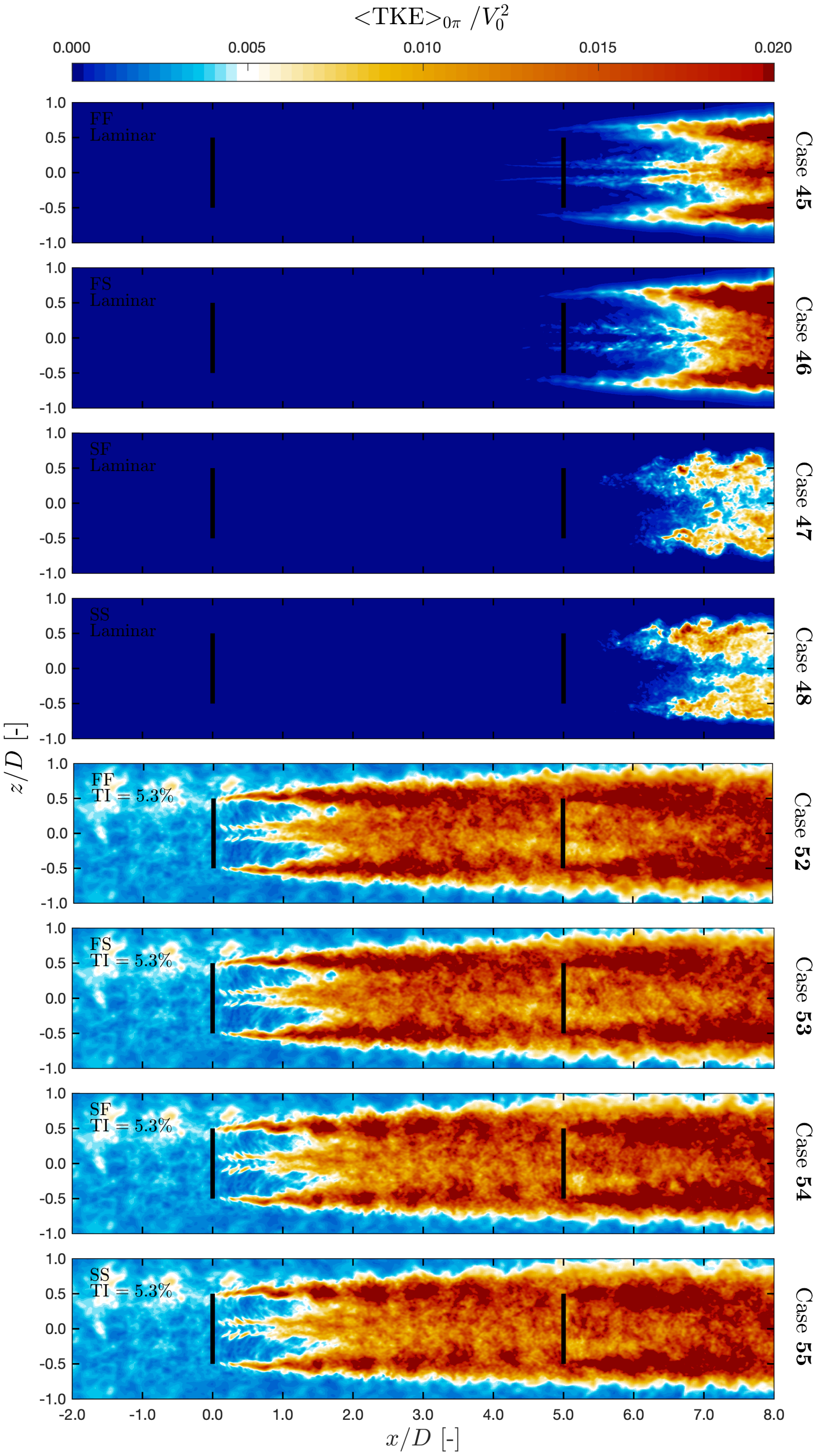

Figure 5.29: Fields of phase-locked averaged turbulent kinetic energy $<\text{TKE}>_{0\pi}$ for dual rotors with $\Delta_D = 5D$ and different surging-fixed combinations.

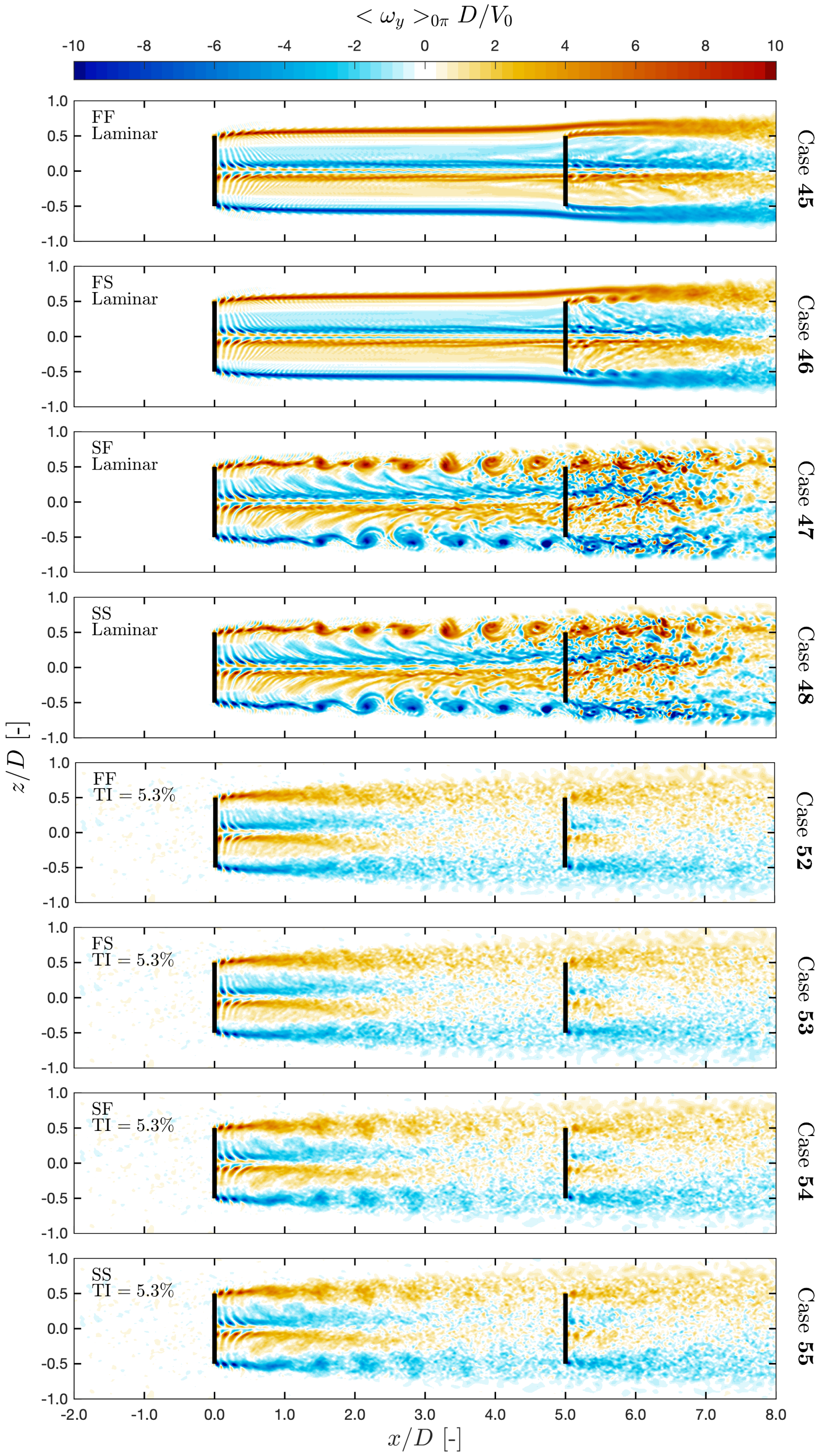

Figure 5.30: Fields of phase-locked averaged y-component vorticity $< \omega_y >_{0\pi}$ for dual rotors with $\Delta_D = 5D$ and different surging-fixed combinations.

5.4 Different $\Delta_{\phi_{S_0}}^{\text{up}}$ with Δ_D being $3D$ Under Laminar and Turbulent Inflow Conditions

This section studies the effects of phase differences between the two surging motions $\Delta_{\phi_{S_0}}$ on the wake interactions between two surging rotors with $\Delta_D = 3D$ both under laminar and turbulent inflow conditions. Eight cases are analyzed, which are cases **34-37** and **41-44** in Table 5.1, and correspond to groups D.5 and D.6 in section 5.1. Effects of $\Delta_{\phi_{S_0}}$ are studied by running cases with $\phi_{S_0}^{\text{up}}$ being 0.0π, 0.5π, 1.0π, or 1.5π while keeping $\phi_{S_0}^{\text{down}} = 0.0\pi$ in Equation 5.1 and 5.2. That is, cases with $\Delta_{\phi_{S_0}}$ being 0.0π, 0.5π, 1.0π, or 1.5π are studied here (Equation 5.3).

For future offshore floating wind farms, whether $\Delta_{\phi_{S_0}}$ would significantly affect the wake interactions between FOWTs is critically important when it comes to wind farm layout design, since it might affect the mode of wake interactions and thus the AEP & LCoE. However, to the best knowledge of the author, research about studying effects of $\Delta_{\phi_{S_0}}$ on wake interactions is still missing. It should be noted that $\Delta_{\phi_{S_0}}$ is not solely depends on Δ_D, but also depends on how fast the waves propagate. In short, $\Delta_{\phi_{S_0}}$ at least depends on Δ_D, hydrodynamics, and sea bed topography; correctly predict $\Delta_{\phi_{S_0}}$ requires high fidelity hydrodynamic simulations and reliable sea states data, which are beyond the scope of this thesis. For this thesis, only whether $\Delta_{\phi_{S_0}}$ will affect wake interactions is focused.

5.4.1 Summarizing Wake Characteristics

Characteristics of $\overline{u}_{\text{Disk}}$ for the eight cases are in Figure 5.31, while $\overline{u}$ profiles of the four laminar cases & the other four turbulent cases are in Figure 5.32 & 5.33. It can be seen that the $\overline{u}_{\text{Disk}}$ are less sensitive to $\Delta_{\phi_{S_0}}$ than the surging-fixed combinations (section 5.2) for both laminar and turbulent inflow conditions. However, if looking at $\overline{u}$ profiles of the laminar cases, the four cases still have significant differences.

5.4.2 Summarizing Rotor Performances

Power coefficients for the upstream and downstream rotors under laminar inflow conditions are summarized in Figure 5.34, while the counterparts for the cases with turbulent inflow conditions are in Figure 5.35. It can be seen that the curves of $< C_P^{\text{up}} >$ clearly presented the effects of $\Delta_{\phi_{S_0}}$ ($\phi_{S_0}^{\text{up}}$) for both laminar and turbulent cases. Notice that here $< t > /T_\Omega^{\text{up}} = 0$ corresponds to $\phi_S^{\text{up}} = 0\pi$ and $< t > /T_\Omega^{\text{up}} = 2$ corresponds to $\phi_S^{\text{up}} = 2\pi$. As for curves of $< C_P^{\text{down}} >$, differences can be found for the laminar cases, while the turbulent cases almost share a same curve. However, considering $\overline{C_P}^{\text{down}}$ for the four turbulent cases in Table 5.1, case $\Delta_{\phi_{S_0}} = 0.5\pi$ (case **42**) has a significant lower value compare to the other cases with different $\Delta_{\phi_{S_0}}$. The lower value are considered relate to the different interactions between the PLSB (periodic low speed bubble) generated by upstream rotor and surging motions of the downstream rotor, which will be visited in later subsections.

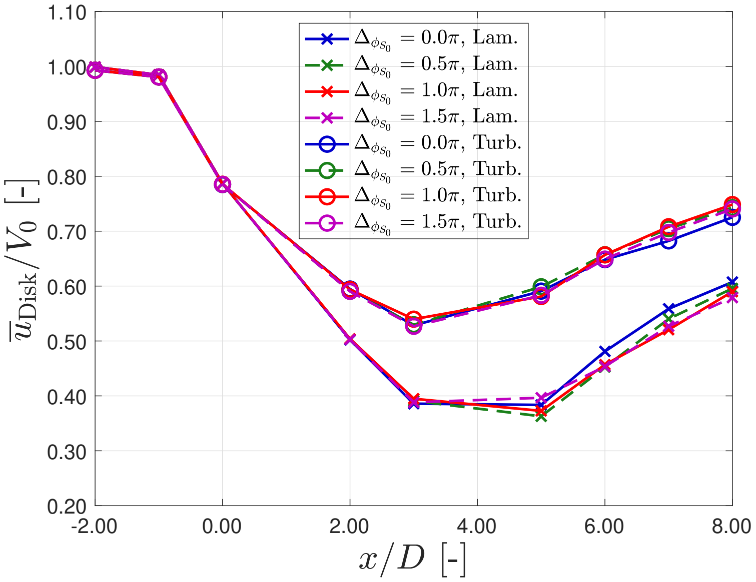

Figure 5.31: $\overline{u}_{\text{Disk}}$ along x-direction for cases of dual rotors with $\Delta_D = 3D$ and different $\Delta_{\phi_{S_0}}$ under laminar and turbulent (TI = 5.3%) inflow conditions.

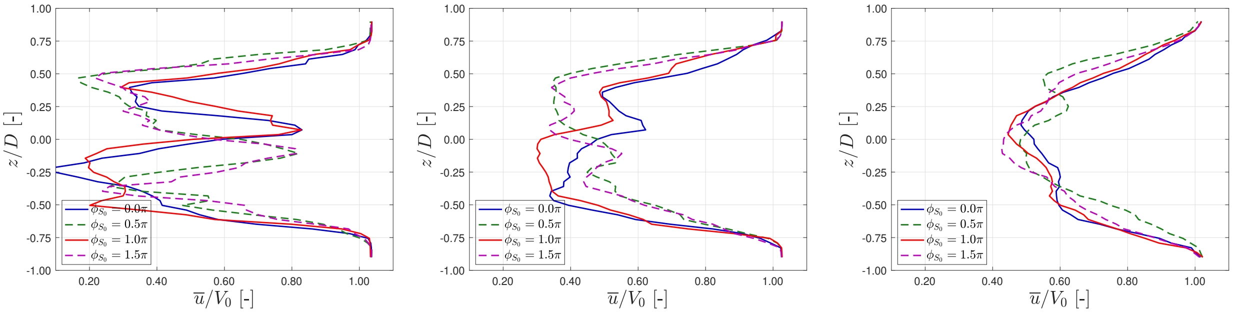

(a) $x/D = 5.0$ (b) $x/D = 6.0$ (c) $x/D = 8.0$

Figure 5.32: Profile of $\overline{u}$ at different x/D for cases of dual rotors with $\Delta_D = 3D$ and different $\Delta_{\phi_{S_0}}$ under laminar inflow conditions.

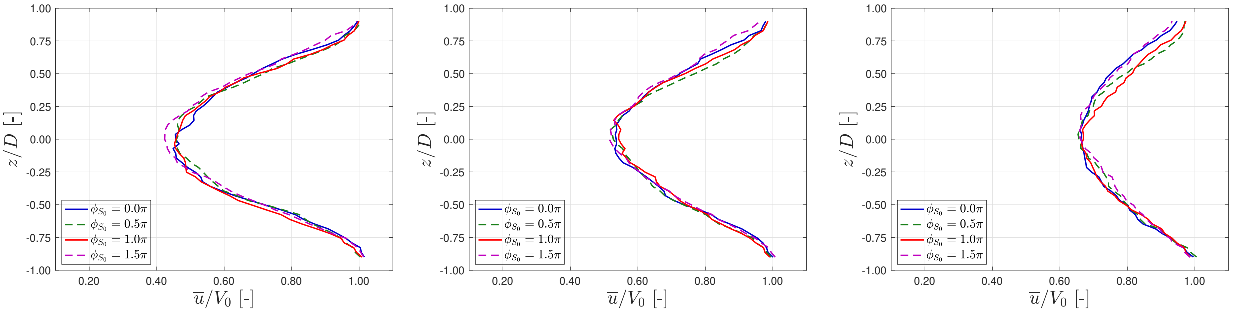

(a) $x/D = 5.0$ (b) $x/D = 6.0$ (c) $x/D = 8.0$

Figure 5.33: Profile of $\overline{u}$ at different x/D for cases of dual rotors with $\Delta_D = 3D$, different $\Delta_{\phi_{S_0}}$, and inflow TI being 5.3%.

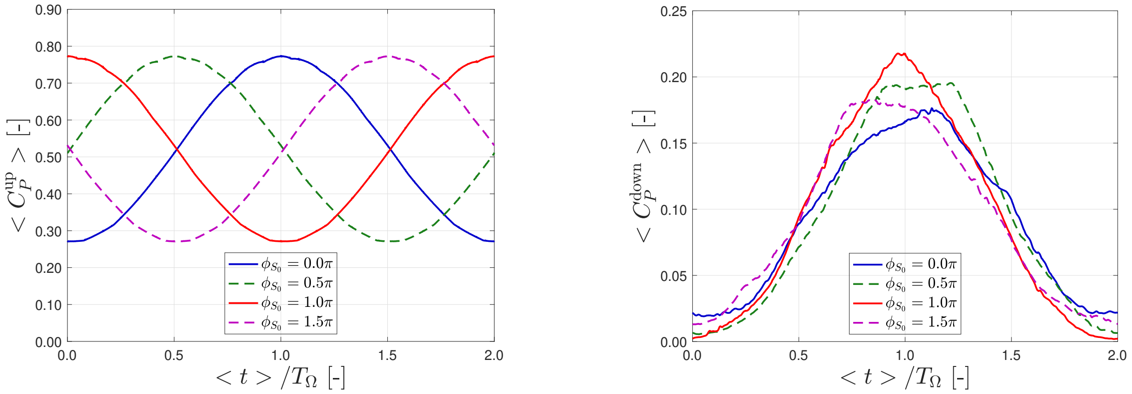

(a) $< C_P^{\mathrm{up}} >$ (b) $< C_P^{\mathrm{down}} >$

Figure 5.34: $< C_P^{\mathrm{up}} >$ and $< C_P^{\mathrm{down}} >$ for cases of dual rotors with $\Delta_D = 3D$ and different $\Delta_{\phi_{S_0}}$ under laminar inflow conditions.

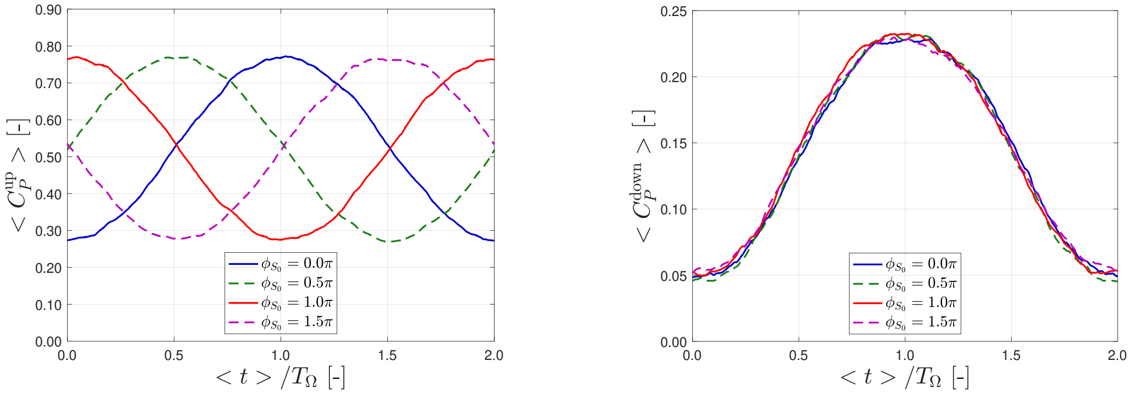

(a) $< C_P^{\mathrm{up}} >$ (b) $< C_P^{\mathrm{down}} >$

Figure 5.35: $< C_P^{\mathrm{up}} >$ and $< C_P^{\mathrm{down}} >$ for cases of dual rotors with $\Delta_D = 3D$, different $\Delta_{\phi_{S_0}}$, and inflow TI being 5.3%.

5.4.3 Summarizing the Field Data

Once again, fields data in this sections share comparable features to the cases in section 5.2. Thus, only fields of u, $< u >_{0\pi}$, and $< \omega_y >_{0\pi}$ are presented in this section. Additionally, fields of $< u >_{1\pi}$ and $< \omega_y >_{1\pi}$ are presented to aid the analysis about the effects of $\Delta_{\phi_{S_0}}$.

For the instantaneous fields u of the four turbulent cases, the effects of different $\phi_{S_0}^{\text{up}}$ are almost not perceivable before the downstream rotor; however, judging by the facts of the u fields, $\phi_{S_0}^{\text{up}}$ do affect the instantaneous wake structures after the downstream rotor.

As for the phase-locked fields $< u >_{0\pi}$, $< u >_{1\pi}$, $< \omega_y >_{0\pi}$, and $< \omega_y >_{1\pi}$, positions of the periodic structures (PLSB) reflect the effects of $\phi_{S_0}^{\text{up}}$ ($\Delta_{\phi_{S_0}}$). Note that phase-locked averaging here are based on ϕ_S^{down}, and ϕ_S^{up} for the cases in the same figure may be different with different $\Delta_{\phi_{S_0}}$. As $\phi_{S_0}^{\text{down}} = 1.0\pi$, the downstream rotor for all eight cases move against the freestream with largest magnitude of $V_{\text{WT}}^{\text{down}}$ within a surging cycle, which will give a bigger apparent inflow velocity $V_{0,\text{app}}^{\text{down}}$ (see Equation 2.27). And one can see that the downstream rotor of case **42** ($\Delta\phi_{S_0} = 0.5\pi$, turbulent inflow conditions) locates in the middle of two pairs of PLSB in the fields of $< \omega_y >_{1\pi}$, indicating it experiences the largest $V_{0,\text{app}}^{\text{down}}$ for the four turbulent cases, and this suggests it experiences the most severe stalling, thus resulting in a relatively lower $\overline{C}_P^{\text{down}}$. This will be confirmed in section 5.7 with plots of $< \alpha^{\text{down}} >$. Note that PLSB, which is namely flow structures with lower speed, are aligned with the higher magnitudes of $< \omega_y >$.

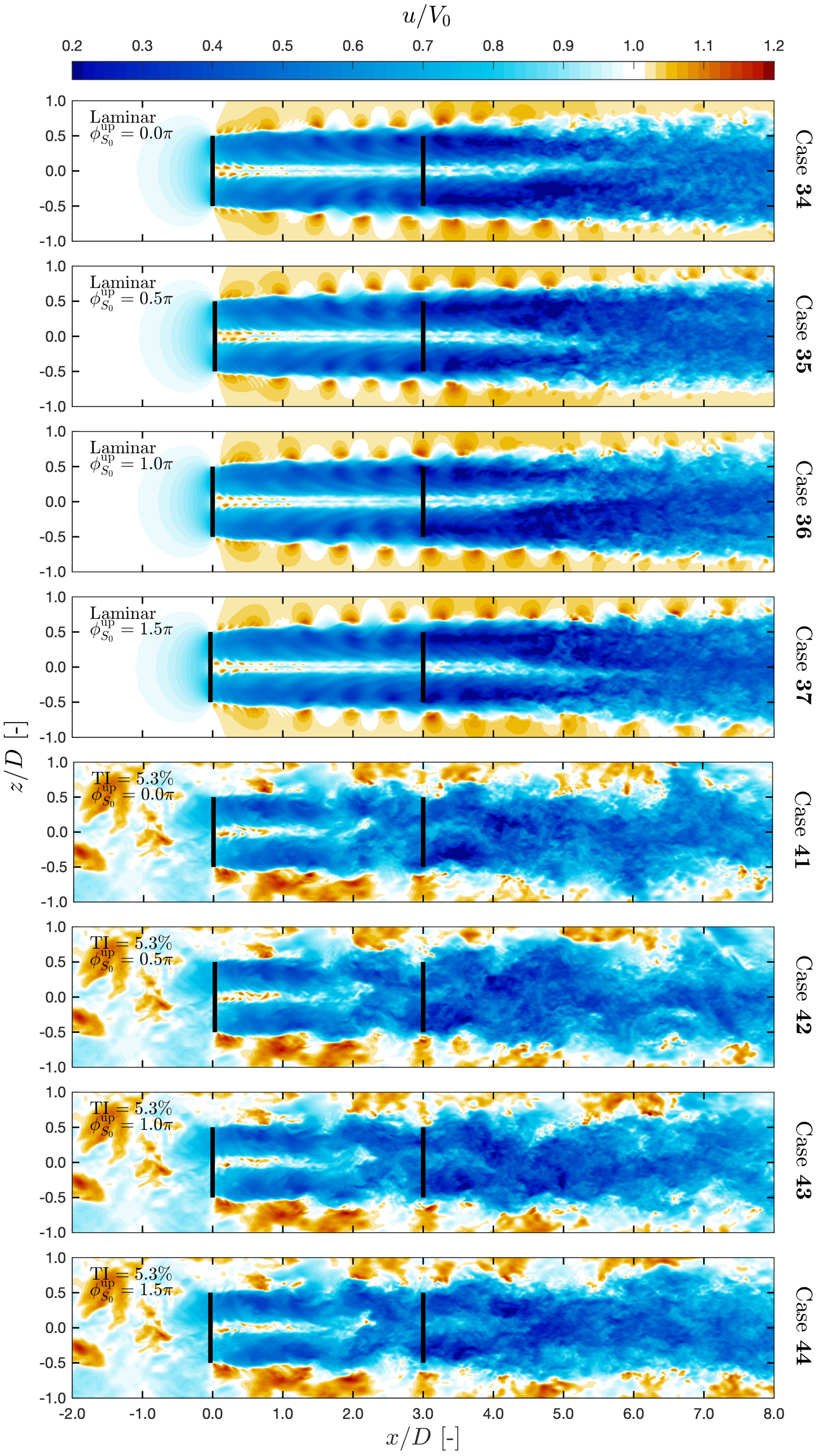

Figure 5.36: Fields of instantaneous streamwise velocity u for dual rotors with $\Delta_D = 3D$ and different $\Delta_{\phi_{S_0}}$.

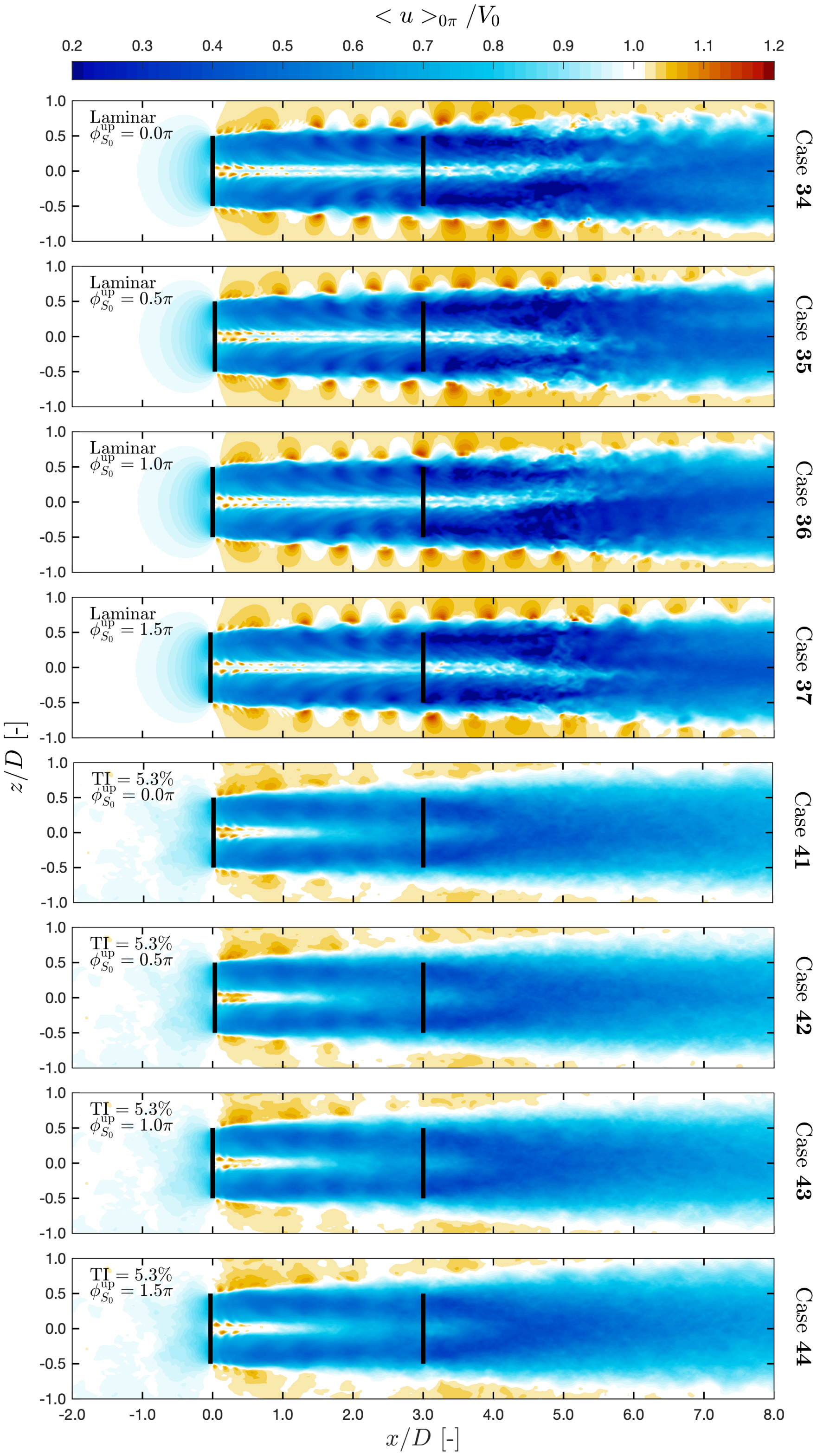

Figure 5.37: Fields of phase-locked averaged streamwise velocity $< u >_{0\pi}$ for dual rotors with $\Delta_D = 3D$ and different $\Delta_{\phi_{S_0}}$.

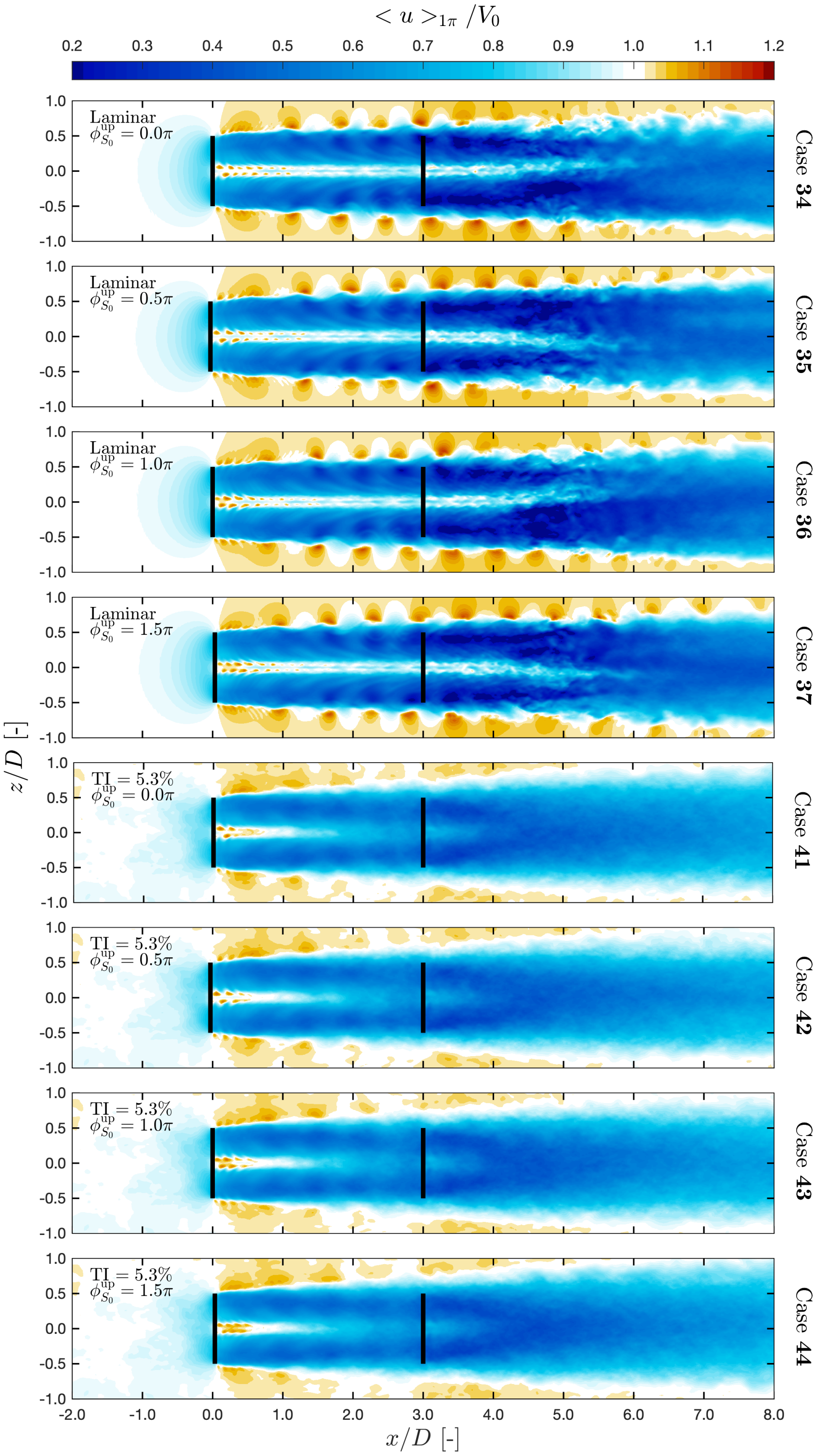

Figure 5.38: Fields of phase-locked averaged streamwise velocity $< u >_{1\pi}$ for dual rotors with $\Delta_D = 3D$ and different $\Delta_{\phi_{S_0}}$.

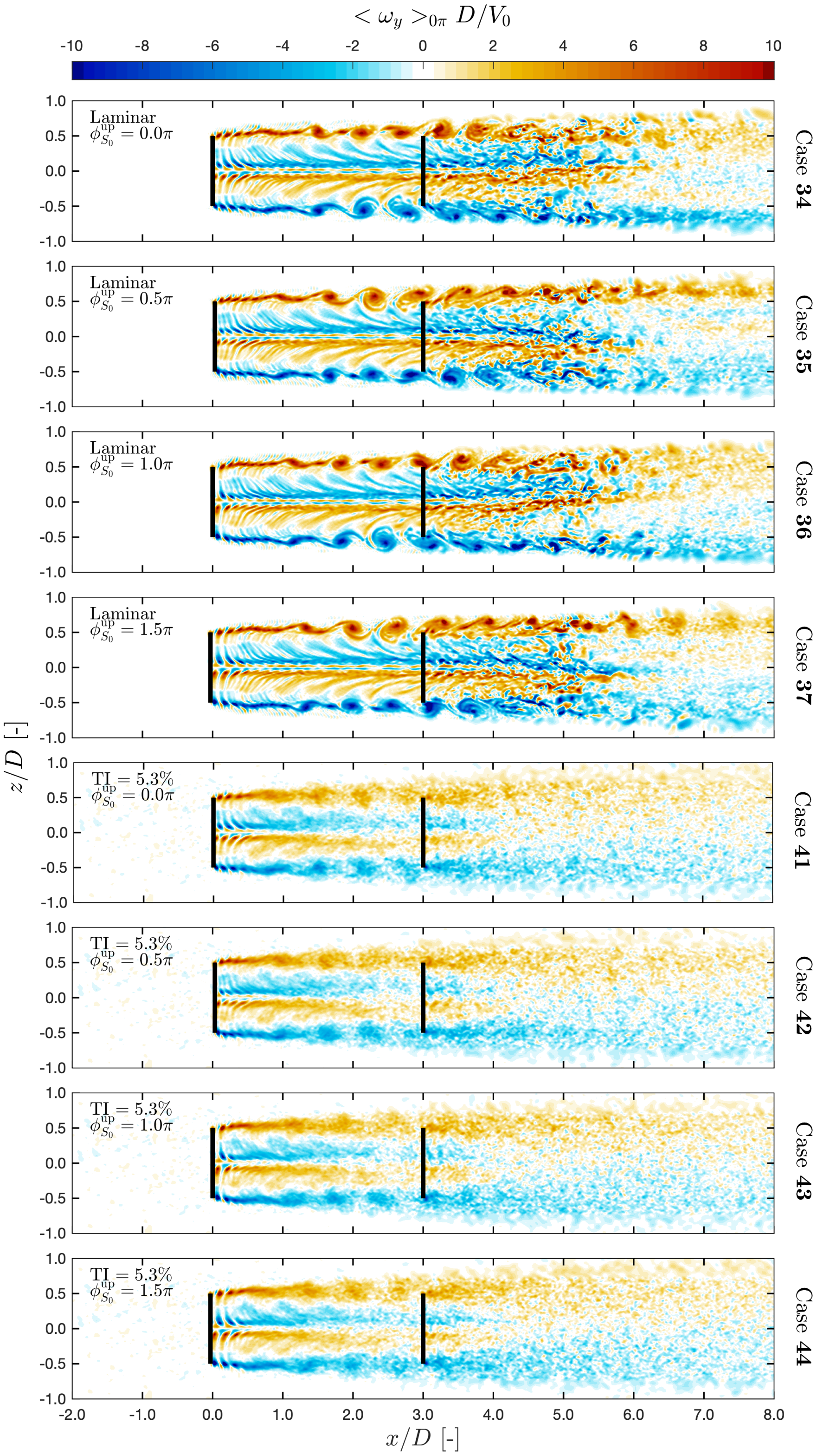

Figure 5.39: Fields of phase-locked averaged y-component vorticity $< \omega_y >_{0\pi}$ for dual rotors with $\Delta_D = 3D$ and different $\Delta_{\phi_{S_0}}$.

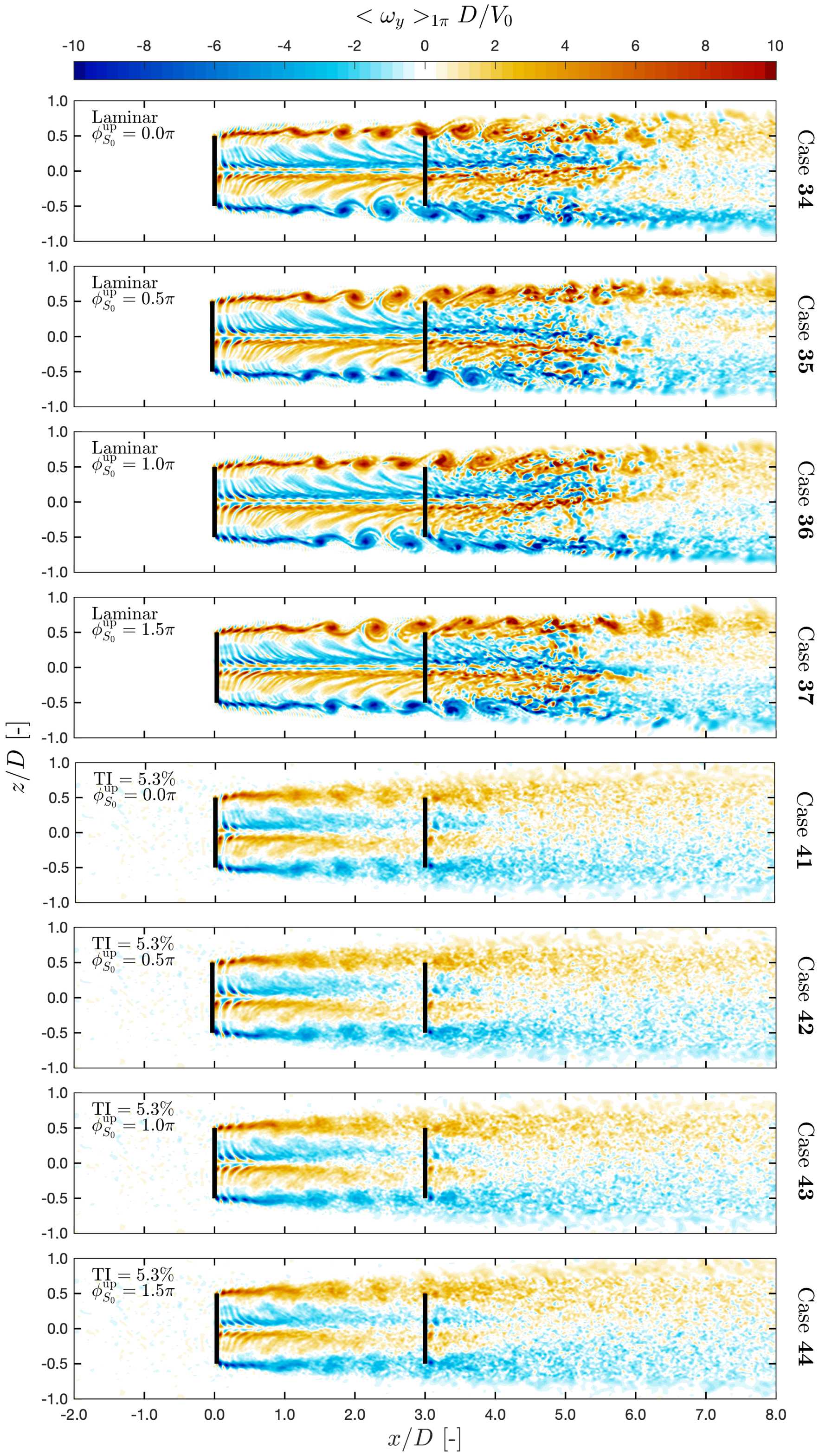

Figure 5.40: Fields of phase-locked averaged y-component vorticity $<\omega_y>_{1\pi}$ for dual rotors with $\Delta_D = 3D$ and different $\Delta_{\phi_{S_0}}$.

5.5 Different $\Delta^{\text{up}}_{\phi_{S_0}}$ with Δ_D being $5D$ Under Laminar and Turbulent Inflow Conditions

This section studies the effects of surging phase angle differences $\Delta_{\phi_{S_0}}$ on the wake interactions between two surging rotors with $\Delta_D = 5D$ both under laminar and turbulent inflow conditions. Generally, the results in this section are quite similar with the cases having different $\Delta_{\phi_{S_0}}$ with $\Delta_D = 3D$ in the previous section (section 5.4). Again, eight cases are presented, which are cases **48-51** and **55-58** in Table 5.1, and correspond to groups D.7 and D.8 in section 5.1.

5.5.1 Summarizing Wake Characteristics

Characteristics of $\overline{u}_{\text{Disk}}$ for the eight cases are in Figure 5.41, while $\overline{u}$ profiles of the four laminar cases & the other four turbulent cases are in Figure 5.42 & 5.43. Similar in section 5.4, $\overline{u}_{\text{Disk}}$ are less sensitive to $\Delta_{\phi_{S_0}}$ than the surging-fixed combinations (section 5.3). However, the four laminar cases share a more similar profiles, suggesting the information of $\phi^{\text{up}}_{S_0}$ carried by wake diminishes as traveling downstream.

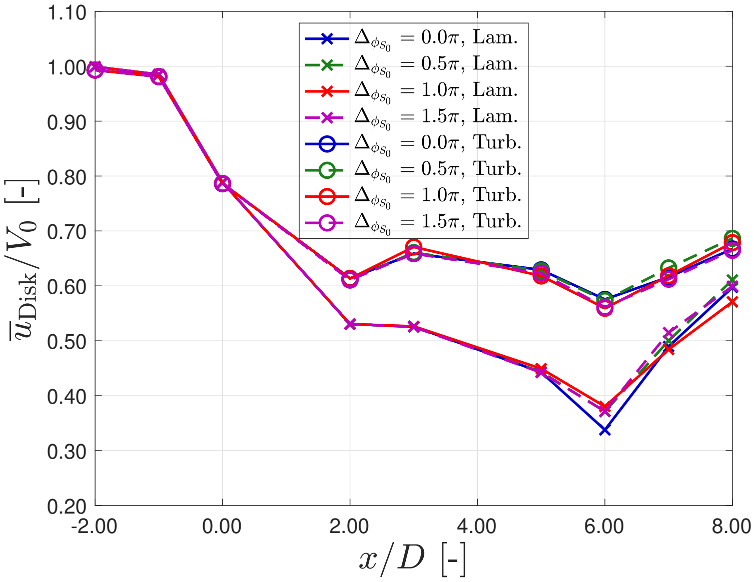

Figure 5.41: $\overline{u}_{\text{Disk}}$ along x-direction for cases of dual rotors with $\Delta_D = 5D$ and different $\Delta_{\phi_{S_0}}$ under laminar and turbulent (TI = 5.3%) inflow conditions.

5.5.2 Summarizing Rotor Performances

Power coefficients for upstream and downstream rotors under laminar inflow conditions are summarized in Figure 5.44, while the counterparts for the cases with turbulent inflow conditions are in Figure 5.45. Clearly that the performances of the upstream rotor ($< C^{\text{up}}_P >$)

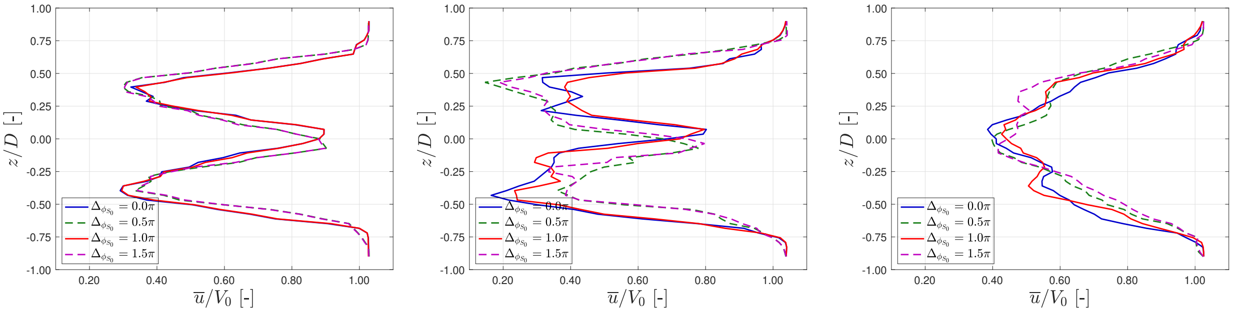

(a) $x/D = 5.0$ (b) $x/D = 6.0$ (c) $x/D = 8.0$

Figure 5.42: Profile of $\overline{u}$ at different x/D for cases of dual rotors with $\Delta_D = 5D$ and different $\Delta_{\phi_{S_0}}$ under laminar inflow conditions.

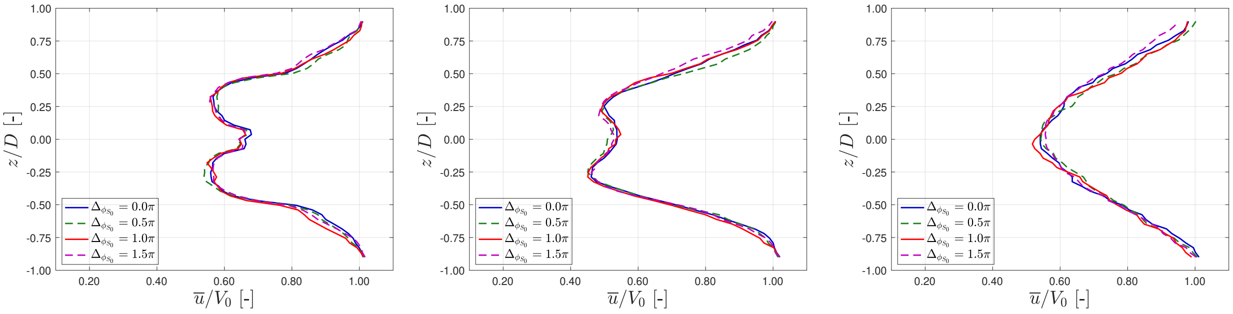

(a) $x/D = 5.0$ (b) $x/D = 6.0$ (c) $x/D = 8.0$

Figure 5.43: Profile of $\overline{u}$ at different x/D for cases of dual rotors with $\Delta_D = 5D$, different $\Delta_{\phi_{S_0}}$, and inflow TI being 5.3%.

with $\Delta_D = 5D$ are seemed to be identical with cases with $\Delta_D = 3D$, again showing that effects of blockage are weak. As for curves of $< C_P^{\text{down}} >$, they behave just as the cases with $\Delta_D = 3D$ as well, laminar cases has similar curves with noticeable differences, while turbulent cases share a very similar curve. As shifting the focus to $\overline{C}_P^{\text{down}}$ (or $\overline{G}_{C_P}^{\text{down}}$) for the four turbulent cases, it can be seen that this time with $\Delta_D = 5D$, the effects of $\Delta_{\phi_{S_0}}$ on $\overline{C}_P$ are less pronounced, this is as expected since the strengths of PLSB gradually diminished as being convected downstream with turbulent inflow conditions.

5.5.3 Summarizing the Field Data

Fields data for the cases in this section are very similar with the cases in section 5.3, and the analysis about effects of $\Delta_{\phi_{S_0}}$ on the field data has also been carried out in section 5.4. Thus, only fields of u, $< u >_{0\pi}$, and $< \omega_y >_{0\pi}$ are presented in this section.

For the instantaneous fields u of the four turbulent cases, the effects of different $\phi_{S_0}^{\text{up}}$ are now perceivable before the downstream rotor, where cases with $\Delta_D = 3D$ are hardly to identified the differences. This shows that the effects of different $\phi_{S_0}^{\text{up}}$ on instantaneous fields of wake require sufficient development to be relevant.

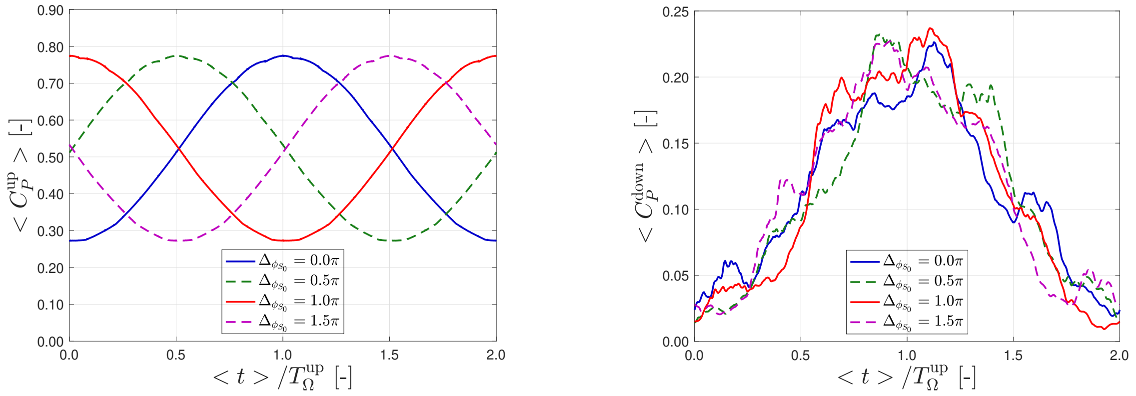

(a) $< C_P^{\text{up}} >$ (b) $< C_P^{\text{down}} >$

Figure 5.44: $< C_P^{\text{up}} >$ and $< C_P^{\text{down}} >$ for cases of dual rotors with $\Delta_D = 5D$ and different $\Delta_{\phi_{S_0}}$ under laminar inflow conditions.

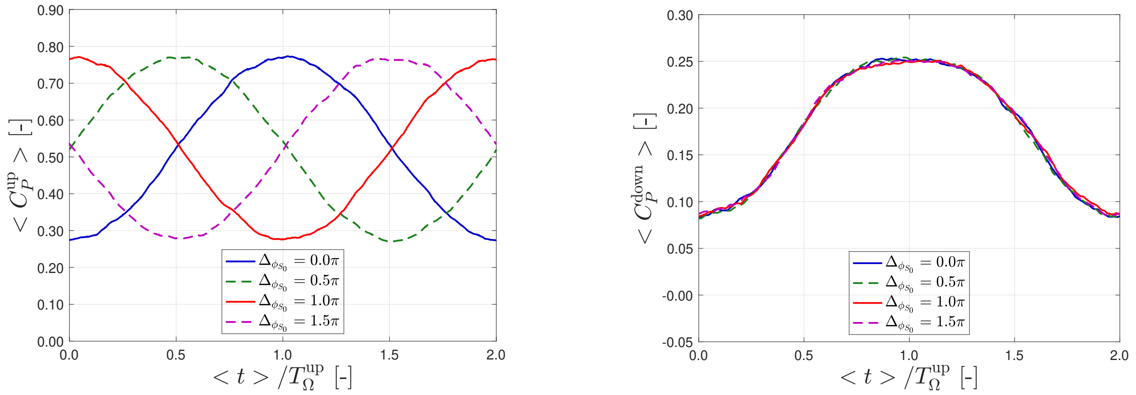

(a) $< C_P^{\text{up}} >$ (b) $< C_P^{\text{down}} >$

Figure 5.45: $< C_P^{\text{up}} >$ and $< C_P^{\text{down}} >$ for cases of dual rotors with $\Delta_D = 5D$ and different $\Delta_{\phi_{S_0}}$ under laminar inflow conditions.

As for the phase-locked averaged fields $< u >_{0\pi}$ and $< \omega_y >_{0\pi}$, effects of $\phi^{\text{up}}_{S_0}$ ($\Delta_{\phi_{S_0}}$) are presented on the positions of the periodic structures (PLSB). Different form the cases with $\Delta_D = 3D$, PLSB are much more diminished as they reach the downstream rotor ($x/D = 5$) for the four turbulent cases; this might be the reason why $\overline{C_P}^{\text{down}}$ for the turbulent cases with $\Delta_D = 5D$ are less different than the cases with $\Delta_D = 3D$.

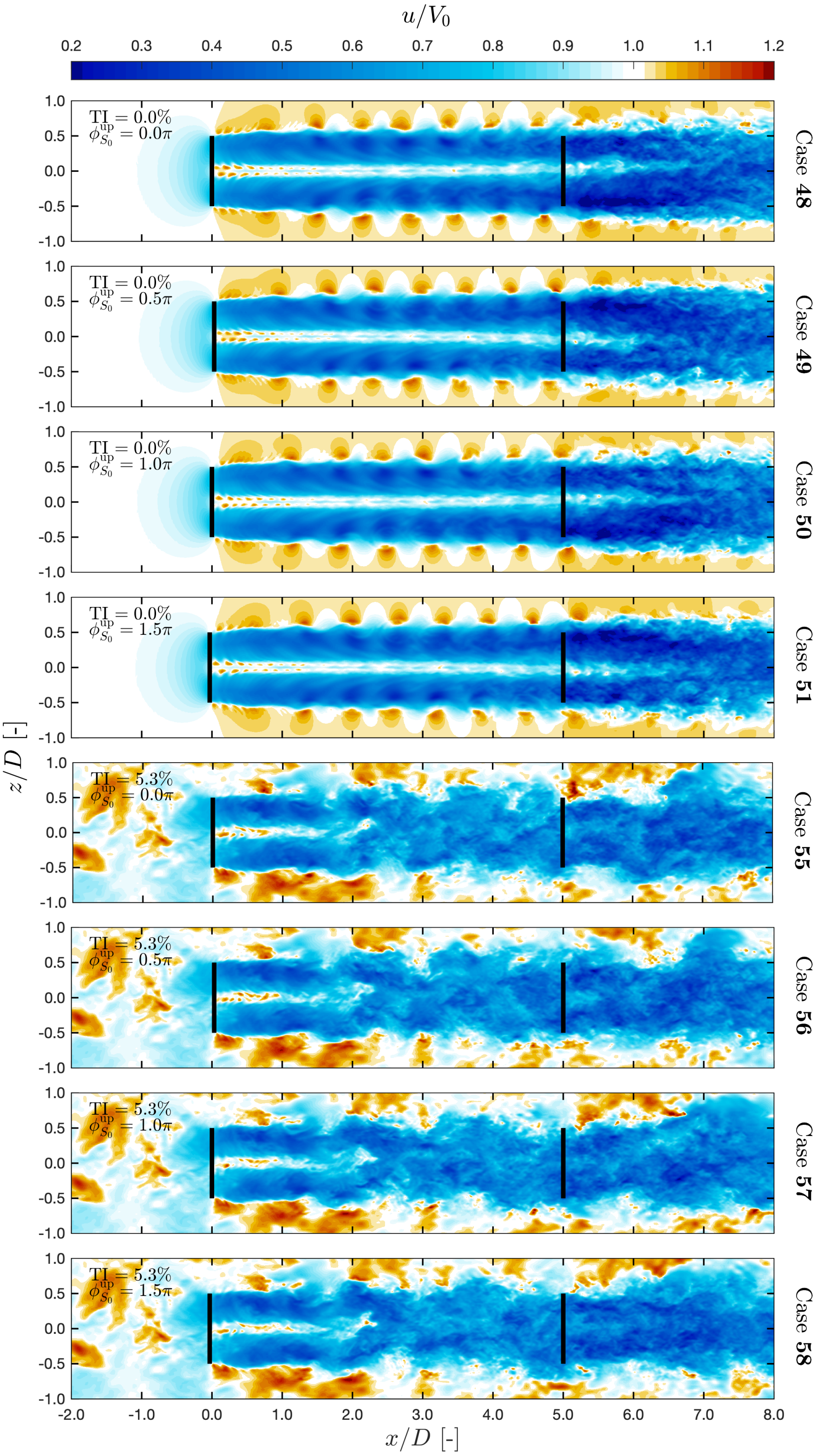

Figure 5.46: Fields of instantaneous streamwise velocity u for dual rotors with $\Delta_D = 5D$ and different $\Delta_{\phi_{S_0}}$.

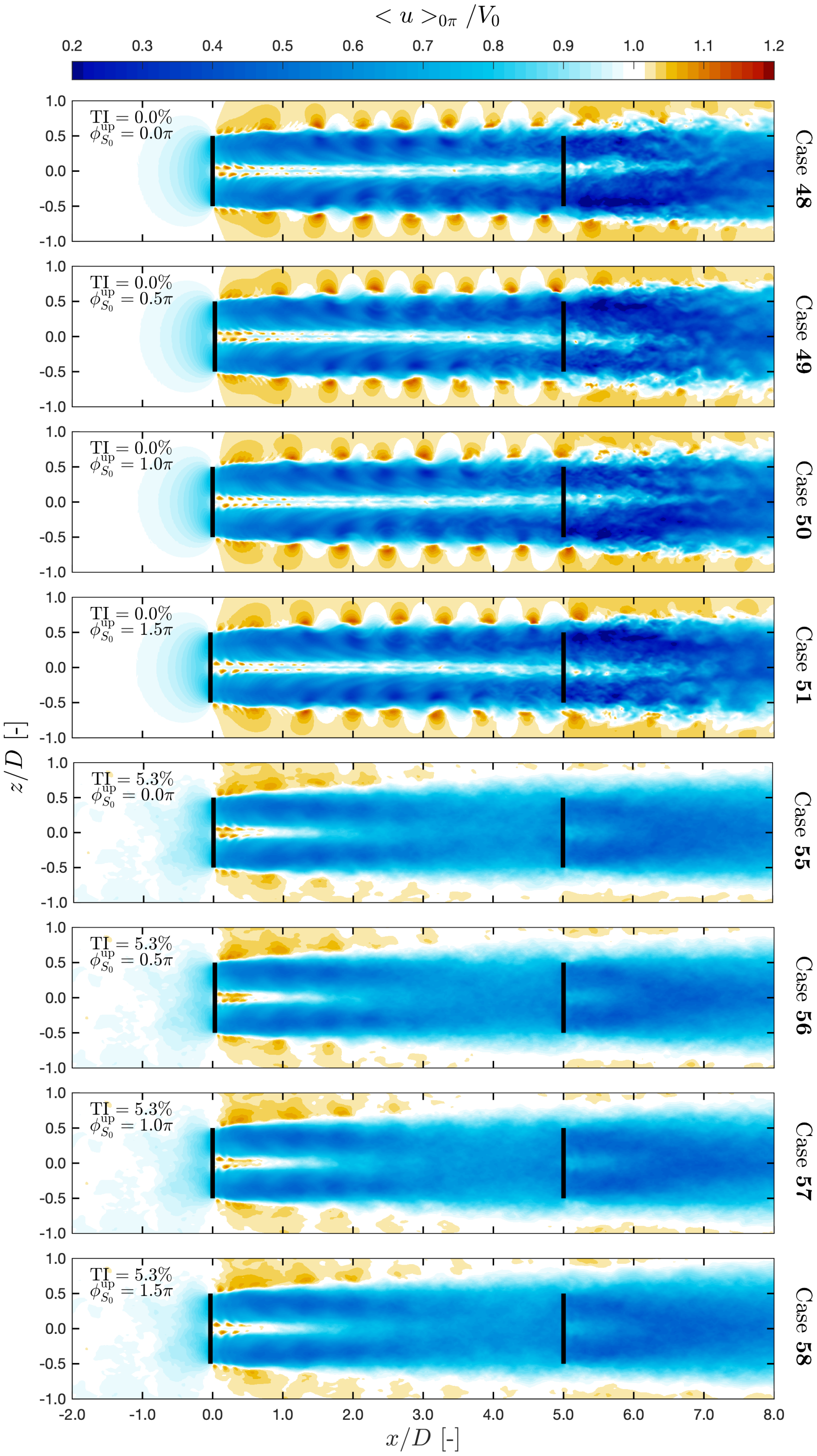

Figure 5.47: Fields of phase-locked averaged streamwise velocity $< u >_{0\pi}$ for dual rotors with $\Delta_D = 5D$ and different $\Delta_{\phi_{S_0}}$.

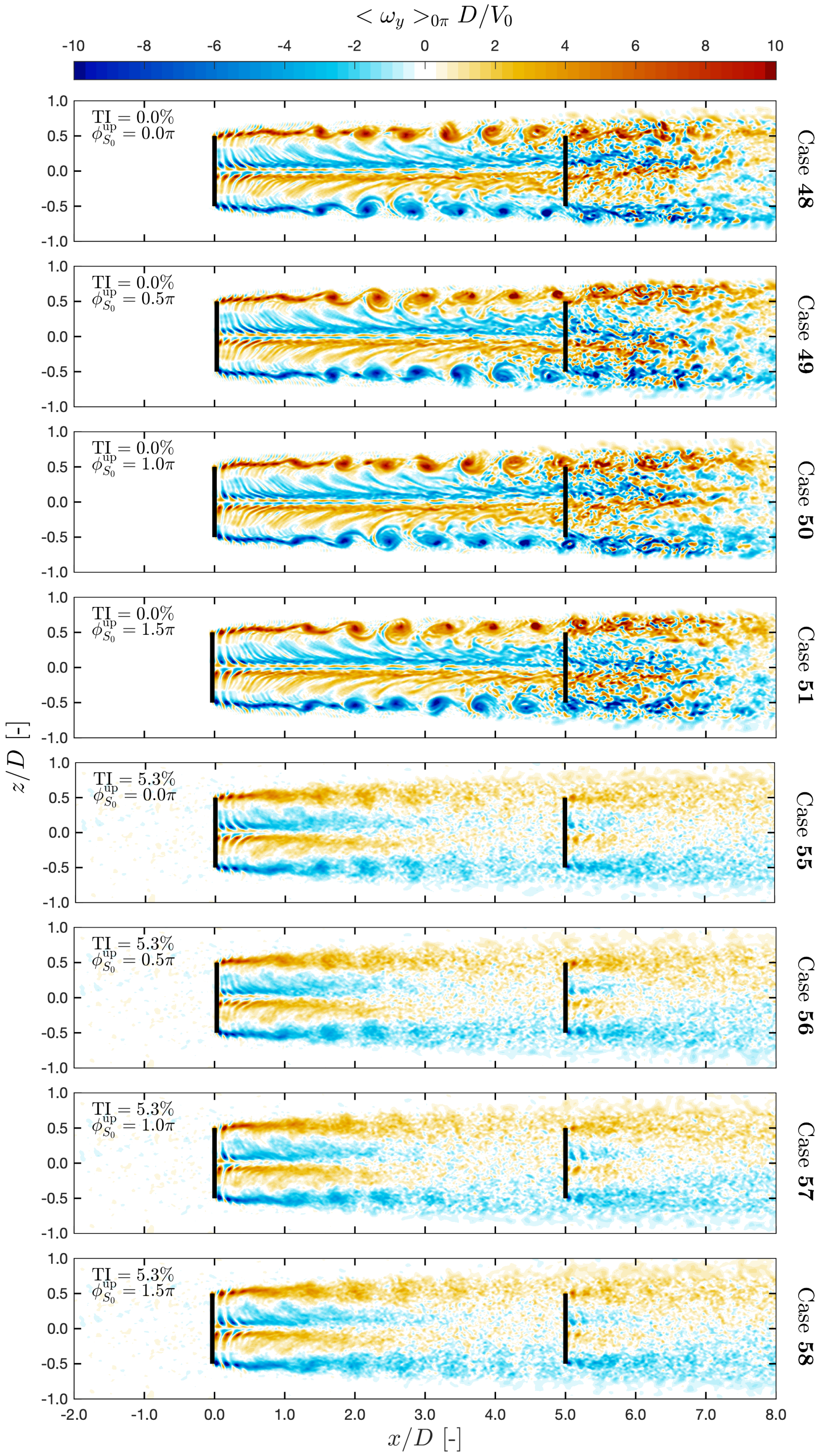

Figure 5.48: Fields of phase-locked averaged y-component vorticity $< \omega_y >_{0\pi}$ for dual rotors with $\Delta_D = 5D$ and different $\Delta_{\phi_{S_0}}$.

5.6 Different Inflow Turbulence Intensities with Dual Rotors being Fixed or Surging

This section investigates the influences of different inflow turbulence intensities on the wake interactions between two fixed or surging FOWT rotors, and both $\Delta_D = 3D$ & $5D$ are looked into. The interested cases in this section belong to groups D.9, D.10, D.11, & D.12 in section 5.1 (16 cases in total). Since most features about wake interactions between two rotors in tandem have been well explored in the previous parts of this chapter, this section will only cover the aspects where inflow turbulence intensities play significant roles, including profiles of $\overline{u}_{\text{Disk}}$, rotor performances of the downstream rotor, and fields of $\overline{u}$, TKE, & $< \omega_y >_{0\pi}$.

5.6.1 Summarizing Wake Characteristics

Figure 5.49 & 5.50 display the profiles of $\overline{u}_{\text{Disk}}$ for the case with $\Delta_D = 3D$ & $\Delta_D = 5D$; each figure presented the cases with fixed or surging rotors with different inflow TI. In general, the trends are comparable with the cases having only a single rotor (Figure 4.2). First, with laminar inflow conditions, recovery rates of $\overline{u}_{\text{Disk}}$ for surging cases are much larger than the fixed cases, and this may relate to the flows of the surging cases go in and come out the wake around the PLSB, which facilitate wake recovery by mixing. Second, for the cases with turbulent inflow conditions, profiles of $\overline{u}_{\text{Disk}}$ for cases with higher inflow TI seems to be larger for the surging cases than the fixed cases, and the differences between cases with TI $= 2.7\%$ & 5.3% once again seem to become smaller as going downstream. Moreover, profiles of $\overline{u}_{\text{Disk}}$ for fixed and surging cases with same TI become much more similar when comparing to the laminar cases, with the surging cases having slightly larger $\overline{u}_{\text{Disk}}$ for most of the cases.

5.6.2 Summarizing Rotor Performances

Figure 5.51 & 5.52 present $< C_P >$ of the upstream and downstream rotor for the fixed & surging cases with $\Delta_D = 3D$ under different inflow TI, while Figure 5.53 & 5.54 present the counterparts for cases with $\Delta_D = 5D$. These figures clearly showed that $< C_P^{\text{up}} >$ is insensitive to Δ_D and inflow TI, which agrees with the previous results. While for the downstream rotors, generally cases with higher inflow TI have larger $< C_P^{\text{down}} >$, both for the fixed or surging cases, suggesting the effective inflow velocities seen by the downstream rotors get bigger with larger inflow TI. Moreover, the extents of stalling of the downstream rotors differ with different inflow TI, especially for the surging cases with $\Delta_D = 5D$ (Figure 5.54b), and this should relate to the different effective inflow velocities seen by the downstream rotor (different $\mathbb{V}^{\text{down}}$). It should be noted that Ω^{down} for all cases in this chapter is prescribed with same value ($\Omega^{\text{down}} = 0.84$ rad/s).

As for $\overline{C}_P^{\text{down}}$ (listed in Table 5.1), again it is clear that larger TI gives bigger $\overline{C}_P^{\text{down}}$ for all fixed & surging cases with $\Delta_D = 3D$ & $\Delta_D = 5D$. However, as comparing $\overline{C}_P^{\text{down}}$ between a pair of fixed and surging cases with same inflow TI & same Δ_D, it is hard to tell whether fixed or surging case gives bigger $\overline{C}_P^{\text{down}}$. The reasons behind this may be complicated,

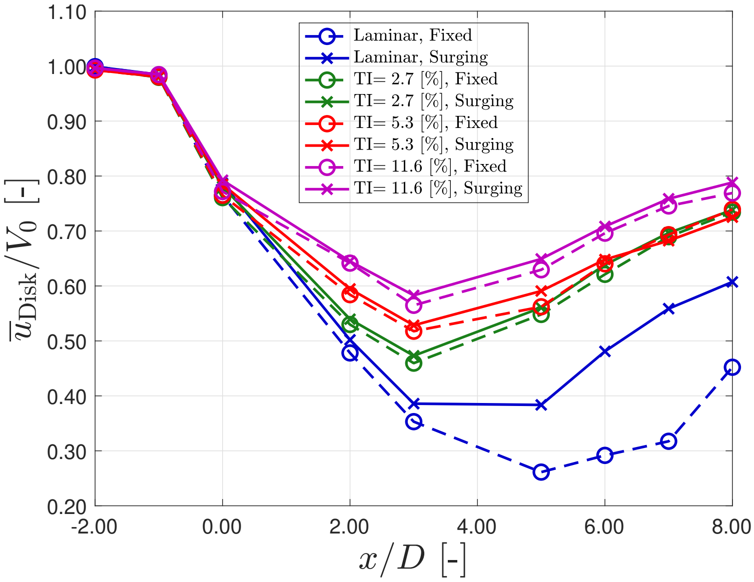

Figure 5.49: $\overline{u}_{\text{Disk}}$ along x-direction for cases of dual fixed or surging rotors with $\Delta_D = 3D$ and different inflow TI.

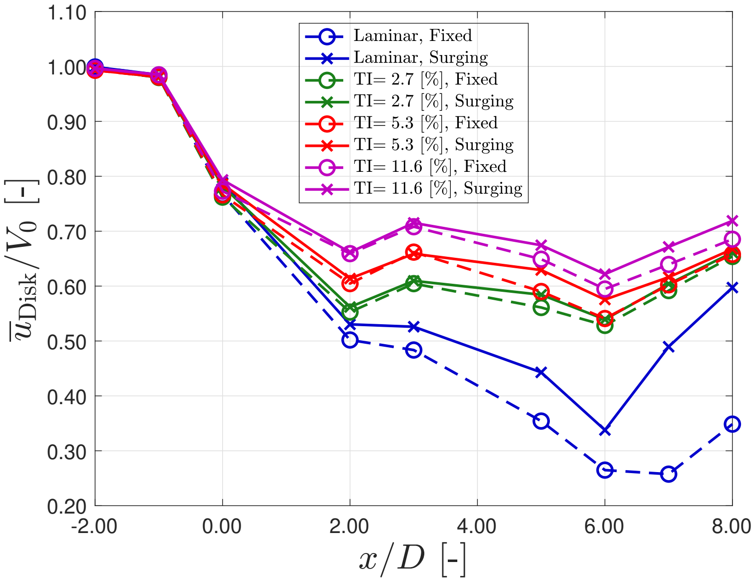

Figure 5.50: $\overline{u}_{\text{Disk}}$ along x-direction for cases of dual fixed or surging rotors with $\Delta_D = 5D$ and different inflow TI.

but the main reason is suggested to be the effects of stalling; this also pointed out a proper controller may be needed to adjust the operational conditions (such as Ω^{down}) when studying wake interactions between wind turbines rotors.

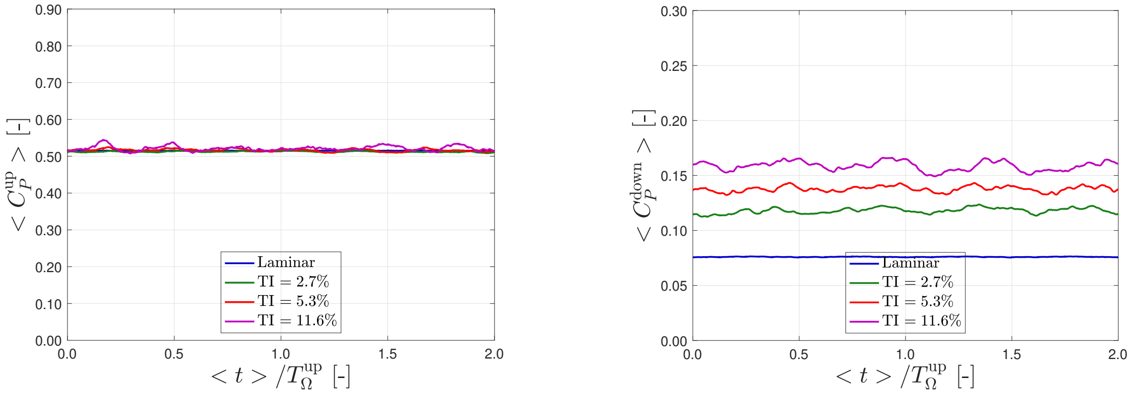

(a) $< C_P^{\mathrm{up}} >$ (b) $< C_P^{\mathrm{down}} >$

Figure 5.51: $< C_P^{\mathrm{up}} >$ and $< C_P^{\mathrm{down}} >$ for cases of dual fixed rotors with $\Delta_D = 3D$ and different inflow TI.

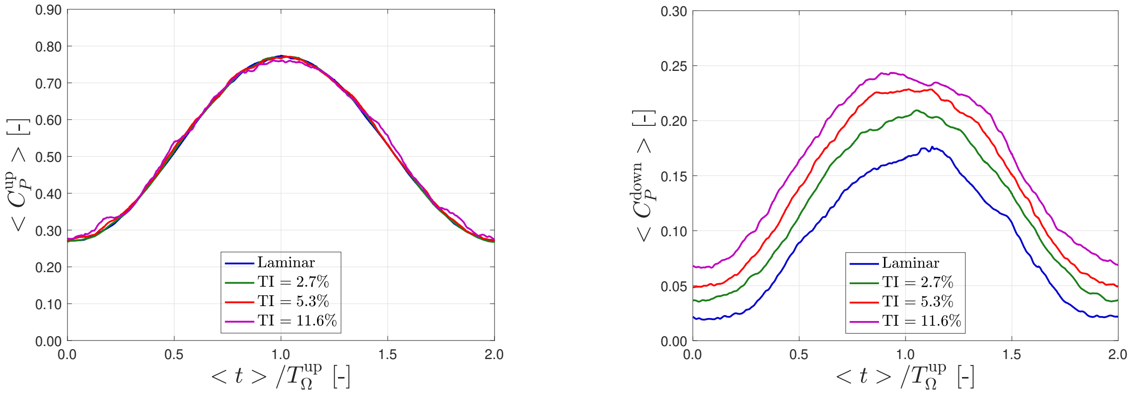

(a) $< C_P^{\mathrm{up}} >$ (b) $< C_P^{\mathrm{down}} >$

Figure 5.52: $< C_P^{\mathrm{up}} >$ and $< C_P^{\mathrm{down}} >$ for cases of dual surging rotors with $\Delta_D = 3D$ and different inflow TI.

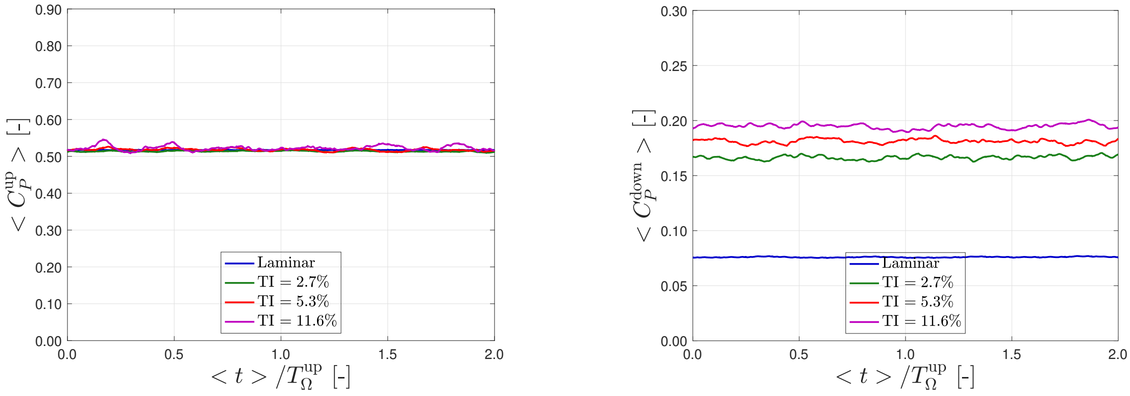

(a) $< C_P^{\mathrm{up}} >$ (b) $< C_P^{\mathrm{down}} >$

Figure 5.53: $< C_P^{\mathrm{up}} >$ and $< C_P^{\mathrm{down}} >$ for cases of dual fixed rotors with $\Delta_D = 5D$ and different inflow TI.

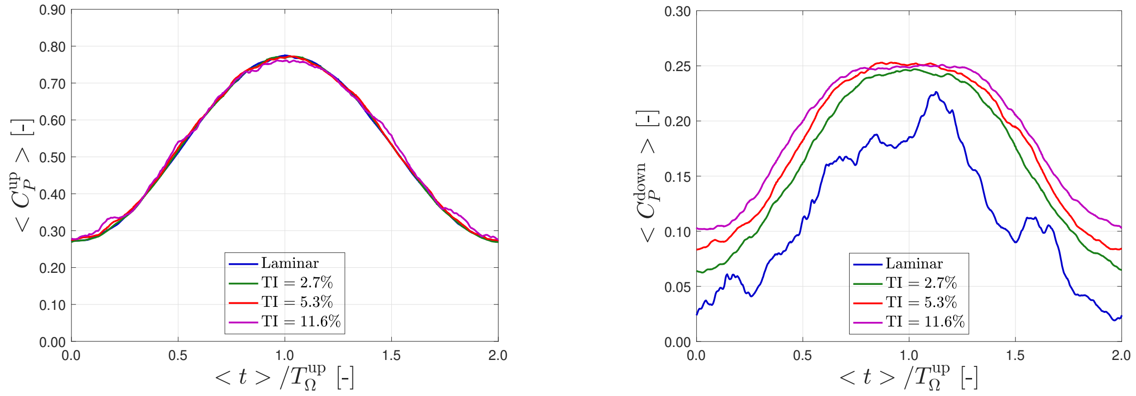

(a) $< C_P^{\mathrm{up}} >$ (b) $< C_P^{\mathrm{down}} >$

Figure 5.54: $< C_P^{\mathrm{up}} >$ and $< C_P^{\mathrm{down}} >$ for cases of dual surging rotors with $\Delta_D = 5D$ and different inflow TI.

5.6.3 Summarizing the Field Data

Figure 5.55 to 5.57 present the fields of $\overline{u}$, TKE, & $< \omega_y >_{0\pi}$ for fixed and surging cases with $\Delta_D = 3D$ under different inflow TI, and Figure 5.58 to 5.60 present the counterparts for cases with $\Delta_D = 5D$. Figure 5.55 & 5.58 show that the $\overline{u}$ fields are generally larger for the cases with higher inflow TI, while the general features for the turbulent cases are not altered by the strength of inflow TI. With the TKE fields displayed by Figure 5.56 & 5.59, it can be seen that the background TKE generally comply with inflow TI, and the wake regions feature higher TI fields. However, a very interesting phenomenon is that the TKE fields after the downstream rotor for the cases with higher inflow TI are not higher than the cases with lower inflow TI; this is most observable with the surging cases, which cases with inflow TI = 2.7% have higher TKE fields after the downstream rotors than cases having 5.3% & 11.6% for both $\Delta_D = 3D$ & $\Delta_D = 5D$. The reasons behind this may related to the interactions between vortical structures and ambient turbulence. Ambient turbulence may trigger the breakdown process of vortical structures (PLSB) by introducing additional instabilities, resulting in higher turbulence intensity; however, if the turbulence intensity is so high that distorted the vortical structures generated by the wind turbine rotors too fast, the breakdown process may be terminated earlier before it could bring additional turbulence. The above-mentioned idea may be supported by the observation that cases with TI = 2.7% have higher TKE fields for the surging cases than the fixed cases after the downstream rotor, while cases with TI = 5.3% & TI = 11.6% have similar TKE fields for the surging and fixed cases; note that surging cases convected large and strong vortical structures after the downstream rotors (see Figure 5.57 & 5.60). Figure 5.57 & 5.60 present the $< \omega_y >_{0\pi}$ fields. Similar with the cases with single rotor under different turbulent inflow conditions (Figure 4.12), the vortical structures related to PLSB become less noticeable with higher inflow TI.

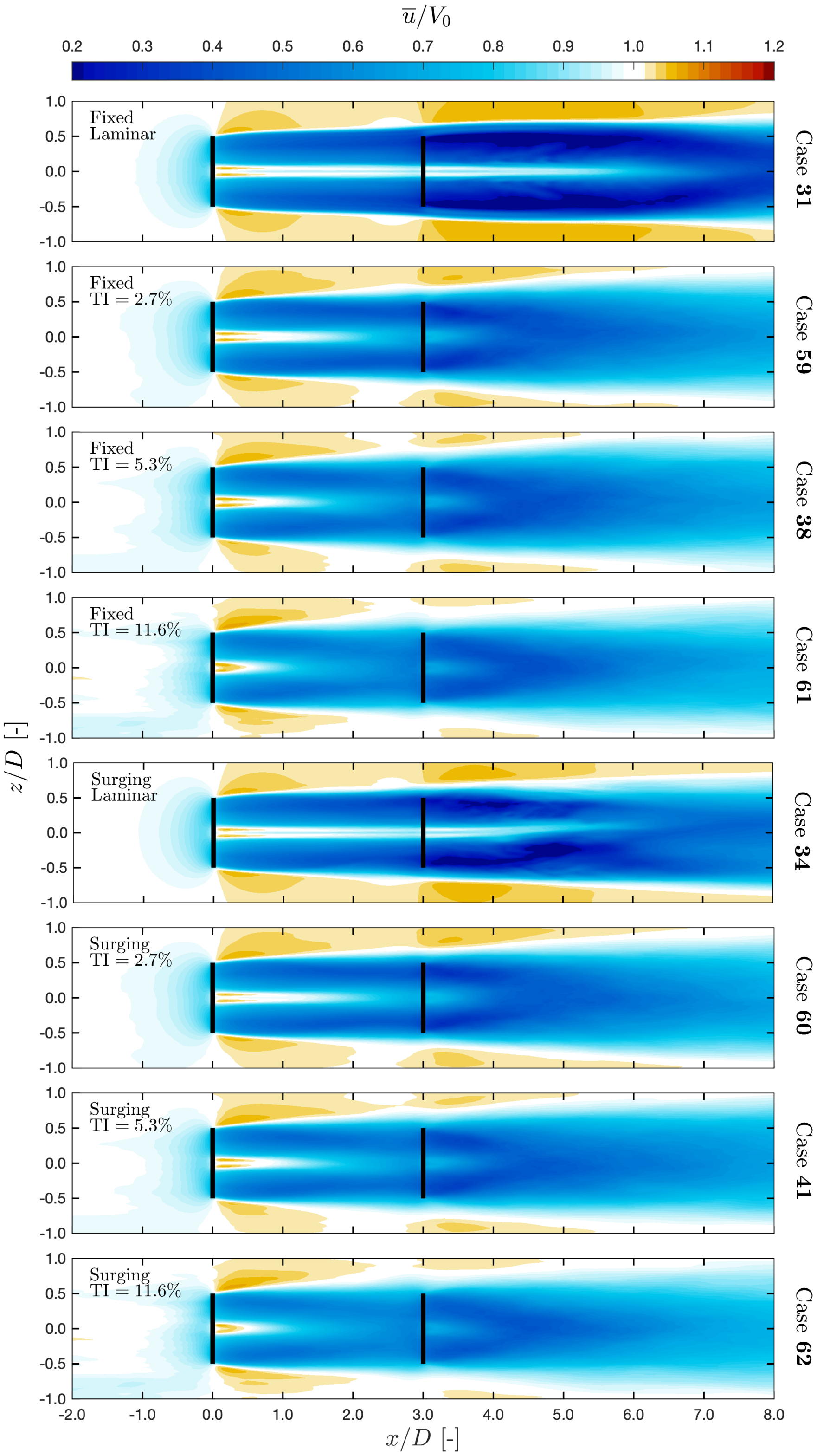

Figure 5.55: Fields of time-averaged streamwise velocity $\overline{u}$ vorticity $< \omega_y >_{0\pi}$ for cases of dual fixed rotors with $\Delta_D = 3D$ and different inflow TI.

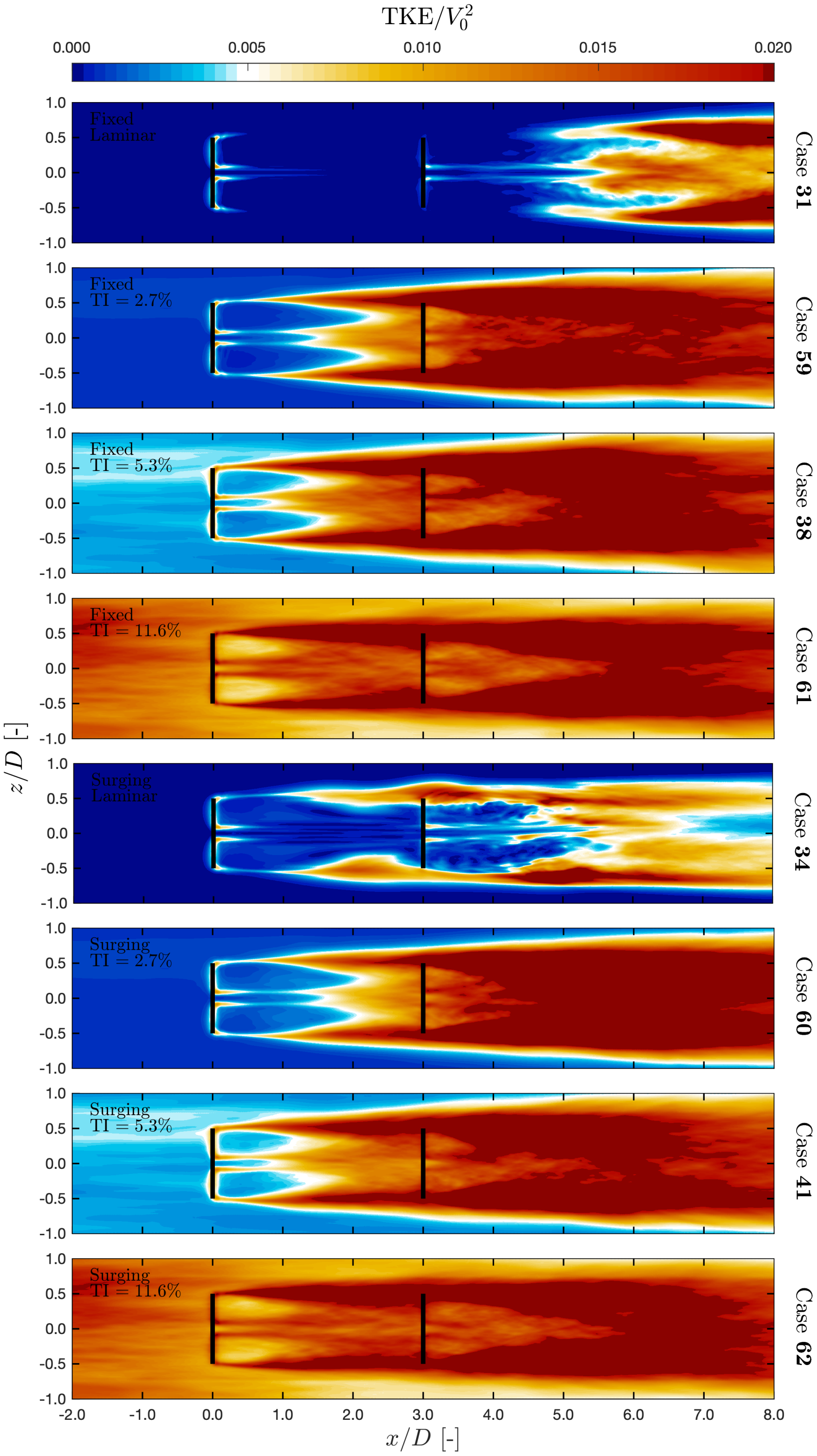

Figure 5.56: Fields of turbulent kinetic energy TKE for cases of dual fixed rotors with $\Delta_D = 3D$ and different inflow TI.

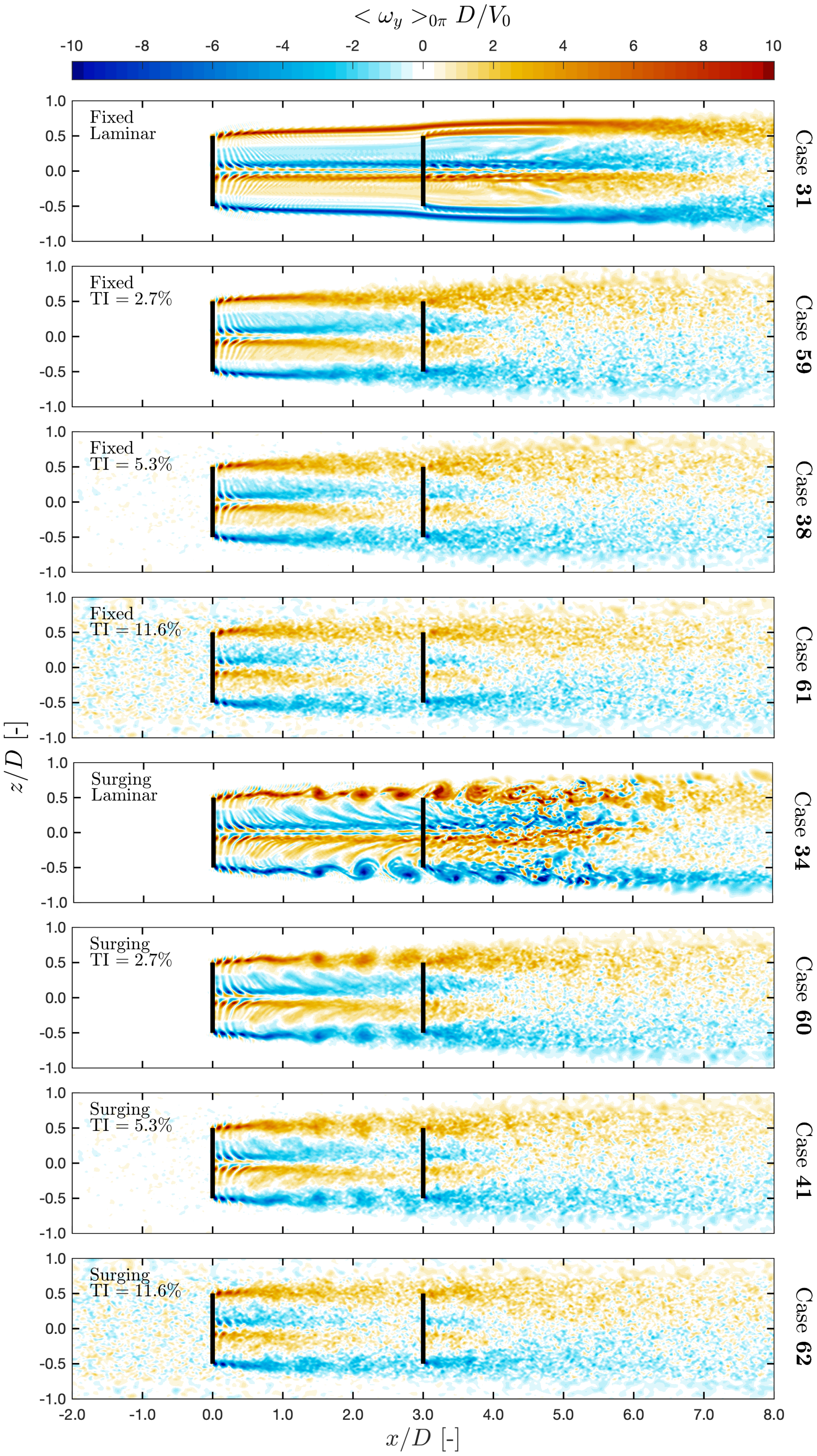

Figure 5.57: Fields of phase-locked averaged y-component vorticity $< \omega_y >_{0\pi}$ for cases of dual fixed rotors with $\Delta_D = 3D$ and different inflow TI.

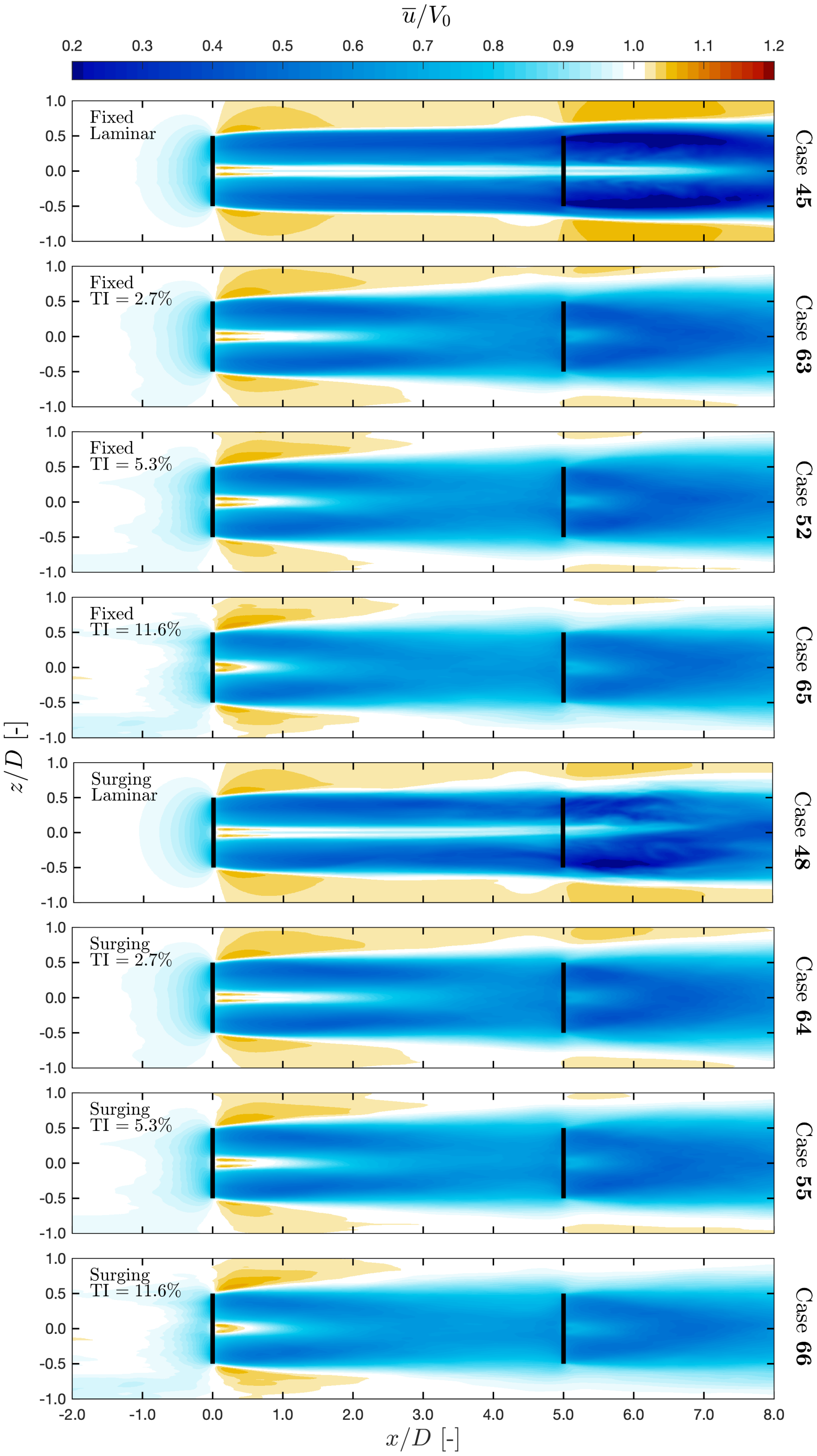

Figure 5.58: Fields of time-averaged streamwise velocity $\overline{u}$ vorticity $< \omega_y >_{0\pi}$ for cases of dual fixed rotors with $\Delta_D = 5D$ and different inflow TI.

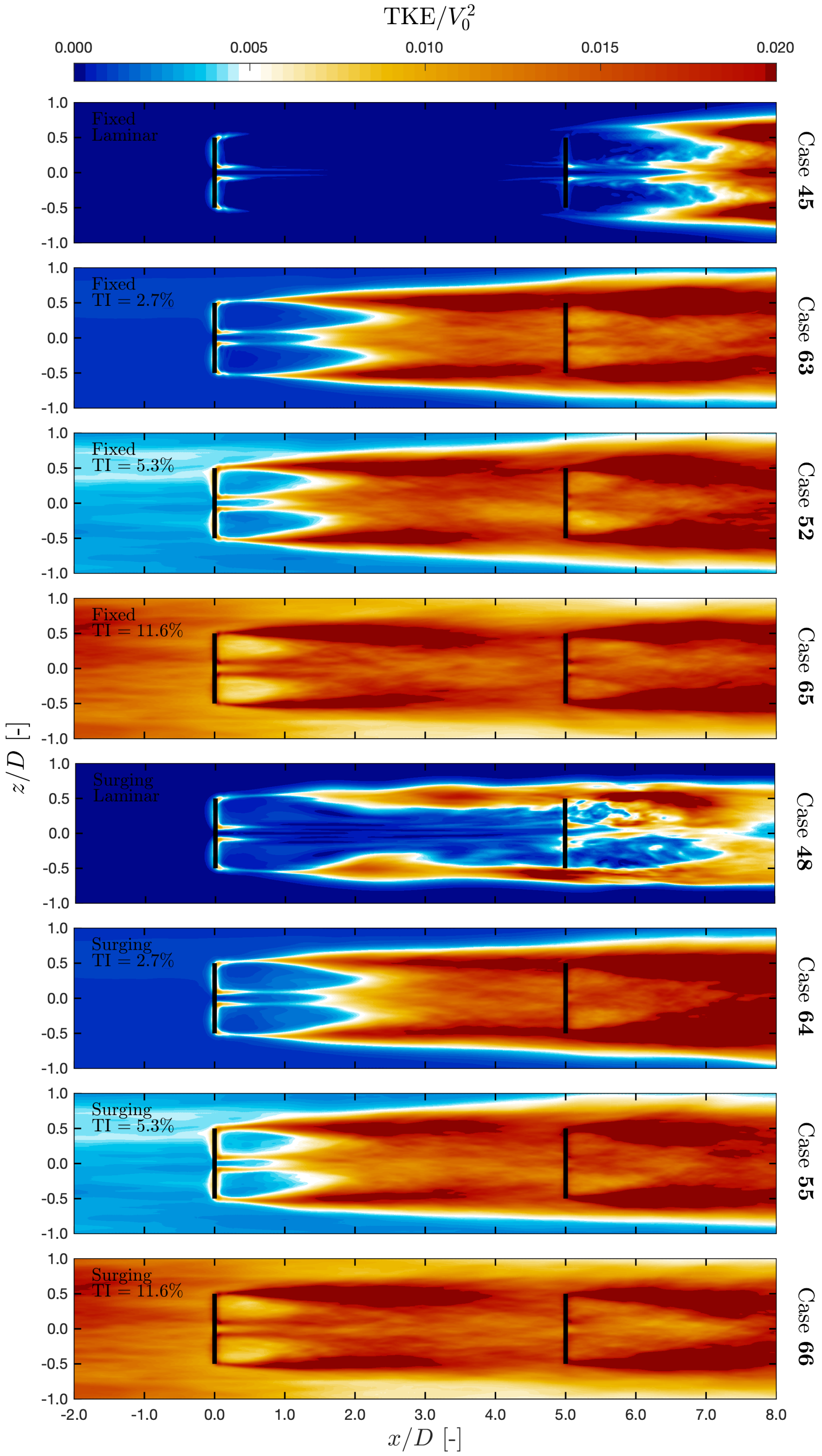

Figure 5.59: Fields of turbulent kinetic energy TKE for cases of dual fixed rotors with $\Delta_D = 5D$ and different inflow TI.

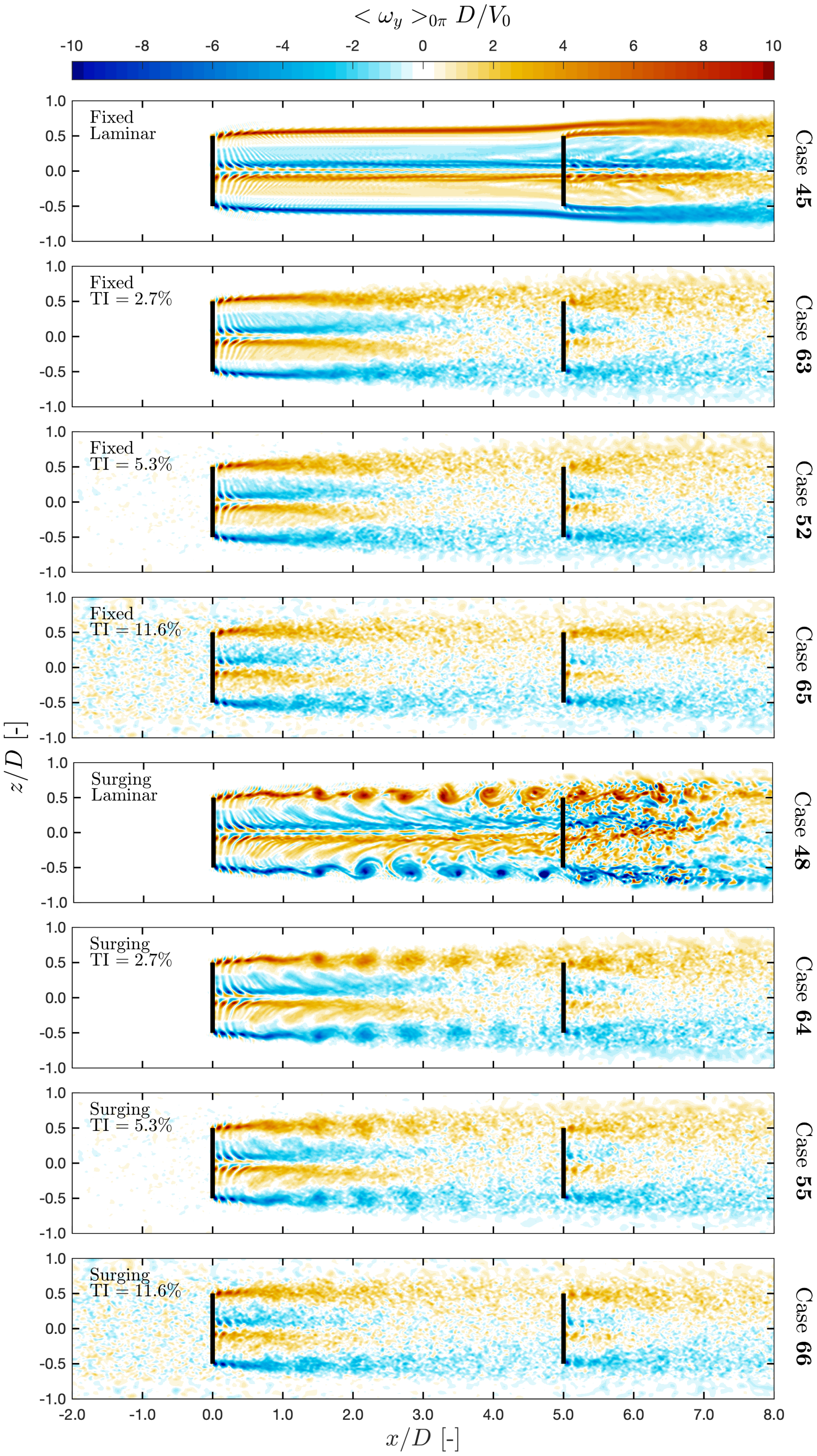

Figure 5.60: Fields of phase-locked averaged y-component vorticity $< \omega_y >_{0\pi}$ for cases of dual fixed rotors with $\Delta_D = 5D$ and different inflow TI.

5.7 Angle of Attack and Stalling of the Downstream Rotor

This section dedicates to explain stalling of the downstream rotor via analyzing its profiles of angle of attack α^{down} due to the effects of surging and wake interactions. The selected cases to analyze are the turbulent cases with inflow TI being 5.3% and separation distances Δ_D being $3D$ or $5D$, and they belong to group D.2, D.4, & D.6 introduced in section 5.1. Note that $A_S = 4$ m and $\omega_S = 0.63$ rad/s are the surging settings for all the surging cases in this section.

Figure 5.62 and 5.63 present the cycle-averaged α^{down} along the blade spans for the cases of different surging-fixed combinations and different $\Delta_{\phi_{S_0}}$ with $\Delta_D = 3D$ under turbulent inflow conditions (TI = 5.3%, see subsection 4.5.3 for α_{stall}). For comparison, Figure 5.61 presents $< \alpha^{\text{up}} >$ along the blade span for case FF and SS with inflow TI = 5.3% and $\Delta_D = 3D$. Note that profiles of $< \alpha^{\text{up}} >$ in Figure 5.61 are very similar to the profiles of $< \alpha >$ for cases with single rotor in Figure 4.50, despite the inflow conditions are changed from laminar to turbulent.

It is worth noting that the rotational speed of the downstream rotor here Ω^{down} is smaller than Ω^{up} and the estimated inflow velocity for the downstream rotor V_0^{down} (7.6 m/s) is smaller than V_0^{up} (11.4 m/s) (the estimated tip speed ratio of the downstream rotors λ^{down} are same as $\lambda^{\text{up}} = 7$, but note that reference velocities for C_T & C_P are 11.4 m/s). However, by comparing $< \alpha^{\text{down}} >$ (Figure 5.62a) and $< \alpha^{\text{up}} >$ (Figure 5.61a) for the case FF with $\Delta_D = 3D$ (case **38**), it can be seen that $< \alpha^{\text{down}} >$ is darker in blue, suggesting V_0^{down} is a bit over estimated based on the velocity triangle.

As it can be seen by comparing $< \alpha^{\text{up}} >$ & $< \alpha^{\text{down}} >$ of the surging rotors with $\Delta_D = 3D$ in Figure 5.63 ($< \alpha^{\text{down}} >$) with Figure 5.61b ($< \alpha^{\text{up}} >$), despite having exactly same A_S and ω_S, $< \alpha^{\text{down}} >$ in Figure 5.63 displays deeper stalling for the downstream surging rotors when comparing with the ones in the upstream in Figure 5.61b. This is as expected since that the inflow angle of the downstream rotor ϕ^{down} is more susceptible to the surging velocity of the downstream rotor $V_{\text{WT}}^{\text{down}}$ (since the effective $\mathbb{V}^{\text{down}}$ is bigger), and this can be explained by the velocity triangle (Figure 2.1) and Equation 2.17 & 2.18. Notice that V_0^{down} is deemed to be over estimated for $\Delta_D = 3D$, thus more severe stalling of the surging downstream rotors for cases **41-44** could not be due to the under estimation of V_0^{down}. Regarding the possibility of more severe stalling for the rotor operating in other FOWT's wakes, controlling strategy of FOWT will be critically important for AEP of the future floating wind farms.

Looking closer to $< \alpha^{\text{down}} >$ in Figure 5.63, it can be seen that case $\Delta_{\phi_{S_0}} = 0.5\pi$ experienced the most severe stalling of the four cases. This may due to that the downstream rotor of case $\Delta_{\phi_{S_0}} = 0.5\pi$ (case **42**) move against the inflow while being right between the PLSB (see Figure 5.38 and 5.40), making it has the highest cycle-averaged $V_{0,\text{app}}^{\text{down}}$; and thus leads to the most severe stalling, which can be confirmed with $< \alpha^{\text{down}} >$ in Figure 5.63. As one may have expected, stalling has negative impacts on the power conversion rates of wind turbine rotors, and this can explain why case $\Delta_{\phi_{S_0}} = 0.5\pi$ has slightly lower $\overline{C}_P^{\text{down}}$ when comparing to the other three cases with different $\Delta_{\phi_{S_0}}$.

As for the cases with $\Delta_D = 5D$, stalling of the downstream rotor is much more pronounced as it can be seen in Figure 5.64. The main reason is that V_0^{down} is now under estimated (since Ω^{down} is prescribed) for case with $\Delta_D = 5D$, and this is based on the color of $< \alpha^{\text{down}} >$ in Figure 5.64a is lighter compared to Ω^{up} in Figure 5.61a. Stalling is so severe that the $\overline{C}_P^{\text{down}}$ for case SS (case **53**) is even lower than case FF (case **50**), making surging negatively impacts the values of $\overline{C}_P^{\text{down}}$.

With the analysis of angle of attack α carried out in this section, it is found that downstream surging rotor is more susceptible to stalling, $\Delta_{\phi_{S_0}}$ affects the wake interaction with $\Delta_D = 3D$ under turbulent inflow conditions through affecting α^{down}, and stalling has negative impacts on $\overline{C}_P$.

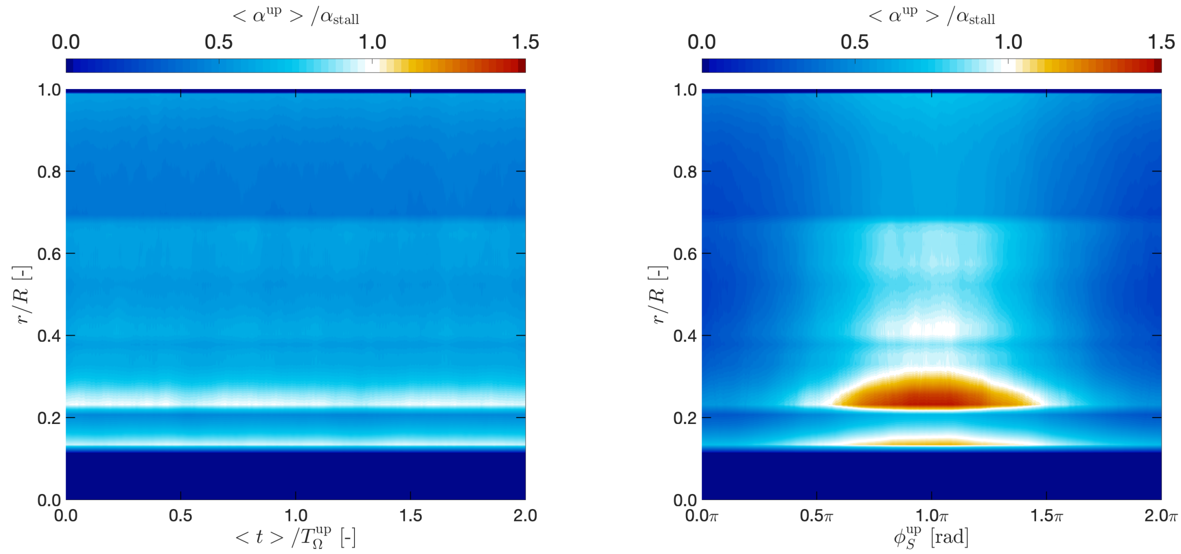

(a) FF (case **38**)

(b) SS (case **41**)

Figure 5.61: Cycle-averaged angle of attack of the upstream rotor $< \alpha^{\text{up}} >$ with $\Delta_D = 3D$ and different surging-fixed combinations under turbulent inflow conditions.

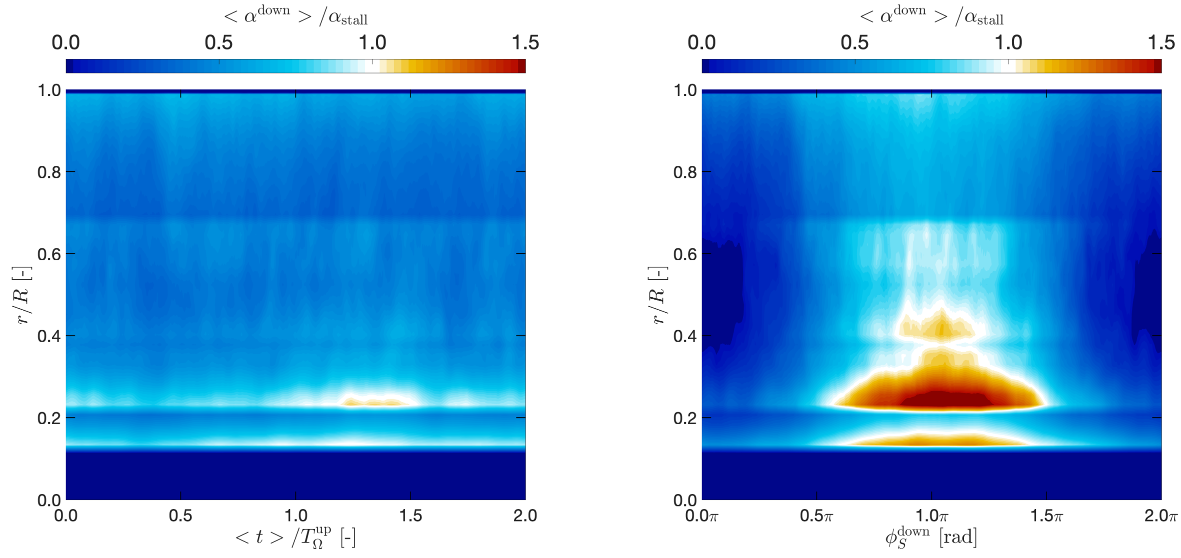

(a) FF (case **38**)

(b) FS (case **39**)

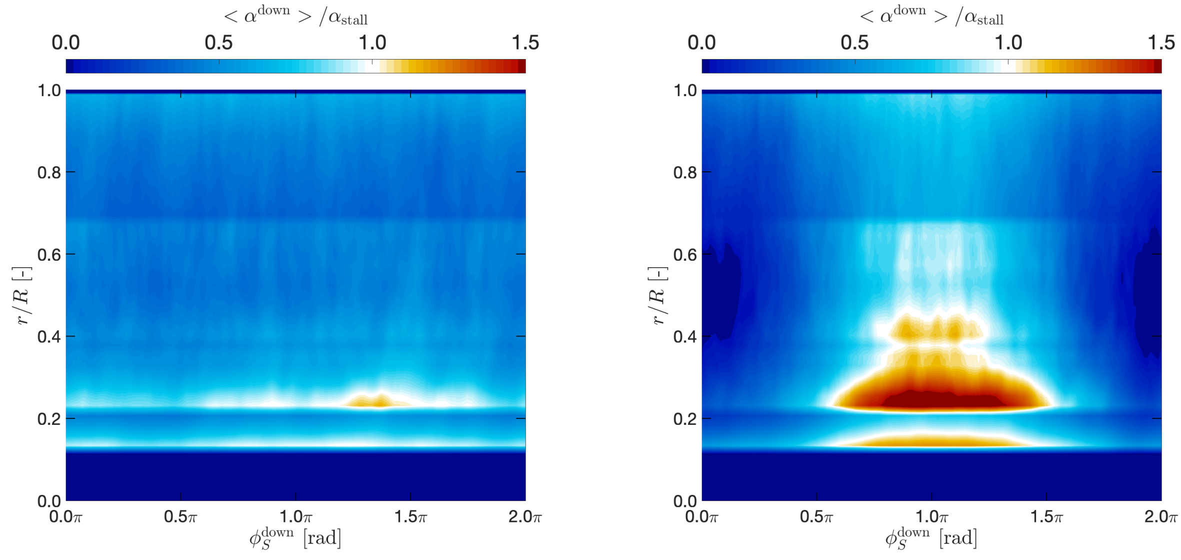

(c) SF (case **40**)

(d) SS (case **41**)

Figure 5.62: Cycle-averaged angle of attack of the downstream rotor $< \alpha^{\mathrm{down}} >$ with $\Delta_D = 3D$ and different surging-fixed combinations under turbulent inflow conditions.

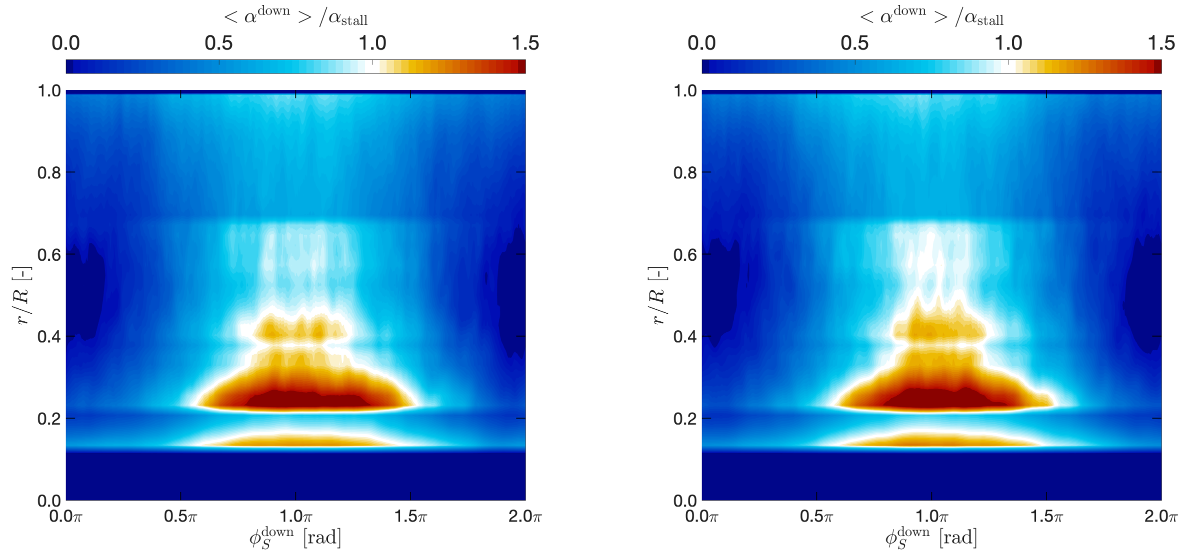

(a) $\Delta_{\phi_{S_0}} = 0.0\pi$ (case **41**)

(b) $\Delta_{\phi_{S_0}} = 0.5\pi$ (case **42**)

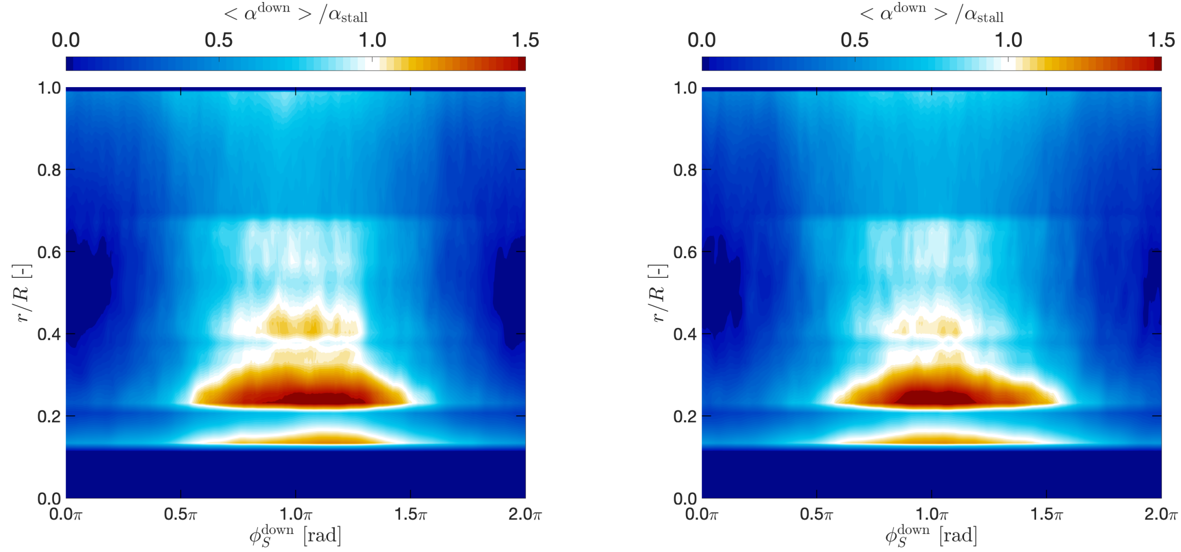

(c) $\Delta_{\phi_{S_0}} = 1.0\pi$ (case **43**)

(d) $\Delta_{\phi_{S_0}} = 1.5\pi$ (case **44**)

Figure 5.63: Cycle-averaged angle of attack of the downstream rotor $< \alpha^{\text{down}} >$ with $\Delta_D = 3D$ and different $\Delta_{\phi_{S_0}}$ under turbulent inflow conditions.

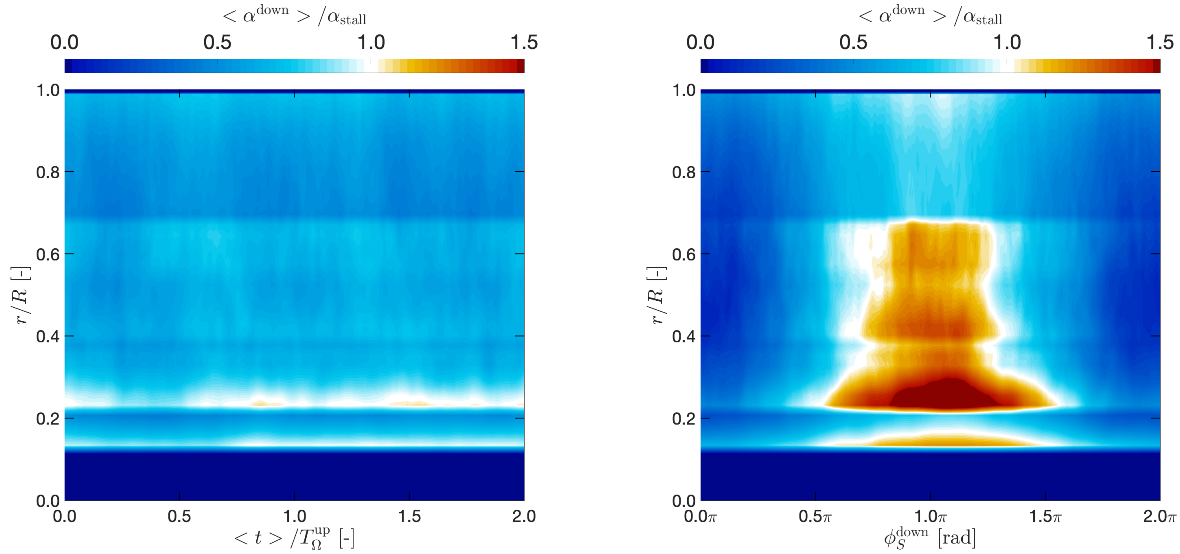

(a) FF (case **50**)

(b) SS (case **53**)

Figure 5.64: Cycle-averaged angle of attack of the downstream rotor $< \alpha^{\mathrm{down}} >$ with $\Delta_D = 5D$ and different surging-fixed combinations under turbulent inflow conditions.

5.8 Summary and Conclusions

In this chapter, comprehensive investigations about wake interactions between two fixed or surging full scale wind turbine rotors in tandem were conducted. The studied parameters include the surging-fixed conformations (FF, FS, SF, & SS), phase differences of the two surging motions ($\Delta_{\phi_{S_0}}$), inflow turbulence intensities (TI), and the separation distance (spacing) between the two rotors (Δ_D). Inflow conditions of laminar and turbulent with TI = 5.3% are most focused. As for the surging cases, $A_S = 4$ m/s & $\omega_S = 0.63$ rad/s are set. The major discoveries and conclusions for this chapter are listed below.

1. Besides from the fields of phase-locked averaged quantities, the instantaneous and time-averaged fields for two rotors in tandem are not significantly altered by the surging conformations as the inflow conditions are turbulent (TI = 2.7, 5.3 or 11.6%, see section 5.2 & 5.6), suggesting the modes of wake interactions between the two rotors are similar either them being fixed or surging as the inflow conditions are turbulent.

2. With the facts that the power performances of the downstream rotor in Table 5.1 become slightly higher if the upstream rotor is surging rather than being fixed (operational conditions of the downstream rotor should be the same for comparison), it can be suggested that surging (of the upstream rotor) do facilitate wake recovery; however, the effects are much less pronounced with the realistic turbulent inflow conditions (1-2% gains for both $\Delta_D = 3D$ & $5D$) compared to the laminar inflow conditions ($\sim$ 10% gains for $\Delta_D = 3D$, $\sim$ 40% gains for $\Delta_D = 5D$).

3. If the surging motions for both upstream and downstream rotor are same (in sense of A_S & ω_S), the power performances (stalling effects) of the downstream rotor is more subjected to the influences of surging motions compare to the upstream rotor in the sense of relative fluctuation amplitudes of C_P. This is due to the fact the the effective ratios between the maximum surging speed and the inflow wind speed seen by the downstream rotor ($\mathbb{V}^{\mathrm{down}}$) will be larger than the upstream one.

4. The instantaneous wake structures of the two rotor are more dominated by the surging conformations (fixed or surging) of the upstream rotor, and the PLSB of the downstream rotor are much less clearer compare to the one of the upstream rotor.

5. PLSB of the upstream rotor do slightly affects the power performance of the downstream rotor with the realistic turbulent inflow conditions (TI = 5.3%) when the inter-distance between the rotors is rather close ($\Delta_D = 3D$), this can be confirmed with the fact that the phase angle differences between the surge motions for the two rotors ($\Delta_{\phi_{S_0}}$) affects the power performance of the downstream rotor. However, the effects of PLSB will significantly diminish with larger Δ_D ($\Delta_D = 5D$, note that $5D$ is rather small compare to the typical Δ_D in the real offshore wind farms), and thus the effects of $\Delta_{\phi_{S_0}}$ become less important and even negligible.

6. Since that the effects of $\Delta_{\phi_{S_0}}$ (phase angle differences between the surge motions for the two rotors) on the wake interactions between the two surging rotor are rather weak,

the phase angle of surging may not be a crucial factor to consider for wake interactions between rotors of FOWT as the inter-distance is large enough ($\Delta_D \geq 5$). This may drastically lower the degree of freedoms when assessing the AEP numerically for the floating offshore wind farms.

7. Wake-wake interactions for cases with laminar inflow conditions differ very significantly to the cases with turbulent inflow conditions. For the laminar cases, the recovery rates of $\overline{u}_{\text{Disk}}$ are heavily influenced by the parameters inputted to the simulations (such as the surging settings of the rotors), and the downstream rotor will trigger the breakdown processes (turbulent transitions). While for the cases with turbulent inflow conditions, their results are much less sensitive to the input parameters (such as surging-fixed conformations & $\Delta_{\phi_{S_0}}$), even with TI which is quite low (2.7%). Since that laminar inflow conditions are unrealistic out in the fields, thus if the goal is to properly simulate wake interactions of FOWTs operating under the real world conditions, turbulent inflow conditions can be deemed as a requirement.
8. Prescribed constant rotational speeds (Ω^{up} & Ω^{down}) for both upstream and downstream rotor may not be the best way for modelling the wake interactions for multiple wind turbine rotors out in fields, especially for FOWT in motions, since that the operational conditions of the rotor will be quite off from the optimal condition (especially for the downstream one), which will not be the case for modern wind turbine with proper controller.

To better understand the full potential of enhancing power outputs for surging rotors in tandem, cases of dual rotors with controller are presented in the next chapter, and some of the cases are compared with the cases in this chapter.

Chapter 6

Results and Discussions of Cases with Simple Controller

6.1 Introduction

For cases in previous chapters, no controlling mechanisms were applied on the rotor of NREL 5MW baseline turbine. Although this configuration is more straightforward and would make the systems simpler to analyze, this is not the actual use case for contemporary multi-megawatt wind turbines. Setup without controller makes the rotor operates with sub-optimal conditions (λ which is not optimal), possibly making ξ_{C_P} in Equation 4.1 substantially lower; moreover, this setup also ends up in severe stalling with some surging settings (see subsection 4.5.4), and thus lowering the power converting rates (ξ_{C_P}). Therefore, to better understand the full potential of floating wind farms, a simple controller (MPPT tracking) described in section 2.7 is added and implemented into the simulation framework used in previous chapters, hoping to make the overall power output ($\overline{C}_P$) higher.

Note that when adjusting the generator torque τ_{Gen} with Equation 2.34 during the simulations in this chapter, $C_{P,\text{opt}} = 0.5177$ and $\lambda_{\text{opt}} = 7.00$ are set, which are based on the $\overline{C}_P$ of case **1** in Table 4.1 (fixed, laminar inflow conditions). Even though the rated conditions are not the optimal conditions in sense of power conversion rate (not exactly optimal but should be close to), it is chosen to make the comparisons with the cases in the previous chapters more straightforward. Values of I (total rotational inertia), I_R (inertia of rotor), I_{Gen} (inertia of drive train), I_B (inertia of single blade), and I_{hub} (inertia of hub) for NREL 5MW baseline turbine are listed in Table 6.1, they are documented in the report of NREL 5MW [62]. Note that parallel axis theorem was applied to obtain the value of I_B from with respect to blade root to with respect to the rotor center, and I_{Gen} is respect to low speed shaft.

Table 6.1: Values of moment inertia for different parts of NREL 5MW baseline turbine.

	I	I_R	I_{Gen}	I_B	I_{hub}
Values [kg m^2]	4.39×10^7	3.87×10^7	5.03×10^6	1.29×10^7	1.16×10^5

In total, there are 19 cases conducted with controller; 8 of them are the main cases and they are summarized in Table 6.2, while the other 11 are the auxiliary cases which are shown in Appendix G. All the eight main cases in Table 6.2 have turbulent inflow conditions of TI = 5.3% (see section G.4 for laminar cases), and they all have two rotors in tandem sharing same surging settings ($\phi_{S_0} = 0\pi$, $\Delta_{\phi_{S_0}} = 0\pi$). They can be further grouped into two, where four of the eight main cases have the separation distance $\Delta_D = 3D$, and the other four have $\Delta_D = 5D$. Each group has a fixed case along with three surging cases having $A_S = 2$, 4, or 8 m, and all the surging cases share a same ω_S of 0.63 rad/s.

Table 6.2: The basic settings and results for cases conducted with dual rotors equipped with basic controller. Calculations of ${}_{\text{sur}}\overline{G}_{C_P}$ are based on the interested case and the fixed case in bold font in the same set.

Case	TI [%]	Δ_D/D	A_S	$\overline{C}_T^{\text{up}}$	$\overline{C}_{P,\text{Gen}}^{\text{up}}$	$\overline{C}_{P,\text{Aero}}^{\text{up}}$	$\overline{C}_{P,\text{Tar}}^{\text{up}}$	$\overline{C}_T^{\text{down}}$	$\overline{C}_{P,\text{Gen}}^{\text{down}}$	$\overline{C}_{P,\text{Aero}}^{\text{down}}$	${}_{\text{sur}}\overline{G}_{C_P}^{\text{up}}$ [%]	${}_{\text{sur}}\overline{G}_{C_P}^{\text{down}}$ [%]	${}_{\text{sur}}\overline{G}_{C_P}^{\text{total}}$ [%]	$\overline{u}_{\text{Disk}}^{8D}/V_0$
81	**5.3**	**3**	**Fixed**	**0.725**	**0.516**	**0.516**	**0.518**	**0.287**	**0.129**	**0.129**	–	–	–	**0.753**
82	5.3	3	2	0.726	0.522	0.522	0.527	0.281	0.126	0.126	1.2	−2.2	0.5	0.753
83	5.3	3	4	0.720	0.530	0.529	0.556	0.267	0.121	0.121	2.6	−5.8	0.9	0.739
84	5.3	3	8	0.664	0.511	0.510	0.670	0.223	0.100	0.100	−1.0	−22.1	−5.2	0.751
85	**5.3**	**5**	**Fixed**	**0.726**	**0.518**	**0.518**	**0.518**	**0.379**	**0.199**	**0.199**	–	–	–	**0.653**
86	5.3	5	2	0.728	0.524	0.523	0.527	0.379	0.202	0.201	1.1	1.3	1.2	0.652
87	5.3	5	4	0.721	0.531	0.531	0.556	0.369	0.201	0.201	2.5	1.3	2.2	0.668
88	5.3	5	8	0.665	0.513	0.512	0.670	0.307	0.167	0.167	−1.0	−16.1	−5.2	0.683

section 2.7 had showed that the working principle of the implemented simple torque controller is by matching generator torque τ_{Gen} with aerodynamic torque τ_{Aero} based on the rotational speed Ω; thus, there will be two instantaneous power, which are the generator power P_{Gen} & aerodynamic power P_{Aero}, and there are also two power coefficients $C_{P,\text{Aero}}$ & $C_{P,\text{Gen}}$, as shown in Table 6.2. Even though $C_{P,\text{Aero}}$ & $C_{P,\text{Gen}}$ (Equation 6.1 & 6.2) may have different values at a given instant, their time-averaged values ($\overline{C}_{P,\text{Aero}}$ & $\overline{C}_{P,\text{Gen}}$) should be same, according to the energy conservation law; note that both $\overline{C}_{P,\text{Aero}}^{\text{up}}$ & $\overline{C}_{P,\text{Gen}}^{\text{up}}$ and $\overline{C}_{P,\text{Aero}}^{\text{down}}$ & $\overline{C}_{P,\text{Gen}}^{\text{down}}$ in Table 6.2 for all cases comply with this. And note that in this chapter (also in Appendix G), C_P by default is based on generator power P_{Gen}, since that this is the output of the wind turbine systems to the electrical systems in the real world, and the reference velocity V_{ref} is set to be $V_{0,\text{rated}} = 11.4$ m/s.

$$C_{P,\text{Aero}} \triangleq \frac{P_{\text{Aero}}}{0.5\rho V_{\text{ref}}^3 \pi R^2}, \qquad P_{\text{Aero}} = \tau_{\text{Aero}}\Omega \tag{6.1}$$

$$C_{P,\text{Gen}} \triangleq \frac{P_{\text{Gen}}}{0.5\rho V_{\text{ref}}^3 \pi R^2}, \qquad P_{\text{Gen}} = \tau_{\text{Gen}}\Omega = K_\tau \Omega^3 \tag{6.2}$$

The controller has been evaluated with inditial tests with 7 of the auxiliary cases under different conditions (inflow velocities V_0) in section G.1, where the controller was turned on at a certain time instant and to see whether the controller perform as expected. The results show that the controller performed quite well based on the outputted Ω & C_P, where the values after the system had reached its quasi-steady states match the predicted values well. Also, the inditial tests show that the time needed for the controller to reach its new quasi-steady states after turning it on is much longer than the surging period T_S considered in this thesis ($T_S = 2T_\Omega$ for most cases). For more information, please check section G.1.

One of the main assumption of the implemented controller is that power conversion rate of the rotor solely depends on λ (blade pitch is fixed in this thesis), and thus C_P can be predicted with different inflow velocity V_0 if Ω is adjusted as the design. While the wind turbine rotor is surging, the apparent inflow velocity $V_{0,\text{app}}$ (Equation 2.27) is affected, and thus the targeted (predicted) Ω (Ω_{Tar}) and C_P ($C_{P,\text{Tar}}$) according to the settings of the controller ($C_{P,\text{opt}}$ & λ_{opt}) are also affected, which are written in Equation 6.3 & 6.4. Note that only the upstream rotor has Ω_{Tar} & $C_{P,\text{Tar}}$ since that V_0 for the downstream rotor cannot be predicted precisely, and the calculations of C_P for the both rotors here are again based on $V_{0,\text{rated}}$. Values of Ω_{Tar} & $C_{P,\text{Tar}}$ are based on quasi-steady solutions, and section G.1 has shown that the estimations based on Equation 6.3 & 6.4 are reliable. Ω_{Tar} & $C_{P,\text{Tar}}$ are plotted against ϕ_S with different surging settings later in this chapter (eg. Figure 6.2a & 6.2b). $\overline{C}_{P,\text{Tar}}$ in Table 6.2 is the time-averaged value of $C_{P,\text{Tar}}$, and $\overline{C}_{P,\text{Tar}}$ is listed out to better estimate the performance of the controller.

$$\Omega_{\text{Tar}} = \frac{\lambda_{\text{opt}} V_{0,\text{app}}}{R} = \frac{\lambda_{\text{opt}} \left(V_0 - V_{\text{WT}}\right)}{R} \tag{6.3}$$

$$C_{P,\text{Tar}} = C_{P,\text{opt}} \left(\frac{V_{0,\text{app}}}{V_{0,\text{rated}}}\right)^3 = C_{P,\text{opt}} \left(\frac{V_0 - V_{\text{WT}}}{V_{0,\text{rated}}}\right)^3 = C_{P,\text{opt}} \left(\frac{V_0(1 - \mathbb{V}\cos\phi_S)}{V_{0,\text{rated}}}\right)^3 \tag{6.4}$$

6.2 Summarizing Wake Characteristics

Figure 6.1 presents the profiles of $\overline{u}_{\text{Disk}}$ along x-direction. In general, just as the previous cases, values of $\overline{u}_{\text{Disk}}$ for surging cases are slightly higher than the fixed cases, especially for the cases with $A_S = 8$ m ($\mathbb{V} = 0.44$).

6.3 Summarizing Rotor Performances

6.3.1 Cycle-Averaged Rotor Performances

Figure 6.2 shows the cycle-averaged Ω & C_P ($< \Omega >$ & $< C_P >$) of the upstream rotor for cases with $\Delta_D = 3D$ (cases **81-84**). Note that the subscripts *Gen*, *Aero*, & *Tar* stand for *generator*, *aerodynamic* & *targeted*, and superscripts again indicating upstream or downstream rotor. To analyze the system, first focus on $< \Omega^{\text{up}} >$ (Figure 6.2a). $< \Omega^{\text{up}}_{\text{Gen}} >$ of the fixed case in Figure 6.2a can be considered as a constant and matches the value of $< \Omega^{\text{up}}_{\text{Tar}} >$ very well, which is as designed. While for the surging cases, aside from the fluctuation amplitudes of $< \Omega^{\text{up}} >$ get bigger with larger A_S for obvious reason, it is very clear that the fluctuation amplitudes of $< \Omega^{\text{up}}_{\text{Gen}} >$ are smaller than $< \Omega^{\text{up}}_{\text{Tar}} >$, and $< \Omega^{\text{up}}_{\text{Gen}} >$ are also significantly lagging behind $< \Omega^{\text{up}}_{\text{Tar}} >$; these suggest the adapting speed of $< \Omega^{\text{up}}_{\text{Gen}} >$ is not fast enough to properly reach $< \Omega^{\text{up}}_{\text{Tar}} >$. Next, looking at Figure 6.2b for $< C^{\text{up}}_P >$, $< C^{\text{up}}_{\text{P,Tar}} >$ and $< C^{\text{up}}_{\text{P,Gen}} >$ also display a similar behaviour as $< \Omega^{\text{up}} >$. Moreover, from here the actual driving force, the differences of $\tau^{\text{up}}_{\text{Aero}}$ & $\tau^{\text{up}}_{\text{Gen}}$ (Equation 2.36), can be evaluated

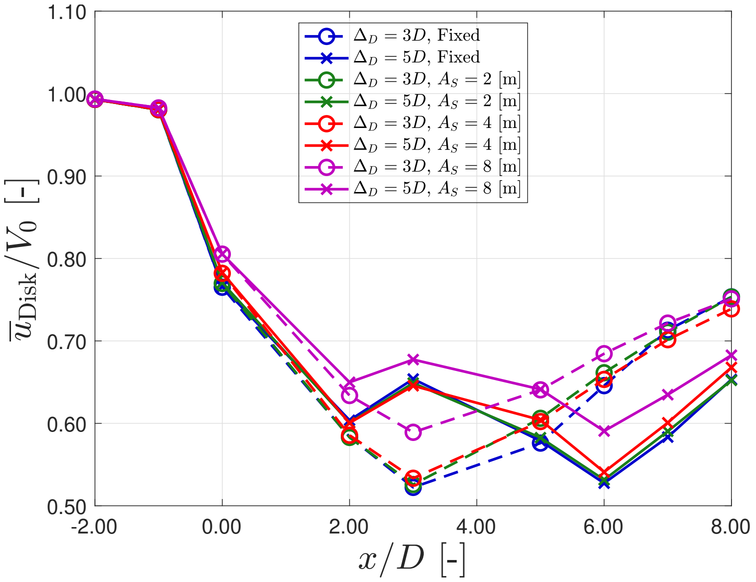

Figure 6.1: $\overline{u}_{\text{Disk}}$ along x-direction for cases with different A_S, controlled rotor, turbulent inflow conditions (TI = 5.3%), and $\Delta_D = 3D$ or $5D$.

through $C^{\text{up}}_{P,\text{Aero}}$ & $C^{\text{up}}_{P,\text{Gen}}$ (from Equation 6.1 & Equation 6.2). It is very clear why $C^{\text{up}}_{P,\text{Gen}}$ lags behind $C^{\text{up}}_{P,\text{Aero}}$, since that $C^{\text{up}}_{P,\text{Gen}}$ solely depends on $\Omega^{\text{up}}_{\text{Gen}}$ and $\Omega^{\text{up}}_{\text{Gen}}$ is the reaction of $C^{\text{up}}_{P,\text{Aero}}$ ($\tau^{\text{up}}_{\text{Aero}} - \tau^{\text{up}}_{\text{Gen}}$). Furthermore, $C^{\text{up}}_{P,\text{Aero}}$ still lags behind $C^{\text{up}}_{P,\text{Tar}}$, and the reason is because $C^{\text{up}}_{P,\text{Aero}}$ also depends on $\Omega^{\text{up}}_{\text{Gen}}$, which does not react quick enough. Another thing worth mentioning is that the fluctuation amplitudes of $C^{\text{up}}_{P,\text{Gen}}$ are smaller than $C^{\text{up}}_{P,\text{Aero}}$, and both of them is further smaller than $C^{\text{up}}_{P,\text{Tar}}$. From here it is quite obvious that the huge rotation inertia I of the system does not allow the system to adapt fast enough with regards of surging, making the fluctuation amplitudes of $\Omega^{\text{up}}_{\text{Gen}}$ & $C^{\text{up}}_{P,\text{Gen}}$ smaller than the targeted or aerodynamic values; these has been confirmed by section G.2 & G.3, where cases with smaller I and smaller ω_S were conducted.

Figure 6.3 shows $< \Omega^{\text{down}} >$ & $< C^{\text{down}}_P >$ for cases with $\Delta_D = 3D$ (cases **81-84**). Note that since the inflow velocity seen by the downstream rotor is difficult to accurately estimate, and it varies case by case, the targeted values for Ω^{down} & C^{down}_P are hard to obtain and thus not presented. Focusing on $< \Omega^{\text{down}} >$, the fixed case has a almost constant value; note that the value (0.797 rad/s) differs form the Ω^{down} used (0.844 rad/s) in chapter 5, indicating the controller was functioning. For the other surging cases, $< \Omega^{\text{down}} >$ fluctuates according to ϕ_S. Interestingly, unlike $< \Omega^{\text{up}} >$, all four cases share a similar mean value, while for $< \Omega^{\text{down}} >$, case with $A_S = 8$ m has a different mean value compare to the other three cases, and this may relate to its severe stalling, which can be seen in subsection 6.3.4. As for $< C^{\text{down}}_P >$, once again it can be seen that $C^{\text{down}}_{P,\text{Gen}}$ lags behind $C^{\text{down}}_{P,\text{Aero}}$, and $C^{\text{down}}_{P,\text{Aero}}$ again has bigger amplitudes; also that curves of $C^{\text{down}}_{P,\text{Gen}}$ is smoother compare to those of $C^{\text{down}}_{P,\text{Aero}}$, and this may relate to the big inertial I of the system filtered out the fluctuations.

$< \Omega >$ & $< C_P >$ of the upstream and downstream rotors for the cases with $\Delta_D = 5D$ (cases **85-88**) are presented in Figure 6.4 & 6.5. Most of the behaviours of $< \Omega >$ & $< C_P >$ are same with the cases with $\Delta_D = 3D$, especially for the upstream rotor, which behaves

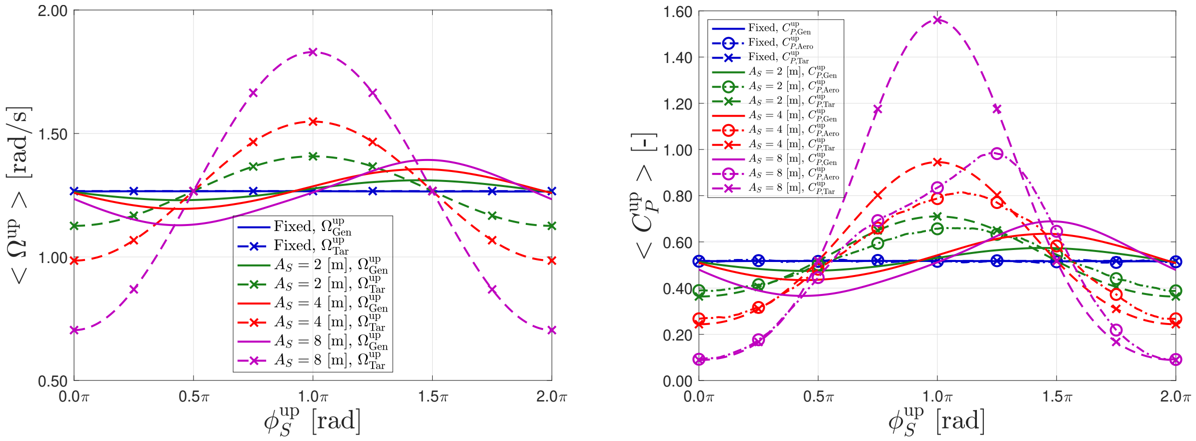

(a) $< \Omega^{\mathrm{up}} >$ (b) $< C_P^{\mathrm{up}} >$

Figure 6.2: $< \Omega^{\mathrm{up}} >$ and $< C_P^{\mathrm{up}} >$ for cases with different A_S, controlled rotor, turbulent inflow conditions, and $\Delta_D = 3D$.

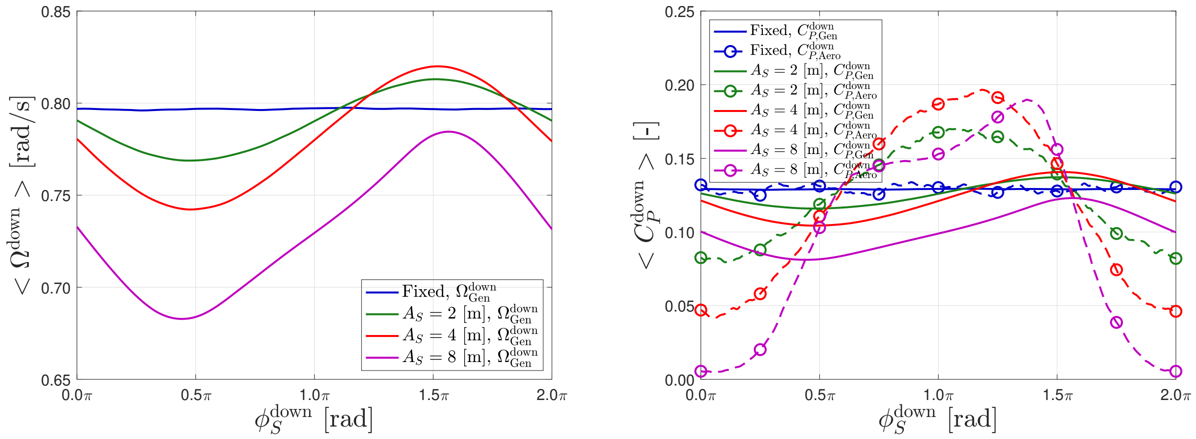

(a) $< \Omega^{\mathrm{down}} >$ (b) $< C_P^{\mathrm{down}} >$

Figure 6.3: $< \Omega^{\mathrm{down}} >$ and $< C_P^{\mathrm{down}} >$ for cases with different A_S, controlled rotor, turbulent inflow conditions, and $\Delta_D = 3D$.

(almost) identically. As for the downstream rotor, one of the major differences is that the mean value of $< \Omega^{\mathrm{down}} >$ & $< C_P^{\mathrm{down}} >$ are higher than the cases with $\Delta_D = 3D$, suggesting the perceived inflow velocities are higher. The mean value of $< \Omega^{\mathrm{down}} >$ for the fixed case is 0.919 rad/s, which is again different form the value in chapter 5.

6.3.2 Time-Averaged Rotor Performances

The time-averaged gain due to surging effects ${}_{\mathrm{sur}}\overline{G}_{C_P}$ (Equation 6.5) listed in Table 6.2 displayed that except for cases with high $\mathbb{V}$ (cases **84** & **88**), surging motions make $\overline{C}_P^{\mathrm{up}}$ slightly higher (1-2%) and simultaneously $\overline{C}_T^{\mathrm{up}}$ may be slightly lower, similar as the previous cases without controller. As for the downstream rotor, $\overline{C}_P^{\mathrm{down}}$ depends both on Δ_D and

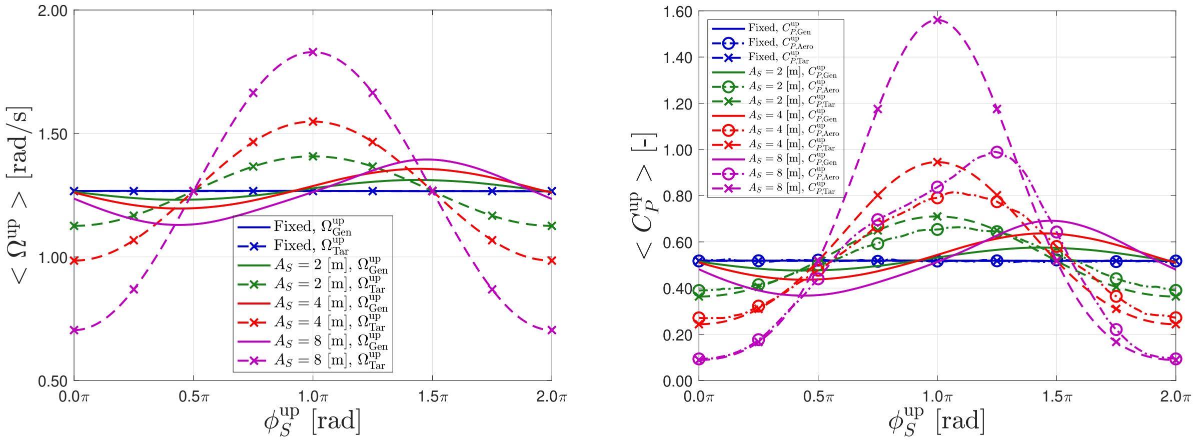

(a) $< \Omega^{\text{up}} >$ (b) $< C_P^{\text{up}} >$

Figure 6.4: $< \Omega^{\text{up}} >$ and $< C_P^{\text{up}} >$ for cases with different A_S, controlled rotor, turbulent inflow conditions, and $\Delta_D = 5D$.

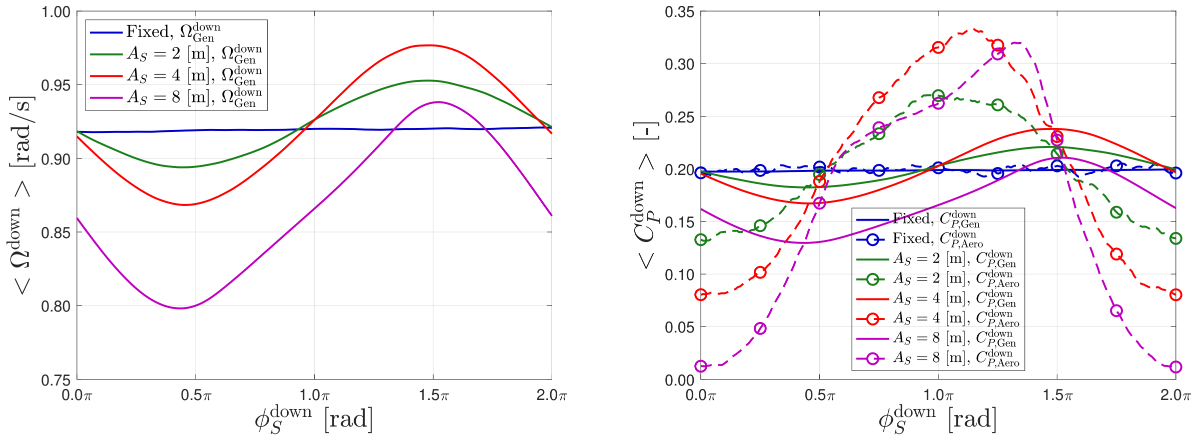

(a) $< \Omega^{\text{down}} >$ (b) $< C_P^{\text{down}} >$

Figure 6.5: $< \Omega^{\text{down}} >$ and $< C_P^{\text{down}} >$ for cases with different A_S, controlled rotor, turbulent inflow conditions, and $\Delta_D = 5D$.

A_S, the main reasons for negative values for gains are related to that the controller cannot response fast enough during the surging cycle and thus severe stalling still occur, and reason for cases with $\Delta_D = 3D$ have more negative values may be due to that the effective $\mathbb{V}^{\text{down}}$ for them is bigger, since that $\overline{u}_{\text{Disk}}$ is less recovered with smaller x/D.

$$ {}_{\text{sur}}\overline{G}_{C_P} \triangleq \left(\frac{\text{power coefficient of the surging case}}{\text{power coefficient of the } \textbf{fixed case}} - 1 \right) \times 100\% \tag{6.5} $$

6.3.3 Compare with Cases without Controller

To estimate the effectiveness of controller on rotor performances, pairs of cases with same settings but one with controller and one without are compared. Note that only single (the upstream) rotor is focused at this point, since that with the controller introduced, there will be too many variables influencing the performance of the downstream rotor operating under wake conditions. And to reduce computational resources, upstream rotor for cases with $\Delta_D = 5D$ (cases **85-88**) are considered as operating alone, since that blockage effects from downstream rotor are negligible ($\leq 0.1\%$); they are compared with the cases **3**, **11**, **13**, & **14** in Table 4.1 (single rotor cases). The interested cases are listed in Table 6.3, and ${}_{\text{con}}\overline{G}_{C_P}$ (definition in Equation 6.6) is the gain of $\overline{C}_P$ due to the implementation of the controller. It can be seen that the two fixed cases in Table 6.3 have the same $\overline{C}_P$, this is as expected since the controller is designed based on case with fixed rotor ($\overline{C}_P$ for cases with fixed single rotor is in-sensitive to TI). As for the surging cases, cases with controller do not have very different $\overline{C}_P$ compare to the cases without controller. However, it is interesting that for the pairs of surging cases, the relation of ${}_{\text{con}}\overline{G}_{C_P}$ and A_S does not seemed to be monotonic, seems that the reaction speed of the controller and stalling affect the values.

$$
{}_{\text{con}}\overline{G}_{C_P} \triangleq \left(\frac{\text{power coefficient of the controlled case}}{\text{power coefficient of the } \textbf{uncontrolled case}} - 1 \right) \times 100\% \qquad (6.6)
$$

Table 6.3: Comparing the effects of applied controller on the fixed or surging rotor. "O" stands for with the controller turned on while "X" stands for without controller. Calculations of ${}_{\text{con}}\overline{G}_{C_P}$ are based on the interested case and the case without controller in bold font with same A_S. Note that all the presented cases have already been showed elsewhere.

Case	TI [%]	Δ_D/D	A_S	Controller	$\overline{C}_T^{(\text{up})}$	$< C_T^{(\text{up})} >^+$	$< C_T^{(\text{up})} >^-$	$\overline{C}_{P\ (\text{Gen})}^{(\text{up})}$	$< C_{P\ (\text{Gen})}^{(\text{up})} >^+$	$< C_{P\ (\text{Gen})}^{(\text{up})} >^-$	${}_{\text{con}}\overline{G}_{C_P}^{(\text{up})}$ [%]
3	**5.3**	**-**	**Fixed**	**X**	**0.726**	**0.731**	**0.723**	**0.518**	**0.526**	**0.510**	**-**
85	5.3	5	Fixed	O	0.726	0.730	0.725	0.518	0.519	0.518	0.0
13	**5.3**	**-**	**2**	**X**	**0.725**	**0.799**	**0.640**	**0.522**	**0.651**	**0.392**	**-**
86	5.3	5	2	O	0.728	0.818	0.638	0.524	0.575	0.476	0.4
11	**5.3**	**-**	**4**	**X**	**0.716**	**0.853**	**0.541**	**0.526**	**0.773**	**0.274**	**-**
87	5.3	5	4	O	0.721	0.900	0.533	0.531	0.637	0.436	1.0
14	**5.3**	**-**	**8**	**X**	**0.673**	**0.867**	**0.345**	**0.516**	**0.853**	**0.098**	**-**
88	5.3	5	8	O	0.665	0.990	0.334	0.513	0.691	0.367	-0.7

Figure 6.6 displays $< C_T >$ & $< C_P >$ of the eight cases listed in Table 6.3. It can be seen that the ranges of $< C_T >$ & $< C_{P,\text{Aero}} >$ (aerodynamic properties) for the cases with controller are bigger than $< C_T >$ & $< C_P >$ for the cases without, while $< C_{P,\text{Gen}} >$ for the cases with controller is smaller than $< C_P >$ for the cases without (their maximum and minimum values are listed in Table 6.3). These show that the controller do effectively adjust its aerodynamic properties during the surging cycle, and the big inertia of the system stabilizes the output generator power. Another thing to point out is that the $< C_{P,\text{Aero}} >$ is no longer symmetry about $\phi_S = 1.0\pi$ for cases with the controller, where $< C_P >$ for the cases without controller (almost) do.

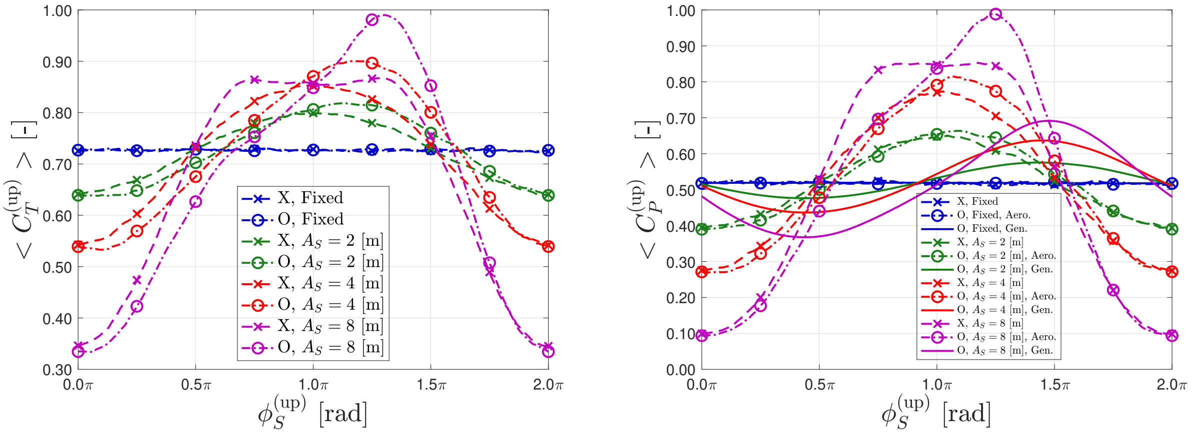

(a) $< C_T^{(\mathrm{up})} >$

(b) $< C_P^{(\mathrm{up})} >$

Figure 6.6: Comparing $< C_T^{(\mathrm{up})} >$ and $< C_P^{(\mathrm{up})} >$ for cases with different A_S and with or without controller. "O" stands for with the controller turned on while "X" stands for without controller.

6.3.4 Angle of Attack

Figure 6.7 & 6.8 display the cycle-averaged angle of attack of the upstream & downstream rotors ($< \alpha^{\mathrm{up}} >$ & $< \alpha^{\mathrm{down}} >$) for case with $\Delta_D = 3D$ (cases **81-84**). By comparing $< \alpha^{\mathrm{up}} >$ (Figure 6.7) with $< \alpha >$ of the single rotor cases without controller in subsection 4.5.4 (the upstream rotor is assumed to be not affected by the downstream rotor), it can be seen that even though the goal of the controller is to alleviate the effects of stalling by fixing α through regulating Ω, extents of stalling effects of the upstream rotor for cases with $\Delta_D = 3D$ are almost unaffected; this is related to the fact that I for the rotor is too big for the controller to properly adjust Ω. In section G.2, $< \alpha^{\mathrm{up}} >$ for the case with much smaller I is displayed and shows that the stalling effects are much cured. As for the downstream rotor ($< \alpha^{\mathrm{down}} >$ in Figure 6.8), stalling effects are more significant than the upstream rotor for the surging cases, the reason behind it may be that the effective $\mathbb{V}$ seen by the downstream rotor is bigger than the upstream one, just as the cases without controller in chapter 5.

For the cases with $\Delta_D = 5D$ (cases **85-88**), only $< \alpha^{\mathrm{down}} >$ are displayed (Figure 6.9) since $< \alpha^{\mathrm{up}} >$ for these cases are almost identical to cases with $\Delta_D = 3D$. It should be noted that except for the case with $A_S = 2$ m (case **86**), behaviours of $< \alpha^{\mathrm{down}} >$ for cases with $\Delta_D = 5D$ are very similar with $\Delta_D = 3D$, only that the surging cases with $\Delta_D = 5D$ have less stalling effects than cases with $\Delta_D = 3D$; probably due to that the effective $\mathbb{V}$ seen by the downstream rotor of cases with $\Delta_D = 5D$ is smaller than with $\Delta_D = 3D$, since V_0^{down} is more recovered for cases with $\Delta_D = 5D$. However, very interestingly, $< \alpha^{\mathrm{down}} >$ for the case with $A_S = 2$ m and $\Delta_D = 5D$ (Figure 6.9b) almost does not experienced stalling, even though $< \alpha^{\mathrm{up}} >$ does (Figure 6.7b), where the upstream rotor indeed has smaller effective $\mathbb{V}$; the actual reason behind this is unclear to author. However, it should be bear in mind that the system dynamics are actually very complicated and hard to precisely predict and explain, since there are multiple variables that influence the varying process of α, such as

I, A_S, Ω_S, the driving force ($\tau_{\text{Aero}} - \tau_{\text{Gen}}$), apparent inflow velocity, induction on velocity fields, turbulence, and even α itself.

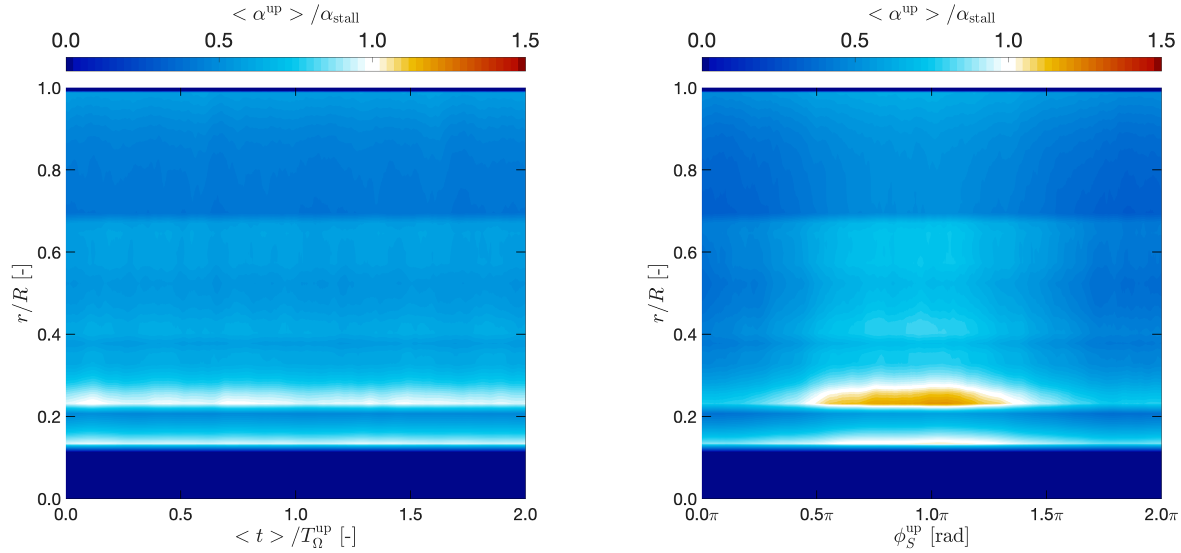

(a) Fixed (case **81**)

(b) $A_S = 2$ m (case **82**)

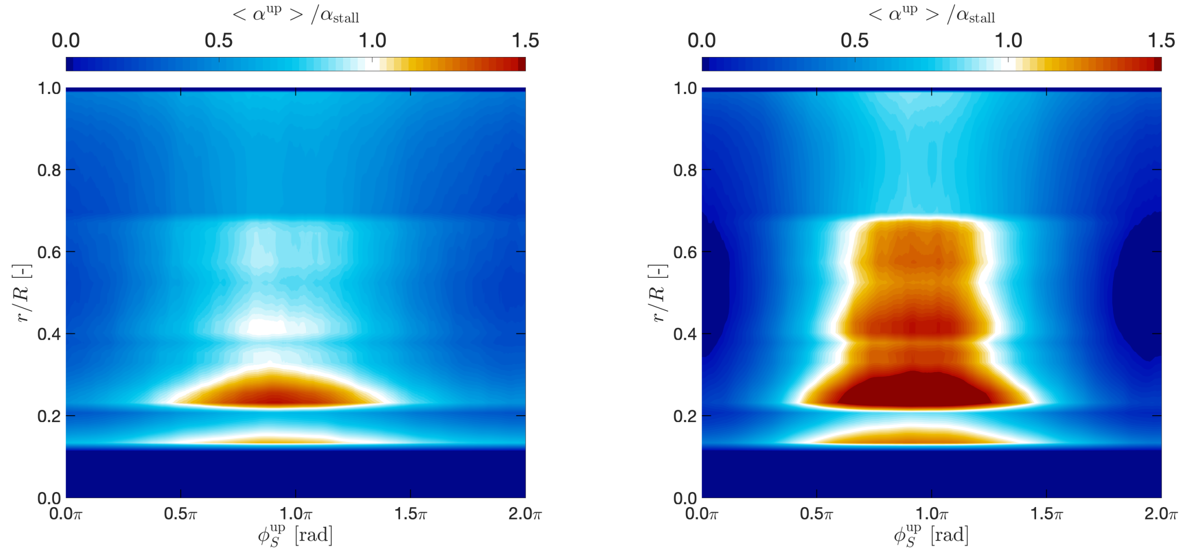

(c) $A_S = 4$ m (case **83**)

(d) $A_S = 8$ m (case **84**)

Figure 6.7: Cycle-averaged angle of attack of the upstream rotor $< \alpha^{\text{up}} >$ with $\Delta_D = 3D$ for cases with controlled rotor under turbulent inflow conditions.

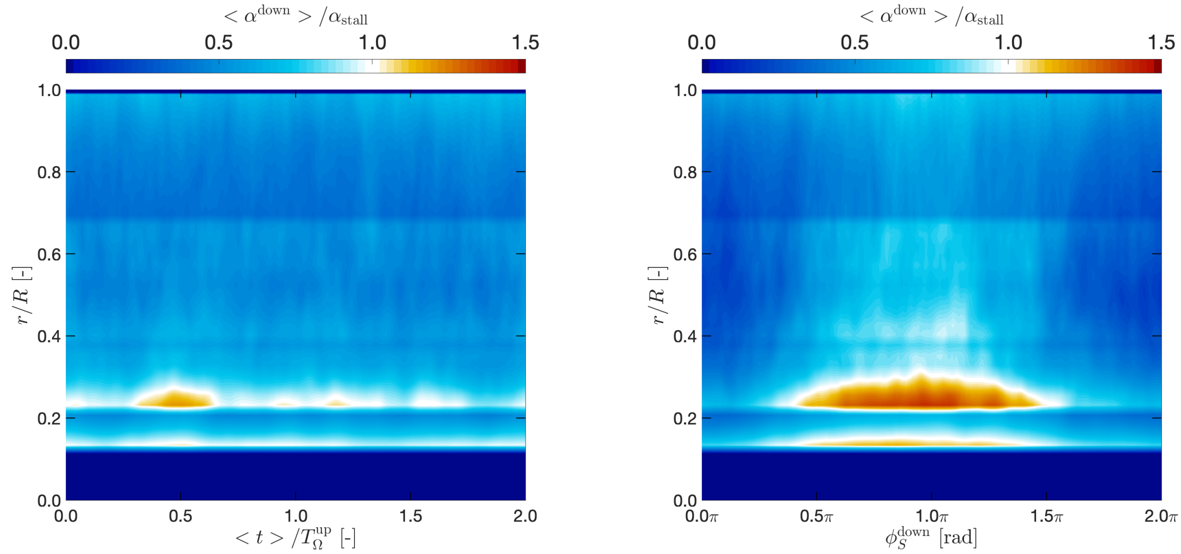

(a) Fixed (case **81**)　(b) $A_S = 2$ m (case **82**)

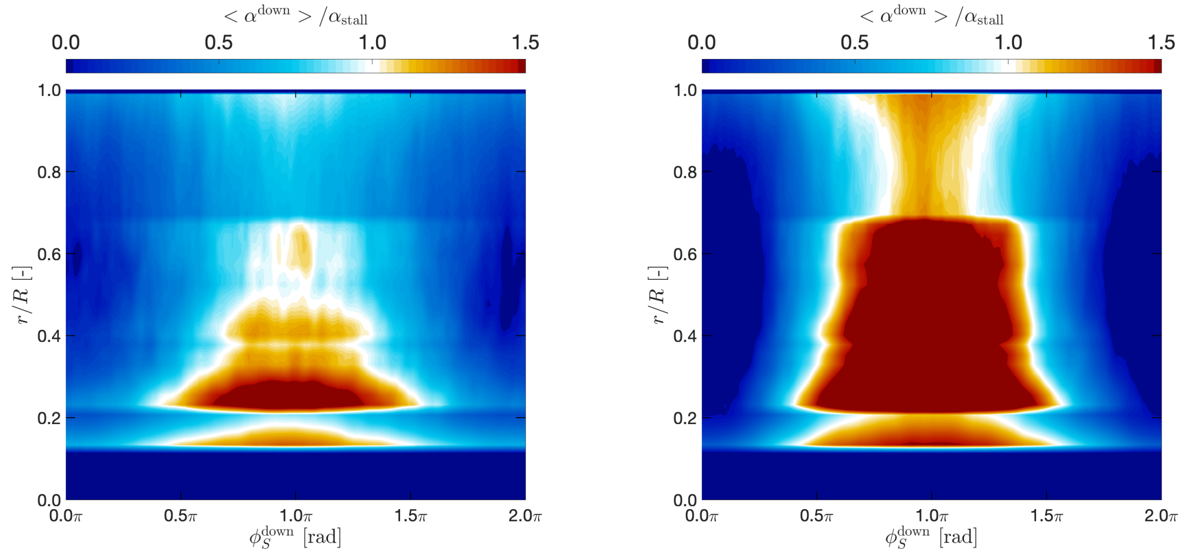

(c) $A_S = 4$ m (case **83**)　(d) $A_S = 8$ m (case **84**)

Figure 6.8: Cycle-averaged angle of attack of the downstream rotor $< \alpha^{\text{down}} >$ with $\Delta_D = 3D$ for cases with controlled rotor under turbulent inflow conditions.

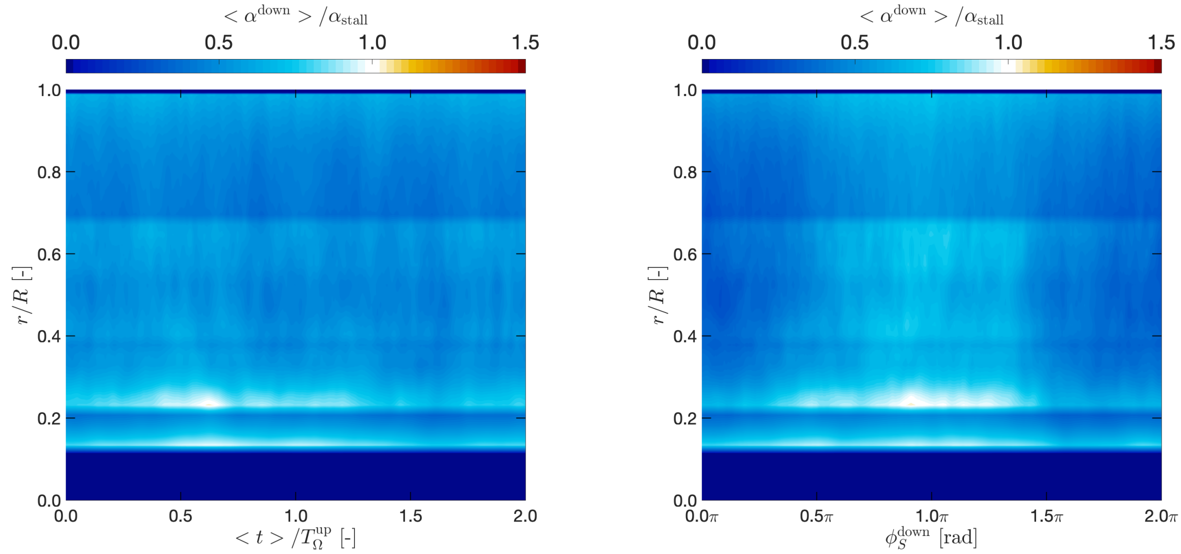

(a) Fixed (case **85**)

(b) $A_S = 2$ m (case **86**)

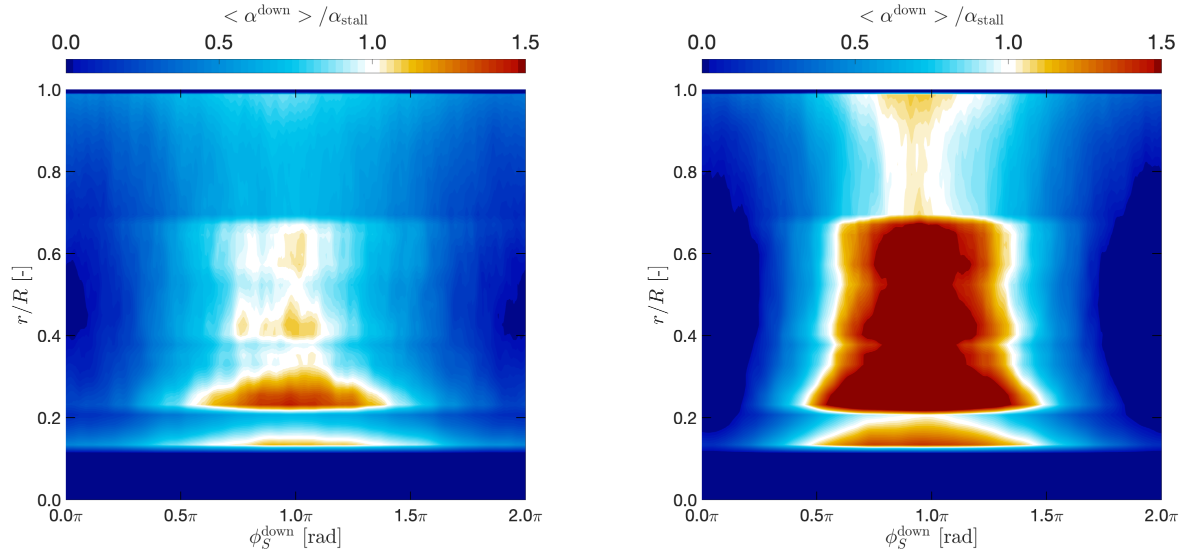

(c) $A_S = 4$ m (case **87**)

(d) $A_S = 8$ m (case **88**)

Figure 6.9: Cycle-averaged angle of attack of the downstream rotor $< \alpha^{\mathrm{down}} >$ with $\Delta_D = 5D$ for cases with controlled rotor under turbulent inflow conditions.

6.3.5 Cross Comparing $\overline{C}_P$

This subsection compares $\overline{C}_P$ of the cases with and without controller with a histogram in Figure 6.10. The interested cases are those listed in Table 6.2 and 6.3 together with four other selected cases with dual rotors without controller from Table 5.1. The selected cases are FF and SS ($\Delta_{\phi_{S_0}} = 0.0\pi$) with TI = 5.3% & $\Delta_D = 3D$ or $5D$. All the cases have inflow TI = 5.3%, and $\omega_S = 0.63$ rad/s for all the surging rotors. The main focus is to compare $\overline{C}_P$ with different A_S (including when the rotors are fixed) and Δ_D with and without the implementation of controller. Case **52** (FF, $\Delta_D = 5D$, without controller) is chosen to be the reference case. By comparing, clearly that for $A_S = 2$ or 4 m, surging motions do make $\overline{C}_P$ larger, and implementation of controller will also improved the values. However, as $A_S = 8$ m, both surging motions and implementation of controller has negative impacts on the power performances, which relate to the reaction speeds and stalling. Moreover, as comparing the fixed cases, blockage effects mentioned earlier can be clearly identified with slightly lower $\overline{C}_P$ for cases having $\Delta_D = 3D$ compare to the single rotor case, while cases having $\Delta_D = 5D$ almost have a identical values of $\overline{C}_P$ to the fixed single rotor case; blockage effects are also detectable for surging cases with $\Delta_D = 3D$ if comparing to the single rotor cases or cases with $\Delta_D = 5D$.

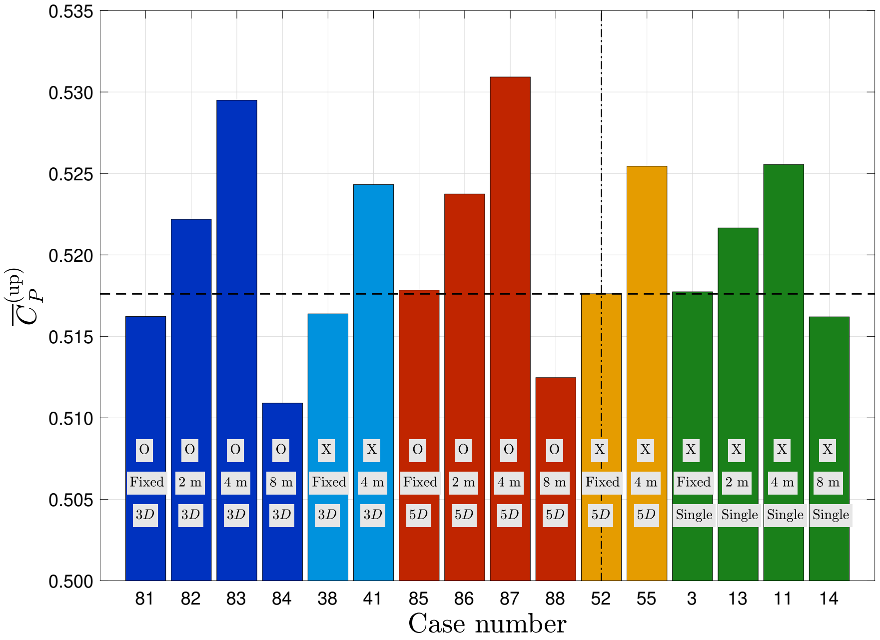

Figure 6.10: Histogram of $\overline{C}_P^{\mathrm{up}}$ (or $\overline{C}_P$) for cases in Table 6.2 & 6.3 together with four other selected cases. The selected cases are FF and SS ($\Delta_{\phi_{S_0}} = 0.0\pi$) with TI = 5.3% & $\Delta_D = 3D$ or $5D$ in Table 5.1. The three entries on each bar stand for whether the rotors are controlled, the values of A_S, & the values of Δ_D for each case. The value of the case FF without controller (case **52**) is chosen to be the reference value for comparison, it is indicated with horizontal dashed line.

6.4 Summarizing the Field Data

Since that the addition of the controller to the system does not alter the field values significantly, only the fields of $< u >_{0\pi}$ & $< \omega_y >_{0\pi}$ are presented;, they are in Figure 6.11 & 6.12. As expected, cases with bigger A_S have PLSB in sharper forms, and PLSB is even still able to be identified after the downstream rotor for the cases with $A_S = 8$ m. Furthermore, by comparing the fields here with the ones of the single rotor cases with the corresponding A_S under the same turbulent inflow conditions of TI $= 5.3\%$ (Figure 4.28 & 4.30), it can be found that the PLSB for the cases with controller is sharper than the one without, suggesting the controller will magnified the strength of PLSB. See section G.4 for the u fields and fields of the cases under laminar inflow conditions.

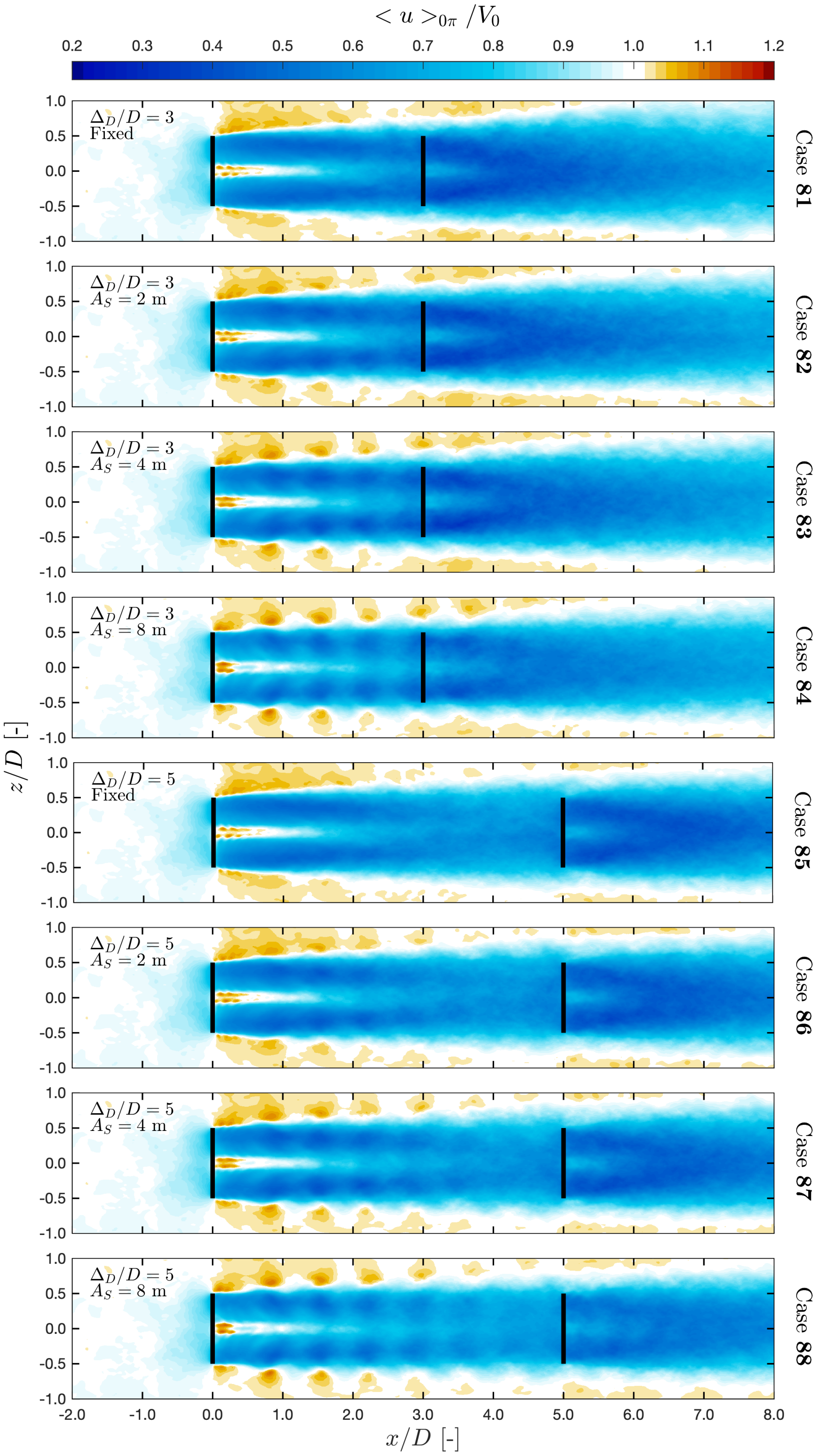

Figure 6.11: Fields of phase-locked averaged streamwise velocity $< u >_{0\pi}$ for dual rotors with controller under inflow conditions with TI = 5.3%.

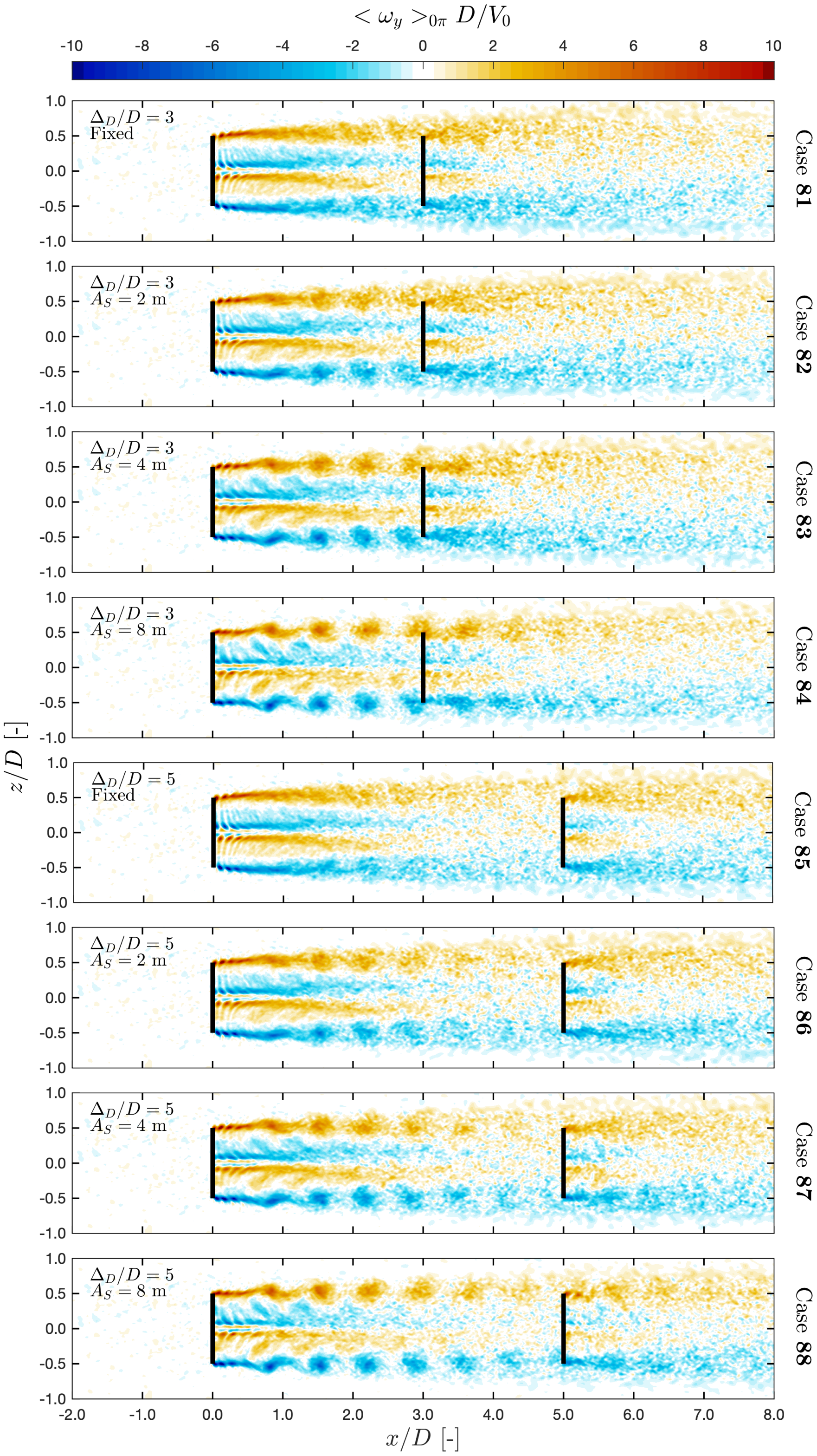

Figure 6.12: Fields of phase-locked averaged y-component vorticity $< \omega_y >_{0\pi}$ for dual rotors with controller under inflow conditions with TI = 5.3%.

6.5 Summary and Conclusions

In this chapter, eight (with another eleven in Appendix G) cases with dual surging or fixed rotors of NREL 5MW baseline turbine have been conducted with the implementation of a validated simple torque (MPPT) controller, and the setups & results are summarized in Table 6.2. All eight cases have realistic turbulent inflow conditions in offshore environment (TI = 5.3%), and four of them have $\Delta_D = 3D$, while $\Delta_D = 5D$ for the other four. Four different A_S are tested, including one being fixed ($A_S = 0$ m). Major discoveries and conclusions are listed below.

1. With the interested surging settings (A_S & ω_S), the implemented controller are not able to adjust the operational conditions (Ω) of the rotor fast enough to allow it to operate under the desired conditions. The main reason is the rotational inertia of the rotor I is quite large.
2. With the large inertia of the rotor, $C_{P,\mathrm{Gen}}$ is significantly lagging behind $C_{P,\mathrm{Aero}}$, and the varying ranges of $C_{P,\mathrm{Gen}}$ are smaller than the ones of $C_{P,\mathrm{Aero}}$ for the surging cases.
3. Stalling for the surging cases are not able to be cured with the implementation of the current controller, both for the upstream and downstream rotors.
4. In general, for the controlled cases considered in this chapter, the total power outputted will be benefited with moderate surging motions (positive ${}_{\mathrm{sur}}\overline{G}_{C_P}$), while there might be losses if surging effects lead to severe stalling.
5. Overall, the benefits of the current controller on $\overline{C}_P$ (${}_{\mathrm{con}}\overline{G}_{C_P}$) depend quite a lot on surging settings, and it may be only 1% with the cases considered in this chapter (there might even be losses), which is much lower than the values estimated with quasi-steady states predictions $\overline{C}_{P,\mathrm{Tar}}$.
6. With the implementation of current controller, the strengths of repeating coherent structures in wakes (PLSB) are magnified.

The results in this chapter suggested that to achieved better power output for FOWT subject to motions, more advanced controlling strategies may have to be implemented, while this topic will be left for future works.

Chapter 7

Conclusions and Recommendations

7.1 Concluding Remarks

This thesis conducted several simulations with high fidelity CFD method (LES with ALM) to comprehensively understand the wake structures, wake interactions, and rotors performances of surging floating offshore wind turbine (FOWT) rotors, including cases with single rotor without controller, cases with dual rotor in tandem without controller, and cases with dual rotor in tandem with controller. Both laminar and turbulent inflow conditions are considered, and the surging motions of FOWT in this thesis are prescribed and harmonic. The simulation framework is described in chapter 3, and it has also been verified and validated. The research questions proposed in section 1.3 are answered by analyzing the data of the simulation cases.

Will surge motions of FOWT significant alter its wake structures under both laminar and turbulent inflow conditions?

In chapter 4, it is found that surging will introduce periodic structures (PLSB) to the wake system after the surging FOWT for cases both under laminar and turbulent inflow conditions; PLSB can be readily observed with instantaneous fields for cases under laminar inflow conditions, while PLSB for cases under turbulent inflow conditions appear after phase-locked averaging. With the laminar cases, it is found that PLSB are formed by the merging of tip vorticies. The repeating rates of PLSB are as surging frequency ω_S, and bigger surging amplitude A_S brings sharper PLSB.

Will the effects of the surging motions on the wakes of FOWT facilitate the recovery rates of $\overline{u}_{\mathrm{Disk}}$?

In chapter 4, it is found that the induction fields of the vortical structures (PLSB) released due to surging facilitate flows to get in and come out of the wake of FOWT for both laminar and turbulent cases, and thus may enhance the mixing process and help recovering $\overline{u}_{\mathrm{Disk}}$. Indeed, $\overline{u}_{\mathrm{Disk}}$ at the downstream positions for the surging cases with laminar inflow conditions is significantly increased compare to the fixed case, but the increase rates are much less for cases with turbulent inflow conditions, and the increase rates do not have an obvious correlation with inflow TI; however, for both laminar and turbulent cases, the increase rates all have positive correlations with $\mathbb{V}$.

Additionally, in chapter 4, for the time-averaged power performances of the rotor $\overline{C}_P$, it is found that it has positive correlations with $\mathbb{V}$ if the rotor does not experience severe stalling during surging cycle. Moreover, surging rotors have lower values of $\overline{C}_T$.

How do the surging motions affect the wake interactions between two wind turbine rotors?

In chapter 5, it is found out that surging conformations do affect the wake interactions between two rotors in tandem a lot with laminar inflow conditions. However, with the turbulent inflow conditions having realistic TI (5.3%), whether the rotors are surging do not change the modes of wake interactions significantly. It is also find out $\Delta_{\phi_{S_0}}$ may slightly affect the power performance of the downstream rotor under turbulent inflow conditions with rather small inter-distance between rotors Δ_D (3D), while the effects of $\Delta_{\phi_{S_0}}$ diminish and become even negligible with larger Δ_D (5D). In general, surging do have positive effects on power performances for the system with two rotors, both making $\overline{C}_P$ itself and $\overline{u}_{\text{Disk}}$ larger, as long as stalling effects are not too severe. Furthermore, results in this chapter show that for same surging settings, performances of rotor operating under wake conditions are more subjected to surging motions than the one operating in freestream. The reason behind is the effective ratio between the inflow wind speed and the maximum surging speed $\mathbb{V}$ is bigger for the downstream rotor; note that this will also make the stalling effects of the downstream rotor stronger.

Is it possible to improve the rotor performances of surging FOWT by implementing simple controlling strategies?

In chapter 6, it is found that the implemented simple controller can only slightly improve the power performances of the two rotors to a little degree with moderate $\mathbb{V}$, the power performances are not improved as significant as the solutions of the quasi-steady states, which mainly relate to the large rotational inertia I of the system.

7.2 Outlooks and Recommendations

With the cases conducted and analysis made in this thesis project, wake structures, wake interactions, and rotors performances of surging FOWTs under both laminar and turbulent inflow conditions are systematically overviewed; to the author's best knowledge, this comprehensive overview had not been done previously, and this may help other fellow to quickly grasp the fundamentals of wake structures and wake interactions of surging FOWTs under both laminar and turbulent inflow conditions.

By comparing the cases with laminar inflow conditions and turbulent inflow conditions, it can be found that their wake structures are significantly different, especially for the surging cases. Thus, for the studies related to wake of FOWT in real world, inflow conditions with realistic TI may be a requirement.

With the analysis carried out with turbulent inflow conditions with realistic turbulent intensities, the differences about $\overline{u}_{\mathrm{Disk}}$ between fixed and surging cases are only about $0.5 \sim 2\%$. This indicates the sampling method should be well designed to capture the statistics accurately and precisely, especially for cases with wake interactions of multiple rotors.

Comparing the cases in chapter 5 and 6, it is found that implementing a simple controller can help adjust the operational conditions of the surging or fixed rotors, especially for the rotors operating under the wake conditions where the inflow velocity is hard to predict. The controller implemented in this thesis is easy to setup and cost negligible computational effort, and the parameters for setting the controller should not be difficult to obtain in most cases.

Results of this thesis show that power performances of surging rotors are highly related to surging settings, especially for those operating under wake conditions with lower effective inflow wind speed; thus, having realistic surging settings are important if the goal is to model systems with realistic FOWT rotors.

For the future works, cases with other degree of freedoms, such as pitching, heaving, swaying, and rolling (or combinations of multiple degree of freedoms), can be tested to better understand the wake structures of FOWT, and turbulent inflow conditions should be considered in order to better simulate real world conditions. Also that cases with more FOWT rotors can be conducted to understand the wake interactions within the floating offshore wind farms more. Furthermore, this framework may also be used to test newer and more advanced controlling strategies designed for floating offshore wind farms.

Bibliography

[1] G. Van Kuik, J. Peinke, R. Nijssen, D. Lekou, J. Mann, J. N. Sørensen, C. Ferreira, J.-W. van Wingerden, D. Schlipf, P. Gebraad *et al.*, "Long-term research challenges in wind energy–a research agenda by the european academy of wind energy," *Wind energy science*, vol. 1, no. 1, pp. 1–39, 2016.

[2] S. Bouckaert, A. F. Pales, C. McGlade, U. Remme, B. Wanner, L. Varro, D. D'Ambrosio, and T. Spencer, "Net zero by 2050: A roadmap for the global energy sector," 2021.

[3] BloombergNEF, "The Next Phase of Wind Power Growth in Five Charts," 2022. [Online]. Available: https://about.bnef.com/blog/the-next-phase-of-wind-power-growth-in-five-charts/

[4] P. Veers, K. Dykes, E. Lantz, S. Barth, C. L. Bottasso, O. Carlson, A. Clifton, J. Green, P. Green, H. Holttinen *et al.*, "Grand challenges in the science of wind energy," *Science*, vol. 366, no. 6464, p. eaau2027, 2019.

[5] S. Butterfield, W. Musial, J. Jonkman, and P. Sclavounos, "Engineering challenges for floating offshore wind turbines," National Renewable Energy Lab.(NREL), Golden, CO (United States), Tech. Rep., 2007.

[6] White House, "FACT SHEET: Biden-Harris Administration Announces New Actions to Expand U.S. Offshore Wind Energy," 2022. [Online]. Available: https://www.whitehouse.gov/briefing-room/statements-releases/2022/09/15/fact-sheet-biden-harris-administration-announces-new-actions-to-expand-u-s-offshore-wind-energy/

[7] Crown Estate Scotland, "ScotWind offshore wind leasing delivers major boost to Scotland's net zero aspirations," 2022. [Online]. Available: https://www.crownestatescotland.com/news/scotwind-offshore-wind-leasing-delivers-major-boost-to-scotlands-net-zero-aspirations

[8] offshoreWIND.biz, "KF Wind wins new license for its 1.2 GW floating wind project in South Korea," 2022. [Online]. Available: https://www.offshorewind.biz/2022/03/03/ocean-winds-aker-offshore-wind-secure-1-2-gw-floating-capacity-in-south-korea

[9] D. Micallef and A. Rezaeiha, "Floating offshore wind turbine aerodynamics: Trends and future challenges," *Renewable and Sustainable Energy Reviews*, vol. 152, p. 111696, 2021.

[10] T. T. Tran and D.-H. Kim, "A CFD study into the influence of unsteady aerodynamic interference on wind turbine surge motion," *Renewable Energy*, vol. 90, pp. 204–228, 2016.

[11] H. M. Johlas, L. A. Martínez-Tossas, M. J. Churchfield, M. A. Lackner, and D. P. Schmidt, "Floating platform effects on power generation in spar and semisubmersible wind turbines," *Wind Energy*, vol. 24, no. 8, pp. 901–916, 2021.

[12] R. Farrugia, T. Sant, and D. Micallef, "A study on the aerodynamics of a floating wind turbine rotor," *Renewable energy*, vol. 86, pp. 770–784, 2016.

[13] A. Fontanella, I. Bayati, R. Mikkelsen, M. Belloli, and A. Zasso, "UNAFLOW: a holistic wind tunnel experiment about the aerodynamic response of floating wind turbines under imposed surge motion," *Wind Energy Science*, vol. 6, no. 5, pp. 1169–1190, 2021.

[14] L. Vermeer, J. N. Sørensen, and A. Crespo, "Wind turbine wake aerodynamics," *Progress in aerospace sciences*, vol. 39, no. 6-7, pp. 467–510, 2003.

[15] J. F. Herbert-Acero, O. Probst, P.-E. Réthoré, G. C. Larsen, and K. K. Castillo-Villar, "A review of methodological approaches for the design and optimization of wind farms," *Energies*, vol. 7, no. 11, pp. 6930–7016, 2014.

[16] P.-Å. Krogstad and L. Sætran, "Wind turbine wake interactions; results from blind tests," in *Journal of Physics: Conference Series*, vol. 625, no. 1. IOP Publishing, 2015, p. 012043.

[17] H. Sarlak, C. Meneveau, and J. N. Sørensen, "Role of subgrid-scale modeling in large eddy simulation of wind turbine wake interactions," *Renewable Energy*, vol. 77, pp. 386–399, 2015.

[18] R. J. Stevens and C. Meneveau, "Flow structure and turbulence in wind farms," *Annual review of fluid mechanics*, vol. 49, pp. 311–339, 2017.

[19] F. Porté-Agel, M. Bastankhah, and S. Shamsoddin, "Wind-turbine and wind-farm flows: a review," *Boundary-Layer Meteorology*, vol. 174, no. 1, pp. 1–59, 2020.

[20] A. Rezaeiha and D. Micallef, "Wake interactions of two tandem floating offshore wind turbines: CFD analysis using actuator disc model," *Renewable Energy*, vol. 179, pp. 859–876, 2021.

[21] A. Arabgolarcheh, S. Jannesarahmadi, and E. Benini, "Modeling of near wake characteristics in floating offshore wind turbines using an actuator line method," *Renewable Energy*, vol. 185, pp. 871–887, 2022.

[22] V. G. Kleine, L. Franceschini, B. S. Carmo, A. Hanifi, and D. S. Henningson, "The stability of wakes of floating wind turbines," *Physics of Fluids*, vol. 34, no. 7, 2022.

[23] S. Mancini, K. Boorsma, M. Caboni, M. Cormier, T. Lutz, P. Schito, and A. Zasso, "Characterization of the unsteady aerodynamic response of a floating offshore wind turbine to surge motion," *Wind Energy Science*, vol. 5, no. 4, pp. 1713–1730, 2020.

[24] Acteon Group, "Floating Wind: What are the Mooring Options?" 2020. [Online]. Available: https://acteon.com/blog/floating-wind-mooring-options/

[25] P. Chen, J. Chen, and Z. Hu, "Review of experimental-numerical methodologies and challenges for floating offshore wind turbines," *Journal of Marine Science and Application*, vol. 19, no. 3, pp. 339–361, 2020.

[26] M. A. Miller, J. Kiefer, C. Westergaard, M. O. Hansen, and M. Hultmark, "Horizontal axis wind turbine testing at high reynolds numbers," *Physical Review Fluids*, vol. 4, no. 11, p. 110504, 2019.

[27] K. Sivalingam, S. Martin, and A. A. Singapore Wala, "Numerical validation of floating offshore wind turbine scaled rotors for surge motion," *Energies*, vol. 11, no. 10, p. 2578, 2018.

[28] A. Cordle and J. Jonkman, "State of the art in floating wind turbine design tools," in *The twenty-first international offshore and polar engineering conference*. OnePetro, 2011.

[29] C. Ferreira, W. Yu, A. Sala, and A. Viré, "Dynamic inflow model for a floating horizontal axis wind turbine in surge motion," *Wind Energy Science*, vol. 7, no. 2, pp. 469–485, 2022.

[30] T. Sebastian and M. Lackner, "Analysis of the induction and wake evolution of an offshore floating wind turbine," *Energies*, vol. 5, no. 4, pp. 968–1000, 2012.

[31] H. Lee and D.-J. Lee, "Effects of platform motions on aerodynamic performance and unsteady wake evolution of a floating offshore wind turbine," *Renewable Energy*, vol. 143, pp. 9–23, 2019.

[32] Y.-T. Wu and F. Porté-Agel, "Large-eddy simulation of wind-turbine wakes: evaluation of turbine parametrisations," *Boundary-layer meteorology*, vol. 138, no. 3, pp. 345–366, 2011.

[33] N. Sedaghatizadeh, M. Arjomandi, R. Kelso, B. Cazzolato, and M. H. Ghayesh, "Modelling of wind turbine wake using large eddy simulation," *Renewable Energy*, vol. 115, pp. 1166–1176, 2018.

[34] S.-P. Breton, J. Sumner, J. N. Sørensen, K. S. Hansen, S. Sarmast, and S. Ivanell, "A survey of modelling methods for high-fidelity wind farm simulations using large eddy simulation," *Philosophical Transactions of the Royal Society A: Mathematical, Physical and Engineering Sciences*, vol. 375, no. 2091, p. 20160097, 2017.

[35] Z. Gao, Y. Li, T. Wang, S. Ke, and D. Li, "Recent improvements of actuator line-large-eddy simulation method for wind turbine wakes," *Applied Mathematics and Mechanics*, vol. 42, no. 4, pp. 511–526, 2021.

[36] J. N. Sorensen and W. Z. Shen, "Numerical modeling of wind turbine wakes," *J. Fluids Eng.*, vol. 124, no. 2, pp. 393–399, 2002.

[37] R. Mikkelsen and J. Sørensen, "Actuator disc methods applied to wind turbines," Ph.D. dissertation, Technical University of Denmark, 2003.

[38] P. Bachant, A. Goude, and M. Wosnik, "Actuator line modeling of vertical-axis turbines," *arXiv preprint arXiv:1605.01449*, 2016.

[39] L. A. Martínez-Tossas, M. J. Churchfield, and S. Leonardi, "Large eddy simulations of the flow past wind turbines: actuator line and disk modeling," *Wind Energy*, vol. 18, no. 6, pp. 1047–1060, 2015.

[40] T. Revaz and F. Porté-Agel, "Large-eddy simulation of wind turbine flows: A new evaluation of actuator disk models," *Energies*, vol. 14, no. 13, p. 3745, 2021.

[41] F. Porté-Agel, Y.-T. Wu, H. Lu, and R. J. Conzemius, "Large-eddy simulation of atmospheric boundary layer flow through wind turbines and wind farms," *Journal of Wind Engineering and Industrial Aerodynamics*, vol. 99, no. 4, pp. 154–168, 2011.

[42] M. Churchfield, S. Lee, and P. Moriarty, "Overview of the simulator for wind farm application (SOWFA)," *National Renewable Energy Laboratory*, 2012.

[43] N. Troldborg, "Actuator line modeling of wind turbine wakes," 2009.

[44] T. Tran, D. Kim, and J. Song, "Computational fluid dynamic analysis of a floating offshore wind turbine experiencing platform pitching motion," *Energies*, vol. 7, no. 8, pp. 5011–5026, 2014.

[45] D. Micallef and T. Sant, "Loading effects on floating offshore horizontal axis wind turbines in surge motion," *Renewable Energy*, vol. 83, pp. 737–748, 2015.

[46] M. Cormier, M. Caboni, T. Lutz, K. Boorsma, and E. Krämer, "Numerical analysis of unsteady aerodynamics of floating offshore wind turbines," in *Journal of Physics: Conference Series*, vol. 1037, no. 7. IOP Publishing, 2018, p. 072048.

[47] M. Draper, A. Guggeri, M. Mendina, G. Usera, and F. Campagnolo, "A large eddy simulation-actuator line model framework to simulate a scaled wind energy facility and its application," *Journal of Wind Engineering and Industrial Aerodynamics*, vol. 182, pp. 146–159, 2018.

[48] J. Wang, C. Wang, O. Castañeda, F. Campagnolo, and C. Bottasso, "Large-eddy simulation of scaled floating wind turbines in a boundary layer wind tunnel," in *Journal of Physics: Conference Series*, vol. 1037, no. 7. IOP Publishing, 2018, p. 072032.

[49] H. Johlas, L. A. Martínez-Tossas, D. Schmidt, M. Lackner, and M. J. Churchfield, "Large eddy simulations of floating offshore wind turbine wakes with coupled platform motion," in *Journal of Physics: Conference Series*, vol. 1256, no. 1. IOP Publishing, 2019, p. 012018.

[50] P. Cheng, Y. Huang, and D. Wan, "A numerical model for fully coupled aero-hydrodynamic analysis of floating offshore wind turbine," *Ocean Engineering*, vol. 173, pp. 183–196, 2019.

[51] T. H. Snedker, "Investigation of wake interaction for floating offshore wind turbines in the atmospheric boundary layer," 2020.

[52] A. S. Wise and E. E. Bachynski, "Wake meandering effects on floating wind turbines," *Wind Energy*, vol. 23, no. 5, pp. 1266–1285, 2020.

[53] F. Xue, H. Duan, C. Xu, X. Han, Y. Shangguan, T. Li, and Z. Fen, "Research on the power capture and wake characteristics of a wind turbine based on a modified actuator line model," *Energies*, vol. 15, no. 1, p. 282, 2022.

[54] X. Shen, J. Chen, P. Hu, X. Zhu, and Z. Du, "Study of the unsteady aerodynamics of floating wind turbines," *Energy*, vol. 145, pp. 793–809, 2018.

[55] G. Chen, X.-F. Liang, and X.-B. Li, "Modelling of wake dynamics and instabilities of a floating horizontal-axis wind turbine under surge motion," *Energy*, vol. 239, p. 122110, 2022.

[56] J. F. Manwell, J. G. McGowan, and A. L. Rogers, *Wind energy explained: theory, design and application.* John Wiley & Sons, 2010.

[57] K. M. Kopperstad, R. Kumar, and K. Shoele, "Aerodynamic characterization of barge and spar type floating offshore wind turbines at different sea states," *Wind Energy*, vol. 23, no. 11, pp. 2087–2112, 2020.

[58] J. A. Frederik, R. Weber, S. Cacciola, F. Campagnolo, A. Croce, C. Bottasso, and J.-W. van Wingerden, "Periodic dynamic induction control of wind farms: proving the potential in simulations and wind tunnel experiments," *Wind Energy Science*, vol. 5, no. 1, pp. 245–257, 2020.

[59] Y. Fang, L. Duan, Z. Han, Y. Zhao, and H. Yang, "Numerical analysis of aerodynamic performance of a floating offshore wind turbine under pitch motion," *Energy*, vol. 192, p. 116621, 2020.

[60] Y. Fang, G. Li, L. Duan, Z. Han, and Y. Zhao, "Effect of surge motion on rotor aerodynamics and wake characteristics of a floating horizontal-axis wind turbine," *Energy*, vol. 218, p. 119519, 2021.

[61] H. S. Chivaee, *Large eddy simulation of turbulent flows in wind energy.* DTU Vindenergi, 2014.

[62] J. Jonkman, S. Butterfield, W. Musial, and G. Scott, "Definition of a 5-MW reference wind turbine for offshore system development," National Renewable Energy Lab.(NREL), Golden, CO (United States), Tech. Rep., 2009.

[63] A. Yakhot, H. Liu, and N. Nikitin, "Turbulent flow around a wall-mounted cube: A direct numerical simulation," *International journal of heat and fluid flow*, vol. 27, no. 6, pp. 994–1009, 2006.

[64] R. Muscari, A. Di Mascio, and R. Verzicco, "Modeling of vortex dynamics in the wake of a marine propeller," *Computers & Fluids*, vol. 73, pp. 65–79, 2013.

[65] G. Erlebacher, M. Y. Hussaini, C. G. Speziale, and T. A. Zang, "Toward the large-eddy simulation of compressible turbulent flows," *Journal of fluid mechanics*, vol. 238, pp. 155–185, 1992.

[66] J. Smagorinsky, "General circulation experiments with the primitive equations: I. the basic experiment," *Monthly weather review*, vol. 91, no. 3, pp. 99–164, 1963.

[67] M. Germano, "Turbulence: the filtering approach," *Journal of Fluid Mechanics*, vol. 238, pp. 325–336, 1992.

[68] F. Porté-Agel, C. Meneveau, and M. B. Parlange, "A scale-dependent dynamic model for large-eddy simulation: application to a neutral atmospheric boundary layer," *Journal of Fluid Mechanics*, vol. 415, pp. 261–284, 2000.

[69] L. A. Martinez-Tossas, M. J. Churchfield, A. E. Yilmaz, H. Sarlak, P. L. Johnson, J. N. Sørensen, J. Meyers, and C. Meneveau, "Comparison of four large-eddy simulation research codes and effects of model coefficient and inflow turbulence in actuator-line-based wind turbine modeling," *Journal of Renewable and Sustainable Energy*, vol. 10, no. 3, p. 033301, 2018.

[70] V. Mendoza, P. Bachant, C. Ferreira, and A. Goude, "Near-wake flow simulation of a vertical axis turbine using an actuator line model," *Wind Energy*, vol. 22, no. 2, pp. 171–188, 2019.

[71] R. Poletto, T. Craft, and A. Revell, "A new divergence free synthetic eddy method for the reproduction of inlet flow conditions for les," *Flow, turbulence and combustion*, vol. 91, pp. 519–539, 2013.

[72] Pete Bachant, Anders Goude, Daa-mec, Martin Wosnik, "turbinesFoam: v0.1.1," 2019. [Online]. Available: https://zenodo.org/record/3542301#.Y9CZ6C-KCJ8

[73] J. Nathan, A. M. Forsting, N. Troldborg, and C. Masson, "Comparison of openfoam and ellipsys3d actuator line methods with (new) mexico results," in *Journal of Physics: Conference Series*, vol. 854, no. 1. IOP Publishing, 2017, p. 012033.

[74] K. O. Dağ and J. N. Sørensen, "A new tip correction for actuator line computations," *Wind Energy*, vol. 23, no. 2, pp. 148–160, 2020.

[75] X. Zhang, J. Jia, L. Zheng, W. Yi, and Z. Zhang, "Maximum power point tracking algorithms for wind power generation system: Review, comparison and analysis," *Energy Science & Engineering*, vol. 11, no. 1, pp. 430–444, 2023.

[76] P. Novak, "On the modelling and partial-load control of variable-speed wind turbines," 1995.

[77] D. Mehta, A. Van Zuijlen, B. Koren, J. Holierhoek, and H. Bijl, "Large eddy simulation of wind farm aerodynamics: A review," *Journal of Wind Engineering and Industrial Aerodynamics*, vol. 133, pp. 1–17, 2014.

[78] I. Bayati, M. Belloli, L. Bernini, H. Giberti, and A. Zasso, "Scale model technology for floating offshore wind turbines," *IET Renewable Power Generation*, vol. 11, no. 9, pp. 1120–1126, 2017.

[79] C. Bak, F. Zahle, R. Bitsche, T. Kim, A. Yde, L. C. Henriksen, M. H. Hansen, J. P. A. A. Blasques, M. Gaunaa, and A. Natarajan, "The dtu 10-mw reference wind turbine," in *Danish wind power research 2013*, 2013.

[80] J. Crank and P. Nicolson, "A practical method for numerical evaluation of solutions of partial differential equations of the heat-conduction type," in *Mathematical proceedings of the Cambridge philosophical society*, vol. 43, no. 1. Cambridge University Press, 1947, pp. 50–67.

[81] DTU Computing Center, "DTU Computing Center resources," 2022. [Online]. Available: https://doi.org/10.48714/DTU.HPC.0001

[82] J. N. Sørensen, R. F. Mikkelsen, D. S. Henningson, S. Ivanell, S. Sarmast, and S. J. Andersen, "Simulation of wind turbine wakes using the actuator line technique," *Philosophical Transactions of the Royal Society A: Mathematical, Physical and Engineering Sciences*, vol. 373, no. 2035, p. 20140071, 2015.

[83] I. Cheeseman, "Fluid-dynamic drag: Practical information on aerodynamic drag and hydrodynamic resistance. sf hoerner. hoerner fluid dynamics, brick town, new jersey. 1965. 455 pp. illustrated. $24.20." *The Aeronautical Journal*, vol. 80, no. 788, pp. 371–371, 1976.

[84] S. Naderi and F. Torabi, "Numerical investigation of wake behind a hawt using modified actuator disc method," *Energy Conversion and Management*, vol. 148, pp. 1346–1357, 2017.

[85] S. B. Pope and S. B. Pope, *Turbulent flows.* Cambridge university press, 2000.

[86] International Electrotechnical Commission, "International Standard IEC 61400-1, Edition 4.0," 2019.

[87] T. N. Nandi and D. Yeo, “Estimation of integral length scales across the neutral atmospheric boundary layer depth: a large eddy simulation study,” *Journal of Wind Engineering and Industrial Aerodynamics*, vol. 218, p. 104715, 2021.

[88] D. A. Pollak, “Characterization of ambient offshore turbulence intensity from analysis of nine offshore meteorological masts in northern europe,” Master’s thesis, Technical University of Denmark, 2014.

[89] S. B. Pope, “Ten questions concerning the large-eddy simulation of turbulent flows,” *New journal of Physics*, vol. 6, no. 1, p. 35, 2004.

[90] P. Li, P. Cheng, D. Wan, and Q. Xiao, “Numerical simulations of wake flows of floating offshore wind turbines by unsteady actuator line model,” in *Proceedings of the 9th international workshop on ship and marine hydrodynamics, Glasgow, UK*, 2015, pp. 26–28.

[91] Z. Yu, X. Zheng, and Q. Ma, “Study on actuator line modeling of two NREL 5-MW wind turbine wakes,” *applied sciences*, vol. 8, no. 3, p. 434, 2018.

[92] A. Fontanella, A. Zasso, and M. Belloli, “Wind tunnel investigation of the wake-flow response for a floating turbine subjected to surge motion,” in *Journal of Physics: Conference Series*, vol. 2265, no. 4. IOP Publishing, 2022, p. 042023.

[93] G. M. Stewart, A. Robertson, J. Jonkman, and M. A. Lackner, “The creation of a comprehensive metocean data set for offshore wind turbine simulations,” *Wind Energy*, vol. 19, no. 6, pp. 1151–1159, 2016.

[94] R. Kyle, Y. C. Lee, and W.-G. Früh, “Propeller and vortex ring state for floating offshore wind turbines during surge,” *Renewable Energy*, vol. 155, pp. 645–657, 2020.

[95] J. Meyers and C. Meneveau, “Optimal turbine spacing in fully developed wind farm boundary layers,” *Wind energy*, vol. 15, no. 2, pp. 305–317, 2012.

[96] N. J. Choi, S. H. Nam, J. H. Jeong, and K. C. Kim, “Numerical study on the horizontal axis turbines arrangement in a wind farm: Effect of separation distance on the turbine aerodynamic power output,” *Journal of Wind Engineering and Industrial Aerodynamics*, vol. 117, pp. 11–17, 2013.

[97] R. J. Stevens, D. F. Gayme, and C. Meneveau, “Effects of turbine spacing on the power output of extended wind-farms,” *Wind Energy*, vol. 19, no. 2, pp. 359–370, 2016.

[98] P. Benard, A. Viré, V. Moureau, G. Lartigue, L. Beaudet, P. Deglaire, and L. Bricteux, “Large-eddy simulation of wind turbines wakes including geometrical effects,” *Computers & Fluids*, vol. 173, pp. 133–139, 2018.

[99] F. Zigunov, “Pod - proper orthogonal decomposition (wrapper).” [Online]. Available: https://www.mathworks.com/matlabcentral/fileexchange/72022-pod-proper-orthogonal-decomposition-wrapper

[100] P. K. Kundu, I. M. Cohen, and D. R. Dowling, *Fluid mechanics.* Academic press, 2015.

[101] N. J. Abbas, A. Wright, and L. Pao, "An update to the national renewable energy laboratory baseline wind turbine controller," in *Journal of Physics: Conference Series*, vol. 1452, no. 1. IOP Publishing, 2020, p. 012002.

Appendix A

Turbulence Noise with Mesh Layouts

As conducting cases of NREL 5MW rotor with laminar inflow conditions, it was found that the minor turbulence triggered by numerical errors may become significant to the overall solution to some extent, and they are related to the mesh layouts. Figure A.2 displays the contour plots of ω_y (instantaneous y-component of the vorticity vector) on the $y = 0$ plane of three cases having identical setups (same as the fixed case in chapter 4) but with minor differences in mesh layouts. For convenience, the three meshes are labeled as configurations 1, 2, and 3, and their schematic diagrams can be found in Figure A.1, 3.1, and 3.2. As can be seen in Figure A.2, the periodic ripples of the vorticities are related to the changing of the mesh resolutions. However, as observed by the author, this ripples were propagated in upstream direction from the rotor at the initial state of the simulations. Moreover, the strength of these ripples seems to be correlated to the rotor loading distributions. Furthermore, if the spatial scheme is switched from second order central differencing (`Gauss linear`) to second order upwind differencing (`Gauss linearUpwind grad(U)`), the ripples can be much more alleviated (not shown here). This agrees with many other studies stating that second order central differencing would suffer bigger numerical oscillations. However, upwind differencing is widely considered being over-dissipative, and it will lead to over dissipate vortical structures in the wakes of wind turbines rotor [61, 98]; thus it is not adopted in this thesis.

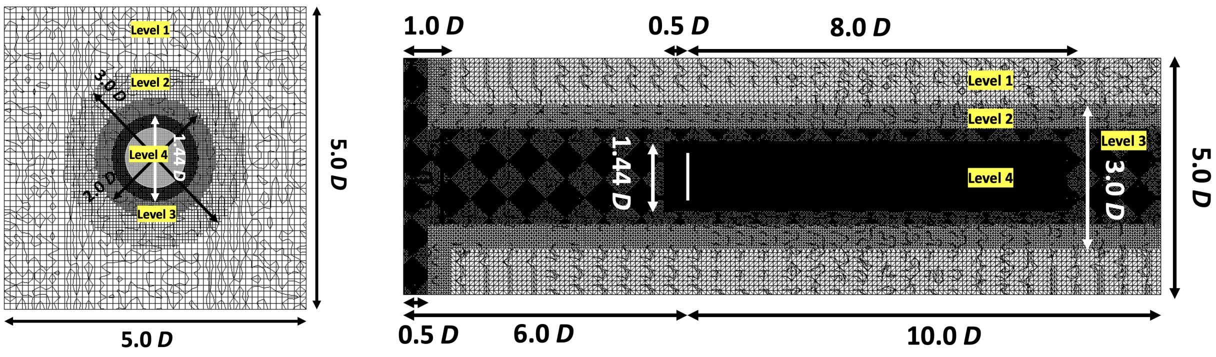

(a) yz plane

(b) xz plane

Figure A.1: Schematic diagrams for mesh layouts of mesh configuration 1. This mesh is an older attempt during the thesis project.

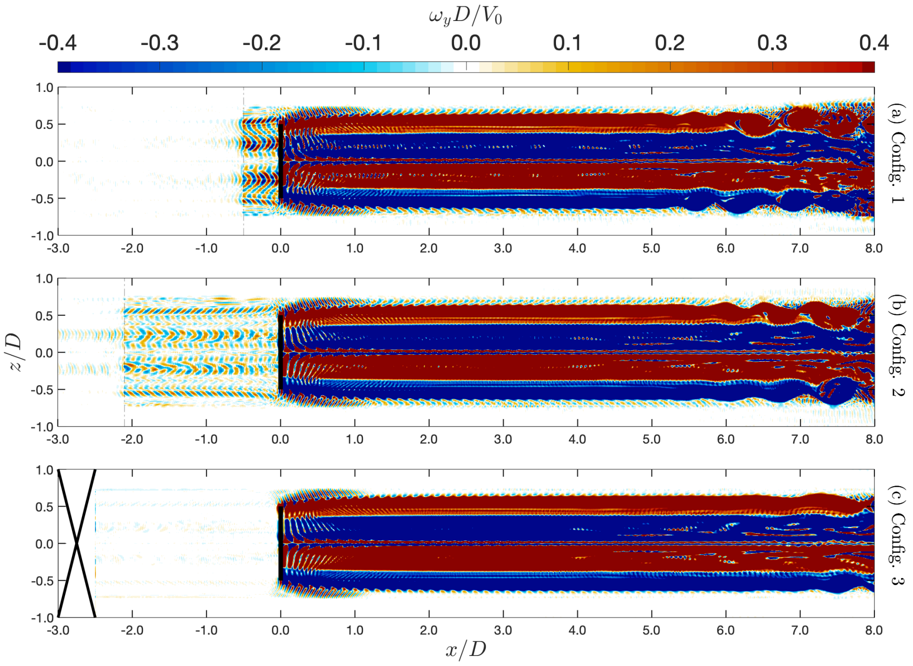

Figure A.2: Contour plots of ω_y with different mesh configurations of laminar inflow cases with NREL 5MW. The dashed-lines indicate the refinement boundaries in streamwise direction.

Even though the errors are relatively small (note the scale in Figure A.2), and are almost insignificant for cases with turbulence inflow conditions, they still cannot be ignored in laminar cases. Since that even with the very minor fluctuations, they will trigger the instability of the wind turbine wake systems and accelerate the break-down process significantly [61]; this can be clearly observed in Figure A.2. Table A.1 and Figure A.3 show more detail information about the turbulence measured at $2.0D$ upstream form the rotor with the three mesh configurations, clearly that there are some periodic-like oscillations and the three configurations shared a very similar oscillation frequencies. After comparing, for the laminar cases, configuration 3 was selected since it retained the laminar properties the most. While for the turbulent cases, concept of configuration 3 was not chosen since the prolonged distance for turbulent flow to develop and refinement regions needed for turbulent inlet will result in too many cells, also that these ripples are much more diluted with the turbulent inflow conditions. Considering that configuration 2 seems able to deliver cleaner laminar flow than configuration 1 (one should notice that $2.0D$ upstream form the rotor falls out the wake refinement region for configuration 1), configuration 2 is thus chosen as the mesh layouts for the turbulent cases.

Table A.1: Turbulence intensities and length scales measured at 2.0D upstream from rotor with three mesh configurations.

Configuration	TI [%]	L_u [m]
1	0.131	8.63
2	0.167	8.64
3	0.116	8.48

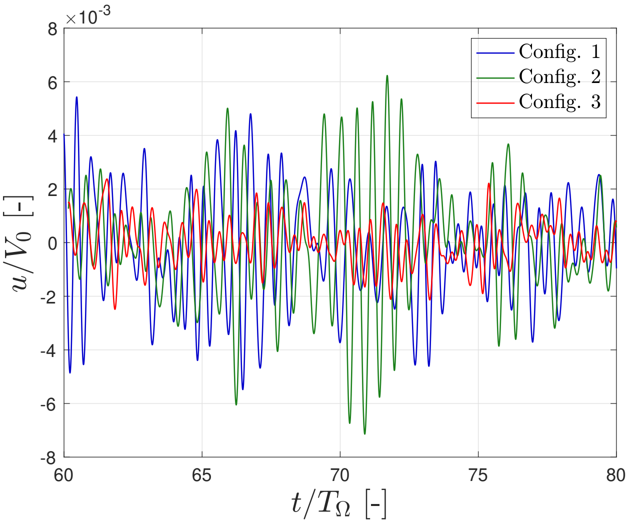

Figure A.3: Time series streamwise velocity data sampled at 2.0D upstream at rotor center with three different mesh configurations ($V_0 = 11.4$ m/s).

Appendix B

Momentum Entertainment

Term $\partial\overline{uu}/\partial x$ can be written as Equation B.1 by applying chain rule and Reynolds decomposition ($u = \overline{u} + u^{'}$). And for the wake regions being free from the projected body force fields of actuator lines, x-component of the filtered Navier-Stokes equations Equation 2.7 can be written as Equation B.2. By taking the time average of Equation B.2, Equation B.3 was arrived. After implementing Reynolds decomposition, chain-rule, and (filtered) continuity equation (Equation 2.3), Equation B.3 can be re-written as Equation B.8 through Equation B.4 to B.7. Plugging Equation B.1 into Equation B.8, Equation B.10 (Equation 2.29) is arrived.

$$\begin{aligned}\frac{\partial\overline{uu}}{\partial x} &= \frac{\partial}{\partial x}\left(\overline{(\overline{u}+u^{'})(\overline{u}+u^{'})}\right) = \frac{\partial}{\partial x}\left(\overline{\overline{u}\,\overline{u} + \underbrace{2\overline{u}u^{'}}_{=0} + u^{'}u^{'}}\right) \\ &= \left(\frac{\partial\overline{u}\,\overline{u}}{\partial x} + \frac{\partial\overline{u'u'}}{\partial x}\right) = 2\overline{u}\frac{\partial\overline{u}}{\partial x} + \frac{\partial\overline{u'u'}}{\partial x} \end{aligned} \tag{B.1}$$

$$\begin{aligned}\frac{\partial u}{\partial t} + u\frac{\partial u}{\partial x} + v\frac{\partial u}{\partial y} + w\frac{\partial u}{\partial z} &= -\frac{1}{\rho}\frac{\partial p}{\partial x} + \frac{\partial}{\partial x}\left[(\nu+\nu_T)\left(\frac{\partial u}{\partial x} + \frac{\partial u}{\partial x}\right)\right] \\ &+ \frac{\partial}{\partial y}\left[(\nu+\nu_T)\left(\frac{\partial u}{\partial y} + \frac{\partial v}{\partial x}\right)\right] + \frac{\partial}{\partial z}\left[(\nu+\nu_T)\left(\frac{\partial u}{\partial z} + \frac{\partial w}{\partial x}\right)\right] \end{aligned} \tag{B.2}$$

$$\begin{aligned}\overline{u\frac{\partial u}{\partial x}} + \overline{v\frac{\partial u}{\partial y}} + \overline{w\frac{\partial u}{\partial z}} &= -\frac{1}{\rho}\frac{\partial\overline{p}}{\partial x} + \overline{\frac{\partial}{\partial x}\left[(\nu+\nu_T)\left(\frac{\partial u}{\partial x} + \frac{\partial u}{\partial x}\right)\right]} \\ &+ \overline{\frac{\partial}{\partial y}\left[(\nu+\nu_T)\left(\frac{\partial u}{\partial y} + \frac{\partial v}{\partial x}\right)\right]} + \overline{\frac{\partial}{\partial z}\left[(\nu+\nu_T)\left(\frac{\partial u}{\partial z} + \frac{\partial w}{\partial x}\right)\right]} \end{aligned} \tag{B.3}$$

$$\left(\overline{\frac{\partial uu}{\partial x}} - \overline{u\frac{\partial u}{\partial x}}\right) + \left(\overline{\frac{\partial uv}{\partial y}} - \overline{u\frac{\partial v}{\partial y}}\right) + \left(\overline{\frac{\partial uw}{\partial z}} - \overline{u\frac{\partial w}{\partial z}}\right) = -\frac{1}{\rho}\frac{\partial \overline{p}}{\partial x}$$
$$+ \overline{\frac{\partial}{\partial x}\left[(\nu+\nu_T)\left(\frac{\partial u}{\partial x}+\frac{\partial u}{\partial x}\right)\right]} + \overline{\frac{\partial}{\partial y}\left[(\nu+\nu_T)\left(\frac{\partial u}{\partial y}+\frac{\partial v}{\partial x}\right)\right]} + \overline{\frac{\partial}{\partial z}\left[(\nu+\nu_T)\left(\frac{\partial u}{\partial z}+\frac{\partial w}{\partial x}\right)\right]} \tag{B.4}$$

$$\left(\overline{\frac{\partial uu}{\partial x}} + \overline{\frac{\partial uv}{\partial y}} + \overline{\frac{\partial uw}{\partial z}}\right) - \overline{u\underbrace{\left(\frac{\partial u}{\partial x}+\frac{\partial v}{\partial y}+\frac{\partial w}{\partial z}\right)}_{\text{continuity}=0}} = -\frac{1}{\rho}\frac{\partial \overline{p}}{\partial x}$$
$$+ \overline{\frac{\partial}{\partial x}\left[(\nu+\nu_T)\left(\frac{\partial u}{\partial x}+\frac{\partial u}{\partial x}\right)\right]} + \overline{\frac{\partial}{\partial y}\left[(\nu+\nu_T)\left(\frac{\partial u}{\partial y}+\frac{\partial v}{\partial x}\right)\right]} + \overline{\frac{\partial}{\partial z}\left[(\nu+\nu_T)\left(\frac{\partial u}{\partial z}+\frac{\partial w}{\partial x}\right)\right]} \tag{B.5}$$

$$\frac{\partial}{\partial x}\left(\overline{u}\,\overline{u}+\overline{u'u'}\right) + \frac{\partial}{\partial y}\left(\overline{u}\,\overline{v}+\overline{u'v'}\right) + \frac{\partial}{\partial z}\left(\overline{u}\,\overline{w}+\overline{u'w'}\right) = -\frac{1}{\rho}\frac{\partial \overline{p}}{\partial x}$$
$$+ \overline{\frac{\partial}{\partial x}\left[(\nu+\nu_T)\left(\frac{\partial u}{\partial x}+\frac{\partial u}{\partial x}\right)\right]} + \overline{\frac{\partial}{\partial y}\left[(\nu+\nu_T)\left(\frac{\partial u}{\partial y}+\frac{\partial v}{\partial x}\right)\right]} + \overline{\frac{\partial}{\partial z}\left[(\nu+\nu_T)\left(\frac{\partial u}{\partial z}+\frac{\partial w}{\partial x}\right)\right]} \tag{B.6}$$

$$\overline{u}\frac{\partial \overline{u}}{\partial x} + \overline{v}\frac{\partial \overline{u}}{\partial y} + \overline{w}\frac{\partial \overline{u}}{\partial z} + \overline{u}\underbrace{\left(\frac{\partial \overline{u}}{\partial x}+\frac{\partial \overline{v}}{\partial y}+\frac{\partial \overline{w}}{\partial z}\right)}_{=0} + \frac{\partial \overline{u'u'}}{\partial x} + \frac{\partial \overline{u'v'}}{\partial y} + \frac{\partial \overline{v'w'}}{\partial z} = -\frac{1}{\rho}\frac{\partial \overline{p}}{\partial x}$$
$$+ \overline{\frac{\partial}{\partial x}\left[(\nu+\nu_T)\left(\frac{\partial u}{\partial x}+\frac{\partial u}{\partial x}\right)\right]} + \overline{\frac{\partial}{\partial y}\left[(\nu+\nu_T)\left(\frac{\partial u}{\partial y}+\frac{\partial v}{\partial x}\right)\right]} + \overline{\frac{\partial}{\partial z}\left[(\nu+\nu_T)\left(\frac{\partial u}{\partial z}+\frac{\partial w}{\partial x}\right)\right]} \tag{B.7}$$

$$\overline{u}\frac{\partial \overline{u}}{\partial x} + \overline{v}\frac{\partial \overline{u}}{\partial y} + \overline{w}\frac{\partial \overline{u}}{\partial z} + \frac{\partial \overline{u'u'}}{\partial x} + \frac{\partial \overline{u'v'}}{\partial y} + \frac{\partial \overline{v'w'}}{\partial z} = -\frac{1}{\rho}\frac{\partial \overline{p}}{\partial x}$$
$$+ \overline{\frac{\partial}{\partial x}\left[(\nu+\nu_T)\left(\frac{\partial u}{\partial x}+\frac{\partial u}{\partial x}\right)\right]} + \overline{\frac{\partial}{\partial y}\left[(\nu+\nu_T)\left(\frac{\partial u}{\partial y}+\frac{\partial v}{\partial x}\right)\right]} + \overline{\frac{\partial}{\partial z}\left[(\nu+\nu_T)\left(\frac{\partial u}{\partial z}+\frac{\partial w}{\partial x}\right)\right]} \tag{B.8}$$

$$\frac{\partial \overline{uu}}{\partial x} = 2\overline{u}\frac{\partial \overline{u}}{\partial x} + \frac{\partial \overline{u'u'}}{\partial x} = -2\overline{v}\frac{\partial \overline{u}}{\partial y} - 2\overline{w}\frac{\partial \overline{u}}{\partial z} - \frac{\partial \overline{u'u'}}{\partial x} - 2\frac{\partial \overline{u'v'}}{\partial y} - 2\frac{\partial \overline{u'w'}}{\partial z} - \frac{2}{\rho}\frac{\partial \overline{p}}{\partial x}$$
$$+2\overline{\frac{\partial}{\partial x}\left[(\nu+\nu_T)\left(\frac{\partial u}{\partial x}+\frac{\partial u}{\partial x}\right)\right]}+2\overline{\frac{\partial}{\partial y}\left[(\nu+\nu_T)\left(\frac{\partial u}{\partial y}+\frac{\partial v}{\partial x}\right)\right]}+2\overline{\frac{\partial}{\partial z}\left[(\nu+\nu_T)\left(\frac{\partial u}{\partial z}+\frac{\partial w}{\partial x}\right)\right]} \tag{B.9}$$

This thesis focuses on $y = 0$ plane to study momentum entrainment. Due to the fact that the wake should be close to axis-symmetric (tower and floor are not considered), terms related to $\partial/\partial y$ are assumed to be negligible and not considered, and thus Equation B.9 becomes Equation B.10. Moreover, effects of $\partial\overline{u'u'}/\partial x$ and the terms related to ν and ν_T (shear terms) are relatively small by compare to the other three terms (see subsection 4.2.4), as shown in Figure B.1 to B.3, which display the fields of the relative terms for cases with single fixed or surging rotor ($A_S = 4$ m & $\omega_S = 0.63$ rad/s) under different inflow TI (note the scale while comparing), and these facts can be applied to all the other cases in this thesis.

$$\frac{\partial \overline{uu}}{\partial x} \simeq -2\overline{w}\frac{\partial \overline{u}}{\partial z} - \frac{\partial \overline{u'u'}}{\partial x} - 2\frac{\partial \overline{u'w'}}{\partial z} - \frac{2}{\rho}\frac{\partial \overline{p}}{\partial x}$$
$$+2\overline{\frac{\partial}{\partial x}\left[(\nu+\nu_T)\left(\frac{\partial u}{\partial x}+\frac{\partial u}{\partial x}\right)\right]}+2\overline{\frac{\partial}{\partial z}\left[(\nu+\nu_T)\left(\frac{\partial u}{\partial z}+\frac{\partial w}{\partial x}\right)\right]} \tag{B.10}$$

$$\frac{\partial \overline{uu}}{\partial x} \simeq -2\left(\overline{w}\frac{\partial \overline{u}}{\partial z} + \frac{\partial \overline{u'w'}}{\partial z} + \frac{1}{\rho}\frac{\partial \overline{p}}{\partial x}\right) \tag{B.11}$$

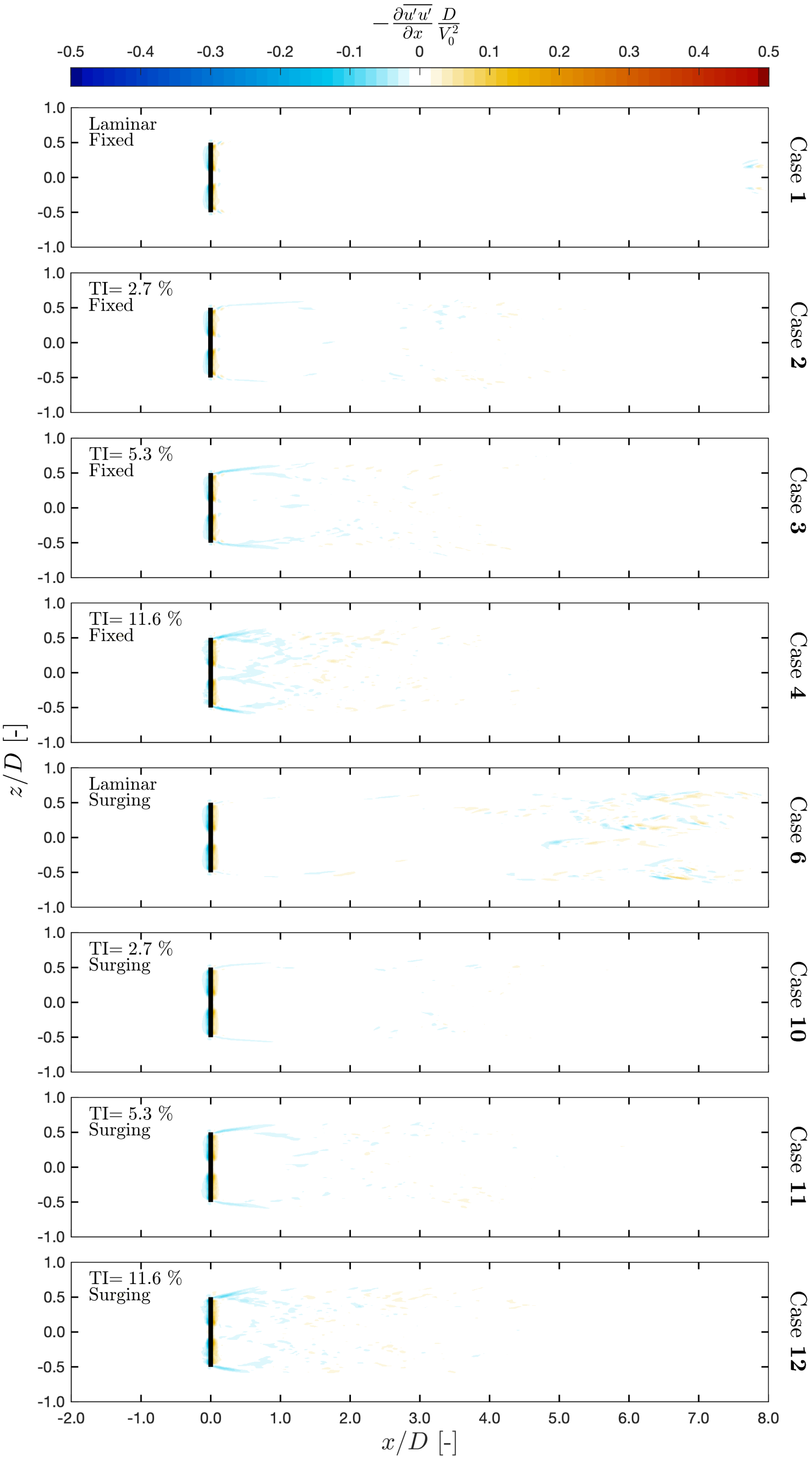

Figure B.1: Fields of $-\partial\overline{u'u'}/\partial x$ for single fixed or surging rotor with different inflow TI.

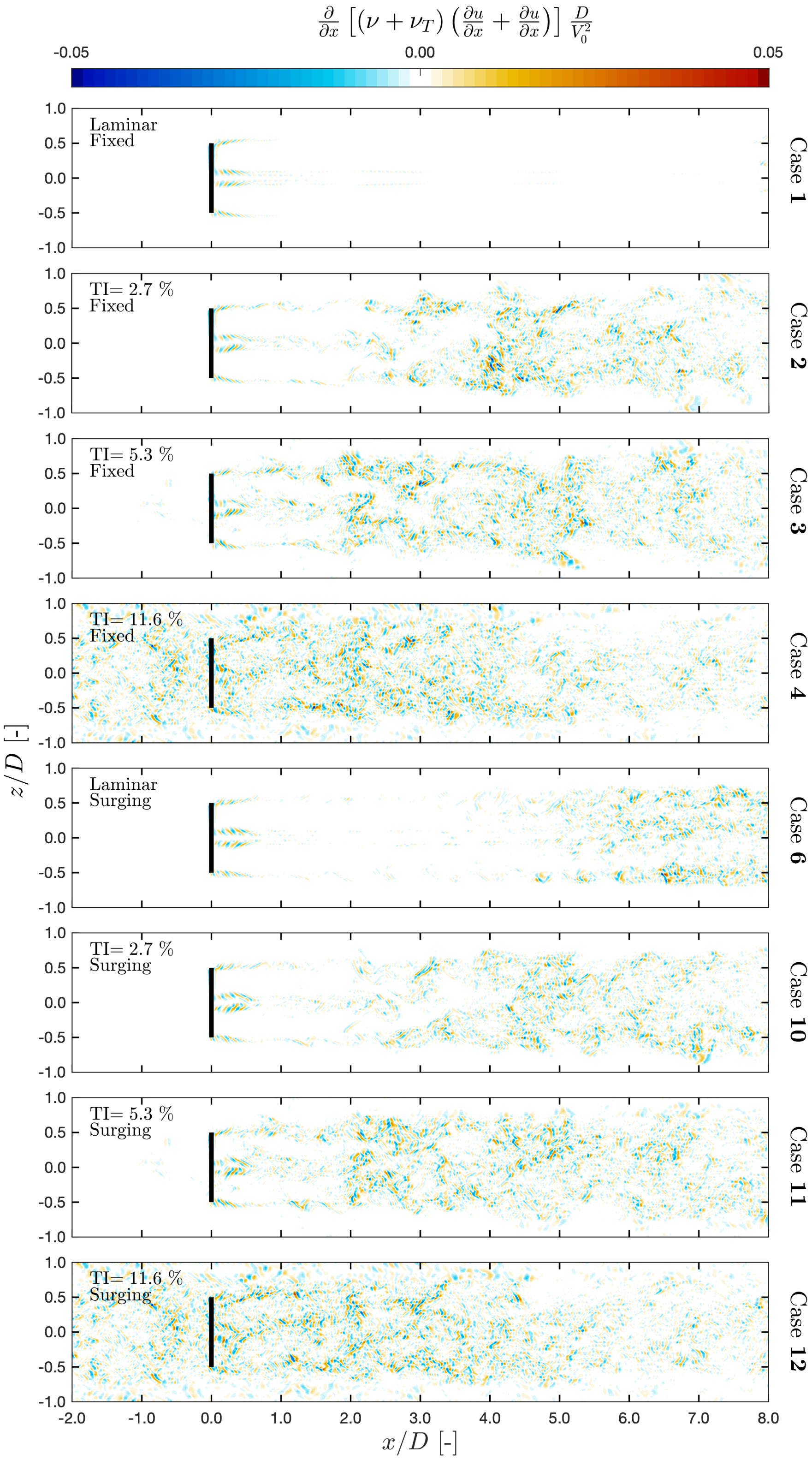

Figure B.2: Fields of $-2\partial\overline{[(\nu+\nu_T)(\partial u/\partial x+\partial u/\partial x)]}/\partial x$ for single fixed or surging rotor with different inflow TI.

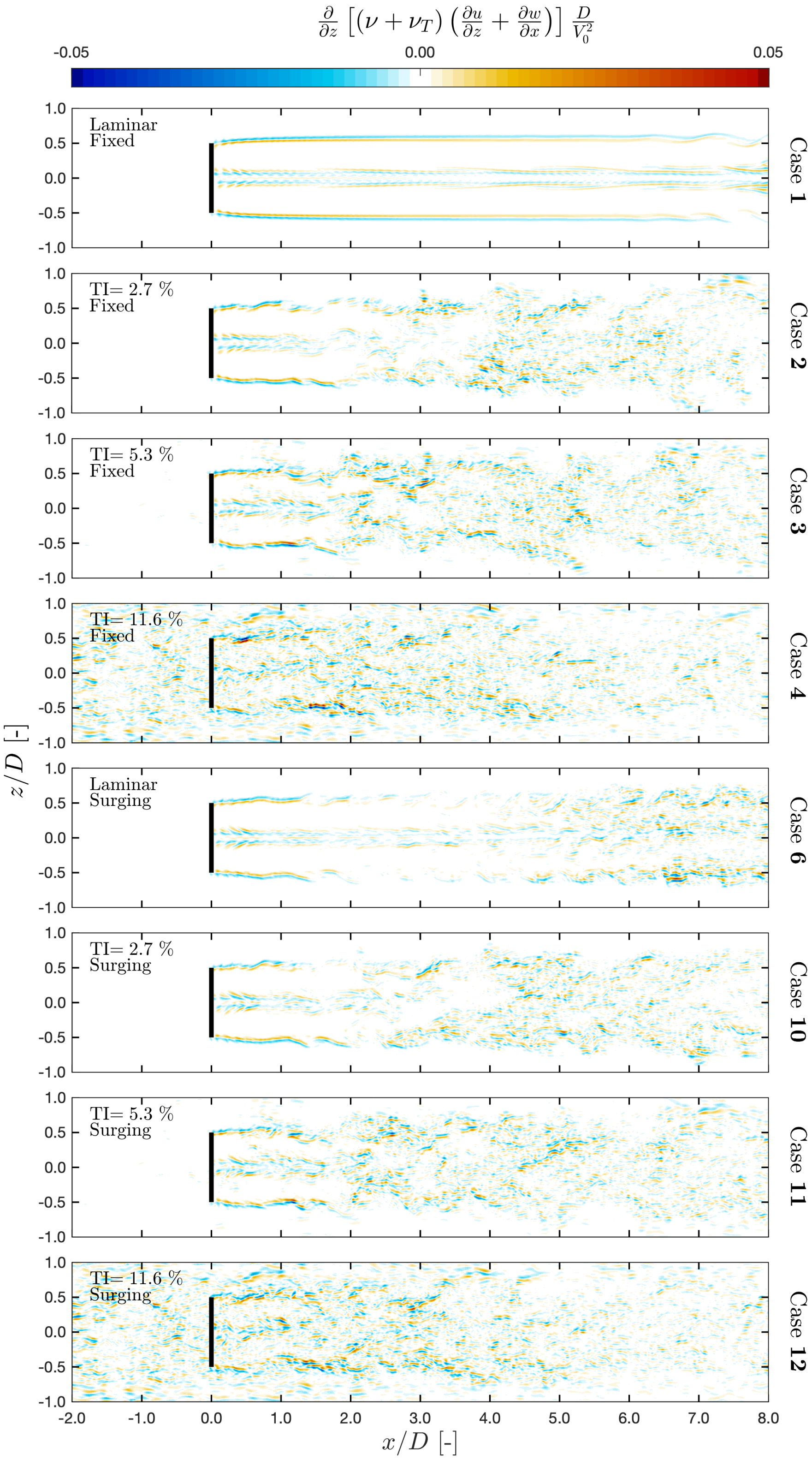

Figure B.3: Fields of $-2\partial\overline{[(\nu+\nu_T)(\partial u/\partial z+\partial w/\partial x)]}/\partial z$ for single fixed or surging rotor with different inflow TI.

Appendix C

Sampling and Averaging Methods with Convergence Test

This chapter describes the sampling and averaging methods. The general strategies for different cases are similar, but the windows considered will vary.

C.1 General Time Scale

In this thesis, T_Ω refer to the time required for NREL 5MW baseline turbine to complete a revolution with its rated condition, and it is 4.96 s. As for the time step size Δt, it is set to satisfy $\Omega \Delta t = 1^\circ$, and its absolute value is 0.01378 s.

C.2 Sampling Frequencies for Probes

For the sampling probes to obtain profiles of $\overline{u}$ such as Figure 4.3, their sampling rate is same as Δt, meaning that every timesteps are considered. For every downstream section, there is 51 probes equally distributed along $-0.9 \leq z/D \leq 0.9$, with a spacing of $0.036D$. And the values sampled by this probes are used to calculate $\overline{u}_{\text{Disk}}$ based on weighted averaging (Equation C.1). Note that a single line was used to represent the complete disk, which would lead to some inevitable errors.

$$\overline{u}_{\text{Disk}} = \frac{\sum_i \overline{u}_i \left(|z_i|^2 - |z_{i-1}|^2 \right)}{\sum_i |z_i|^2}, \qquad \text{for} \quad r_{\text{hub}} < |z_i| < R \tag{C.1}$$

C.3 Sampling Frequencies for Cutting Planes

For the fields data (cutting planes, contours plots) in this thesis, the sampling rate is $15\Delta t$, which is equivalent to sample 24 times for a single rotor revolution under its rated conditions, and its absolute value is 0.207 s.

C.4 Sampling Windows

This section describes the sampling window for the simulation cases, note that these windows also applies to phase-locked averaging.

C.4.1 Single Rotor with Laminar Inflow Conditions

For the single rotor cases with laminar inflow conditions, the total run-time is $80T_\Omega$ for all cases, and the window between $60T_\Omega \leq t \leq 80T_\Omega$ is selected for analyzing statistics, this corresponds to 5, 10, or 20 complete surging cycles for cases with ω_S being 0.32, 0.63, or 1.27 rad/s. The relative small window is based on the fact that phase-locked averaged TKE ($<$TKE$>_{0\pi}$) fields are very low for all the cases with laminar inflow conditions, suggesting the results are not just converged but simply repeating themselves.

C.4.2 Single Rotor with Turbulent Inflow Conditions

As for the single rotor cases with turbulent inflow conditions, the sampling windows are from $60T_\Omega \leq t \leq 110T_\Omega$, corresponds to 13, 25, or 50 complete surging cycles for cases with ω_S being 0.32, 0.63, or 1.27 rad/s (for cases with $\omega_S = 0.32$ rad/s, the sampling window was extended to $112T_\Omega$). Note that this means there will be (at least) 1201 samples for the cutting plane $y/D = 0$.

C.4.3 Dual Rotors

The sampling windows for cases with dual rotors (without & with controller implemented) are completely identical with cases of single rotor with turbulent inflow conditions.

C.4.4 Exception

The sampling window for obtaining time-averaged fields on yz-planes (x-normal planes) for turbulent cases (eq. Figure 4.48) is $90T_\Omega \leq t \leq 110T_\Omega$, which is smaller than the window for $y = 0$ plane.

C.5 Convergence Tests

In order to test whether the interested statistics are converged for the simulation cases, a brief convergence test with case **41** in Table 5.1 (dual rotors, SS, $\Delta_D = 3D$, TI $= 5.3\%$) was carried out. The convergence test was conducted by probing how $\overline{u}$, $\overline{v}$, $\overline{w}$, σ_u, σ_v, & σ_w, vary with the simulation time (number of samples) at certain positions. The interested points are at $x/D = -2$, 3, 6, & 8 with $(y, z) = (0.0D, 0.5D)$ $(z = R)$, and the interested time window is the one mentioned in subsection C.4.3 ($60T_\Omega \leq t \leq 110T_\Omega$, with the length of t being $50T_\Omega$). The results of convergence test are shown in Figure C.1 & Figure C.2. It can be seen that both first order statistics ($\overline{u}$, $\overline{v}$ & $\overline{w}$) and second order statistics (σ_u, σ_v,

& σ_w) are well converged. Moreover, in order to test the statistics related to phase-locking (see Equation 2.22), convergence of $< u >_{0\pi}$, $< v >_{0\pi}$, $< w >_{0\pi}$, $< \sigma_u >_{0\pi}$, $< \sigma_v >_{0\pi}$, & $< \sigma_w >_{0\pi}$ are also tested, and they are shown in Figure C.3 & Figure C.4. Note that when doing analysis with phase-locking data, only 26 samples are available. In general, statistics related to the phase-locking data also converged, while the convergence of the second order statistics ($< \sigma_u >_{0\pi}$, $< \sigma_v >_{0\pi}$, & $< \sigma_w >_{0\pi}$) are not as good as σ_u, σ_v, & σ_w.

As for the laminar cases, their solutions are deemed to be converged based on their very low <TKE>$_{\phi_S}$ fields (eg. Figure 4.29 & 5.12), and thus there is no need of conducting convergence test with them.

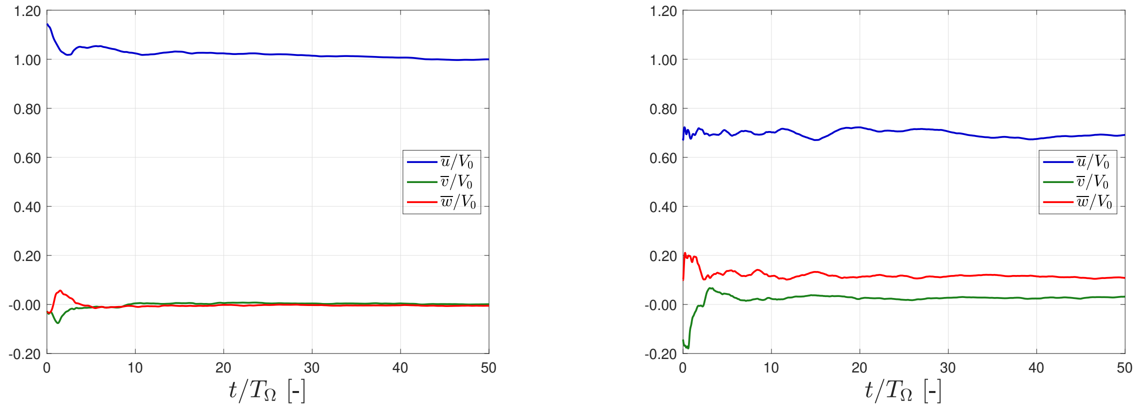

(a) $x/D = -2$

(b) $x/D = 3$

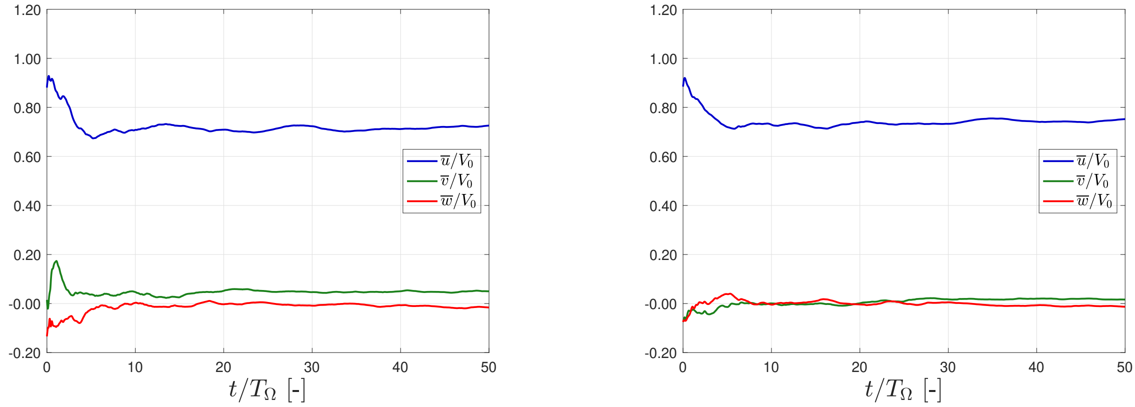

(c) $x/D = 6$

(d) $x/D = 8$

Figure C.1: Convergence test of $\overline{u}$, $\overline{v}$, & $\overline{w}$ for case **41** at $z/D = 0.5$ on $y = 0$ plane with different x-positions.

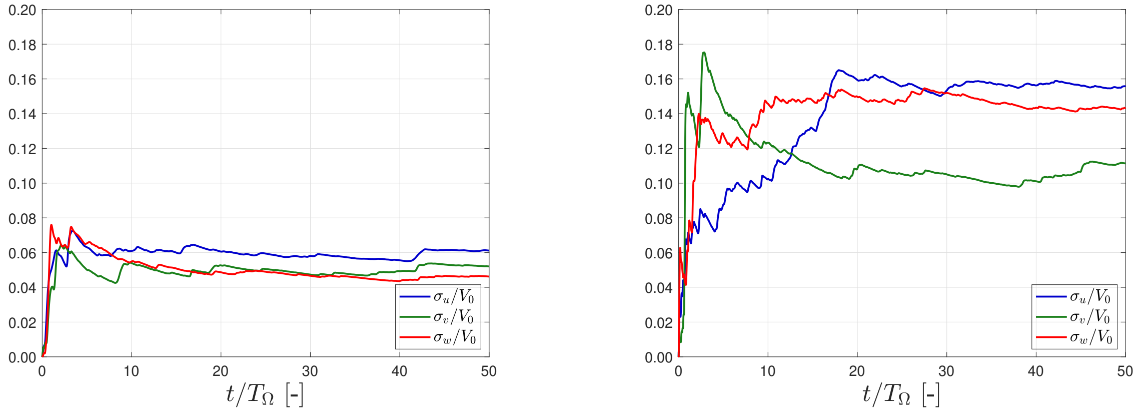

(a) $x/D = -2$ (b) $x/D = 3$

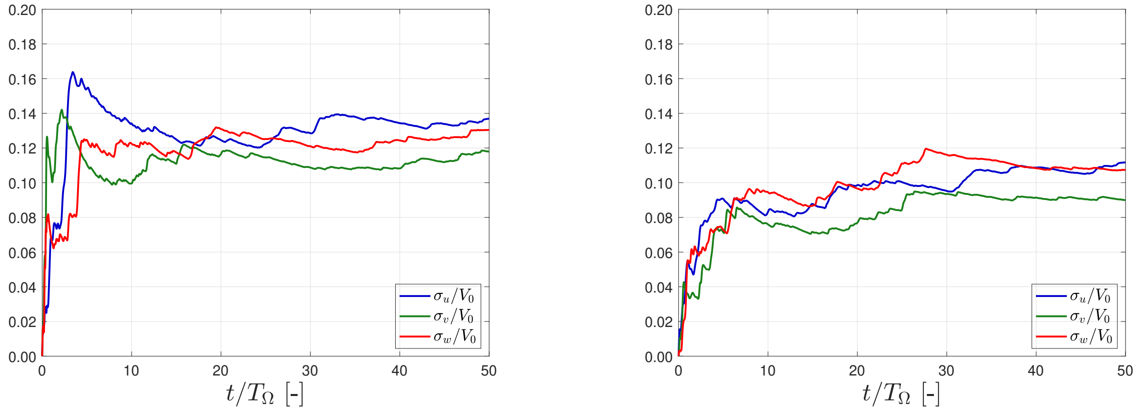

(c) $x/D = 6$ (d) $x/D = 8$

Figure C.2: Convergence test of σ_u, σ_v, & σ_w for case **41** at $z/D = 0.5$ on $y = 0$ plane with different x-positions.

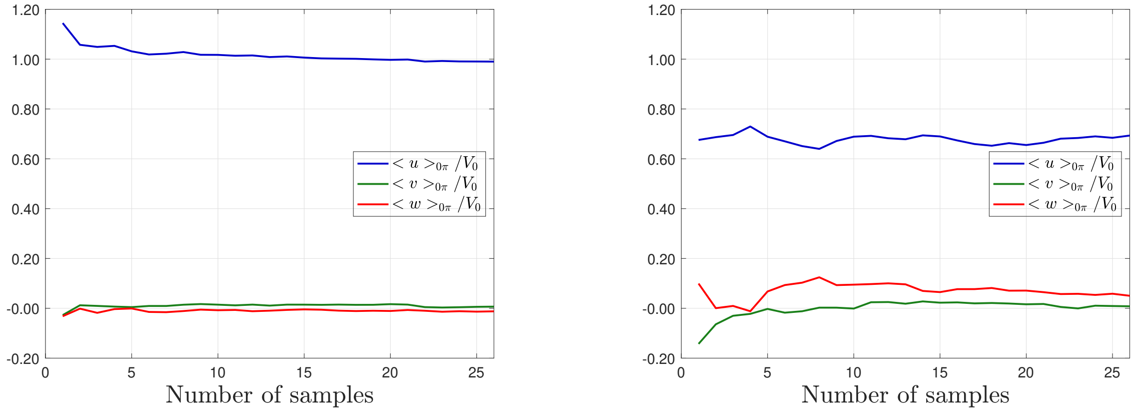

(a) $x/D = -2$

(b) $x/D = 3$

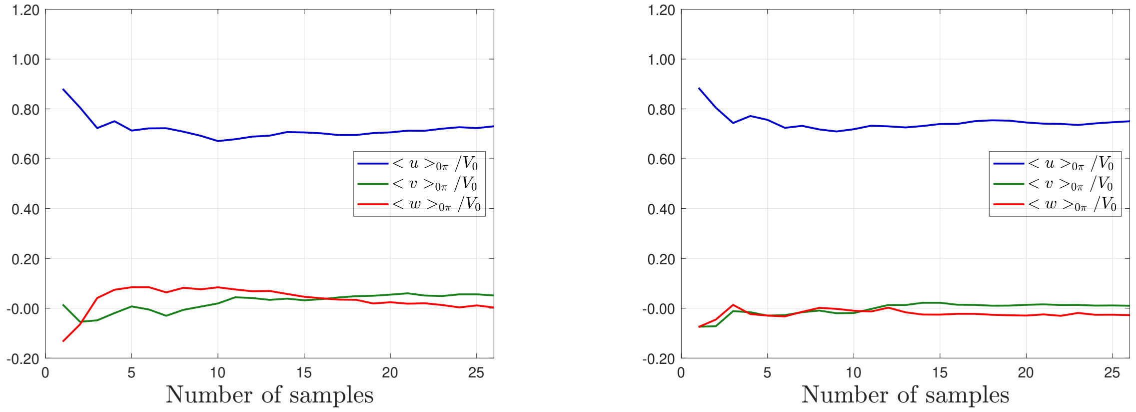

(c) $x/D = 6$

(d) $x/D = 8$

Figure C.3: Convergence test of $< u >_{0\pi}$, $< v >_{0\pi}$, & $< w >_{0\pi}$ for case **41** at $z/D = 0.5$ on $y = 0$ plane with different x-positions.

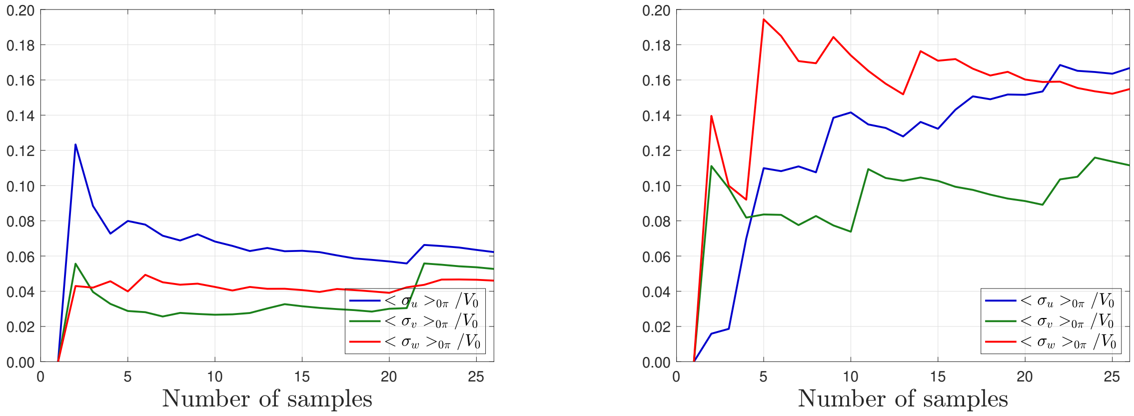

(a) $x/D = -2$

(b) $x/D = 3$

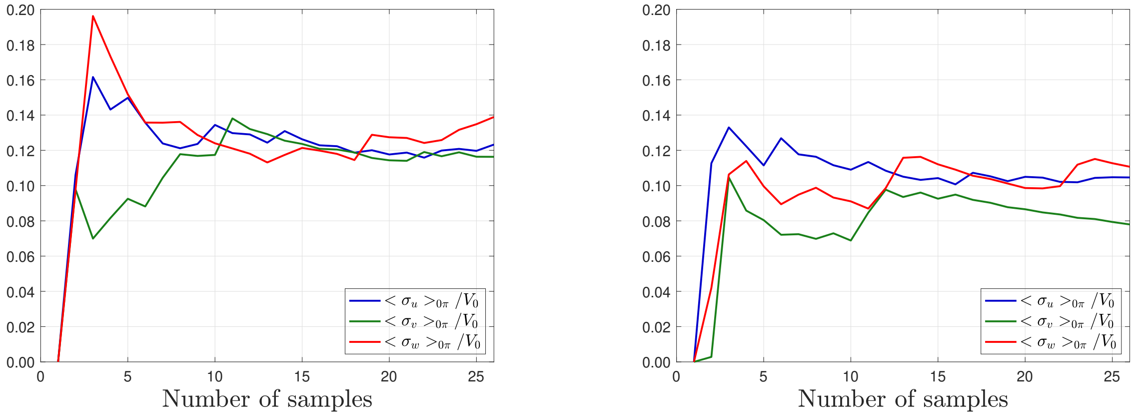

(c) $x/D = 6$

(d) $x/D = 8$

Figure C.4: Convergence test of $< \sigma_u >_{0\pi}$, $< \sigma_v >_{0\pi}$, & $< \sigma_w >_{0\pi}$ for case **41** at $z/D = 0.5$ on $y = 0$ plane with different x-positions.

C.6 Remarks

The sampling window for the turbulent cases may not be long enough for for the cases to be completely converged, especially for the second-order statistics of the phase-locked data. However, in general, the sampling window are long enough to obtain the desired information, considering most of the first and second order statistical quantities do converge.

Appendix D

A Brief Proper Orthogonal Decomposition Analysis

A brief proper orthogonal decomposition analysis is conducted in this chapter. The main purpose of the analysis is to check if the phase-locked quantities of wakes in this thesis have any other significant modes other than the phase-locked averaged one (mode **1** is equivalent to the averaged value). In order to do so, cases with single fixed & surging rotor under both laminar and turbulent (TI $= 5.3\%$) inflow conditions (cases **1**, **3**, **6**, & **11**) are tested, they are selected to represent the cases considered in this thesis. In the analysis, $\omega_{y,0\pi}$ are looked into, since $< \omega_y >_{0\pi}$ are able to represent the PLSB clearly. Note that only the phase-locked quantities are looked into, since that the vortical structures in the wakes are repeatable in time and space, considering the data of all the available timesteps will dilute the distinct repeatable structures (PLSB).

The POD analysis conducted in this thesis is through the MATLAB function `pod`, which is developed by Zigunov [99]. `pod` wrapped the MATLAB built-in function `svd` (singular value decomposition), to make the analysis with series of $2D$ data (snapshots) easier. The general concept are shown in Equation D.1 (`[U, S, V] = pod(X)`), and Einstein notation is adapted. Subscripts i & j label the coordinates (x & z for the cases here), t indicates the serial number (timing index) of the inputted $2D$ snapshots series, k is the index for the mode shapes, and δ is Kronecker delta; as for the matrices, $\mathbf{X}$ is the series of the $2D$ snapshots being analyzed, $\mathbf{U}$ is the outputted mode shapes, $\mathbf{S}$ is the (root of) energy content for the outputted mode shapes, and $\mathbf{V}$ is the coefficients for the mode shapes at instant t.

$$X_{ijt} = U_{ijk} S_k \delta_{kp} V_{pt} \tag{D.1}$$

Note that the mode shapes number that $\mathbf{U}$ has is same as the snapshots number that $\mathbf{X}$ has, and the energy content of k-th mode shapes is $S_k S_p \delta_{kp}$. Note that the outputted mode shapes $\mathbf{U}$ are sequenced base on their energy content. With the sampling windows mentioned in Appendix C, the laminar cases will have 10 phase-locked samples while the turbulent cases have 26. In order to better understand the importance of each mode shapes, their energy content are represented as *mode energy fraction*, which is described in Equation D.2.

$$\text{Mode Energy Fraction of the } k \text{ th mode} = \frac{S_k \delta_{kp} S_p}{S_q S_q} \tag{D.2}$$

D.1 POD with the Surging Cases

Results of POD analysis of $\omega_{y,0\pi}$ (note the vorticity fields are non-dimensionalized with the factor D/V_0) with the surging cases (cases **6** & **11**) are in Figure D.1. D.2, & D.3, where the first is the fractions of energy content (S_k), the second is the coefficients for the mode shapes at different time instants (V_{kt}), and the third is the mode shapes (U_{ijk}, only the first four modes are shown). In Figure D.1, it can be seen that mode **1** (averaged-values) for both laminar and turbulent cases has much more energy content than the others, especially for the laminar case; moreover, the energy contents of the the turbulent case does not drop significantly after mode **2**. Looking at Figure D.2, it can be seen that except for mode **1**, coefficients for the other three modes fluctuate significant, indicating the three modes are not persist in all of the considered snapshots. While for mode **1**, its coefficients are almost constant, suggesting the expression of the mode is persist in every snapshots. As viewing the mode shapes (Figure D.3), mode **1** for both cases are essentially identical to their $< \omega_y >_{0\pi}$ fields (Figure 4.12). While modes **2**-**4** for the laminar case seems to represent the random fluctuations after the breakdown of the wake. As for the turbulent case, modes **2**-**4** seem to display the released trailing & shedded voticites at the regions just after the rotor, however, rest of the regions seem to display random fluctuations related to inflow turbulence as well, and no periodic features related to ω_S can be found; also that their timing coefficients are not persist as well.

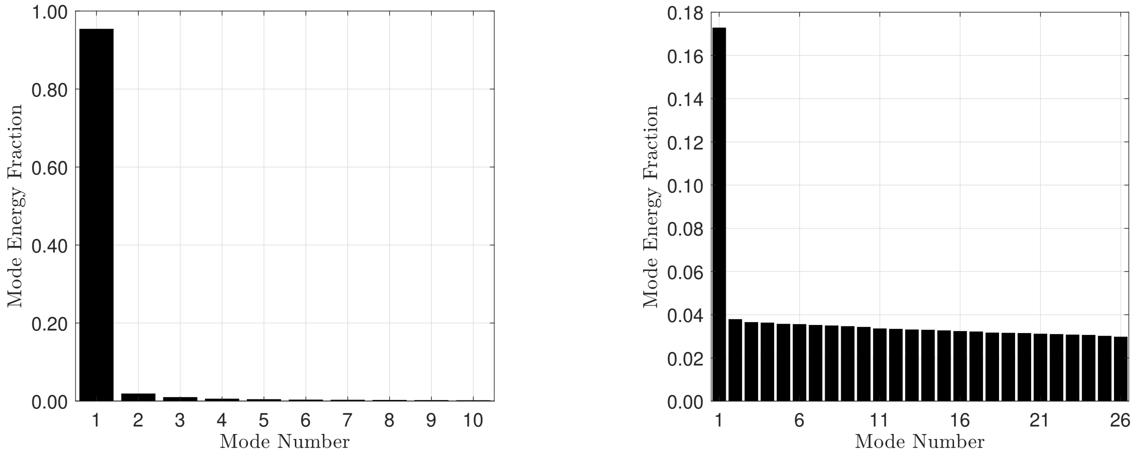

(a) Laminar

(b) Turbulent (TI = 5.3%)

Figure D.1: Energy fractions of each modes for $\omega_{y,0\pi}$ of the surging cases with laminar (case **6**) and turbulent (case **11**) inflow conditions.

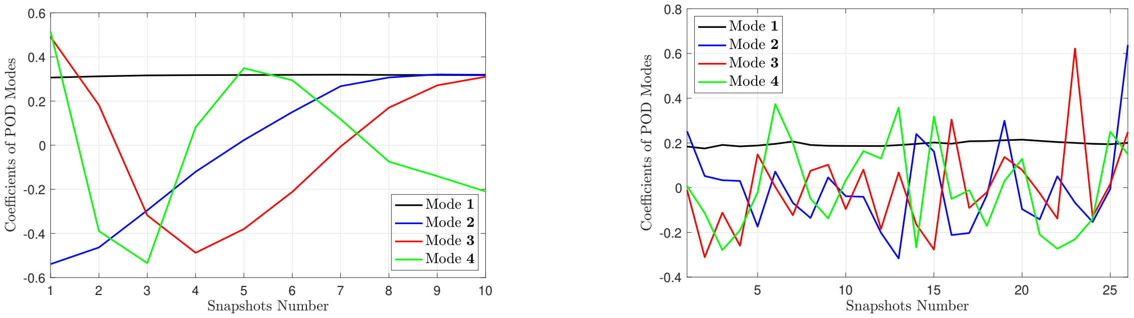

(a) Laminar (b) Turbulent (TI = 5.3%)

Figure D.2: Coefficients of each modes at different time instants for $\omega_{y,0\pi}$ of the surging cases with laminar (case **6**) and turbulent (case **11**) inflow conditions.

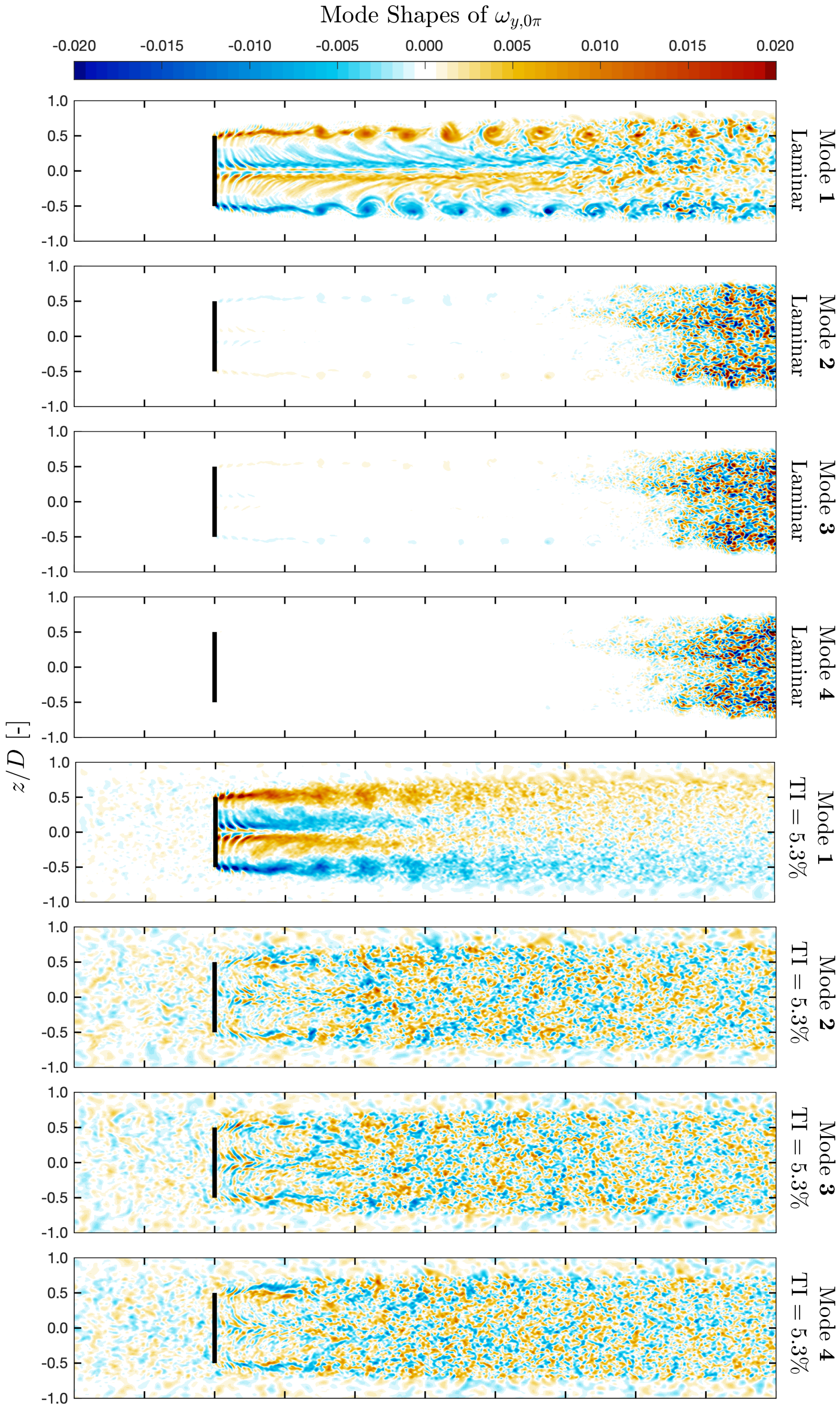

Figure D.3: Mode shapes obtained after POD analysis for $\omega_{y,0\pi}$ of the surging cases with laminar (case **1**) and turbulent (case **3**) inflow conditions.

D.2 POD with the Fixed Cases

Results of POD analysis of $\omega_{y,0\pi}$ with the fixed cases (cases **6** & **11**) are in Figure D.4. D.5, & D.6, where the first is the fractions of energy content (S_k), the second is the coefficients for the mode shapes at different time instants (V_{kt}), and the third is the mode shapes (U_{ijk}, only the first four modes are shown). Aside from the absent of PLSB, general features for the energy fractions, timing coefficients, and the mode shapes are basically very similar with the surging cases just analyzed. One of the only few differences is the patterns of mode **2-4** for the laminar case with fixed rotor, since there seems to have repeatable features. However, judging by the facts that their energy contents are very low and their timing coefficients fluctuates significantly, they are not likely to contribute much to the wake dynamics.

D.3 Remarks

Considering the POD analysis with $\omega_{y,0\pi}$ fields in this chapter, mode **1** ($<\omega_y>_{0\pi}$) has much more importance compare to the other modes. This is based on the facts that the energy contents of mode **1** are significantly higher than the other modes, and that the timing coefficients of mode **1** are almost constant for all modes, where the coefficients of the other modes fluctuate significantly.

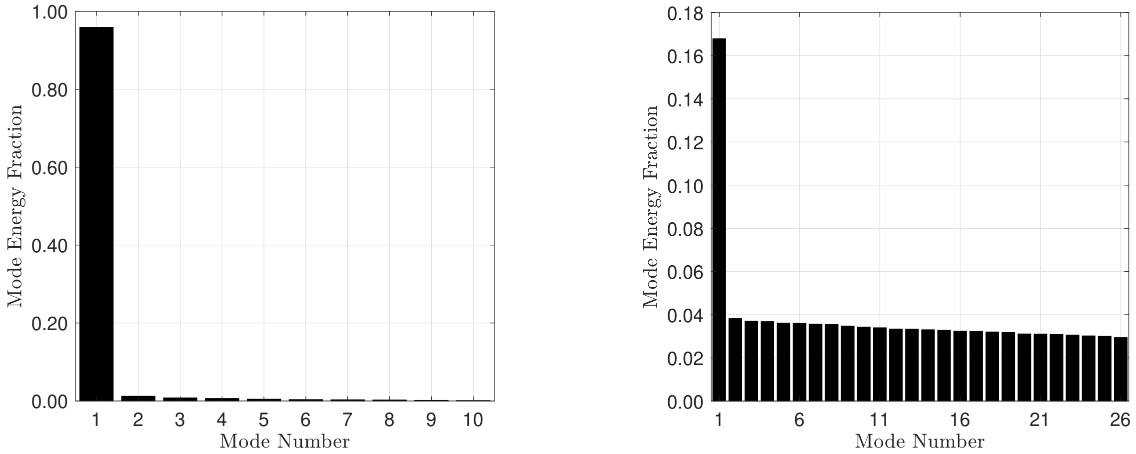

(a) Laminar (b) Turbulent (TI = 5.3%)

Figure D.4: Energy fractions of each modes for $\omega_{y,0\pi}$ of the fixed cases with laminar (case **6**) and turbulent (case **11**) inflow conditions.

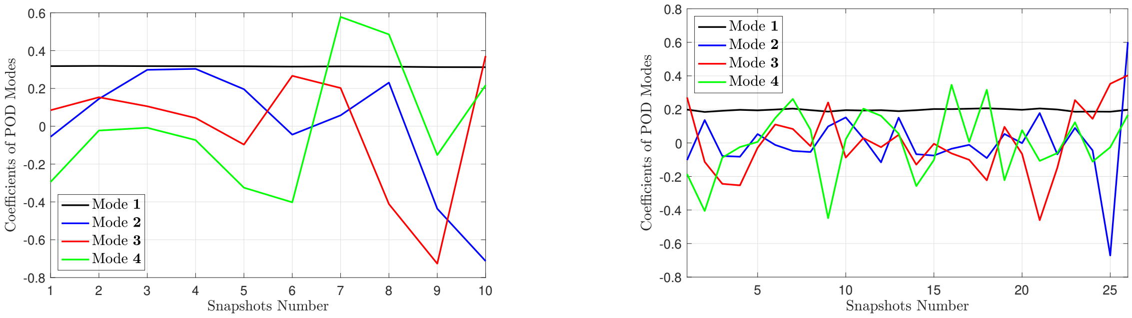

(a) Laminar

(b) Turbulent (TI = 5.3%)

Figure D.5: Coefficients of each modes at different time instants for $\omega_{y,0\pi}$ of the fixed cases with laminar (case **6**) and turbulent (case **11**) inflow conditions.

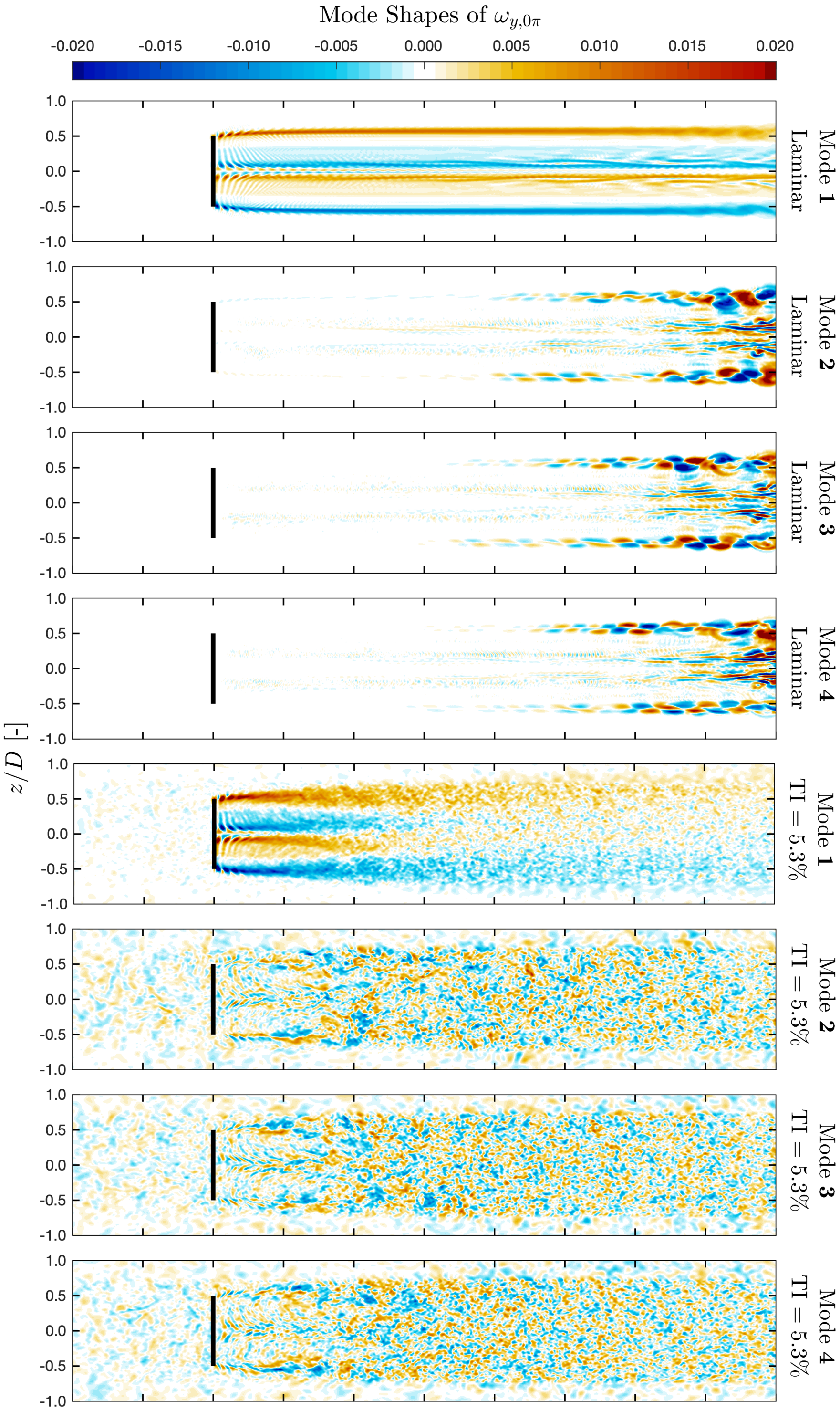

Figure D.6: Mode shapes obtained after POD analysis for $\omega_{y,0\pi}$ of the fixed cases with laminar (case **1**) and turbulent (case **3**) inflow conditions.

Appendix E

Supplementary Information for Cases with Single Rotor

E.1 Different Inflow TI with Single Fixed or Surging Rotor

Figure E.1 and E.2 display the phase-locked averaged and time-averaged vertical velocity fields ($< w >_{0\pi}$ & $\overline{w}$) (note the scales are rather small). The blockage effects of the rotor are clearly shown. Interestingly, for the $< w >_{0\pi}$ fields of the surging cases, values of $< w >_{0\pi}$ fields are alternating along the downstream direction significantly even with TI $= 5.3\%$, which is very unlike to the fixed rotor cases. This indicates that surging in sinusoidal manner facilitates the flow to go into and out from the wake, and they are also related to the vortical structure discussed in subsection 4.2.3. As for the $\overline{w}$ fields of turbulent cases, the trends are similar, both showing that the flows are entrained from outside the wake region for $x/D > 1$.

The instantaneous and phase-locked averaged pressure fields for the eight cases (Δp & $< \Delta p >_{0\pi}$) are displayed in Figure E.3 and E.4. In the fields of Δp for the four turbulent cases, local minimum and maximum exist, suggesting vortical structures were formed. And similar with u fields, Δp fields for surging rotor cases are similar with the ones of fixed rotor cases when inflow TI is higher. For the fields of $< \Delta p >_{0\pi}$ for the turbulent cases with fixed rotor, there seems to be some weak local minimums orderly distributed along the streamwise direction. They might related to the modes of the interactions between tip-vorticies or Karman vortex street. However, effects of them are not observed in the phase-locked averaged vorticity field (Figure 4.12), and considering the relatively low magnitudes scale, they were not further investigated. While for the fields of $< \Delta p >_{0\pi}$ for the turbulent cases with surging rotor, periodic structures are clearly observed once again, and the periodic structures are more visible for the cases with lower TI. Moreover, note that higher and lower Δp & $< \Delta p >_{0\pi}$ bubbles are featured mostly at $z/D > 0$, which are as expected since both cases all only consider time steps with $\phi_{\Omega} = 0\pi$, as one of the blades (actuator lines) is pointing upward.

The phase-locked averaged x and z-component of the vorticity ($< \omega_x >_{0\pi}$ & $< \omega_z >_{0\pi}$) are presented in Figure E.5 and E.6. Fields of $< \omega_x >_{0\pi}$ mainly indicate the wake rotations with respect to x-axis, and the distributions of them are as expected (the wakes rotate in counter-direction of the rotors' rotations. The direction of the wake rotations were deduced with Stokes' theorem). Fields of $< \omega_z >_{0\pi}$ are presented here for observing shedded vorticies, which are weak for the fixed cases; while surging cases possess noticeable values of $< \omega_z >_{0\pi}$ just behind the rotor, especially for the laminar cases. Shedded vorticies are an indicator of whether the lift distributions along the blades (actuator lines) remain close to constant or not (deduced with Kutta Joukowski theorem together with Kelvin Helmholtz theorem [100]), and here can see that the lift distributions of the cases with surging rotor vary in time, while the ones of fixed cases remain almost constant.

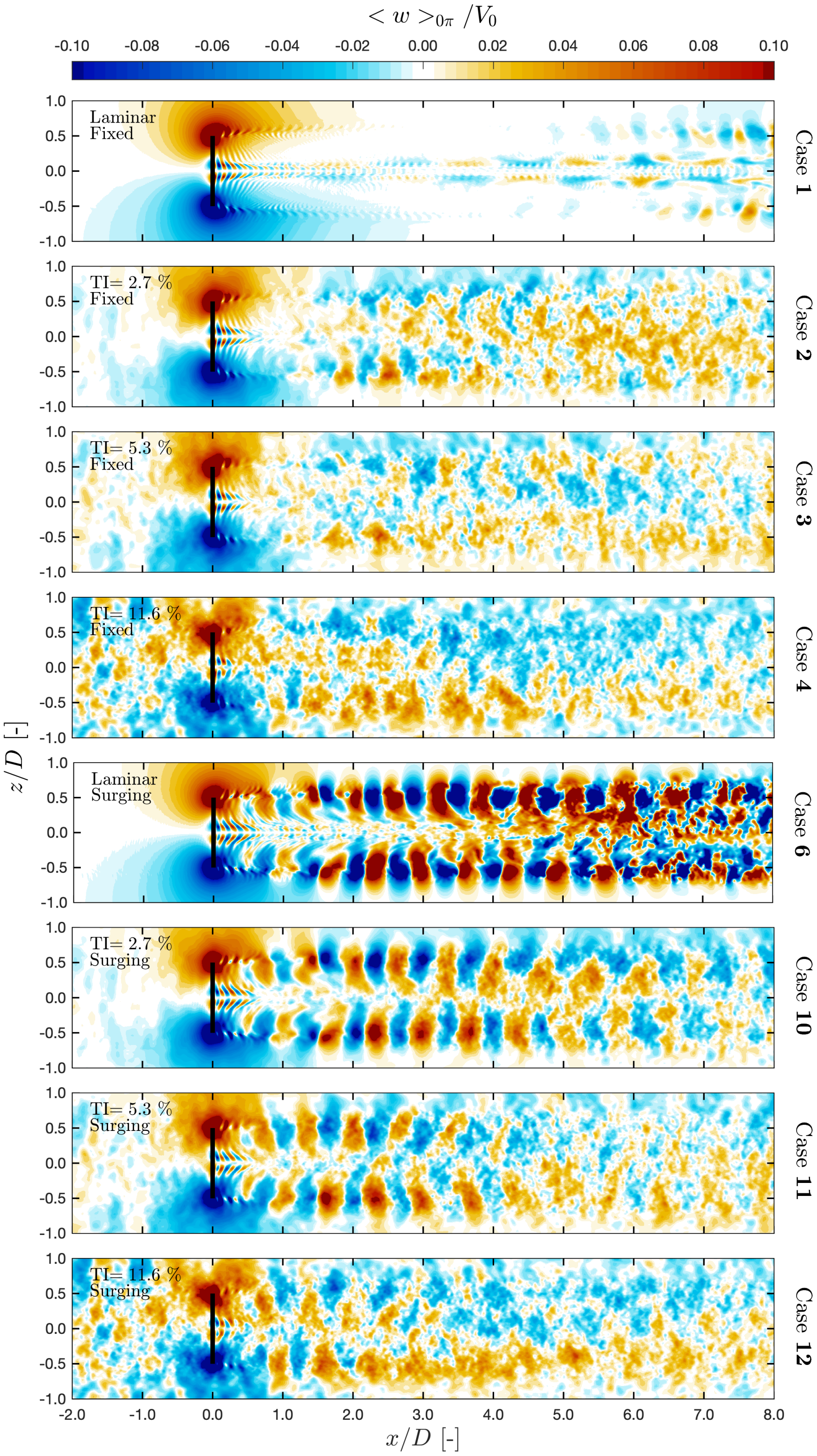

Figure E.1: Fields of phase-locked averaged vertical velocity $< w >_{0\pi}$ for single fix or surging rotor with different inflow TI.

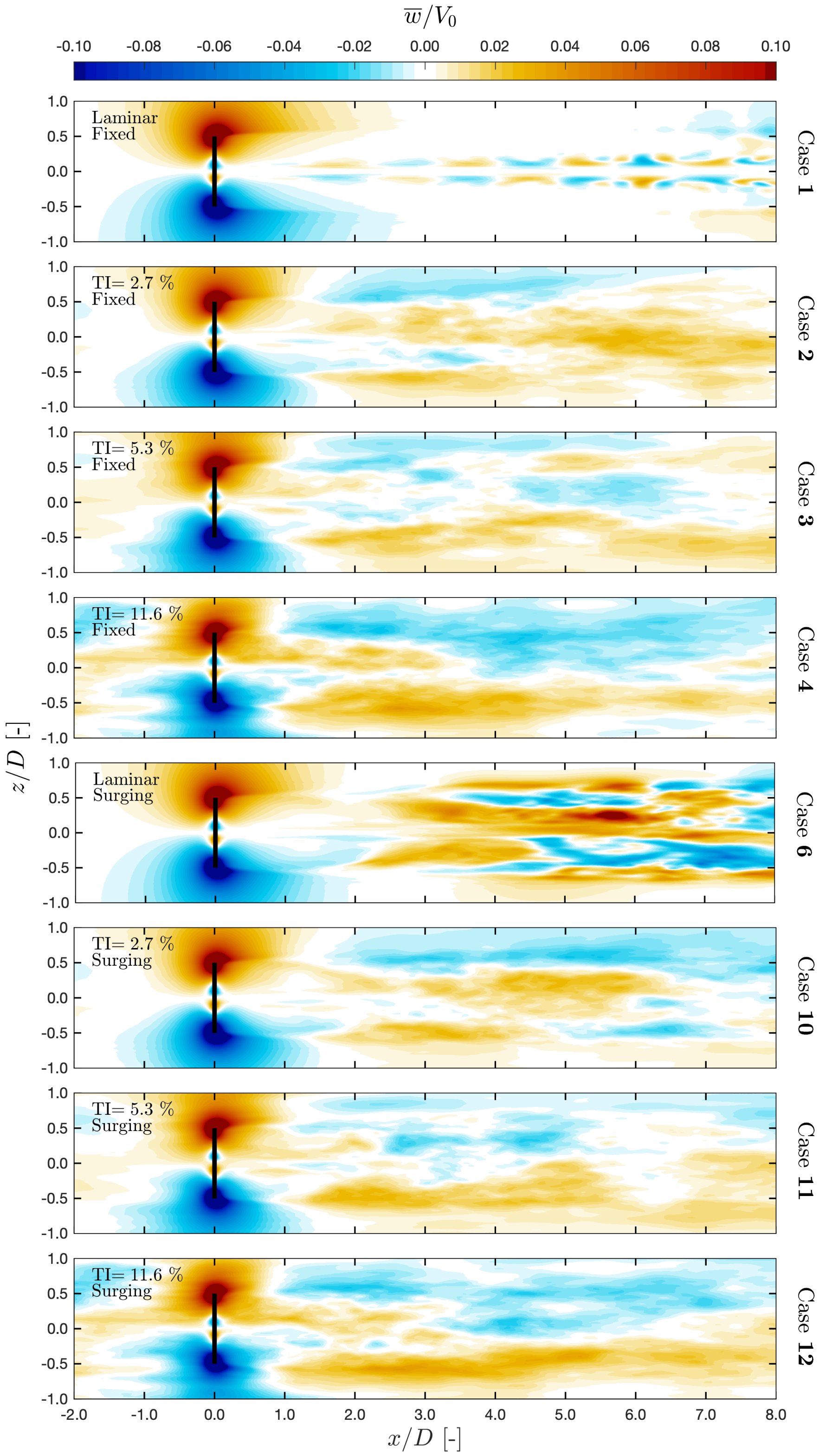

Figure E.2: Fields of time-averaged vertical velocity $\overline{w}$ for single fix or surging rotor with different inflow TI.

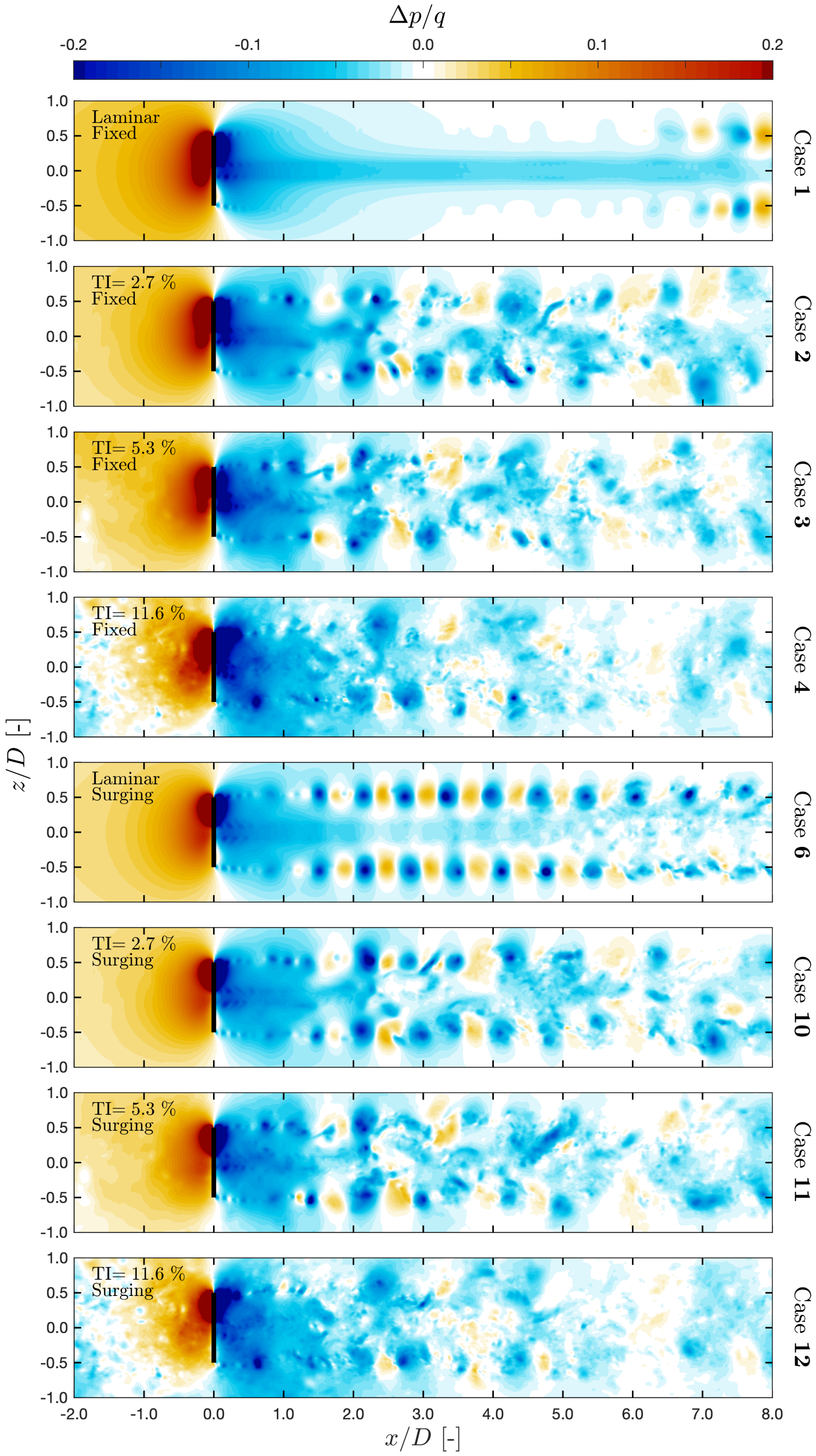

Figure E.3: Fields of instantaneous pressure Δp for single fix or surging rotor with different inflow TI.

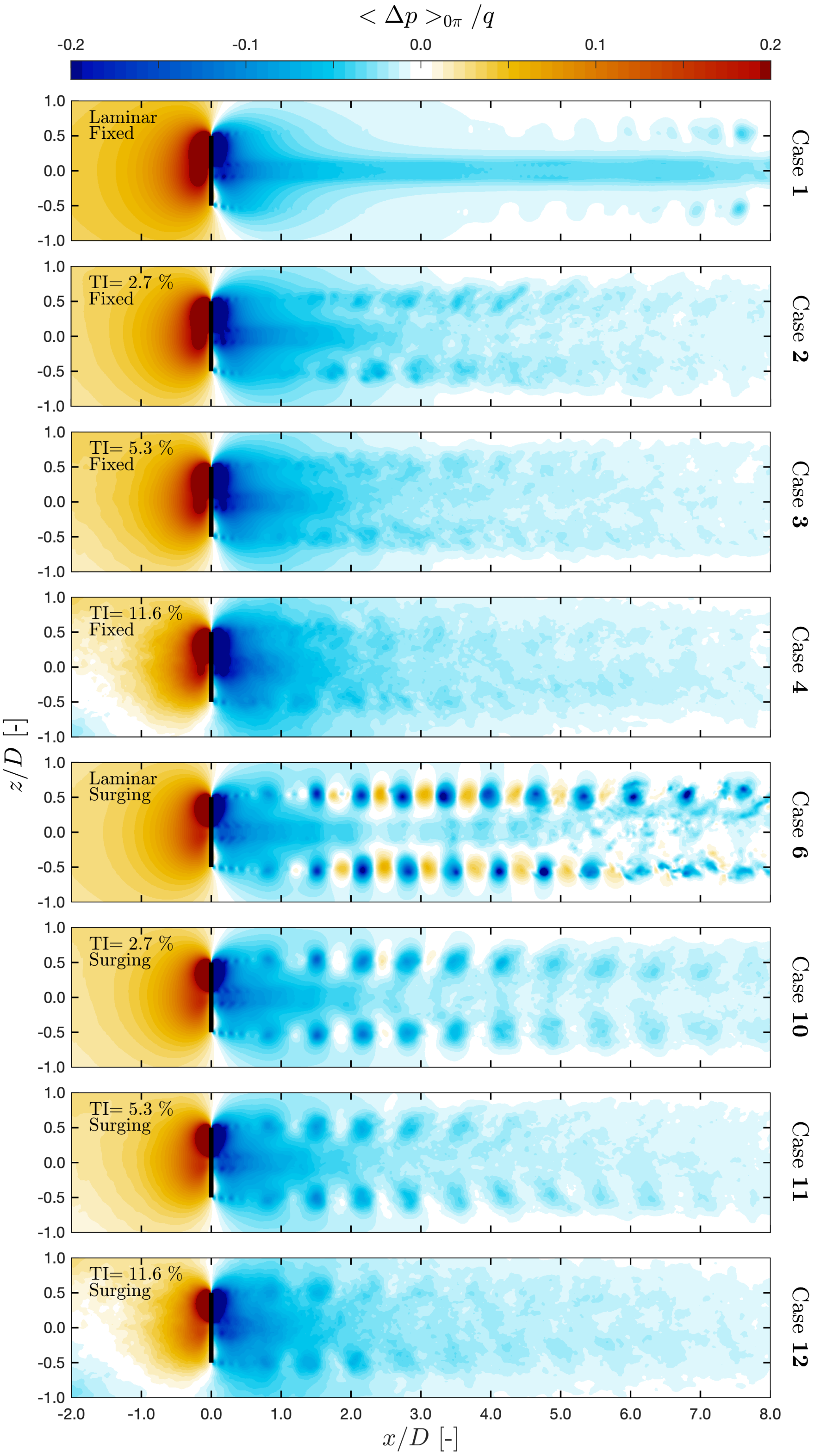

Figure E.4: Fields of phase-locked averaged pressure $< \Delta p >_{0\pi}$ for single fix or surging rotor with different inflow TI.

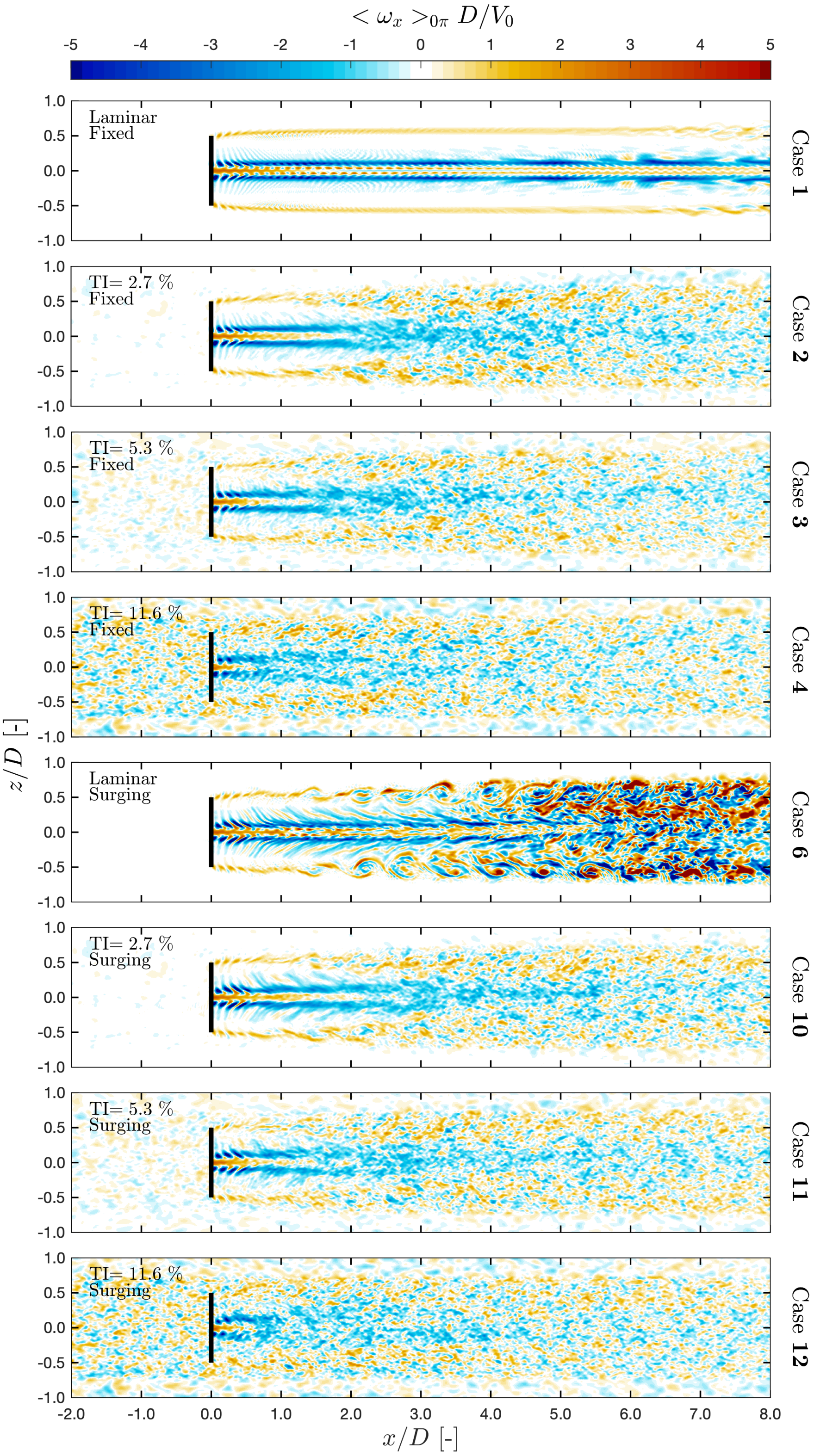

Figure E.5: Fields of phase-locked averaged x-component vorticity $< \omega_x >_{0\pi}$ for single fix or surging rotor with different inflow TI.

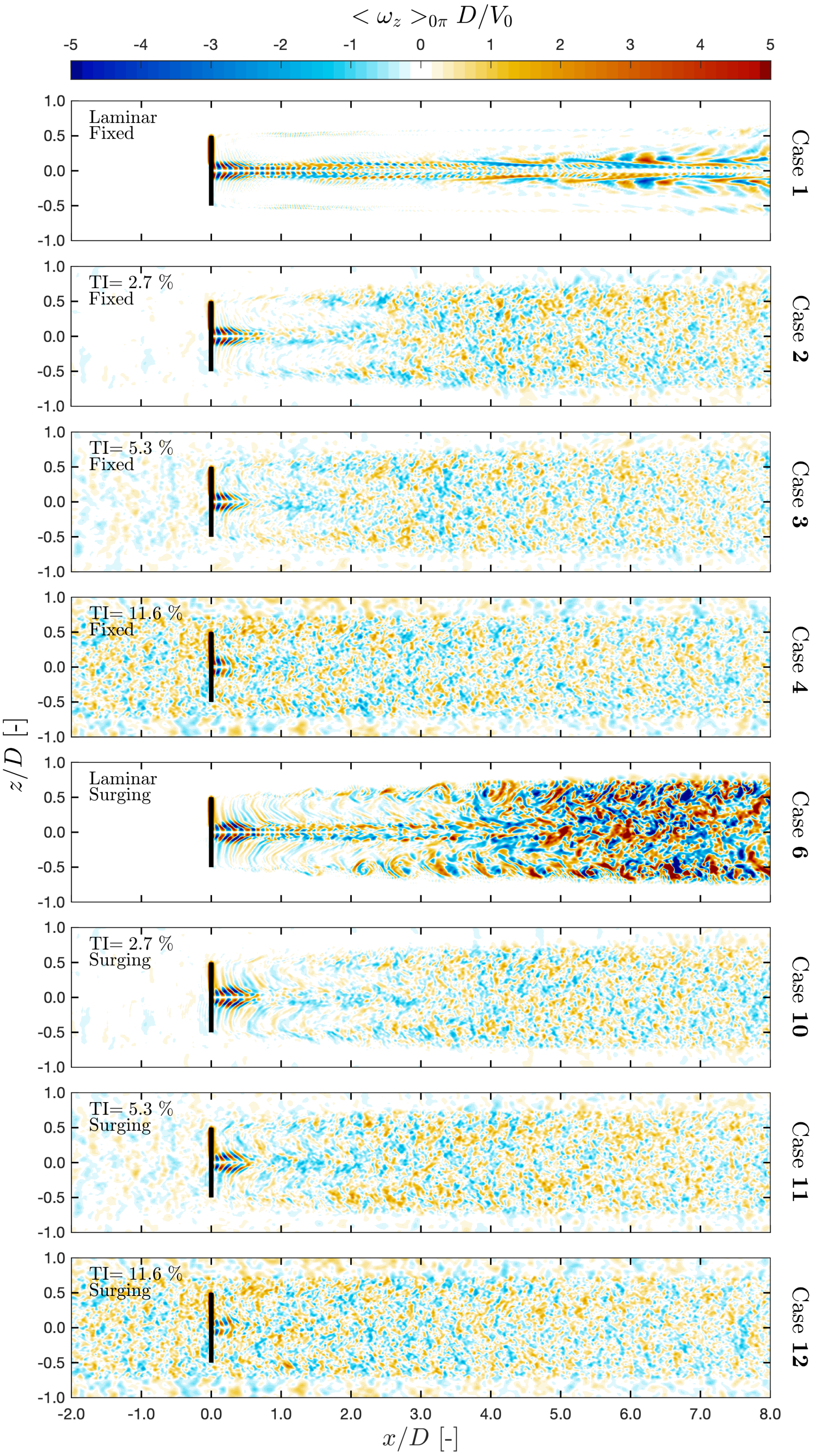

Figure E.6: Fields of phase-locked averaged z-component vorticity $< \omega_z >_{0\pi}$ for single fix or surging rotor with different inflow TI.

E.2 Laminar Inflow Conditions with Different A_S and ω_S

The fields of $\overline{u}$ are displayed in Figure E.7. It can be seen that $\overline{u}$ fields for cases with surging rotor recover significantly, while little to no recovery for the fixed case. And interestingly, for case $\omega_S = 1.27$ rad/s (= 0.2016 Hz), the wake seemed to be skewed a bit upward, this may be related to the fact that the wake is not fully asymmetric, and this had been further displayed and discussed in subsubsection 4.5.2.

The fields of $< w >_{0\pi}$ are presented in Figure E.8. For cases with surging rotor, there are alternating pattern of $< w >_{0\pi}$ with significant values, and their patterns are related to ω_S, while the structures for the case with higher ω_S seems to lose their forms earlier. These patterns already suggest there will be some structures having significant values for out-of-plane vorticity component (ω_y). Also these patterns shows that the flow will flow in and out the wakes. Fields of $\overline{w}$ are very similar for the three surging cases, and thus they are not shown. One can find contour of $\overline{w}$ for surging case with $A_S = 4$ m and $\omega_S = 0.63$ rad/s under laminar inflow conditions in case **6** of Figure E.1.

The fields of $< \omega_z >_{0\pi}$ are presented in Figure E.9. Once again, periodic structures are revealed. Notably in fields of $< \omega_z >_{0\pi}$, effects of shedded vorticies are much stronger for larger $\mathbb{V}$, especially for the case with $\omega_S = 1.27$ rad/s. As expected, shedded vorticies are much stronger with cases having larger $\mathbb{V}$ as displayed in the fields of $< \omega_z >_{0\pi}$. Again, though both the fields of $< \omega_z >_{0\pi}$ and $< \omega_y >_{0\pi}$ (Figure 4.23) seemed to be very chaotic; however, low values of $<\mathrm{TKE}>_{0\pi}$ fields (Figure 4.21) suggest the flows are highly repeatable. Fields of $< \omega_x >_{0\pi}$ are not displayed since they have similar features for the five surging cases here.

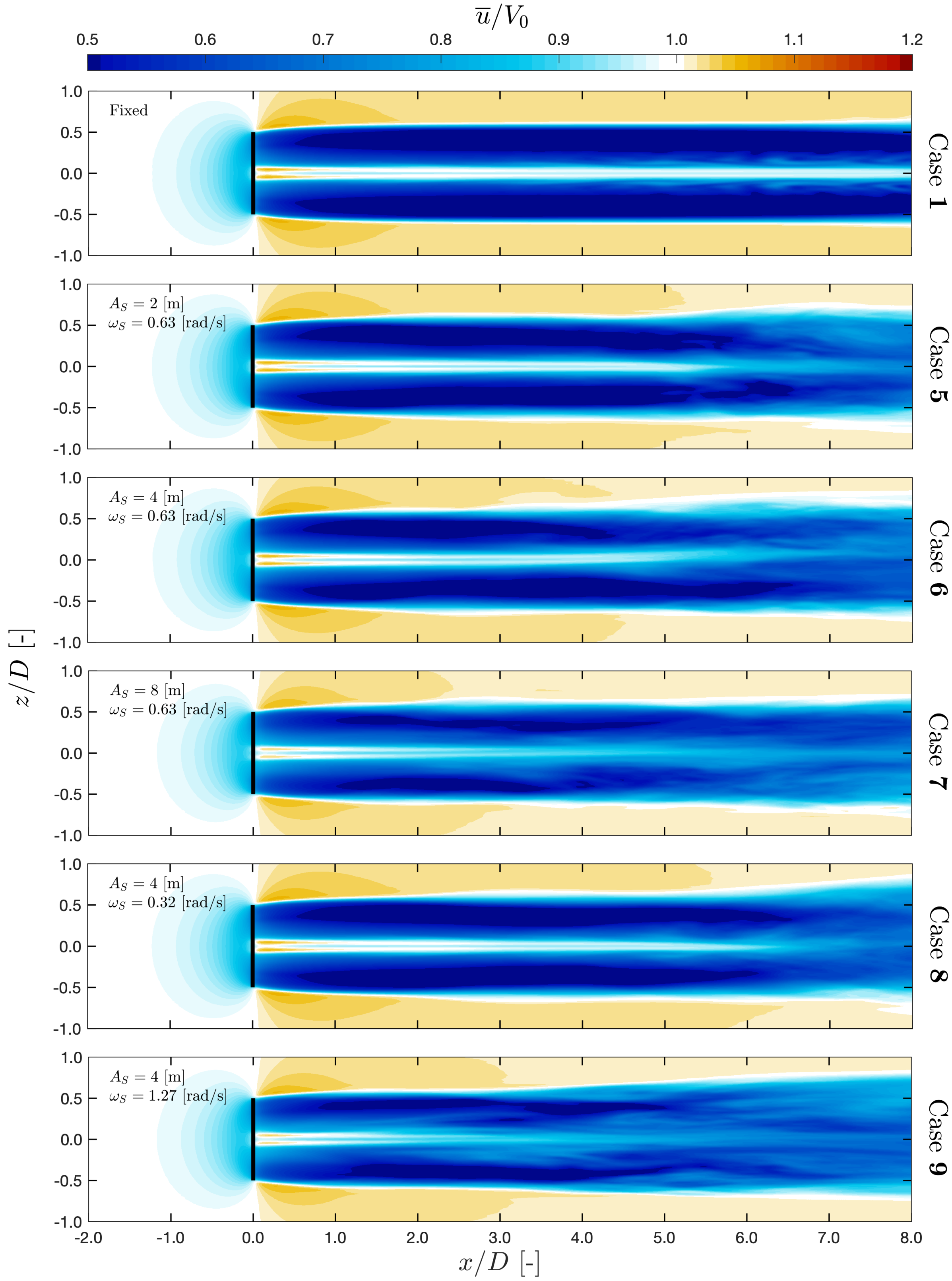

Figure E.7: Fields of time-averaged streamwise velocity $\overline{u}$ for single rotor with different A_S and ω_S under laminar inflow conditions.

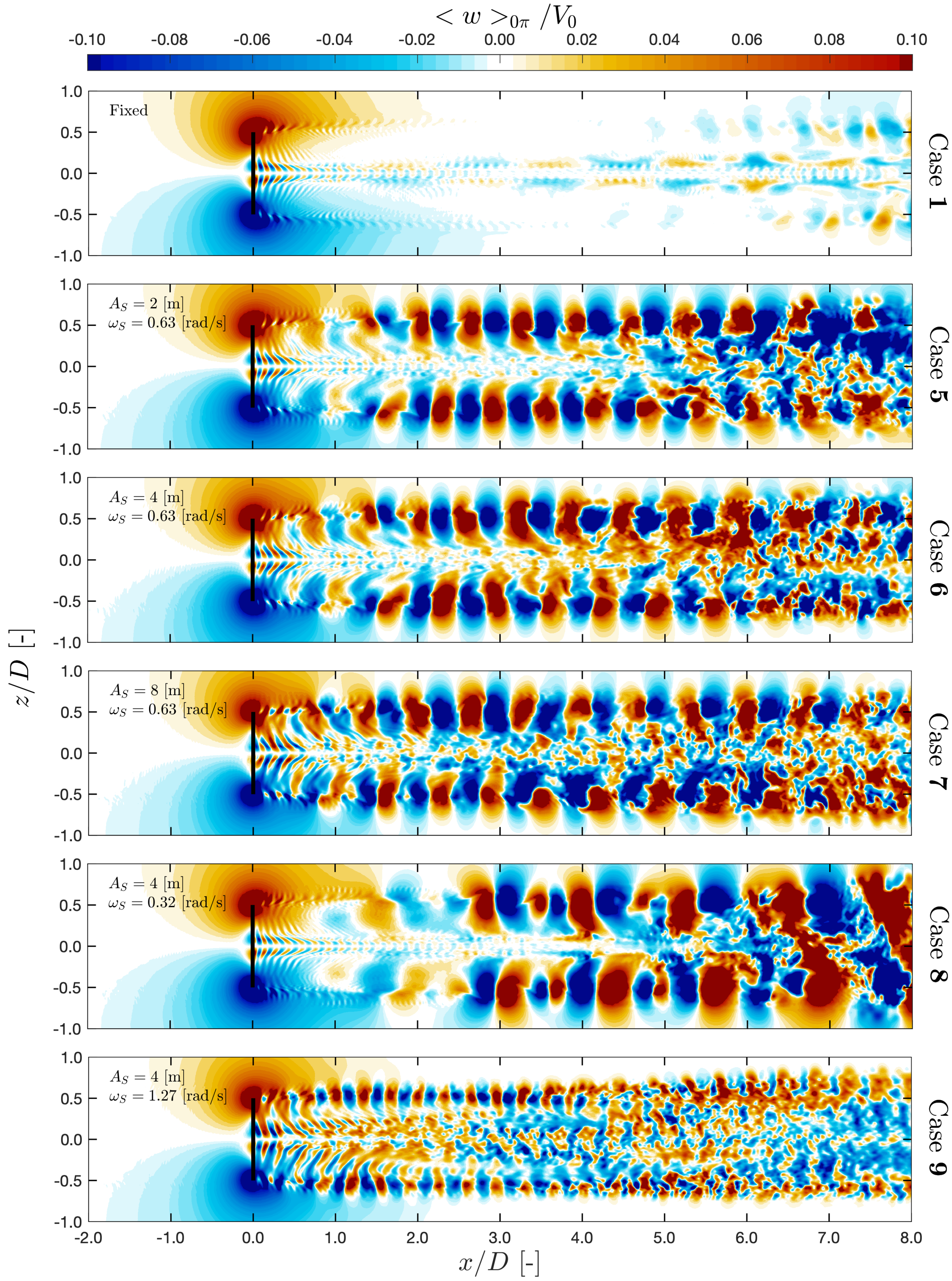

Figure E.8: Fields of phase-locked averaged vertical velocity $< w >_{0\pi}$ for single rotor with different A_S and ω_S under laminar inflow conditions.

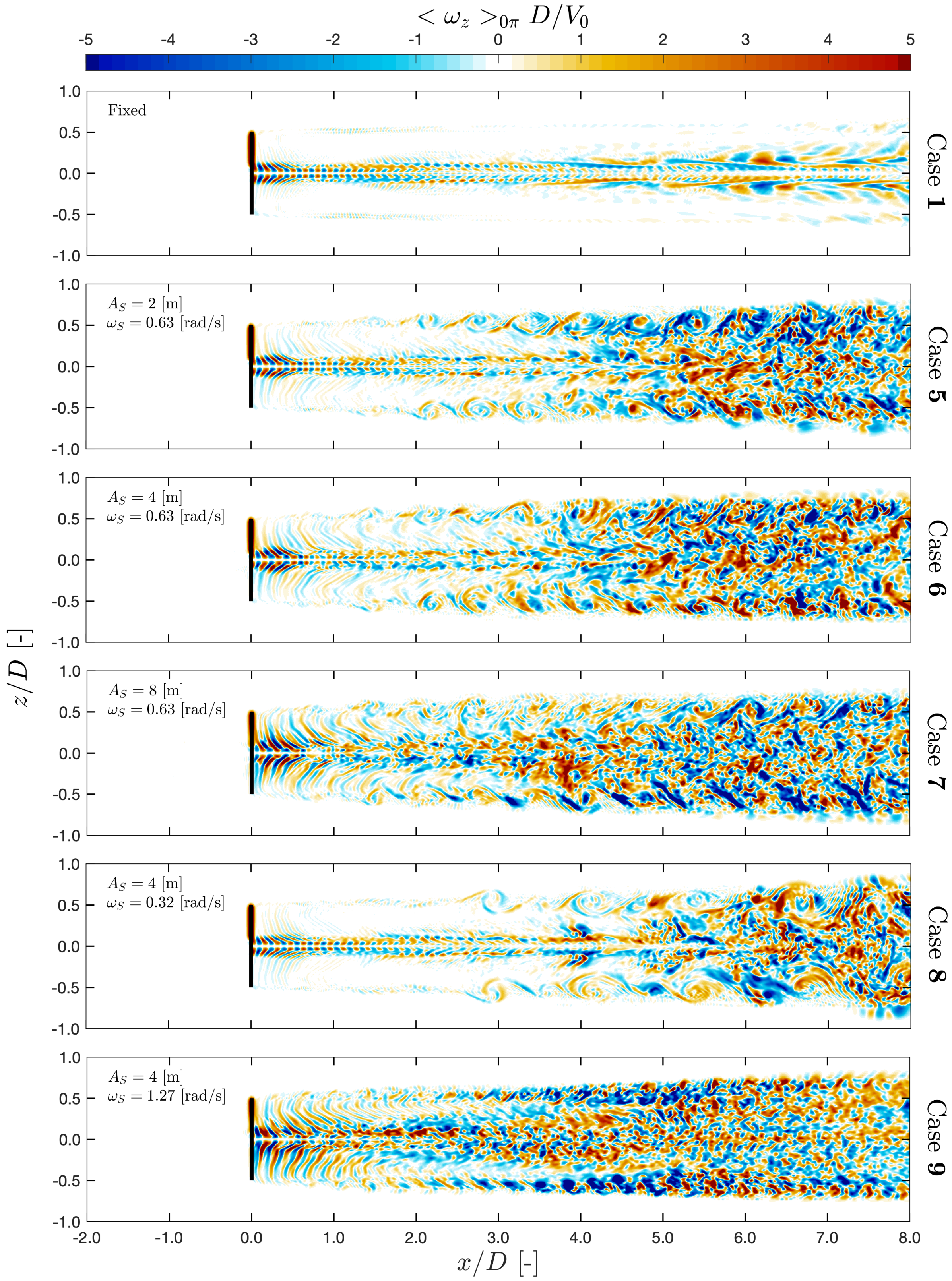

Figure E.9: Fields of phase-locked averaged z-component vorticity $< \omega_z >_{0\pi}$ for single rotor with different A_S and ω_S under laminar inflow conditions.

E.3 Turbulent Inflow Conditions with Different A_S and ω_S

The fields of $\overline{u}$ of the six cases are displayed in Figure E.10. The six cases share very similar structures despite significant different can be seen in fields of $< u >_{0\pi}$ (Figure 4.28).

The fields of $< w >_{0\pi}$ are presented in Figure E.11. Alternating patterns with significant values are once again visible, and the repeating rates clearly related to ω_S. Moreover, the dissipation rates of the structures are higher with higher ω_S and smaller A_S. And now their values attenuate much faster compare to the laminar cases due to the ambient turbulence. As for fields of $\overline{w}$, the six cases share similar patterns, and thus they are not displayed.

The fields $\Delta\overline{p}$ for the six cases are displayed in Figure E.12, and fields of Δp & $< \Delta p >_{0\pi}$ are not shown due to the similarity between the cases considered here. For the fields of $\Delta\overline{p}$, they share similar features as the laminar cases in section 4.3, except that stripes of lower values are not presented. Trend of pressure bubbles for $\Delta\overline{p}$ getting smaller with the cases having bigger $\mathbb{V}$ is also observed in the turbulent cases here.

The fields of $< \omega_z >_{0\pi}$ are presented in Figure E.13. Unlike $< \omega_y >_{0\pi}$, fields of $< \omega_z >_{0\pi}$ here are practically indistinguishable except for the very near wake regions where $< \omega_z >_{0\pi}$ fields reflect the effects of shedded vorticies (cases with larger $\mathbb{V}$ have more significant values). This indicates that $< \omega_y >_{0\pi}$ is the major component of vorticity that surging affects. Note that fields of $< \omega_z >_{0\pi}$ for the laminar cases display periodic structures clearly (Figure E.9).

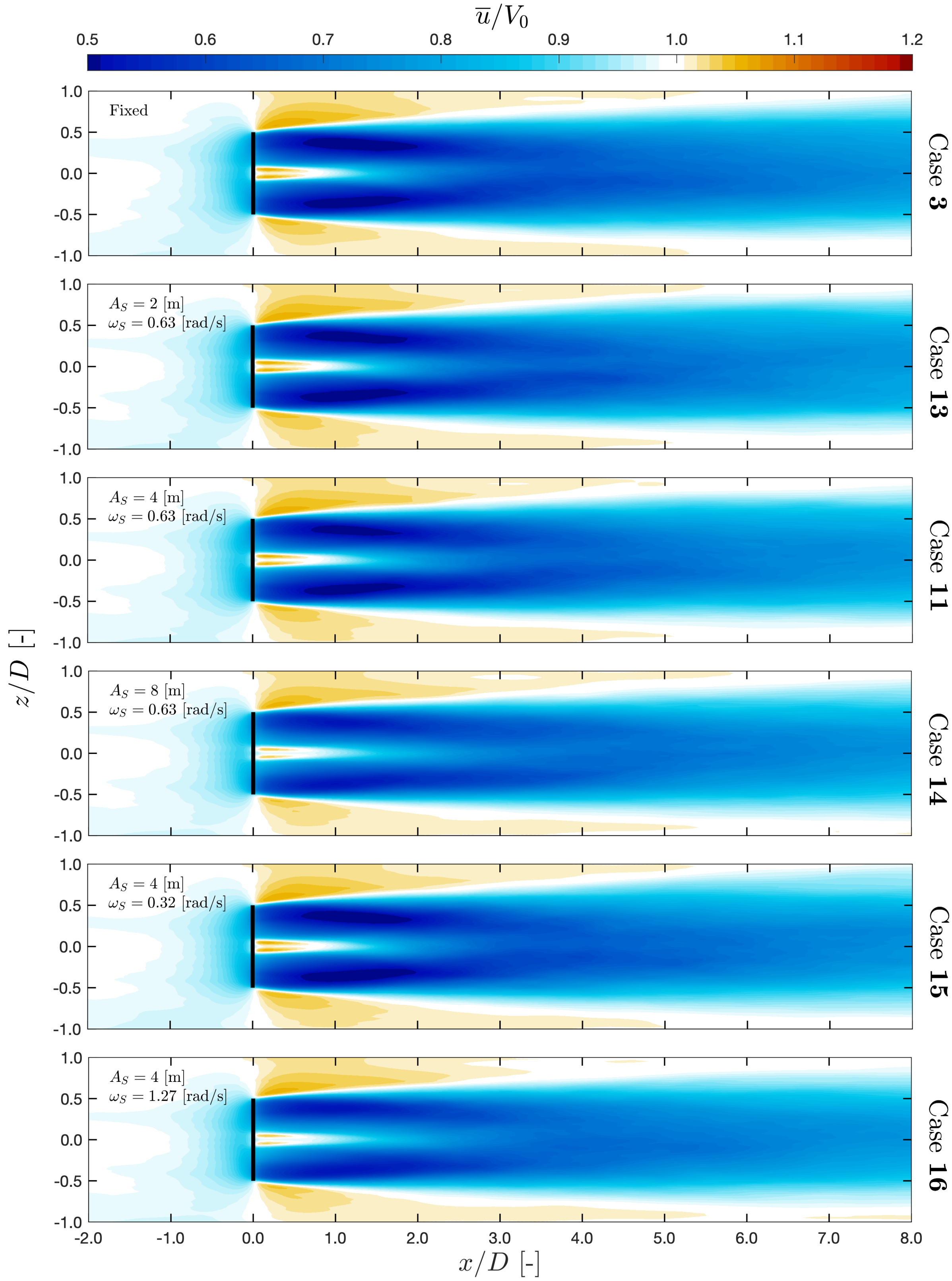

Figure E.10: Fields of time-averaged streamwise velocity $\overline{u}$ for single rotor with different A_S and ω_S under turbulent inflow conditions of TI = 5.3%.

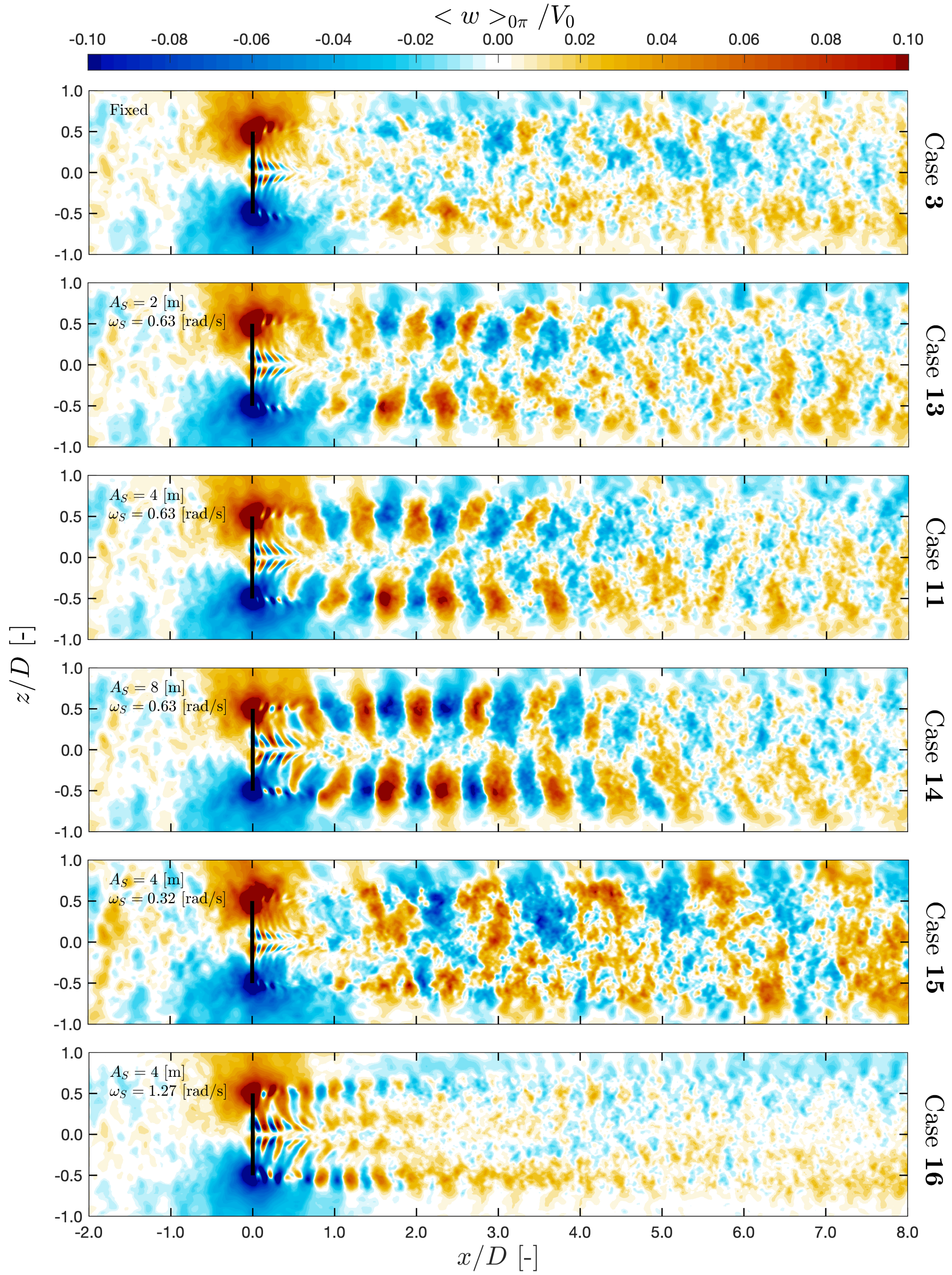

Figure E.11: Fields of phase-locked averaged vertical velocity $< w >_{0\pi}$ for single rotor with different A_S and ω_S under turbulent inflow conditions of TI = 5.3%.

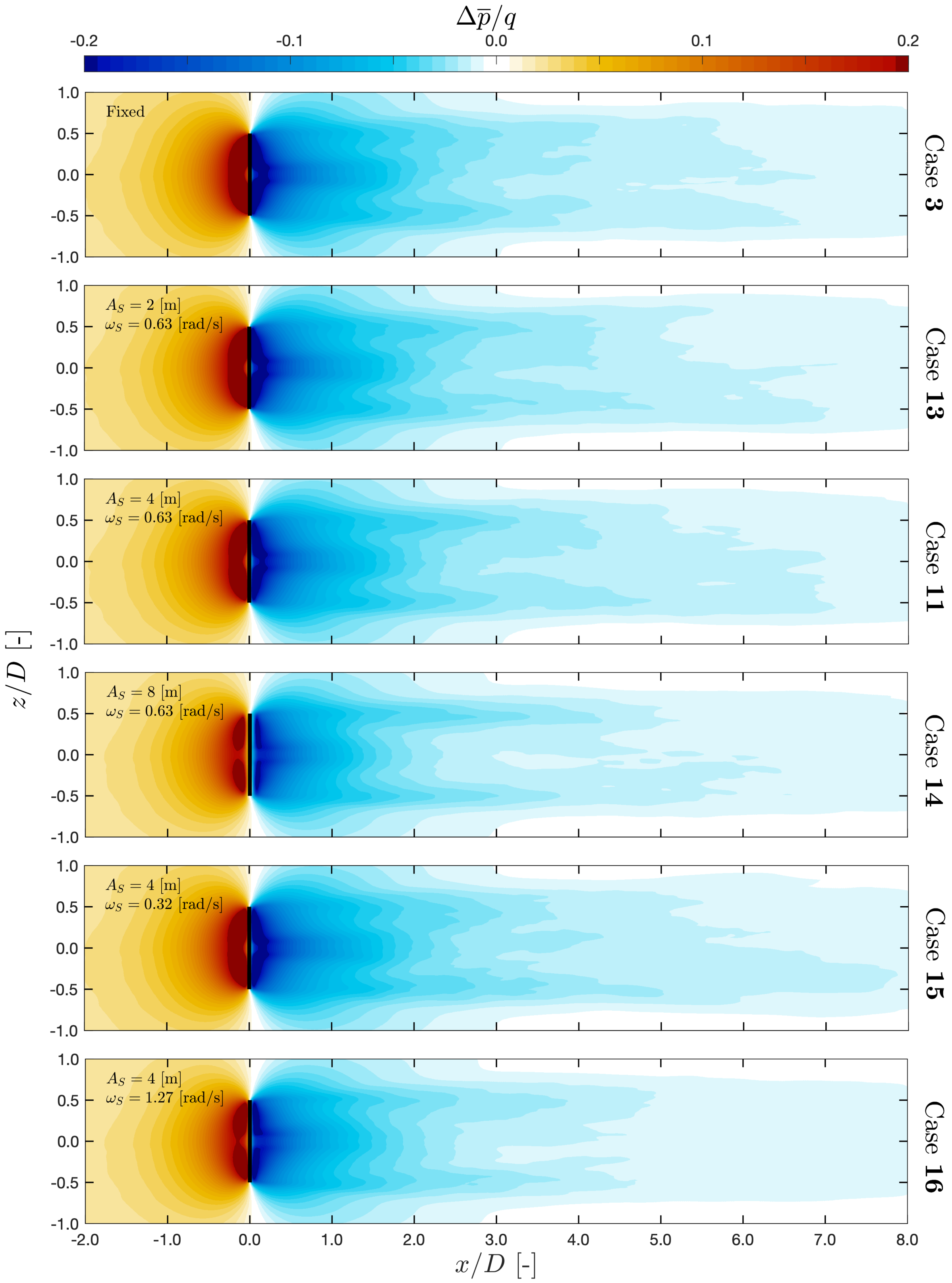

Figure E.12: Fields of time-averaged pressure $\Delta\overline{p}$ for single rotor with different A_S and ω_S under turbulent inflow conditions of TI = 5.3%

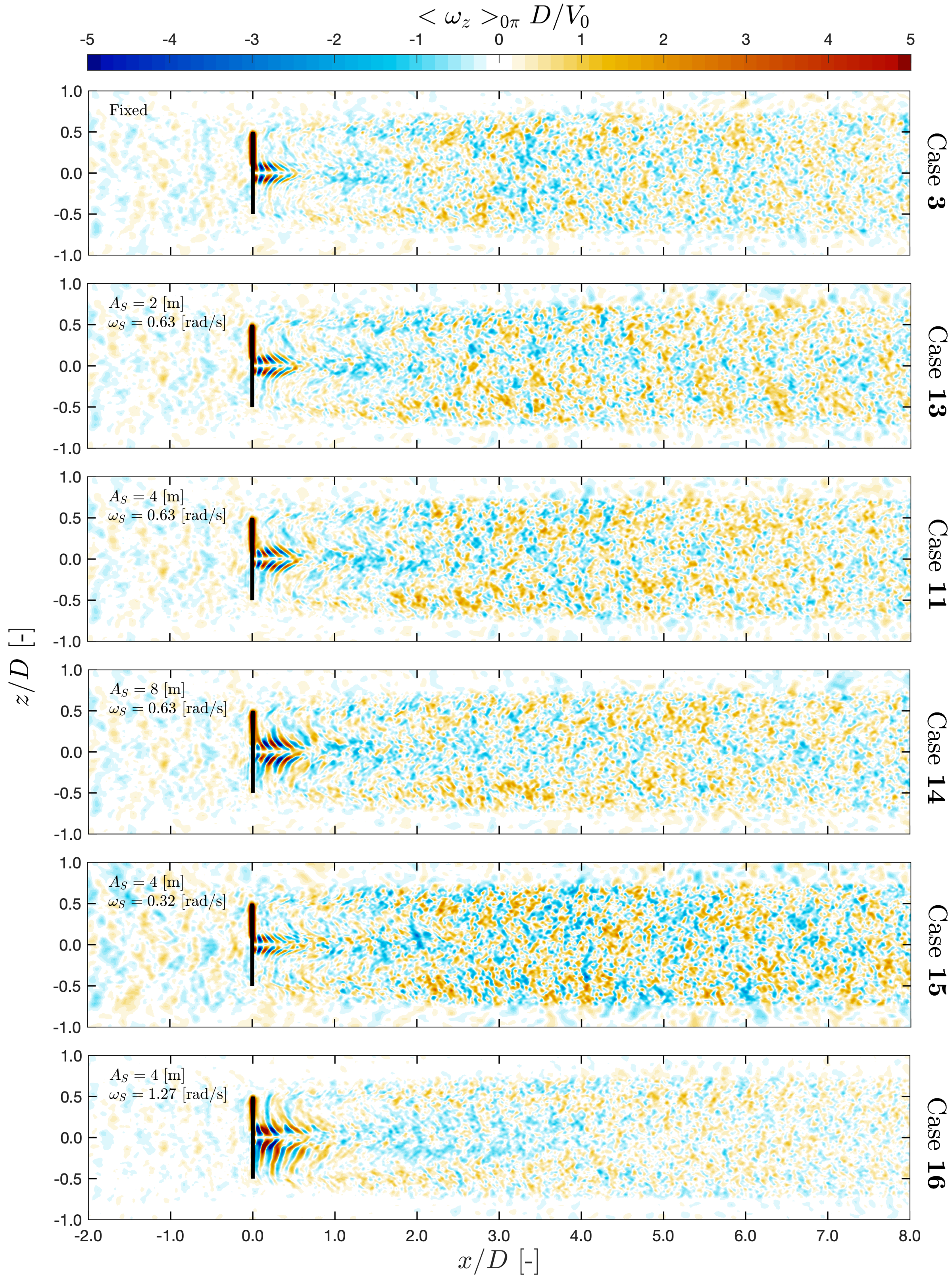

Figure E.13: Fields of phase-locked averaged z-component vorticity $< \omega_z >_{0\pi}$ for single rotor with different A_S and ω_S under turbulent inflow conditions of TI = 5.3%

Appendix F

Supplementary Information for Cases with Dual Rotors

F.1 Combinations of Fixed and Surging with Δ_D being $3D$ Under Laminar and Turbulent Inflow Conditions

Instantaneous fields of Δp are presented in Figure F.1. They present very similar information with u fields in Figure 5.9, both showing the wake structures are mostly affected by the inflow turbulence and conformation of the upstream rotor.

$< \omega_x >_{0\pi}$ and $< \omega_z >_{0\pi}$ fields for the eight cases are displayed in Figure E.5 and E.6. The two fields behave very similar with the cases of single surging rotor (section 4.3 & 4.4), where $< \omega_x >_{0\pi}$ fields indicate the rotation of wake systems and $< \omega_z >_{0\pi}$ fields indicate shedded vorticies. The biggest noticeable different with the cases of single rotor is that values of $< \omega_x >_{0\pi}$ and $< \omega_z >_{0\pi}$ fields are smeared out for the laminar cases in the further downstream regions due to the wake-wake interactions, just as the fields of $< \omega_y >_{0\pi}$.

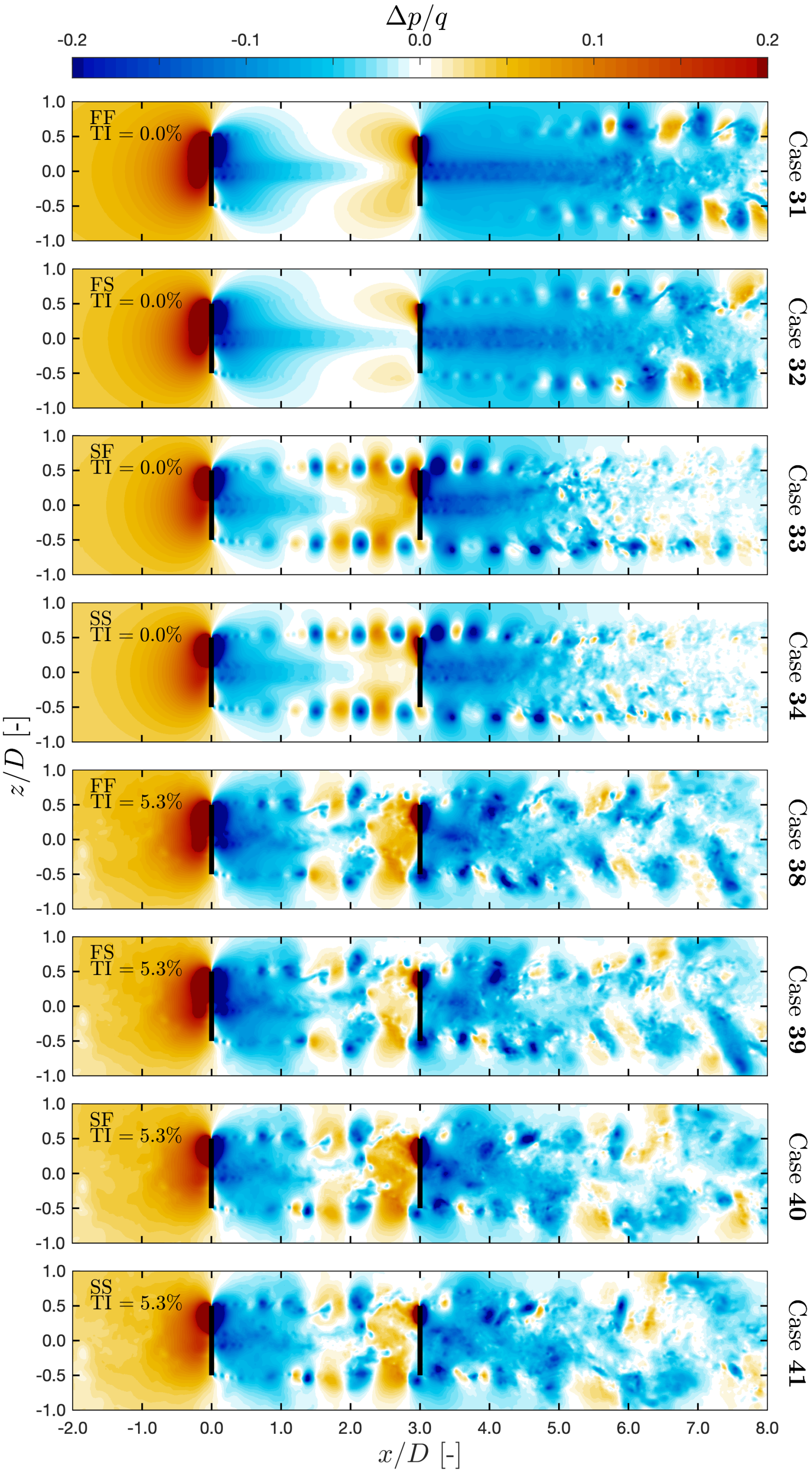

Figure F.1: Fields of instantaneous pressure Δp for dual rotors with $\Delta_D = 3D$ and different surging-fixed combinations.

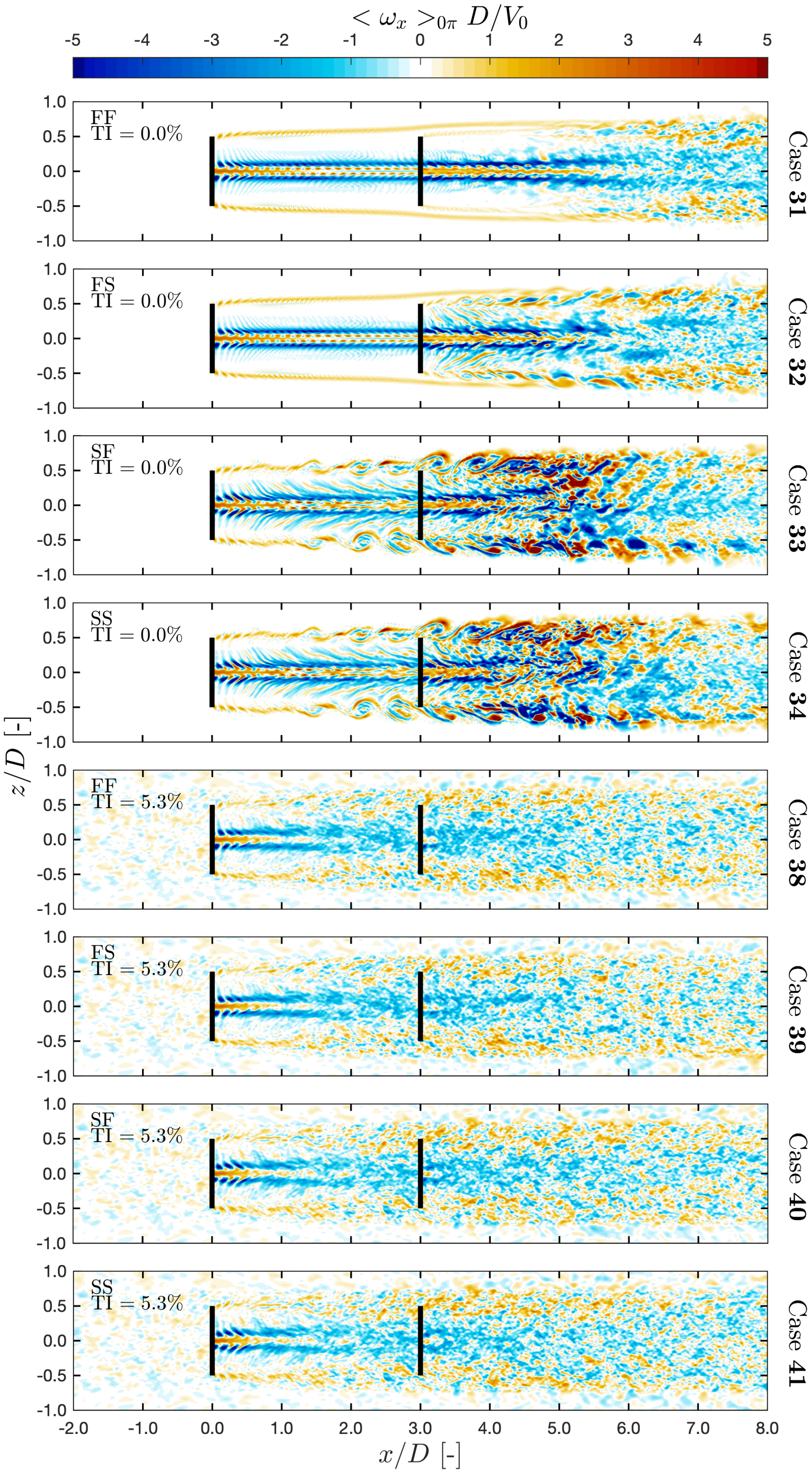

Figure F.2: Fields of phase-locked averaged x-component vorticity $< \omega_x >_{0\pi}$ for dual rotors with $\Delta_D = 3D$ and different surging-fixed combinations.

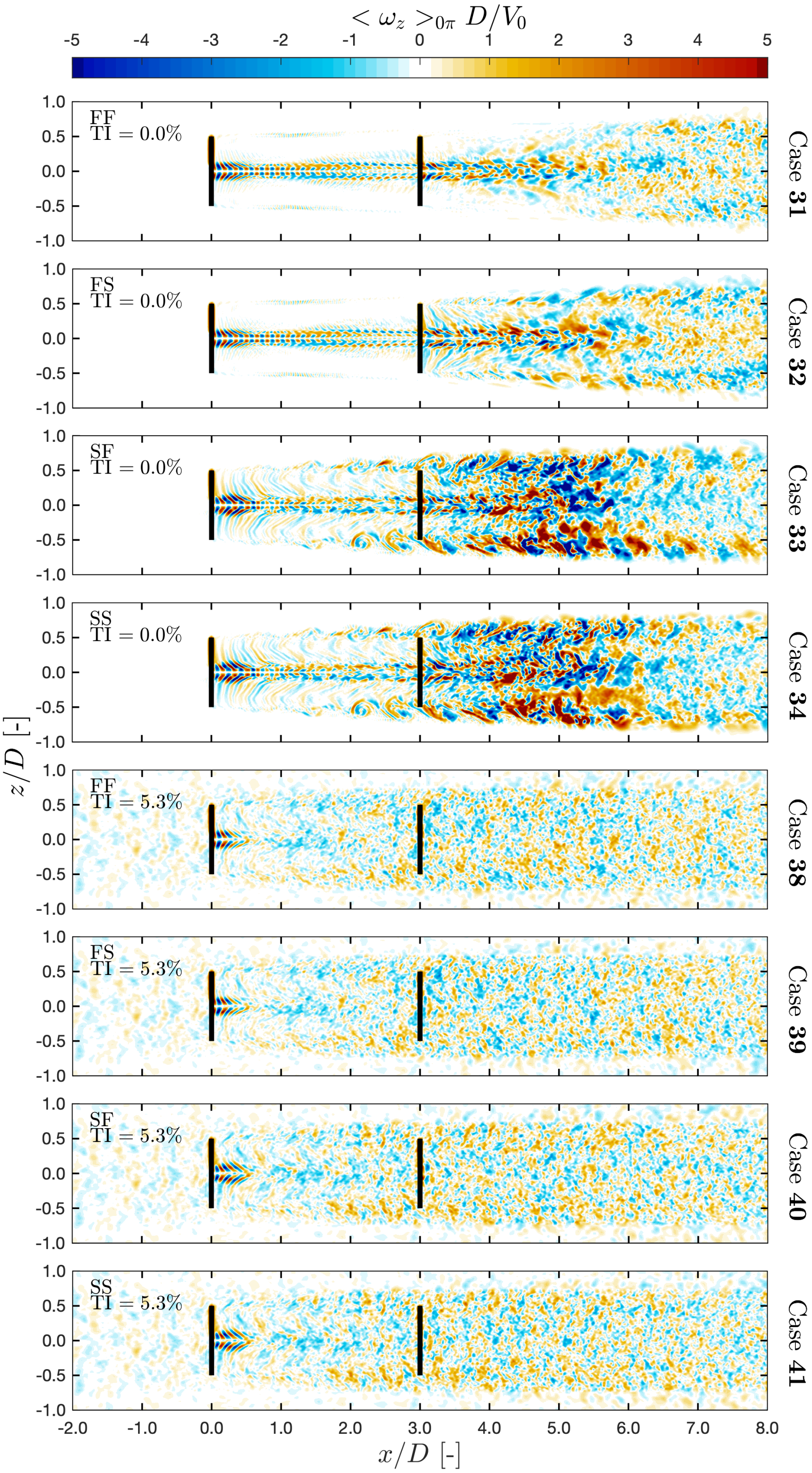

Figure F.3: Fields of phase-locked averaged z-component vorticity $< \omega_z >_{0\pi}$ for dual rotors with $\Delta_D = 3D$ and different surging-fixed combinations.

Appendix G

Supplementary Information for Cases with Simple Controller

In order to better validate the simple torque controller applied in chapter 6 (described in section 2.7), several additional simulations were carried out. The tested aspects includes the responding speed of the controller, quasi-steady states performances, effects of the inertia of the rotor system, behaviours of the controller when subjects to different surging frequencies, and system dynamics when under laminar inflow conditions.

G.1 Inditial Tests

To better understand the effectiveness of the simple torque controller, several additional simulations about the inditial responds of controller were undertaken. For the setups of inditial tests, a single fixed NREL 5MW rotor is placed under the laminar inflow conditions with different inflow velocities V_0 (they are chosen based on the interested $V_{0,\text{app}}$ in this thesis, and the idea is same as the cases in Table 4.2), and the controller was activated at a certain time instant after the system had reached its quasi-steady state; before activating the controller, the rotor is operating with rotational frequency of $\Omega = \Omega_{\text{rated}} = 1.27$ rad/s, which is the Ω for its rated condition. After the activation of the controller, the evolving histories of C_P (both aerodynamic and generator, $C_{P,\text{Aero}}$ & $C_{P,\text{Gen}}$) and Ω are recorded. As the system reached its new quasi-steady state, both $\overline{\Omega}$ and $\overline{C}_P$ (with reference velocity being $V_{0,\text{rated}} = 11.4$ m/s) are examined (called them $\overline{\Omega}^{\text{quasi}}$ & $\overline{C}_P^{\text{quasi}}$); since their targeted values ($\overline{\Omega}_{\text{Tar}}^{\text{quasi}}$ & $\overline{C}_{P,\text{Tar}}^{\text{quasi}}$) can be predicted with Equation G.1, the effectiveness of the controller thus can be evaluated. Moreover, the responding speeds of the controller under different conditions of V_0 can also be studied.

$$\overline{\Omega}_{\text{Tar}}^{\text{quasi}} = \Omega_{\text{rated}} \left(\frac{V_0}{V_{0,\text{rated}}} \right), \qquad \overline{C}_{P,\text{Tar}}^{\text{quasi}} = C_{P,\text{opt}} \left(\frac{V_0}{V_{0,\text{rated}}} \right)^3 \tag{G.1}$$

Table G.1 summarized the results of the cases for inditial tests together with their targeted values. As it can be seen, the values of $\overline{\Omega}^{\text{quasi}}$ & $\overline{C}_{P,\text{Gen}}^{\text{quasi}}$ matched quite well with

$\overline{\Omega}^{\text{quasi}}_{\text{Tar}}$ & $\overline{C}^{\text{quasi}}_{P,\text{Tar}}$, suggesting the controller perform as expected. Figure G.1 plotted out the evolving histories of Ω & C_P, and note that the time frame has been shifted, and that the controller was turned on at $t/T_\Omega = 0$ for all the cases. And as it can be seen from Figure G.1, Ω & C_P needs at least $3T_\Omega$ to $5T_\Omega$ to be settled to the new quasi-steady states (T_Ω is the rotational period of the rated condition), and Abbas et al. [101] also reported a similar time scale for settling down with their inditial test (step increase of V_0 under below rated condition, region 2 in Figure 2.3, note there are differences with the inditial tests carried out in this sections) of NREL 5MW baseline turbine equipped with same controller applied in this thesis using OpenFAST. The responding time is quite long when compared to the ω_S considered in this thesis (for most cases $T_S = 2T_\Omega$), and slow responding speed is one of the major drawbacks of the applied controller [75]. Also that it is very clear that $C_{P,\text{Gen}}$ always lagged behind $C_{P,\text{Aero}}$; and note that before the controller was turned on, $C_{P,\text{Gen}}$ is not considered (or can be viewed as being identical as $C_{P,\text{Aero}}$).

Table G.1: The basic settings and results for cases of inditial tests. These cases have a single rotor operating under laminar inflow conditions with different V_0. Note that the reference velocity for calculation of C_P is 11.4 m/s ($V_{0,\text{rated}}$), not V_0.

Case	$V_0/V_{0,\text{rated}}$	$\overline{\Omega}^{\text{quasi}}$	$\overline{\Omega}^{\text{quasi}}_{\text{Tar}}$	$\overline{C}^{\text{quasi}}_{P,\text{Gen}}$	$\overline{C}^{\text{quasi}}_{P,\text{Tar}}$
91	0.56	0.689	0.704	0.083	0.089
92	0.78	0.974	0.985	0.236	0.244
93	0.89	1.119	1.126	0.357	0.364
94	1.00	1.266	1.267	0.517	0.518
95	1.11	1.415	1.407	0.721	0.710
96	1.22	1.565	1.548	0.976	0.945
97	1.44	1.869	1.830	1.663	1.560

G.2 Inertia Tests

The results in chapter 6 and section G.1 showed that the controller needs a relatively long periods (compared to the interested surging periods) to respond, and the large rotational inertia I of the rotor system (rotor plus drive train) is suspected to be the cause of it. To test the hypothesis, an additional case was ran with smaller rotational inertia, which is 1/50 of the regular rotational inertia. The test case used the setups of case **83**, that is dual rotors with $\Delta_D = 3D$, turbulent inflow conditions with TI $= 5.3\%$, and with $A_S = 4$ m & $\omega_S = 0.63$ rad/s; rotor performances of the two cases are compared, and the results are summarized in Table G.2.

Figure G.2 plots out $< \Omega^{\text{up}} >$ & $< C_P^{\text{up}} >$ for the test case (smaller I) and case **83** (regular I). It can be seen that $C^{\text{up}}_{P,\text{Aero}}$ & $C^{\text{up}}_{P,\text{Gen}}$ for cases with smaller I in Figure G.2b almost follow a same curve, with $C^{\text{up}}_{P,\text{Gen}}$ lagging only a very little bit; this follows the nature of Equation 2.36. And very obvious that the fluctuating amplitude of $C^{\text{up}}_{P,\text{Gen}}$ for the test case is much bigger than the regular case. More interestingly, curve of $< C^{\text{up}}_{P,\text{Gen}} >$ differs quite a lot

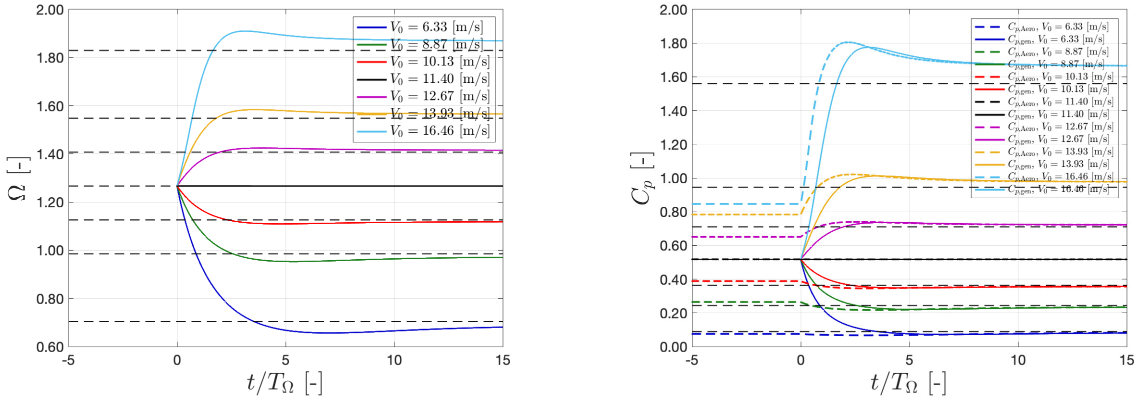

(a) History of Ω (b) History of C_P

Figure G.1: Time histories of Ω, $C_{P,\mathrm{Aero}}$, and $C_{P,\mathrm{Gen}}$ for the cases of inditial tests listed in Table G.1. The controller was activated at $t = 0$, and the horizontal dashed lines are the values of $\overline{\Omega}^{\mathrm{quasi}}_{\mathrm{Tar}}$ & $\overline{C}^{\mathrm{quasi}}_{P,\mathrm{Tar}}$.

with $< C^{\mathrm{up}}_{P,\mathrm{Tar}} >$, even though there are almost no phase difference. This suggest that effects of dynamic inflow might play a bigger role here compare with the surging cases without controller (see Figure 4.19 for the discussions about the dynamic inflow effects of previous cases), and this may related to that now the test case experience changing of Ω, which the cases without controller do not. Additionally, the fluctuating amplitude of $< C^{\mathrm{up}}_{P,\mathrm{Gen}} >$ is bigger than the $< C^{\mathrm{up}}_{P,\mathrm{Tar}} >$, which might related to the overshoot effects that Figure G.1 had already displayed. Lastly, looking the data in Table G.2, it can be seen that $\overline{C}^{\mathrm{up}}_{P,\mathrm{Gen}}$ is even bigger than $\overline{C}^{\mathrm{up}}_{P,\mathrm{Tar}}$ for the test case, suggesting the test case is able to harvest more power than the quasi-steady state solutions. However, unfortunately, very small rotational inertia is unrealistic in the real life.

As for the downstream rotor, $< \Omega^{\mathrm{down}} >$ & $< C^{\mathrm{down}}_{P} >$ are plotted in Figure G.3. In general, $< \Omega^{\mathrm{down}} >$ & $< C^{\mathrm{down}}_{P} >$ behaves very similar compare to the counterparts of the upstream rotor. Moreover, $\overline{C}^{\mathrm{down}}_{P}$ of the test case also out performed the regular case, despite the upstream rotor already had harvested more aerodynamic power from the incoming flow.

The cycle-averaged angle of attack of the upstream & downstream rotor $< \alpha^{\mathrm{up}} >$ & $< \alpha^{\mathrm{down}} >$ for the test case are in Figure G.4. As can be seen, with the controller, the stalling phenomena are greatly alleviated both for the upstream & downstream as comparing to the previous cases (Figure 5.61b, 5.62d, 6.7, & 6.8). However, stalling still occurs as $V_{0,\mathrm{app}}$ become smaller, and this may due to that the driving force ($\tau_{\mathrm{Aero}} - \tau_{\mathrm{Gen}}$) will be smaller when $V_{0,\mathrm{app}}$ is smaller, making the reactions of the rotor slower.

G.3 Responses with Lower ω_S

Since that the inertial (lagging) effects are significant for the implemented controller, an additional test case is carried out with lower ω_S (0.32 rad/s) to briefly evaluate the frequency

Table G.2: The basic settings and results for the cases with smaller I. Another cases with regular I is also listed for comparison. The values for A_S & ω_S are 4 m & 0.63 rad/s.

Case	I [kg m^2]	TI [%]	Δ_D/D	$\overline{C}_T^{\text{up}}$	$\overline{C}_{P,\text{Gen}}^{\text{up}}$	$\overline{C}_{P,\text{Aero}}^{\text{up}}$	$\overline{C}_{P,\text{Tar}}^{\text{up}}$	$\overline{C}_T^{\text{down}}$	$\overline{C}_{P,\text{Gen}}^{\text{down}}$	$\overline{C}_{P,\text{Aero}}^{\text{down}}$	$\overline{u}^{8D}_{\text{Disk}}/V_0$
83	4.39×10^7	5.3	3	0.720	0.530	0.529	0.556	0.267	0.121	0.121	0.739
98	8.77×10^5	5.3	3	0.752	0.581	0.581	0.556	0.279	0.146	0.146	0.749

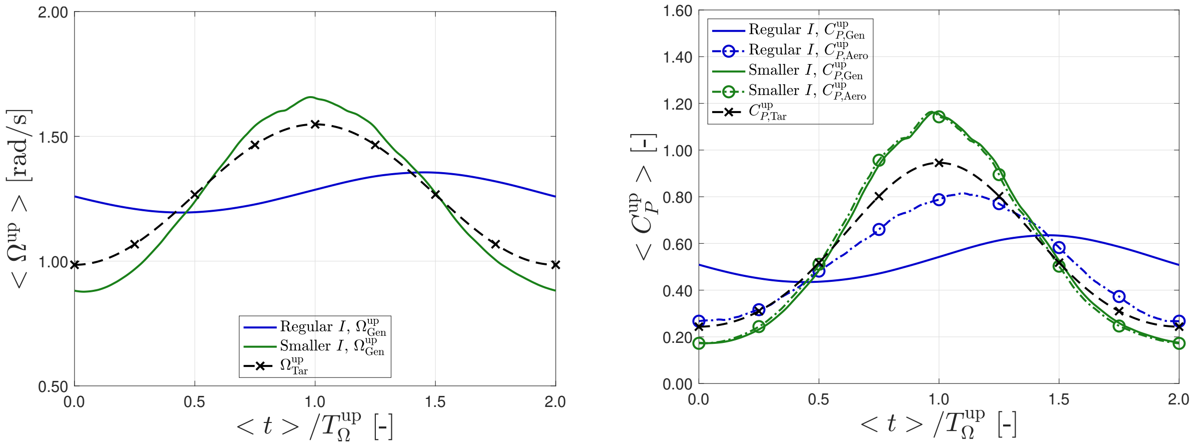

(a) $< \Omega^{\text{up}} >$

(b) $< C^{\text{up}}_{P,\text{Gen}} >$ & $< C^{\text{up}}_{P,\text{Aero}} >$

Figure G.2: $< \Omega^{\text{up}} >$ and $< C_P^{\text{up}} >$ for cases of surging controller rotor with smaller and regular I.

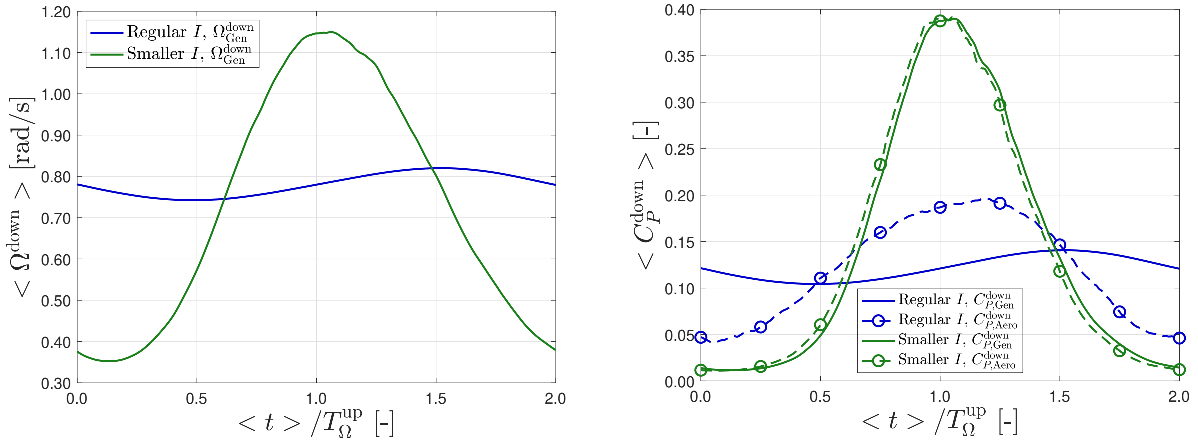

(a) $< \Omega^{\text{down}} >$

(b) $< C^{\text{down}}_{P,\text{Gen}} >$ & $< C^{\text{down}}_{P,\text{Aero}} >$

Figure G.3: $< \Omega^{\text{down}} >$ and $< C_P^{\text{down}} >$ for cases of surging controlled rotor with smaller and regular I.

respond. The parameters and results for the test case are summarized in Table G.3 along with other relevant cases for comparison.

Figure G.5 compared the curves of $< \Omega^{\text{up}} >$ & $< C_P^{\text{up}} >$ of the three cases listed in Table G.3. Two comparisons are focused, the first is having the same value of $\mathbb{V}$ but

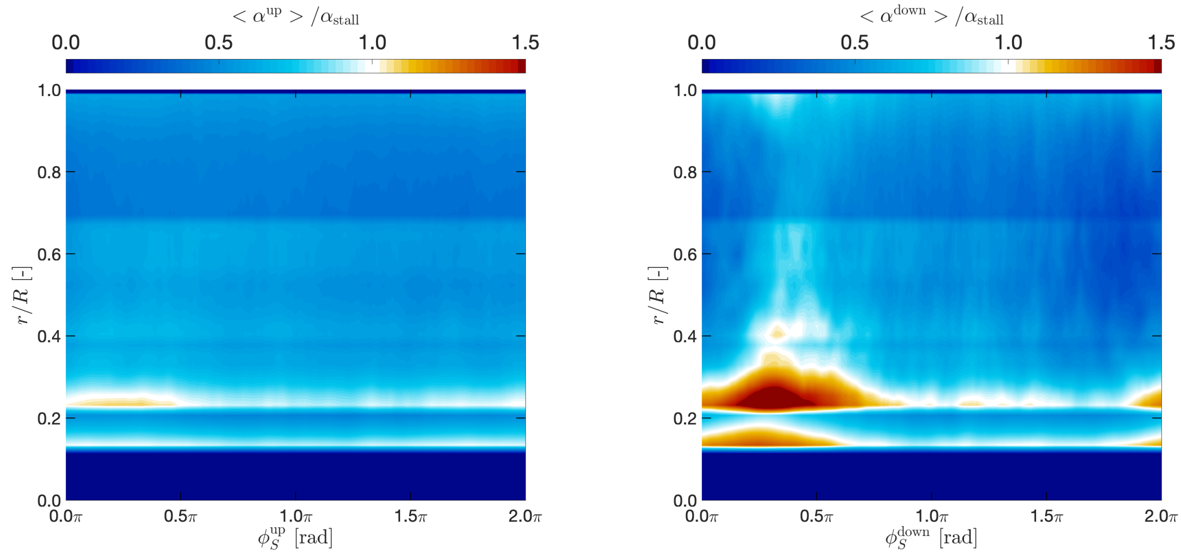

(a) $< \alpha^{\mathrm{up}} >$

(b) $< \alpha^{\mathrm{down}} >$

Figure G.4: $< \alpha^{\mathrm{up}} >$ & $< \alpha^{\mathrm{down}} >$ for the test case with smaller I (case **98**).

different surging settings, the second is having same A_S but different ω_S. For the case with same $\mathbb{V}$, they will share the same curves of $< \Omega^{\mathrm{up}}_{\mathrm{Tar}} >$ & $< C^{\mathrm{up}}_{P,\mathrm{Tar}} >$. Based on the facts that $< C^{\mathrm{up}}_{P,\mathrm{Gen}} >$ for the case with lower ω_S (case **99**) lags the least from its $< C^{\mathrm{up}}_{P,\mathrm{Tar}} >$, the implemented controller is considered to perform more effectively with smaller ω_S. Moreover, considering $\overline{C}^{\mathrm{up}}_{P,\mathrm{Gen}}$ for the case with lower ω_S is closer to the value of its $\overline{C}^{\mathrm{up}}_{P,\mathrm{Tar}}$ compared to case **82**, current controlling strategy may be more beneficial for surging settings with lower ω_S.

Table G.3: The basic settings and results for the cases equipped with the controller subjected different ω_S & A_S.

Case	TI [%]	Δ_D/D	A_S	ω_S	$\mathbb{V}$	$\overline{C}^{\mathrm{up}}_{P,\mathrm{Gen}}$	$\overline{C}^{\mathrm{up}}_{P,\mathrm{Aero}}$	$\overline{C}^{\mathrm{up}}_{P,\mathrm{Tar}}$	$\overline{C}^{\mathrm{down}}_{P,\mathrm{Gen}}$	$\overline{C}^{\mathrm{down}}_{P,\mathrm{Aero}}$	$\overline{C}^{\mathrm{total}}_{P,\mathrm{Gen}}$	$\overline{u}^{8D}_{\mathrm{Disk}}/V_0$
99	5.3	3	4	0.32	0.11	0.524	0.524	0.527	0.132	0.132	0.656	0.724
82	5.3	3	2	0.63	0.11	0.522	0.522	0.527	0.126	0.126	0.648	0.753
83	5.3	3	4	0.63	0.22	0.530	0.529	0.556	0.121	0.121	0.651	0.739

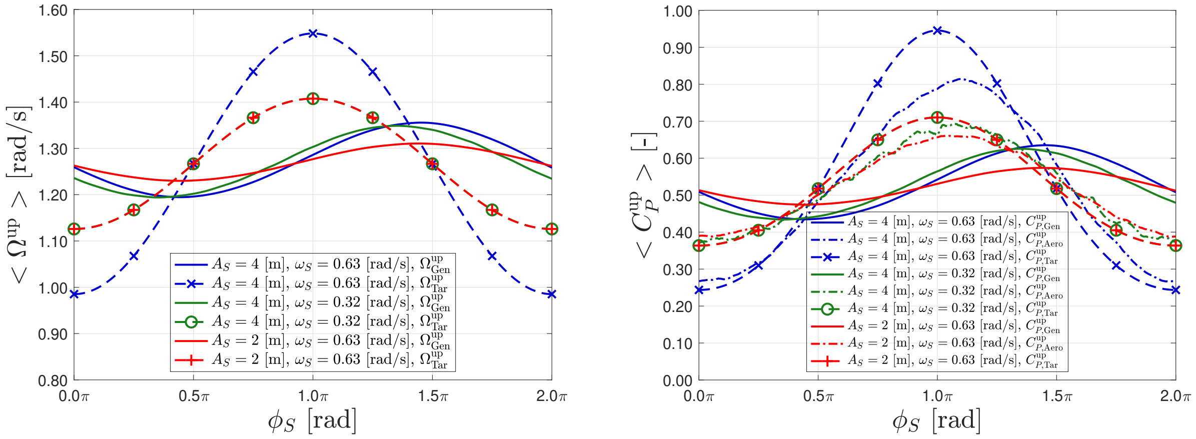

(a) $< \Omega^{\mathrm{up}} >$ (b) $< C_P^{\mathrm{up}} >$

Figure G.5: $< \Omega^{\mathrm{up}} >$ and $< C_P^{\mathrm{up}} >$ for cases of surging controller rotor with different ω_S & A_S.

G.4 Results Under Laminar Inflow Conditions

Two additional cases (cases **100** & **101**) are presented in this section to display the system dynamics of controlled rotors under laminar inflow conditions. Case **100** has two fixed rotors in tandem with $\Delta_D = 3D$ and case **101** has two surging rotors ($A_S = 4$ m & $\omega_S = 0.63$ rad/s) in tandem with same Δ_D, where the both cases are equipped with the same controller applied in chapter 6. The basic settings and results are summarized in Table G.4. Figure G.6 to G.8 plots the u, $< \omega_y >_{0\pi}$, & <TKE>$_{0\pi}$ fields of the two cases together with other selected cases for comparison, including cases without controller under laminar inflow conditions (cases **31** & **34**) and cases with/without controller under turbulent inflow conditions (cases **81** & **83** and **38** & **41**, TI = 5.3%). Figure G.6 shows that u fields are not significantly altered by the controller (comparing cases **100** & **31** and **101** & **34**), and wake recovery are still absent for the controlled fixed case under laminar inflow conditions. Figure G.7 shows that with the controller turned on, the periodic vortical structures (PLSB) will be more preserved after the downstream rotor for the laminar surging case (case **101**) when comparing to the case without the controller (case **34**); this observation comply with the findings in chapter 6, showing that turbulent cases with the controller turned on have sharper PLSB than the ones without the controller. Figure G.8 shows that the values of <TKE>$_{0\pi}$ fields for the laminar cases with the controller are still quite low, but not as low as the cases without the controller, especially at the regions vicinity to the rotors as well as the paths of the convected tip/root voticies. It is as expected that the values of <TKE>$_{0\pi}$ fields very close to the rotors for the laminar cases with controller are higher than those without controller, since with the controller introduced, Ω will not be guaranteed to be exactly a constant, and the phase-locked relationship between Ω and ω_S may not be maintained.

Table G.4: The basic settings and results for auxiliary cases conducted with dual rotors equipped with basic controller under laminar inflow conditions.

Case	TI [%]	Δ_D/D	A_S	$\overline{C}_T^{\mathrm{up}}$	$\overline{C}_{P,\mathrm{Gen}}^{\mathrm{up}}$	$\overline{C}_{P,\mathrm{Aero}}^{\mathrm{up}}$	$\overline{C}_{P,\mathrm{Tar}}^{\mathrm{up}}$	$\overline{C}_T^{\mathrm{down}}$	$\overline{C}_{P,\mathrm{Gen}}^{\mathrm{down}}$	$\overline{C}_{P,\mathrm{Aero}}^{\mathrm{down}}$	${}_{\mathrm{sur}}\overline{G}_{C_P}^{\mathrm{up}}$ [%]	${}_{\mathrm{sur}}\overline{G}_{C_P}^{\mathrm{down}}$ [%]	${}_{\mathrm{sur}}\overline{G}_{C_P}^{\mathrm{total}}$ [%]	$\overline{u}_{\mathrm{Disk}}^{8D}/V_0$
100	**Lam.**	**3**	**Fixed**	**0.725**	**0.515**	**0.515**	**0.518**	**0.194**	**0.062**	**0.062**	–	–	–	**0.497**
101	Lam.	3	4	0.717	0.526	0.526	0.556	0.190	0.066	0.066	2.4	6.3	2.5	0.655

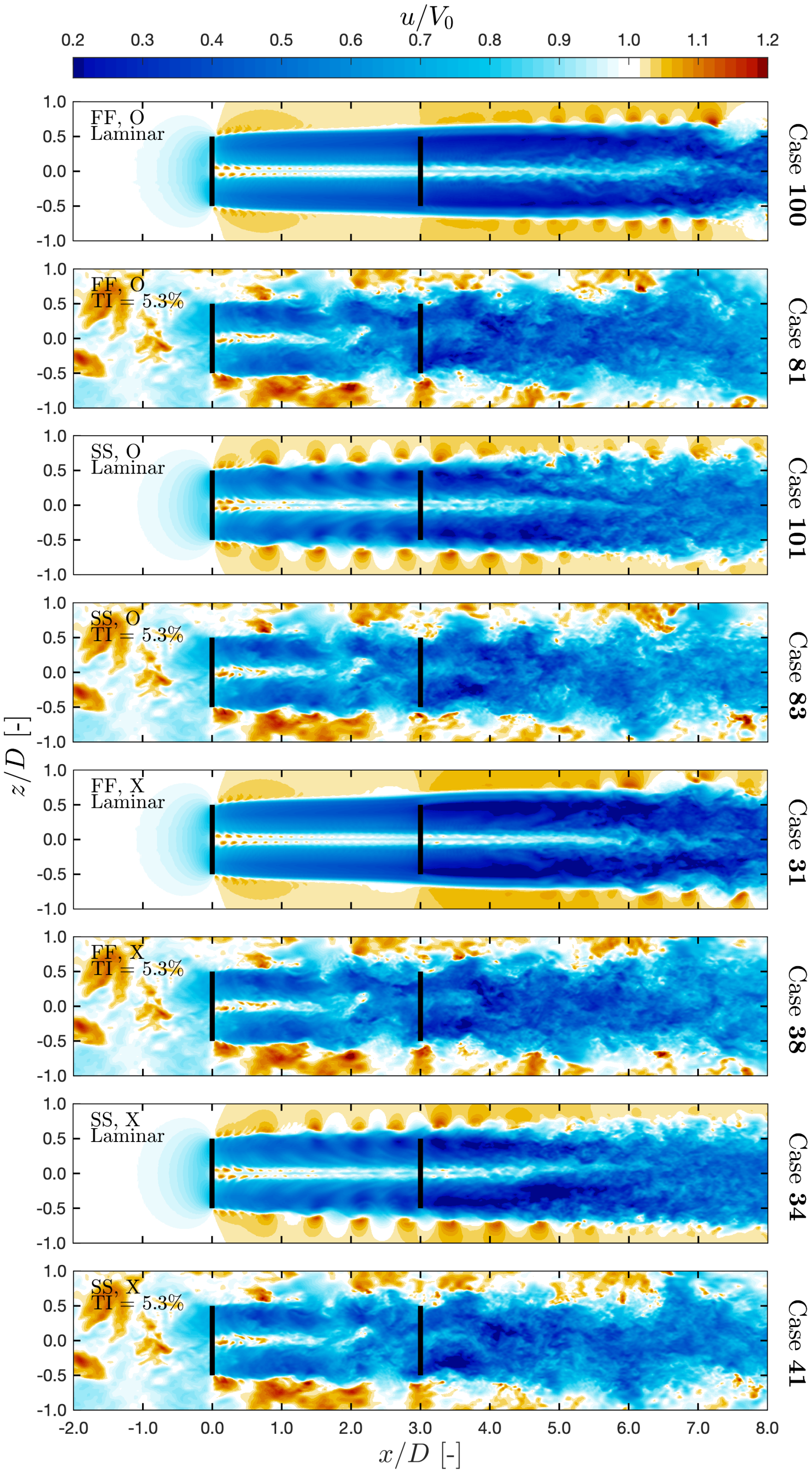

Figure G.6: Fields of instantaneous streamwise velocity u for dual fixed/surging rotors with/without controller under laminar/turbulent inflow conditions.

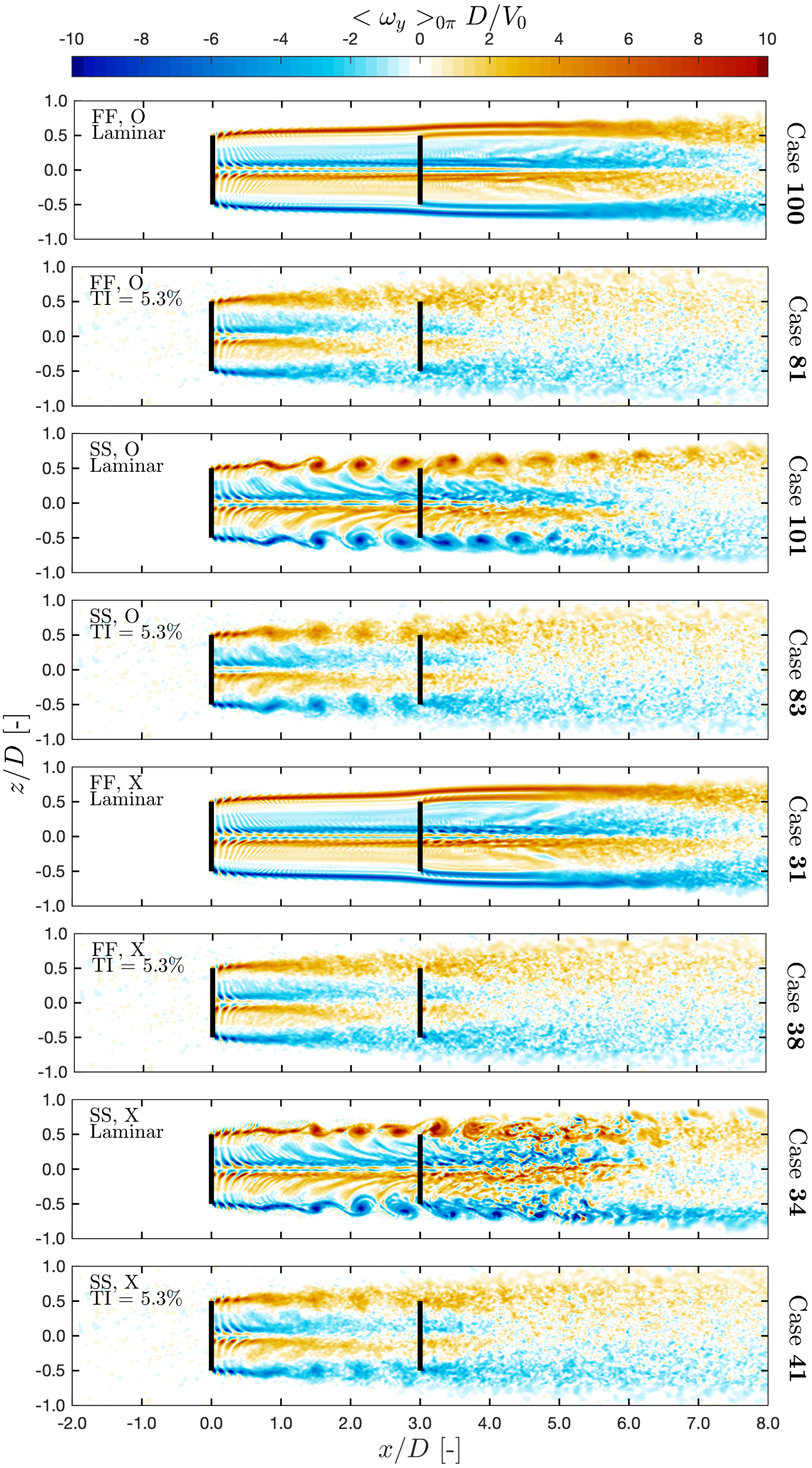

Figure G.7: Fields of phase-locked averaged y-component vorticity $< \omega_y >_{0\pi}$ for dual fixed/surging rotors with/without controller under laminar/turbulent inflow conditions.

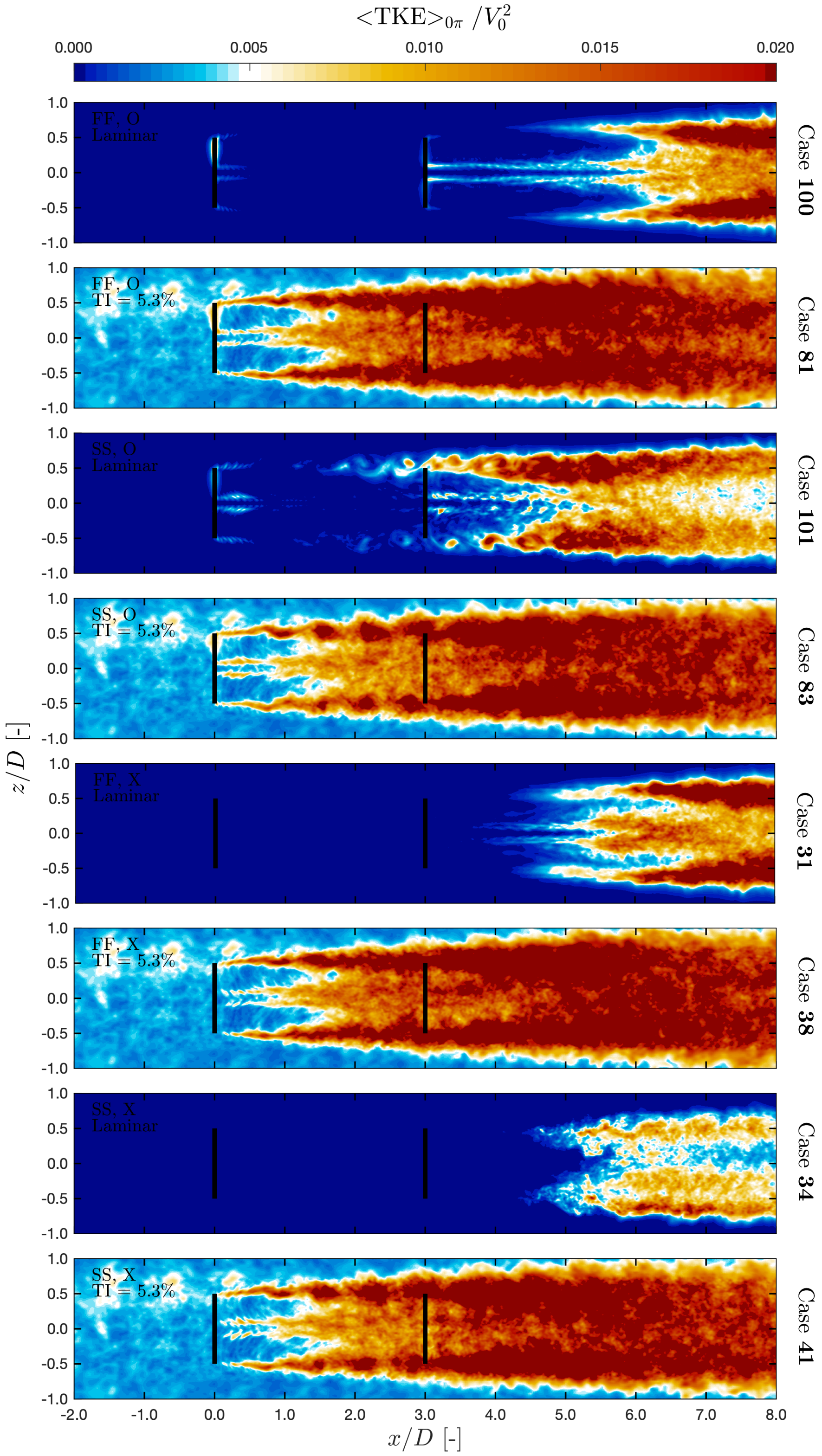

Figure G.8: Fields of phase-locked averaged turbulent kinetic energy <TKE>$_{0\pi}$ for dual fixed/surging rotors with/without controller under laminar/turbulent inflow conditions.

European Wind
Energy Master
Rotor Design

https://www.tudelft.nl/ewem